Computer Aided Medical Procedures
Prof. Dr. Nassir Navab

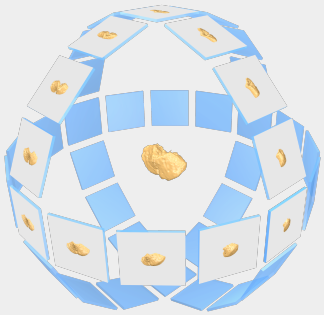

Dissertation

Anisotropic X-ray Dark-field Tomography

Matthias Wieczorek

Fakultät für Informatik
Technische Universität München

Technische Universität München
Fakultät für Informatik
Lehrstuhl für Informatikanwendungen in der Medizin

Anisotropic X-ray Dark-field Tomography

Matthias Wieczorek

Vollständiger Abdruck der von der Fakultät für Informatik der Technischen Universität München zur Erlangung des akademischen Grades eines

Doktors der Naturwissenschaften (Dr. rer. nat.)

genehmigten Dissertation.

Vorsitzende(r):	Prof. Bernd Brügge, Ph.D.
Prüfer der Dissertation:	1. Priv.-Doz. Dr. Tobias Lasser 2. Prof. Dr. Franz Pfeiffer 3. Prof. Dr. Michel Defrise

Die Dissertation wurde am 31.05.2017 bei der Technischen Universität München eingereicht und durch die Fakultät für Informatik am 25.10.2017 angenommen.

Matthias Wieczorek
Anisotropic X-ray Dark-field Tomography
Dissertation, Version 2.0

Technische Universität München
Fakultät für Informatik
Lehrstuhl für Informatikanwendungen in der Medizin
Boltzmannstraße 3
85748 Garching bei München

Zooooooooort

— **Pinky**
Pinky and the Brain

Abstract

Modern X-ray based imaging enables recording of phase-contrast (refraction) and dark-field (Small Angle X-ray Scattering) information using Talbot-Lau interferometry. These X-ray imaging modalities provide improved contrast where standard absorption based imaging only provides poor to none. The task of Computed Tomography (CT) amounts to reconstruction of the physical quantities within the imaged object which caused a specific observation/measurement. A major prerequisite for tomographic reconstruction is first a model of the physical properties, e.g. using scalars, vectors or tensors. Second, a forward model is required which enables simulation of measurements from a given 3D representation of the physical properties. For X-ray based absorption CT, this describes the task of computing the accumulative effect on the X-ray beam traversing through the object. The combination of a forward model and corresponding measurements form an inverse problem. Mathematically, the task of CT corresponds to the inversion of the forward model which can be computed using according numerical methods.

While tomographic reconstruction for modalities different than X-ray CT often employs very similar mathematical concepts, software frameworks are often strictly focused on a specific modality. The first contribution presented in this thesis is the development of an abstract software framework for tomographic reconstruction. Within this framework the numerical methods are implemented independently from the specific forward model which enables adaptation and application of methods for multiple modalities. Additionally, the framework supports the composition of various common approaches such as regularization methods which allows for intensive comparison and evaluation of specific methods for multiple modalities. Within the scope of this work, this framework will be applied to tomographic reconstruction of the dark-field signal.

Reconstruction of the dark-field signal poses a particularly challenging problem, as the scattering within an object depends on the X-ray beam's direction as well as the grating orientation in contrast to absorption and phase-contrast imaging. Thus, the physical quantity at each position cannot be modeled by a scalar entity, but requires a more complex model instead. A first method has been presented previously in form of X-ray Tensor Tomography (XTT) where a rank-2 tensor is used to describe the scattering happening in each location of the measured object. This tensor combines information on the scattering strength as well as its directional distribution which provides an insight into orientation of microstructures within the object.

A major limitation of the XTT approach is that a tensor is restricted to a single microstructure direction. In order to cope with this problem within this thesis a general closed-form, continuous forward model of the Anisotropic X-ray Dark-field Tomography will be presented. This

model contains the XTT model under specific assumptions and in addition enables the tomographic reconstruction of a spherical function representing the whole scattering profile in each location of the object. This novel approach provides strongly improved reconstructions using spherical harmonics. All this is achieved at a computational complexity comparable to that required by XTT. Additionally, an approach to extract the orientation of the microstructures causing the scattering will be presented. Experiments show that the method of AXDT is capable of reconstructing multiple scattering orientations and the corresponding microstructure orientations.

Finally, a first biomedical experiment on a sample of a human cerebellum indicates that AXDT could provide a complementary imaging modality for imaging nerve fibers within the Central Nervous System (CNS).

Zusammenfassung

Moderne Röntgen-Bildgebung ermöglicht Aufnahmen von Phasenkontrast- (Brechung) und Dunkelfeld-Informationen (Kleinwinkel-Röntgenstreuung) mittels Talbot-Lau Interferometrie. Diese Röntgen-Modalitäten bieten einen verbesserten Kontrast in Fällen, in denen die standardmäßig auf Absorption basierende Röntgen-Bildgebung nur schlechten bis keinen Kontrast liefert. Die Aufgabe der Computertomographie (CT) besteht in der Rekonstruktion der physikalischen Größen innerhalb des abgebildeten Objekts, welche eine spezifischen Beobachtung/Messung verursacht haben. Eine wesentliche Voraussetzung für die tomographische Rekonstruktion ist zunächst ein Modell der physikalischen Eigenschaften, z.B. mit Hilfe von Skalaren, Vektoren oder Tensoren. Darüber hinaus ist ein Vorwärtsmodell erforderlich, welches die Simulation von Messungen aus einer gegebenen 3D-Darstellung der physikalischen Eigenschaften ermöglicht. Für Röntgen-basiertes Absorptions-CT stellt sich die Aufgabe, die akkumulierte Auswirkung auf Röntgenstrahlenbündel, welche das Objekt durchqueren, zu berechnen. Die Kombination aus Vorwärtsmodell und zugehörigen Messungen bildet ein inverses Problem. Mathematisch entspricht die Aufgabe der Computertomographie der Inversion des Vorwärtsmodells, die mit Hilfe numerischer Methoden berechnet werden kann.

Während die tomographische Rekonstruktion für andere Modalitäten als Röntgen-CT häufig sehr ähnliche mathematische Konzepte einsetzt, sind Software-Frameworks oft streng auf eine bestimmte Modalität beschränkt. Der erste Beitrag, der in dieser Arbeit vorgestellt wird, ist die Entwicklung eines abstrakten Software-Frameworks für tomographische Rekonstruktion. Innerhalb dieses Frameworks werden die numerischen Methoden unabhängig eines spezifischen Vorwärtsmodells implementiert, welches die Anpassung und Anwendung von Methoden auf weitere Modalitäten ermöglicht. Darüber hinaus unterstützt dieses Framework die Zusammenstellung verschiedener gängiger Ansätze, darunter Regularisierungsmethoden. Dies ermöglicht umfassende Vergleiche und Auswertungen spezifischer Methoden für verschiedene Modalitäten. Im Rahmen dieser Arbeit wird das entwickelte Framework auf die tomographische Rekonstruktion des Dunkelfeldsignals angewendet.

Die Rekonstruktion des Dunkelfeldsignals stellt ein besonders anspruchsvolles Problem dar, da, im Gegensatz zur Absorptions- und Phasenkontrast-Bildgebung, die Streuung innerhalb eines Objektes von der Strahlrichtung und der Gitterorientierung abhängt. So kann die physikalische Größe, an jeder Position, nicht durch eine skalare Entität modelliert werden, sondern erfordert ein komplexeres Modell. Eine erste Methode stellt die „X-ray Tensor Tomography (XTT)“ dar. Innerhalb dieser Methode wird ein Rang-2-Tensor verwendet, um die Streuung in jeder Position des Messobjekts zu beschreiben. Dieser Tensor vereint Informationen über die Streustärke sowie die Richtungsverteilung, welche einen Einblick in die Orientierung der Mikrostrukturen innerhalb des Objekts liefern.

Jedoch besteht eine wesentliche Einschränkung des Ansatzes von darin, dass ein Tensor auf eine einzige Mikrostrukturrichtung beschränkt ist. Um diesem Problem zu begegnen wird innerhalb dieser Arbeit ein neuartiges, allgemeines, geschlossenes und kontinuierliches Vorwärtsmodell für „Anisotropic X-ray Dark-field Tomography (AXDT)“ vorgestellt. Es zeigt sich, dass dieses Modell das XTT Modell unter bestimmten Annahmen enthält und darüber hinaus die tomographische Rekonstruktion einer sphärischen Funktion, welche das Streuungsprofil an jeder Position des Objekts ermöglicht. Dieser neuartige Ansatz ermöglicht mittels Kugelflächenfunktionen deutlich verbesserte Rekonstruktionen. All dies wird bei einer zu XTT vergleichbaren Berechnungsdauer erreicht. Zusätzlich wird ein Ansatz zur Extraktion der Orientierung der Mikrostrukturen, welche die Streuung verursachen, präsentiert. Experimente deuten darauf hin, dass die Methode der AXDT in der Lage ist, mehrere Streuungsorientierungen und die entsprechenden Mikrostrukturorientierungen zu rekonstruieren.

Abschliessend weist ein erstes biomedizinisches Experiment an einer Probe eines menschlichen Cerebellum (Kleinhirn) daraufhin, dass AXDT eine komplementäre bildgebende Methode zur Abbildung von Nervenfasern innerhalb des Zentralnervensystems liefern könnte.

Acknowledgements

The presented thesis concludes my time at Technische Universität München and is the result of several years of research. Throughout the past years there was a steady flow of influences[1] and support which enabled me to present this work. From a retrospective point of view I have realized that many of these influences were of a subtle nature which shaped me as a scientists and therefore indirectly affected this work nonetheless. I would like to take this chance to wholeheartedly thank anyone who contributed to enabling me to write this thesis. These contributions span from family support to scientific arguments and/or simply being a friend.

First of all I kindly thank Tobias Lasser for making me part of his reconstruction group which enabled me to work in this amazing field of research. Thank you Tobias, for providing a PhD environment which I found to be the best for me in succeeding to write this thesis. However, I would have never gotten to know Tobias's group if not for Nassir Navab. I am deeply thankful to Nassir, for supporting and trusting my research for all these years and for drawing my attention to Tobias' group when I became interested in doing a PhD.

The chair of Nassir provided an exceptional environment which allowed for many interdisciplinary influences and discussion, for which I am very thankful. Therefore, I thank every member of the chair for contributing to this environment! Special thanks go to Oliver Kutter, Ahmad Ahmadi, André Aichert, Wolfgang Wein, Jakob Vogel, José Gardiazabal, Bernhard Fürst, Maximilian Baust, Richard Brosig, Oliver Zettinig, Christian Schulte zu Berge, Nicola Rieke, Julia Rackerseder, Sebastian Pölsterl, Ralf Stauder, Christoph Hennersperger, Martina Hilla, and Dennis Hilla. Furthermore, I want to thank all the exceptionally talented students which I had the pleasure to supervise. Special thanks go to Anca Stefanoiu, Nathanael Schilling, David Frank, Maximilian Endrass, Tushar Upadhyay, Maximilian Hornung, Julian Viereck, and Hessam Roodaki.

The kind of interdisciplinary research as presented here would never have been possible if not for the great and close collaboration with the chair of Franz Pfeiffer. Thank you Franz, for giving me the opportunities that have originated from this collaboration. Many thanks go to all members of this chair. Special thanks go out to Elena Eggl, Julia Herzen, Klaus Achterhold, and Jonathan Schock.

[1] I took the chance and included some of the influences originated from series in form of quotes throughout this thesis.

Directly related, I am also very thankful for the two interdisciplinary meeting groups of first the "XTT/AXDT meeting" of Tobias Lasser and second the "Recon meeting" of Peter B. Noël. Both provided grounds for many interesting arguments. I therefore want to thank Florian Schaff, Christoph Jud, Yash Sharma, and Saeed Seyyedi. Particularly big thanks again to Florian Schaff. Our arguments led to the main ideas presented in this thesis. Furthermore I highly thank Sebastian Allner, Andreas Fehringer, Lorenz Hehn, Mathias Marschner, Wolfgang Noichl, Maximilian v. Teuffenbach, Korbinian Mechlem, Felix Kopp, Kai Mei, Fabio De Marco, Nicolas Triltsch, Clemens Schmid, Sebastian Ehn, and Thorsten Sellerer. I want to particularly thank Peter and Tobias for providing this frame for countless valuable debates.

Furthermore I want to thank those who shaped my mathematical understanding of the topic of Computed Tomography. Thanks for debate, feedback, and the great collaboration go to Laurent Demaret, Jürgen Frikel, Martin Storath, Andreas Weinmann, and Per Christian Hansen.

I also thank Thomas Köhler for various input and discussions, Daniela Pfeiffer for providing clinical insight into modern medical imaging, and Philipp Bruckbauer for providing me with carbon fibers. Furthermore I want to thank A. Winkler for providing the Brainer project and M. Hortsch for his attempt to provide me with an access to the histology dataset from the University of Michigan.

What remains is to thank the most important group of people whose steady stream of love and support made this possible – my family and friends. Thank you so much! Special thanks to my parents for everything! It was because of you that I was able to go to university in the first place, and it was you who supported me throughout the whole adventure. It is hard to express how thankful I am but rest assured that I am more than glad to be your son! Additionally, I want to thank all of my family, my grandparents, my sister and her boyfriend, as well as my mother in law and her husband. Each one of you contributed to this thesis in their own way and I am really glad that you all are part of my life. Furthermore, many thanks to all my friends! It is a pleasure to have you and I always enjoyed the time we spent together. Special thanks at this point to Stephanie Ehrenberg and Martin Jungowski for proofreading this thesis.

Finally, I want to thank my wife for all her love and support throughout all these years! It is my greatest pleasure to discuss ideas with you and I highly value your input. Many ideas throughout the last years originated from our debates and I am highly thankful for every single second we spent together. You've helped me to become the person I am today and without you, my love, this would have never been possible. Thank you so much!

Contents

Part I

Introduction

1 Introduction

> *. . . where no man has gone before*
>
> **— opening credits**
> Star Trek: The Original Series

To me, one of the most impressive visions for non-invasive medical diagnostics and non-destructive material analyzing, is presented in *Star Trek: The Original Series* (1966–1969). During several occasions throughout the series so-called *tricorders* are used in order to scan, analyze, and record data. All of these three purposes are achieved in a non-destructive manner and the device is used for inorganic and organic matter as well as medical purposes.

At the very beginning of the aforementioned *scanning and analyzing*, an object needs to be observed/sensed. Among others, the ability to *see*, i.e. to sense and analyze the information of the spectrum of visible light (compare fig. 1.1) and how it interacts with material, is a natural example of the human ability to achieve exactly what is described above.

However, the ability to sense naturally is limited. E.g. as long as you are restricted to this modality of sensing, gaining insight into objects which are opaque to the visible light spectrum is only possible if the object is opened. Throughout history some of the major advancements in sensing have been achieved by the discovery of means to sense additional parts of the electromagnetic spectrum (an illustration is given in fig. 1.1). Due to the close relation to "sight" the following methods are typically referred to as imaging methods.

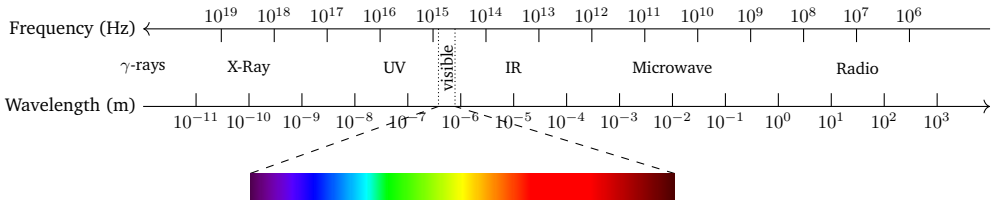

Figure 1.1 Electromagnetic spectrum

One of the most significant discoveries in order to overcome the borders of natural sight was the discovery of X-rays by Wilhelm Conrad Röntgen (1845–1923) in 1895 [309] (engl. translation [308]). Compared to visible light, the energy of X-rays is much higher, i.e. the wavelength is much lower (in the magnitude of 0.01 to 10 nm). Therefore, this spectrum of electromagnetic waves is capable of penetrating matter that is opaque to the spectrum of visible light (see fig. 1.1 for an overview of the Electromagnetic spectrum). In his initial publication Röntgen presented the very first radiography of his wife's hand, showing the finger bones and a ring. This finding marks the birth of modern non-invasive imaging methods and represents an enormous breakthrough for scanning and analyzing materials. For his discovery

of X-rays, Röntgen was rewarded with the very first Nobel Price in 1901 [on16]. While Röntgen (c.f. [309]) tried to measure refraction and scattering using prisms and powdered samples, the only effect which he was able to observe was the absorption of X-rays, i.e. the intensity loss of an X-ray beam while traversing the object. X-ray absorption based radiography soon became a standard tool for Non-Destructive Testing (NDT) and medical diagnostics up until today.

This discovery provided a huge advancement in the field of sensing objects as it was now possible to sense and analyze objects which are opaque to sight. This incredible improvement aside radiography suffers from one major drawback[1] – the projective nature of radiographic images. After an X-ray beam passed through an object, the measured intensity of this beam corresponds to the accumulated absorption information along the whole path through the object. Consequently, essential depth information is lost and radiologists for example have to rely on training and experience to correctly interpret X-ray radiographs.

For roughly 70 years there was an ongoing effort of refinement and improvement of systems. Many of these advancements targeted the improvement of the subsequent analysis drawn from this imaging modality. As a disquisition on these developments would go far beyond the scope of this thesis we refer the interested reader to the book *From the Watching of Shadows* by S. Webb [372].

We skip these years and move directly to 1963. In 1963 and 1964 Allan M. Cormack (1924–1998) [106, 107] described a method to mathematically invert the imaging process happening in X-ray imaging. This method enabled the observer to restore a function representing the individual effects on the X-ray beam in each single position within the measured object. It became clear later on that Cormack had partially reinvented mathematical principles which had already been studied in 1917 in a pure mathematical context by Johann Radon (1887–1956) [286, 287]. Based on the work of Cormack, Sir Godfried Hounsfield (1919–2004) [184] developed the first scanner for Computed Tomography (CT) in the 70's. For their contribution both Cormack and Hounsfield were rewarded with the Nobel Price in Medicine 1979 [108, 185].

Meanwhile, in the visible light regime Frits Zernike (1888–1966) developed phase-contrast microscopy in 1935 [389, 390, 391]. This imaging modality benefits from the fact that a beam of electromagnetic waves, such as light, is not only changed with respect to its intensity but also its phase when traversing through an object. This imaging technique provided contrast especially for regions which showed poor to none visibility with the previously existing methods. For this remarkable finding, Zernike was granted the Nobel Price in 1953 [392].

Due to the weak interaction of X-rays in comparison to visible light it took roughly 60 years to adapt this concept for X-ray imaging (c.f. [279]). This was enabled by the development of the first X-ray interferometer in the 1960s by Bonse and Hart [68]. Several methods were developed to enrich X-ray imaging with the additional phase-contrast. However, these methods were limited to highly brilliant synchrotron sources which provide monochromatic and coherent radiation.

[1] Beside its ionizing nature, obviously.

This changed dramatically with the work of Momose, Weitkamp, and Pfeiffer who proposed a Grating Based Imaging (GBI) system based on Talbot-Lau interferometry [255, 256, 278, 279, 373]. For the very first time this system allowed for the imaging of the additional phase-contrast and dark-field using X-ray sources and detectors as used for example in modern clinical radiology.

Before we take a closer look at modern X-ray imaging and possible applications we want to briefly summarize what exact effects cause the X-ray beam to change.

1.1 Inside X-ray Imaging

The key basics of X-ray based imaging is that the interaction of this highly energetic electro-magnetic wave and matter is comparably weak, i.e. X-rays are able to traverse matter which is opaque to e.g. visible light. Directly equivalent to photography, the key concept of X-ray based imaging is that properties of the X-ray beam are modulated while traversing material. The task of CT requires understanding of the effects caused by the observed modulations.

In the special case of X-ray imaging we therefore need to consider how the properties of the X-ray beam are changed while traversing through an object. Consequently, we are going to provide an overview on the microscopic and macroscopic interactions of X-ray photons/beams with matter below. The following summary is based on [37, 78, 160, 271, 366, 370] and many discussions within our X-ray Tensor Tomography (XTT)/Anisotropic X-ray Dark-field Tomography (AXDT) group[2]. The interested reader therefore may refer to these works for a more detailed view on these topics.

On the microscopic scale the interaction of X-rays with matter comes down to the interaction of X-ray photons and the electrons of an atom. Depending on the kind of interaction one typically distinguishes between **photoelectric absorption**, **Thomson-** (elastic) and **Compton** (inelastic) **scattering**, and **pair production**. The significance of the single effects varies first of all with the wavelength λ and thus the energy[3] of the involved X-rays. Second, it also depends on the matter with which the interaction takes place.[4] For the wavelengths considered within the scope of this thesis and especially for the experiments which were carried out in the context of part IV, the two dominant effects are **photoelectric absorption** and **Thomson scattering** (see fig. 1.2 for an illustration).

Photoelectric absorption (see fig. 1.2a) is caused if an incoming X-ray photon is absorbed by an electron. The absorbed energy of the photon causes the electron to leave the orbit. The atom is left behind ionized. Consequently, the total amount of absorption is linked to the number of electrons within the object. Additionally, it depends on the energy of the X-ray photons [78].

[2] Special thanks to F. Schaff for many valuable discussions.
[3] The energy of an electro-magnetic wave is given as $E = hc/\lambda$ with $c = 2.998 \times 10^8\,\mathrm{m\,s^{-1}}$ denoting the speed of light, and $h = 4.136 \times 10^{-15}\,\mathrm{eV\,s}$ denoting Planck's constant.
[4] See [78, p. 41ff] for plots of the relevance of these effects depending on the energy and several materials.

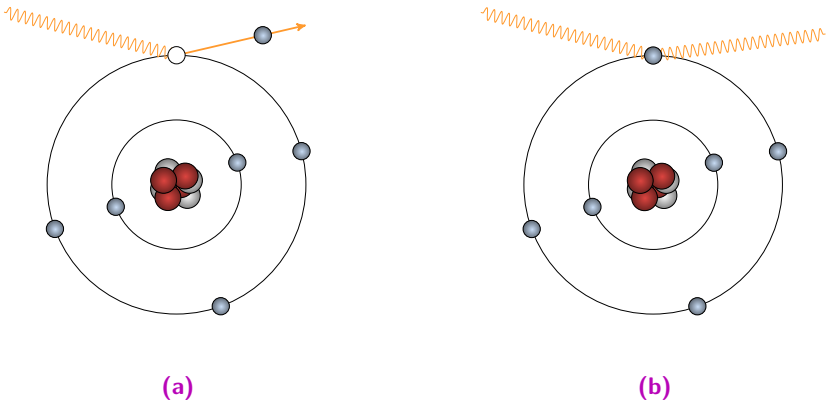

(a) (b)

Figure 1.2 Illustration of the main X-ray interaction with matter for the energies considered within the scope of this thesis. (a) shows the photoelectric absorption of an X-ray photon by an electron of the outer shell. In (b) we display the case of elastic scattering, i.e. Thomson scattering.

On a macroscopic level the linear attenuation coefficients $\mu : \mathbb{R}^3 \to \mathbb{R}$, which provide a scalar map of the amount of absorption happening in each location $x \in \mathbb{R}^3$ within an object, are introduced. The intensity of an X-ray beam after traversing a sample on path L is given according to the Beer-Lambert law (c.f. [78, p. 32f]),

$$I = I_0 \exp\left(-\int_L \mu(x)\, dx\right), \tag{1.1}$$

with I_0 denoting the initial intensity of the X-ray beam[5]. In fig. 1.3 this law is illustrated for a piece-wise constant linear attenuation.

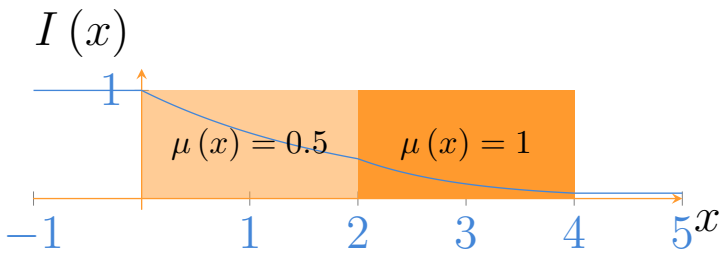

Figure 1.3 Illustration of the Beer-Lambert law for a piece-wise constant linear attenuation μ, $\mu(x) = 0.5$, for $x \in (0, 2)$ and $\mu(x) = 1$ for $x \in (2, 4)$. The initial intensity was fixed to $I_0 = 1$.

Due to the weak interaction of X-rays with matter, absorption based imaging was for a long time the only and still is the predominant X-ray based imaging method – e.g. for medical applications. The relation to the number of electrons and therefore the atomic number of the material effectively states that objects with a high density lead to stronger absorption than objects with a lower density. Consequently, in medical diagnostics one obtains strong contrast for strongly absorbing tissue, such as bones, while soft tissue provides low to no contrast.

Thomson scattering (see fig. 1.4) is the elastic scattering of X-rays by electrons. In this case of X-ray matter interaction, an incoming X-ray photon causes the electron to oscillate. This

[5] To be precise, this formula neglects the polychromatic X-ray spectrum emitted by common tubes. While more accurate models for polychromatic cases exist, this is still the commonly applied model.

causes the oscillating electron to emit dipole radiation. There is no absorption, i.e. energy loss, involved, and consequently the emitted radiation has the same energy as the incoming X-ray. This also explains why this process is called elastic scattering.

Moving from a single X-ray photon to an X-ray beam a common simplification is the first Born approximation – only a single-scattering is considered along an X-ray traversal. Scattering of multiple X-rays of a beam at different locations by the same angle results in a phase-shift between these X-rays. This phase-shift is linked to the momentum transfer vector q. Modeling the incoming and the scattered X-ray beam by their wave-vectors k_{in}, k_{out} the vector q is illustrated in fig. 1.4.

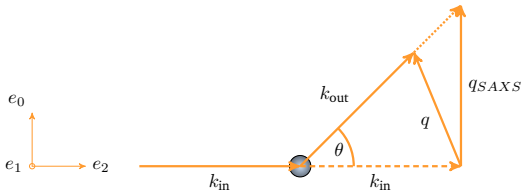

Figure 1.4 Illustration of elastic scattering of an X-ray beam by a small object. Additionally, the Small Angle X-ray Scattering (SAXS) approximation is illustrated.

As the energy of the X-rays does not change, the following holds

$$|k_{\text{in}}| = |k_{\text{out}}| = \frac{2\pi}{\lambda}. \tag{1.2}$$

Consequently, the magnitude of the momentum transfer vector q is given by simple trigonometry as

$$|q| = |k_{\text{in}}| \sin\theta, \tag{1.3}$$

with θ denoting the scattering angle.

In order to account for all possible scattering incidents one employs the concept of electron density $\rho : \mathbb{R}^3 \to \mathbb{R}$ giving the number of electrons per volume element [160, p. 19]. The scattered intensity for the moment transfer vector q is given by (c.f. [160, p. 19]),

$$I(q) = \left(\int \rho(r)\, e^{iqr} dx \right)^2 = \mathcal{F}_3(\rho * \rho)(q). \tag{1.4}$$

Please note that the inner part of the second term, i.e. the integral, assembles a Fourier transform of ρ[6].

Within the scope of this thesis we focus on Small Angle X-ray Scattering (SAXS), i.e. the scattering angle θ is small such that $|q|$ is much smaller than $|k_{\text{in}}|$. With respect to fig. 1.4

[6] We use a slightly different form of the Fourier transform (see section 2.1) but nevertheless use the $\mathcal{F}$ symbol in this context.

this effectively means that $q \approx q_{SAXS}$. This enables several simplifications as for small angles ($\sin\theta \approx \tan\theta \approx \sin\theta$) [271, p. 90]:

$$|q| \approx |k_{\text{in}}|\,\theta \tag{1.5}$$

$$q_2 \approx 0 \tag{1.6}$$

According to Friedel's law [37, p. 290] these intensities are symmetric, i.e.

$$I(q) = I(-q)\,. \tag{1.7}$$

For completeness, **Compton scattering** can be considered as the case in-between the two aforementioned effects. Here, the energy of an incoming X-ray photon is only partially absorbed by an electron. This once again results in the electron leaving the orbit of the atom, but in contrast to absorption, X-rays of lower energy are emitted. This also explains why this is commonly considered to be the equivalent of inelastic scattering for X-rays.

We omit the discussion of X-ray generation, which would go beyond the scope of this thesis and refer to e.g. [78].

1.2 Tomographic Reconstruction

From an abstract point of view tomographic reconstruction, also known as Computed Tomography (CT) in the context of X-ray imaging, amounts to restoring the quantity that caused an observation. This typically involves taking multiple measurements and an understanding of how an observation is cause. This knowledge can be used to "invert" the imaging process. Mathematically this falls in the scope of inverse problems and we will dedicate part II to this topic.

Nevertheless, at this point we want to give a quick overview on the principle and the X-ray absorption may serve as an example. Previously we have discussed that the physical model (compare eq. (1.1)) for standard X-ray CT is based on the Beer-Lambert law, i.e. for an X-ray beam along path L the attenuation is given as (c.f. [78, p. 32f]).

$$I = I_0 \exp\left(-\int_L \mu(x)\,dx\right), \tag{1.8}$$

with $\mu : \mathbb{R}^2 \to \mathbb{R}$ denoting the linear attenuation coefficients[7] and I_0 denoting the initial intensity of the beam.

A common scheme is to take the negative logarithm which leads to the following equation[8]

$$-\ln\frac{I}{I_0} = \int_L \mu(x)\,dx. \tag{1.9}$$

[7] In this case modeled in two dimensions (2D).

[8] To use or not to use the negative logarithm is an ongoing discussion within the scientific community. Throughout this thesis we will focus on the linearized form.

The left side of this equation is commonly referred to as attenuation. According to this forward model for a single X-ray measurement, the mathematically interesting question is how a function is related to integral values along straight lines through the underlying domain. It should be noted that the key achievement of Cormack in 1963 [106, 107] was to provide an inversion formula for eq. (1.9), assuming multiple measurements from various viewpoints are given. At this point Cormack was unaware that a similar problem was investigated in a purely mathematical context by Radon in 1917 [286, 287]. In the field of radio astronomy Bracewell [74] developed an inversion formula for a very similar problem in 1956.

Now, in order to restore μ at each location $x = (x_0, x_1) = x_0 e_0 + x_1 e_1$ multiple measurements are required[9]. Thus, intensities I are recorded from different points of view, which then enable the inversion of the forward model eq. (1.9). We illustrate the two-dimensional (2D) imaging process in fig. 1.5.

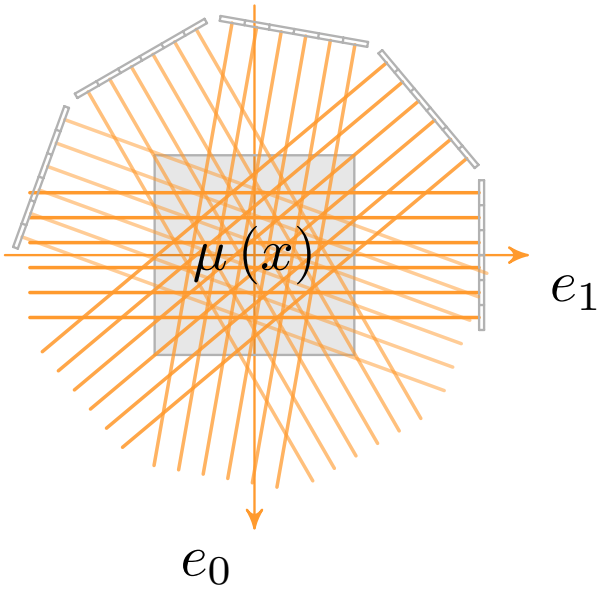

Figure 1.5 Illustration of a CT scan. Multiple X-ray images are recorded from different positions which allows for the inversion of the imaging process.

The concept carries over to other imaging modalities providing a suitable model that relates the cause and the effect, also known as *forward model*. We will postpone a more detailed explanation to part II. For now the key point is that tomographic reconstruction aims at the restoration of quantities describing the cause of an observed/measured effect. The interested reader may refer to e.g. [78, 179, 186, 204, 205, 261, 264]. With this in mind we proceed to modern X-ray imaging methods.

1.3 X-ray Imaging

The methods to image X-ray absorption are as old as the discovery of X-rays. They became the predominant X-ray based imaging method for decades. Diffraction, refraction, and scattering

[9] With $e_i, i \in \{0, \dots, N-1\}$ denoting the standard basis in the Euclidean space of dimension N.

based X-ray imaging took much longer to develop and have been limited to synchrotron setups with coherent and monochromatic radiation at first. In the following a brief overview of advanced X-ray imaging approaches will be presented.

The first and implicitly already mentioned method is SAXS, which can be imaged with X-ray scanning microscopy. Here a pencil beam is used and the probe is scanned in a raster fashion (c.f. [77, 141, 166, 259, 312, 318, 350]). For each single beam one records the full diffraction profile, which provides an insight in distribution and orientation of nano-scale structures to the imaged object [77, 141]. A review on SAXS for imaging biological macromolecules is given in [351].

Tomographic reconstruction of integral SAXS intensities has been studied e.g. in [318] and further discussed in [141]. Only recently Schaff *et al.* [325] proposed a CT approach that preserves the orientation of the SAXS signal during reconstruction. A spherical harmonics based approach has been presented by Liebi *et al.* [235].

Additionally to SAXS, phase-contrast and dark-field modalities emerged. The most common ones are Diffraction-Enhanced Imaging (DEI) [10] [92, 114, 148, 189], crystal-interferometer phase-contrast imaging [68, 257], propagation-based phase-contrast imaging imaging [294, 340], and phase-contrast using Grating Based Imaging (GBI) [255, 373]. The application of these methods was limited though, as they required coherent and monochromatic X-ray beams. The method of DEI has been generalized in order to extract scattering in addition to the refraction information in [98, 302, 303].

There have been various experimental evaluations of SAXS diffraction as well as refraction and scattering for medical purposes and material testing. As these studies highlight the potential of such advanced imaging methods, we want to provide a brief overview. Several studies focused on human breast tissue, and the SAXS signal has been shown to yield significantly different contrast between tumorous and healthy tissues [138, 143, 144, 233, 338]. Improved image contrast for micro calcifications in breast tissue has been demonstrated in [213]. In [115, 139] the authors present contrast improvements for imaging human cerebral myelin sheath. Further studies related to cerebral structures of SAXS CT have been presented by Jensen *et al.* [195, 196]. Improved contrast has additionally been found for tooth [210], bone [347] and cartilage [87] samples. The novel SAXS CT approach of Schaff *et al.* [325] also considered bone and teeth, while Liebi *et al.* [235] focused on collagen fibrils in a human trabecula bone. Based on the contrast caused by scattering, Arfelli [44] proposed to use micro-bubbles filled with highly scattering material as contrast-agents. In [232] possible applications to materials testing have been demonstrated.

While providing additional information on the imaged object, the practical application was limited due to the restriction to synchrotron setups. This changed dramatically by the work performed by Momose, Weitkamp and Pfeiffer, who proposed a GBI system based on Talbot-Lau interferometry [255, 256, 278, 279, 373]. This for the very first time enabled the imaging of phase-contrast (refraction) [278] and dark-field (scattering) [279] with conventional X-ray imaging setups. A first preclinical scanner has been demonstrated by Tapfer *et al.* [352].

[10] A recent review is given in [105].

All experiments performed within the scope of part IV have been performed with a setup as proposed by Pfeiffer *et al.* [278, 279]. Thus, we will give a brief introduction into GBI below.

1.3.1 Grating Based Imaging

Modern GBI based on Talbot-Lau interferometry allows the extraction of X-ray refraction and scattering information in addition to absorption. In order to do so, a standard X-ray imaging setup consisting of a source and a detector is augmented with three gratings **G0**, **G1** and **G2** (see fig. 1.6 for an illustration) [278, 279]. In the following we are going to provide a summary of the GBI based system as proposed in [255, 256, 278, 279, 373]. For a general overview on GBI setups we refer to [125].

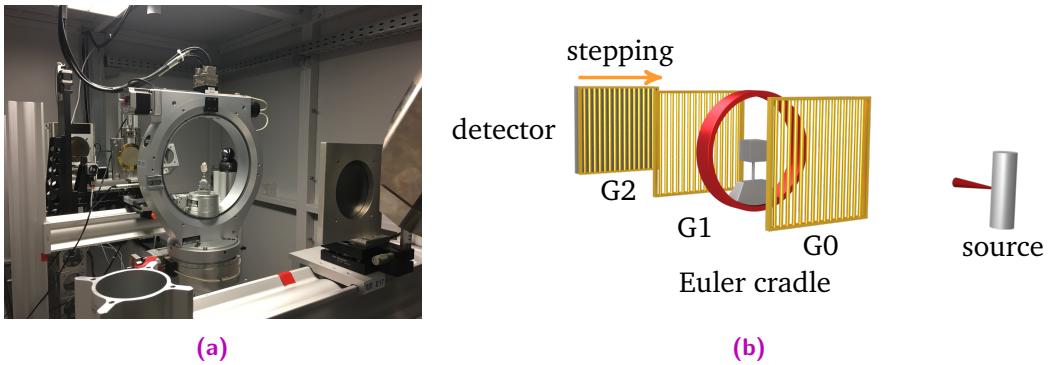

Figure 1.6 Talbot-Lau X-ray GBI setup. In (a) an image of a GBI setup is shown. Additionally, (b) shows an illustration with several annotations.

The *source grating* **G0** creates multiple sources with sufficiently high coherence to allow for a periodic interference behind the *phase grating* **G1**. Finally the analyzer grating **G2** allows to measure the interference pattern with conventional X-ray detectors. During a measurement process, multiple images are recorded while the relative lateral position of **G2** is shifted relatively to **G1**[11]. This translates the interference pattern which is too small to be measured directly with a conventional detector, to an intensity modulation of the detector read-out. The key physical effects involved are the Talbot- and the Lau-effect. The relative placement of the gratings depend on the period of the gratings as well as the wavelength of the X-rays (c.f. [278]).

In fig. 1.7 we show resulting images for three different positions of **G2** of a biomedical sample. For each single detector pixel this stepping effectively results in sampling a periodic function which can be described by [373]

$$I\left(x_g\right) \approx a_0 + a_1 \cos\left(\varphi + \frac{2\pi}{p_2} x_g\right) \tag{1.10}$$

with p_2 denoting the period of **G2** and x_g denoting the phase-stepping, respectively. Furthermore, φ denotes the phase of the intensity curve.

[11] Alternatively other parts of the setup can be stepped too.

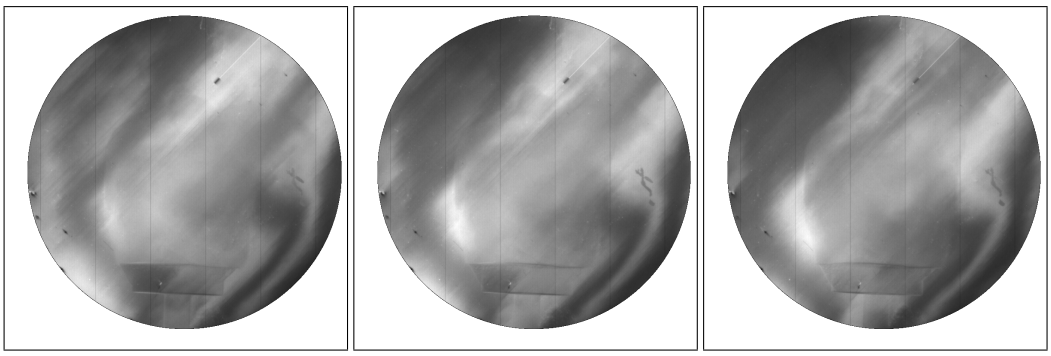

(a) (b) (c)

Figure 1.7 Three images obtained by a Talbot-Lau GBI imaging setup. The sample is a biomedical sample also used in part IV.

From a scan I_s with a sample placed within the setup and a reference scan I_r without, multiple signals can be extracted (c.f. [59, p. 36]). The different signals and their relation to the sample as well as the reference scan are illustrated in fig. 1.8.

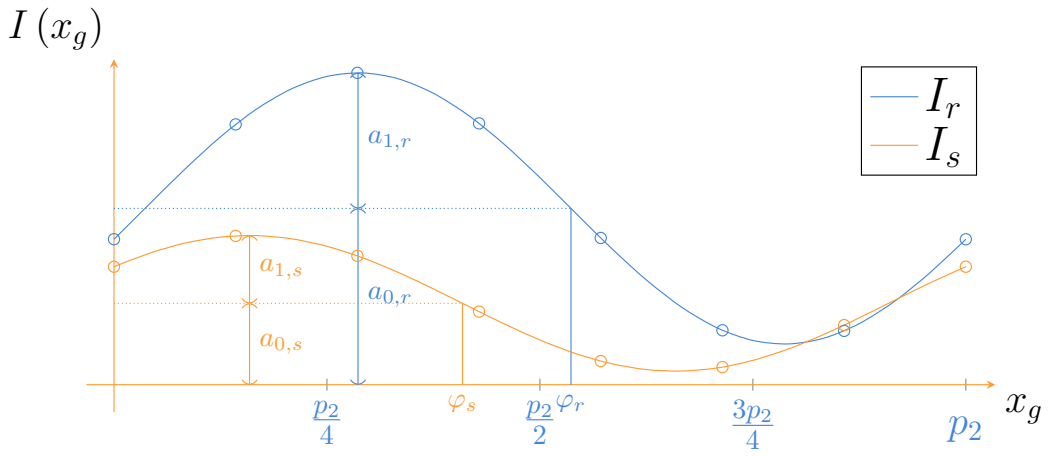

Figure 1.8 Illustration of the intensity curve obtained by a single detector of a Talbot-Lau GBI system. We illustrate two curves, one of a reference scan I_r without a sample and one of the measurement with a sample placed within the beam I_s. The circles mark the sampling points based on the stepping of the grating.

First, the absorption a is given by the ratio of the mean intensities. In addition to the standard absorption, the differential phase-contrast $\triangle\varphi$ and the dark-field signal d can be extracted which yield additional information on the electromagnetic wave. These quantities are computed as (c.f. [279])

$$a = \frac{a_{0,s}}{a_{0,r}}, \quad \triangle\varphi = \varphi_s - \varphi_r, \quad d = \frac{a_{1,s}a_{0,r}}{a_{0,s}a_{1,r}}, \tag{1.11}$$

with $a_{.,s}$, $a_{.,r}$ denoting the $a_.$ in eq. (1.10) of I_s and I_r, respectively. The quotient of $a_{1,s}$ and $a_{0,s}$ is referred to as visibility V_s, with the reference visibility V_r being defined accordingly.

In fig. 1.9 we display the signals extracted from the raw data shown in fig. 1.7.

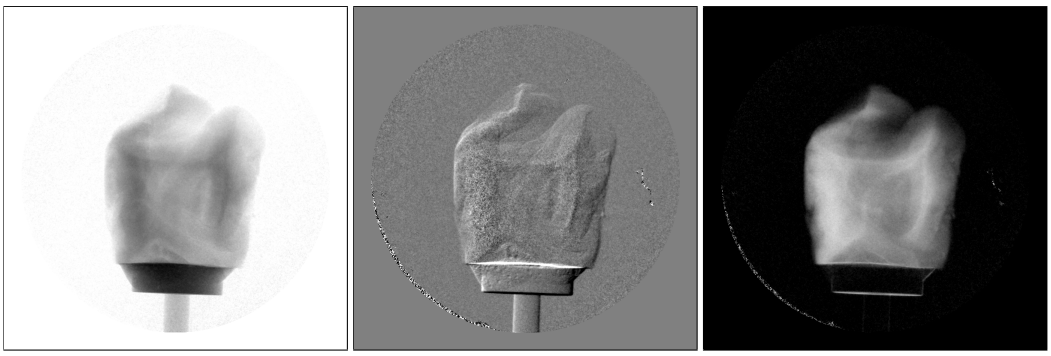

(a) (b) (c)

Figure 1.9 The three signals absorption (a), differential phase-contrast (b), and dark-field (c) for a biomedical sample. The absorption has been windowed to values in the range of $[0, 0.33]$. In case of the differential phase-contrast the interval $\left[-\frac{\pi}{8}, \frac{\pi}{8}\right]$ was used. The dark-field images are displayed using a reverse colormap window for the interval $[0, 1]$ with 1 displayed as black and 0 as white, respectively.

The cause of the phase-contrast is the refraction of the X-ray beam (c.f. [278]) while the dark-field contrast is linked to SAXS (c.f. [279])[12]. Within the scope of this thesis we focus on the considerations of the dark-field signal and a very interesting characteristic unique to this signal, namely anisotropy. The anisotropy of the dark-field signal is displayed in fig. 1.10 for a sample of a cross made out of two wooden sticks.

The dark-field signal obtained using the interferometry-based setup resolves the part of the SAXS that happens orthogonal to the grating orientation (c.f. [62, 63, 96, 104, 238, 253, 368, 384, 385])[13]. Thus the measured dark-field intensities vary if the measured object is rotated in-plane to the gratings [192, 193, 194] as illustrated in fig. 1.10. In the following we will provide a brief summary on the capabilities and developments related to dark-field imaging[14]. For a review on dark-field imaging and its possible applications we refer to [383].

Similar to absorption, the dark-field signal follows an exponential decay [62, 368]. Based on this finding, Bech *et al.* [62] proposed the first tomographic reconstruction of the dark-field for isotropic scattering samples, i.e. the scattering within the object has no predominant direction and can be modeled as a scalar entity.

Due to the connection to SAXS, the dark-field signal provides contrast related to structures which are much smaller than the pixel resolution of the detectors. This signal therefore enables the measurement of very small structures within larger objects. Again, we want to provide a brief overview on some related studies. Improved contrast and discriminative statistics have been evaluated for lung imaging [64, 321, 322, 344, 382]. Pulmonary emphysema has been studied by Schleede *et al.* [321], Meinel *et al.* [249, 251], Yaroshenko *et al.* [382], Tapfer *et al.* [352], pulmonary nodules by Meinel *et al.* [250]. Breast imaging has been studied by Schleede *et al.* [320], Stampanoni *et al.* [344], Anton *et al.* [42], Michel *et al.* [252], Hauser *et al.* [177], and Ando [39]. In [326] the authors proposed X-ray dark-field imaging

[12] Additionally, dark-field contrast can be related to beam-hardening [386] or strong refraction [378, 381] which will not be considered within the scope of this thesis. Kaeppler *et al.* [202] proposed a method for isolating the pure small-angle scattering in the dark-field signal.
[13] Recently Kagias *et al.* [203] proposed a special grating design to extract all directions with a single shot.
[14] Focusing on dark-field imaging, we omit the large body of literature on phase-contrast imaging.

for differentiation of kidney stones. Wen *et al.* [376], Potdevin *et al.* [280], Schaff *et al.* [323], and Thüring *et al.* [354] focused on musculoskeletal imaging. Thüring *et al.* [354] presented dark-field radiography of an entire adult human hand. In [364] Velroyen *et al.* studied the dark-field signal for the application of microbubbles as contrast-agents similar to the work of Arfelli *et al.* [44]. Detection of sub-pixel fractures have been investigated in [224]. The anisotropic information has been extracted to detect the orientation of collagen by Shimao *et al.* [334, 335]. Revol *et al.* [297, 298, 300] used the dark-field signal for material testing. They used prior information in order to separate isotropic and anisotropic parts of the signal. Only recently Schaff *et al.* employed dark-field CT for the characterization of welds [328].

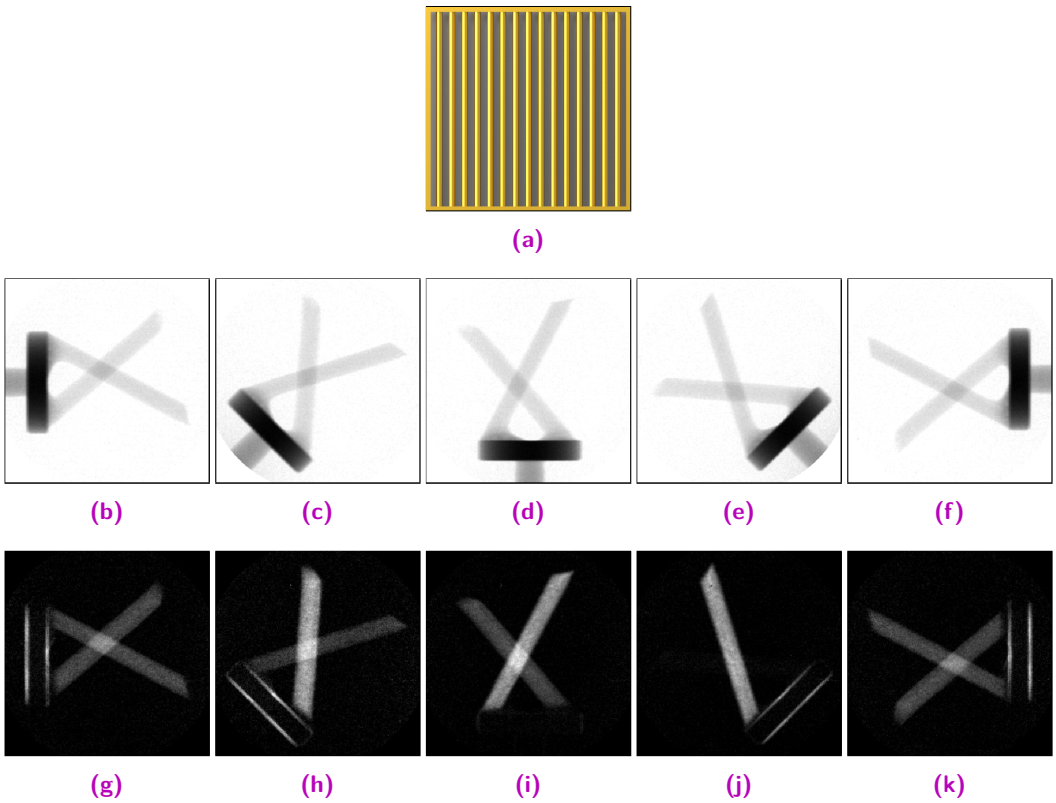

Figure 1.10 Illustration of the anisotropy of the dark-field signal (lower row) in comparison to the absorption signal (center row) according to the grating orientation (upper row). If a sample is rotated orthogonally to the beam direction, the dark-field signal changes, while the absorption stays constant. Again a reverse colormap was used for the dark-field signal. The images of each signal have been windowed to the same intensity regions.

In directional dark-field imaging, also known as X-ray Vector Radiography (XVR), the sample is rotated (e.g. using an Euler cradle as illustrated in fig. 1.6b) around the central beam direction [55, 193, 194, 280]. This imaging method yields information on local orientation of a sample due to the anisotropic part of the signal [238, 243, 299, 376, 384]. A corresponding model has been presented in [57, 243, 299]. A numerical simulation framework has been presented by Malecki *et al.* [241]. This method has been proposed to predict mechanical properties of a sample by Malecki *et al.* [245]. In [323] Schaff *et al.* used this method of directional dark-field radiography to analyze the bone-micro-architecture of a femur cube imaged using a Micro-CT (μCT) scanner. They showed that this yields information correlating with the trabecular microstructure. A highly complete model for dark-field signal has recently

been discussed by Strobl [349] and experimentally validated by Prade *et al.* [282]. This model is based on methods originating from another imaging modality, namely Spin-Echo Small-Angle Neutron Scattering (SESANS) (c.f. [40]).

The anisotropy of the dark-field signal makes the dark-field CT, which accounts for anisotropy, particularly challenging. In contrast to a scalar field, one needs to consider the anisotropic nature in each location within the sample. The first CT approach using a more sophisticated scattering model was proposed by Malecki *et al.* [244]. This method employes rank-2 tensors and is called X-ray Tensor Tomography (XTT). The measurement process becomes more complicated and the rotation around a single axis is not sufficient. Malecki *et al.* [244] therefore proposed to use an Euler cradle (compare fig. 1.6b) in order to rotate the sample freely in a three-dimensional (3D) fashion. Sharma *et al.* [10, 3, 15, 5] evaluated acquisition schemes and their effects on tomographic reconstructions. The XTT approach is based on the forward model for directional dark-field imaging [299, 300] and the superposition principle formulated in [243]. Instead of directly reconstructing the tensors, Malecki proposed to choose K scattering directions which are supposed to be uniformly distributed on a sphere. Further, scattering is only modeled in these directions. The total amount of scattering is approximated by a weighted sum of the scattering happening in these directions. The weighting is related to the scattering direction, the relative orientation of the grating orientation as well as the beam direction [243]. For each of these scattering directions the scattering strength is then reconstructed using a specially crafted variant of the Simultaneous Algebraic Reconstruction Technique (SART) [41]. Schaff *et al.* [329] recently proposed to employ a non-iterative approach to reconstruct these scattering strengths. Within the final reconstruction step, a rank-2 tensor is fitted to the pairs consisting of directions and corresponding scattering magnitudes. As scattering is strongest orthogonal to microstructures, the direction of such is given by the smallest half-axis of the tensor. Only recently Jud *et al.* [200] showed that the reconstructed orientations correlate with the orientation of dentinal tubules within a tooth sample. In contrast to XTT, these tubules where not visible in a μCT and the tooth had to be irreversible cut in order to be investigates under a microscope.

A different reconstruction approach has been proposed by Bayer *et al.* [58]. Here the authors reconstruct the isotropic part as scalar value and the anisotropic part as vectorial entity while using only the standard tomographic axis. This leads to a projection of the anisotropic scattering onto the plane perpendicular to the tomographic axis. In order to achieve 3D vectorial information this work has been extended in [187] flipping the probe for a second scan, which yields a complementary projection onto one of the remaining two planes.

Recently, Vogel *et al.* [7] presented multiple improvements to XTT. First, a reformulation of the formulas stated by Malecki *et al.* [244] to a linear problem. Second, constrained reconstruction was proposed. Here after each iteration either a soft pushing to or a hard enforcing of the tensor structure were applied. For both, a tensor is fitted to the reconstructed scattering strengths. In case of the soft pushing, these strengths are partially scaled towards the corresponding tensor value, while in case of the hard enforcing the values are reset with those of the fitted tensor. Both approaches provided a strongly improved reconstruction result from a visual perspective. Last but not least a visualization method based on fiber tracking along the least scattering direction was presented.

1.4 Excursus: Other Modalities

While the presented thesis focuses on X-ray based CT, the general idea of tomographic reconstruction is shared with many other modalities, including but not limited to Magnetic Resonance Imaging (MRI) [225], photo-acoustic imaging [379], Positron Emission Tomography (PET) [353], Single-Photon Emission Computed Tomography (SPECT) [217], Magnetic Particle Imaging (MPI) [161] and optical tomography [222].

Special attention is drawn to MRI, which enables another anisotropic imaging method. For their pioneering work on MRI, Paul C. Lauterbur and Peter Mansfield received the Nobel Price in medicine in 2003 [223, 247]. The corresponding anisotropic imaging modality is called Diffusion Magnetic Resonance Imaging (D-MRI). The interested reader may refer to e.g. [48, 198] for further readings. In this case, MRI is used in order to image the diffusion of water within the human body [54, 227]. This proved especially valuable for imaging structures belonging to the Central Nervous System (CNS). The first approach, termed Diffusion Tensor Imaging (DTI), uses rank-2 tensors to model the diffusion. In contrast to XTT, the main axis represents the orientation of the structure. For tensor fitting, which is the reconstruction in case of DTI, two major approaches are used in the scope of DTI, both derived from the Stejskal-Tanner equation [346]. The first approach is given by least-squares tensor fitting (c.f. [214]). The second one is based on a maximum a posteriori approach [146]. While the least-squares approach is based on the assumption of Gaussian noise, the second one copes with Rician noise [53, 146]. Basu *et al.* [53] showed that the Rician noise model is more suitable for DTI imaging. This noise model is shared partially with dark-field imaging as shown by Chabior *et al.* [88]. As tensors do not live in the Euclidean space, Pennec *et al.* [276, 277] established a Riemannian manifold for the space of tensors (Pos_3). This framework enables for instance interpolation and measuring of distances between tensors in a more meaningful way than the space of matrices.

DTI has strongly improved the scientific investigation of the CNS. Research of embryonic development of morphological connection and resulting communication have been studied e.g. in [130, 371, 387]. Additionally, the information on neurological connectivity is crucial for surgical planning [269]. For resection of tumors which are closely located to functional areas the insight gained from DTI provides a great benefit [65]. Further, D-MRI has been applied for investigation of autism [36], detection of brain ischemia [226] and neurodegenerative pathologies such as schizophrenia [147, 216] or Huntington's disease [310]. Assaf *et al.* [47] provides a great review on this subject.

In DTI especially for junctions the simple tensor model is insufficient as it is only capable of representing a single orientation (c.f. [34]). Pasternak *et al.* [274] use a multi-tensor approach instead. Alternative approaches use more general formulations based on spherical functions e.g. q-ball imaging [360, 361].

Due to its similarity, it is reasonable to investigate related approaches and their applicability to the tomographic reconstruction of the anisotropic dark-field component.

1.5 Structure of this Thesis

Subject of this thesis is the tomographic reconstruction of the anisotropic dark-field signal. One major field of research during the preparation of this thesis was the development of an abstract software framework for inverse problems, such as tomographic reconstruction. The first part of this thesis is therefore dedicated to the mathematics of inverse problems (part II). Targeting the specific tomographic problem related to X-ray imaging in particular, we discuss inverse problems, their discretization and approaches to actually compute a solution. Additionally, a detailed discussion of the SAXS and the dark-field signal will be provided.

Tomographic reconstruction for modalities different than X-ray CT often employs very similar mathematical concepts. The first contribution presented within this thesis is the development of an abstract software framework for tomographic reconstruction. Within this framework the numerical methods are implemented independently from the specific forward model which enables adaptation and application of methods for multiple modalities. Additionally, the framework supports the composition of various common approaches such as regularization methods which allows for intensive comparison and evaluation of specific methods for multiple modalities. This framework is presented in part III.

In the final part (part IV) we will focus on the tomographic reconstruction of anisotropic dark-field signal. Starting with the original work of Malecki *et al.* [244] we will provide a review of XTT in chapter 18. The resulting tensor field combines information on the scattering strength as well as its directional distribution, which provides an insight into orientation of the microstructure within the object. We will discuss weaknesses and strengths of this approach as well as a method of denoising based on the manifold on rank-2 tensors developed by Pennec *et al.* [277]. A major limitation of the XTT approach is that a tensor is restricted to a single orientation. Within this thesis we will present a novel general closed-form continuous forward model of the AXDT. We will show that this model contains the XTT model under specific assumptions, but also enables an additional highly improved approach based on spherical harmonics. Additionally, we will present a method to extract the orientation of the microstructures from their scattering profiles. A first preclinical experiment based on a dried sample of a part of a human brain indicates that this method could in the future provide complementary information for imaging the CNS to state of the art methods such as D-MRI.

Part II

Mathematical Basics

2 Disclaimer and Notations

> *The only thing better than a cow is a human! Unless you need milk. Then you really need a cow.*
>
> **— Dr. Walter Bishop**
> Fringe

The following part is dedicated to providing an overview and a summary of the mathematical concepts needed for the numerical computation of solutions to inverse problems, such as tomographic reconstruction. We will start in the continuous domain and discuss mathematical tools that enable description of the imaging process in form of integral transforms. Following this continuous description we will discuss a mathematical framework which enables the discretization of such problems in order to actually compute tomographic reconstructions using computers. The presented mathematical tools will be mapped into a flexible software framework in part III. Further on, as this thesis mainly focuses on Anisotropic X-ray Dark-field Tomography we will discuss the physical concepts behind dark-field imaging and how they are modeled mathematically.

Disclaimer: With the kind of broad summary given below it is nearly impossible to provide a deep insight into each topic. Consequently, a common rule is to keep one's discussion as narrow as possible. Nevertheless, this rule unfortunately does not apply in this case as one of the main work packages was the development of the already mentioned software framework of part III for linear inverse problems. We therefore need to provide a broad introduction summarizing the key concepts related to inverse problems and attempts to solve them.

Before we dig into the theory of inverse problems and especially the problem of tomographic reconstruction, we will provide an overview on common notations used in the following.

2.1 Notations

Consider two vectors $x = (x_0, \dots, x_{N-1})$, $y = (y_0, \dots, y_{N-1})$ of the Euclidean space $\mathbb{R}^N$ of dimension $\dim\left(\mathbb{R}^N\right) = N$. We denote the standard basis as e_n, $0 \leq n \leq N-1$. For the inner product of x and y the following notations are used synonymously:

$$\langle x, y \rangle = xy = x \cdot y := \sum_{n=0}^{N-1} x_n y_n. \tag{2.1}$$

The complex conjugate of a number $z \in \mathbb{C}$ is written as z^*. For a matrix $A \in \mathbb{K}^{N \times M}$, with $\mathbb{K} \in \{\mathbb{R}, \mathbb{C}\}$, we denote the adjoint as A^* with the special notation for the adjoint in $\mathbb{R}$, i.e. the transpose $A^\top$. Further we denote the subspace of $\mathbb{R}^{3\times3}$ of symmetric matrices by Sym_3 and the further subset of symmetric and positive definite matrices by Pos_3.

In addition to the standard Euclidean space we are going to use the following notations of special sets:

$$
\begin{aligned}
u^\perp &:= \left\{ w \in \mathbb{R}^N \ : \ \langle u, w \rangle = 0 \right\} && (u \in \mathbb{R}^N) \\
\mathbb{S}^{N-1} &:= \left\{ x \in \mathbb{R}^N \ : \ \|x\|_2 = 1 \right\} && (\text{unit sphere in } \mathbb{R}^N) \\
\mathbb{H}^{N-1}(s,u) &:= \left\{ v \in \mathbb{R}^N \ : \ \exists w \in u^\perp, v = su + w \right\} && (u \in \mathbb{S}^{N-1},\, s \in \mathbb{R}) \\
\mathbb{T}^N &:= \left\{ (x,u) \in \mathbb{R}^N \times \mathbb{S}^{N-1} \ : \ x \in \mathbb{H}^{N-1}(u) \right\} && (\text{tangent bundle of } \mathbb{S}^{N-1}) \\
\mathbb{L}(x,u) &:= \left\{ v \in \mathbb{R}^N \ : \ \exists t \in \mathbb{R}, v = x + tu \right\} && ((x,u) \in \mathbb{T}) \\
\mathbb{C}(u) &:= \left\{ w \in \mathbb{S}^{N-1} \ : \ \langle u, w \rangle = 0 \right\} && (\text{great circles on } \mathbb{S}^{N-1})
\end{aligned}
$$

Note: We further use the short notation $\mathbb{H}^{N-1}(u) = \mathbb{H}^{N-1}(0,u)\,(= u^\perp)$ for the standard hyperplanes and $\mathbb{L}(u) = \mathbb{L}(0,u)$ for lines through the origin. We omit the dimension subscript of the sets above if it is clear or implicitly given by the arguments.

At some points we require a subdivision of a given set into multiple smaller sets. For this purpose we will use the following definition of a partition.

Definition 2.1 **(Partition)** A partition of a set X is a collection of sets $\{A_n\}_{n=0}^{N-1}$, $A_n \subset X$ with the following properties:

$$A_n \cap A_m = \emptyset, \quad n \neq m, \tag{2.2}$$

$$X = \bigcup_{n=0}^{N-1} \overline{A_n}, \tag{2.3}$$

with $\overline{A_n}$ denoting the closure of A_n.

For a subset $A \subset X$ we denote the indicator function by

$$\chi_A : X \to [0,1], x \mapsto \begin{cases} 1 & x \in A \\ 0 & x \notin A. \end{cases} \tag{2.4}$$

Throughout the following chapters we will consider multiple function spaces. The space of all functions $f : X \to Y$ mapping from the domain $\text{dom}(f) = X$ to the range $\text{ran}(f) = Y$ is denoted as X^Y. The image of f is denoted as $\text{im}(f) = f(X)$ and the support is denoted as $\text{supp}(f) := \{x \in X \ : \ f(x) \neq 0\}$. Furthermore, the space of continuous functions on a domain Ω is written as $C(\Omega)$, while the space of k-times continuous differentiable functions is denoted as $C^k(\Omega)$. The special case of k-times continuous differentiable functions with compact support, i.e. $\text{supp}(f)$ is a compact subset of X, is written as $C_c^k(\Omega)$. For the space of continuous linear mappings we write $\mathcal{L}(X,Y)$. The space of infinitely differentiable and rapidly decreasing functions on $\mathbb{R}^N$ is written as $\mathcal{S}(\mathbb{R}^N)$ [330] (c.f. [167, Definition 2.2.1]).

For the class of L^p spaces we use the following common definition (c.f. [315]).

Definition 2.2 **(L^p-spaces)** Let $(\Omega, \mathcal{A}, \mu)$ be a measure space, $\mathbb{K} \in \{\mathbb{R}, \mathbb{C}\}$, $1 \leq p < \infty$. The Banach space of L^p-functions over $\mathbb{K}$ is defined as,

$$L^p(\Omega, \mathcal{A}, \mu) = \mathcal{L}^p(\Omega, \mathcal{A}, \mu)/\mathcal{N}, \tag{2.5}$$

with

$$\|f\|_{\mathcal{L}^p} := \left(\int_\Omega |f(x)|^p \, d\mu(x)\right)^{\frac{1}{p}}, \tag{2.6}$$

$$\mathcal{L}^p(\Omega, \mathcal{A}, \mu) := \{f : \Omega \to \mathbb{K} \ : \ f \text{ measurable}, \|f\|_{\mathcal{L}^p} < \infty\}, \tag{2.7}$$

$$\mathcal{N} := \{f \in \mathcal{L}^p \ : \ \|f\|_{\mathcal{L}^p} = 0\}. \tag{2.8}$$

Note: In cases where the choices of $\mathcal{A}$ and μ are obvious, such as in case of the Euclidean space, they will be omitted.

For any element of the equivalence class $[f] \in L^p$, we use the norm definition $\|[f]\|_{L^p} := \|f\|_{\mathcal{L}^p}$ and omit the $[\cdot]$ subsequently. The special class of $L^2(\Omega)$, which constitutes a Hilbert space, possesses the following inner product for $f, g \in L^2(\Omega)$:

$$\langle f, g \rangle_{L^2(\Omega)} := \int_\Omega f(x) \, g(x)^* d\mu(x). \tag{2.9}$$

Furthermore we denote the corresponding sequence counterparts by ℓ^p (c.f. [167, p. 2]). Analogous to the continuous case, norms are given by

$$\|x\|_{\ell^p} := \left(\sum_{n \in \mathbb{N}} |x_n|^p\right)^{\frac{1}{p}}. \tag{2.10}$$

We will use the short-hand notations $\|\cdot\|_p$ for $\|\cdot\|_{L^p}$ and $\|\cdot\|_{\ell^p}$ if it is obvious which space is considered. Finally we use the notation $\|\cdot\|_{p,w}$ for the weighted L^p_w- and ℓ^p_w-norms, which are defined as:

$$\|\cdot\|_{L^p_w(\Omega)} := \left(\int_\Omega w(x) \, |f(x)|^p \, d\mu(x)\right)^{\frac{1}{p}}, \quad (w : \Omega \to \mathbb{R}_+), \tag{2.11}$$

$$\|\cdot\|_{\ell^p_w(\Omega)} := \left(\sum_{n \in \mathbb{N}} w_n \, |x_n|^p\right)^{\frac{1}{p}}, \quad \left(w = (w_n)_{n \in \mathbb{N}}, w_n \in \mathbb{R}_+\right). \tag{2.12}$$

For two integrable functions $f, g \in L^1\left(\mathbb{R}^N\right)$ we denote the *convolution* by

$$(f * g)(x) := \int_{\mathbb{R}^N} f(y) \, g(y - x) \, dy. \tag{2.13}$$

One of the most powerful tools for analyzing functions is given by the Fourier transform. Throughout this thesis we will use the following definition of the Fourier transform.

Definition 2.3 **(Fourier transform (N-dimensional))** (c.f. [167, pp. 99ff]) Let $f \in \mathcal{S}\left(\mathbb{R}^N\right)$, we define the Fourier transform $\mathcal{F}_N f$ of f as

$$\mathcal{F}_N f\left(\xi\right) := \int_{\mathbb{R}^N} f\left(x\right) e^{-2\pi i x\xi} dx. \tag{2.14}$$

The inverse transformation is given as

$$\mathcal{F}_N^{-1} f\left(x\right) := \mathcal{F}_N f\left(-x\right). \tag{2.15}$$

Note: For $L^1\left(\mathbb{R}^N\right)$ and $L^2\left(\mathbb{R}^N\right)$ we use the usual extension (c.f. [167]). If the dimension of f is clearly stated we use the abbreviations $\mathcal{F} f = \mathcal{F}_N f$ and $\mathcal{F}^{-1} f = \mathcal{F}_N^{-1} f$.

For convolution and Fourier transform an interesting relationship dramatically simplifying convolution exists, i.e. the convolution theorem.

Theorem 2.4 **(Convolution theorem)** (c.f. [167, Proposition 2.3.22.]) Let $f, g \in L^1\left(\mathbb{R}^N\right)$ then the following equality holds:

$$\mathcal{F}\left(f * g\right) = \left(\mathcal{F} f\right)\left(\mathcal{F} g\right). \tag{2.16}$$

This theorem states that convolution is reduced to a pure multiplication within the Fourier domain.

This closes all notations needed within this thesis and we proceed with the consideration of the mathematical model of X-ray tomography.

3 Forward Model for X-ray Imaging

During the introduction, we have already mentioned that the forward model for absorption of a single X-ray beam can be expressed in terms of the linear attenuation coefficients as

$$-\ln \frac{I}{I_0} = \int_L f(x)\, dx, \tag{3.1}$$

with I denoting the measured and I_0 denoting the initial beam intensity (compare eq. (1.9)). Therefore, the question how a function is related to its integral values and what is required to perform an inversion of this process arises. This is of special interest, as the problem of AXDT shares this key elements with attenuation CT. For discussion beyond the scope of this thesis we refer to [78, 116, 178, 179, 186, 204, 261, 264, 284] on which this summary is based.

We start with the definition of two X-ray related transforms. These transforms state the forward models for eq. (3.1). These models are the prerequisite to formulating an inverse problem as described in chapter 4. We start with the original Radon transform which is defined as follows.

Definition 3.1 **(Radon transform (N-dimensional))** (c.f. [264, 286]) Let $f : \mathbb{R}^N \to \mathbb{R}$ be sufficiently nice. The mapping $\mathcal{R}f : \left(f : \mathbb{R}^N \to \mathbb{R}\right) \to \left(\mathcal{R}f : \mathbb{R} \times \mathbb{S}^{N-1} \to \mathbb{R}\right)$ of f to integral values over affine hyperplanes $\mathbb{H}^{N-1}(s, u)$ with normal $u \in \mathbb{S}^{N-1}$ and offset $s \in \mathbb{R}$ to the origin,

$$\mathcal{R}f(s, u) = \int_{\mathbb{H}^{N-1}(s,u)} f(v)\, dv, \tag{3.2}$$

is called **Radon transform**.

Note: For $N = 2$ the hyperplanes are lines which match the model for X-ray imaging. The result in this case is commonly referred to as *sinogram*.

As the note already states, this transform provides a forward model for X-ray imaging in 2D with parallel X-ray beams (see fig. 3.1a). For non-parallel geometries (compare figs. 3.1c and 3.2b) a re-parametrization, also known as rebinning, is needed (c.f. [186]). In 3D this transform no longer suits the tomographic problem, as the hyperplanes no longer represents lines but planes instead. Therefore, the Radon transform is not suitable to model the X-ray imaging process in 3D.

This led to the definition of the so called X-ray transform, which instead of integral values over hyperplanes considers integrals along straight lines.

Definition 3.2 **(X-ray transform (N-dimensional))** (c.f. [264]) Let $f : \mathbb{R}^N \to \mathbb{R}$ be sufficiently nice. The mapping $\mathcal{X}f : \left(f : \mathbb{R}^N \to \mathbb{R}\right) \to \left(\mathcal{X}f : \mathbb{R}^N \times \mathbb{S}^{N-1} \to \mathbb{R}\right)$ of f to integral values along lines $\mathbb{L}(x, u)$, $u \in \mathbb{S}^{N-1}, x \in \mathbb{R}^N$

$$\mathcal{X}f(x, u) = \int_{L(x,u)} f(v)\, dv \tag{3.3}$$

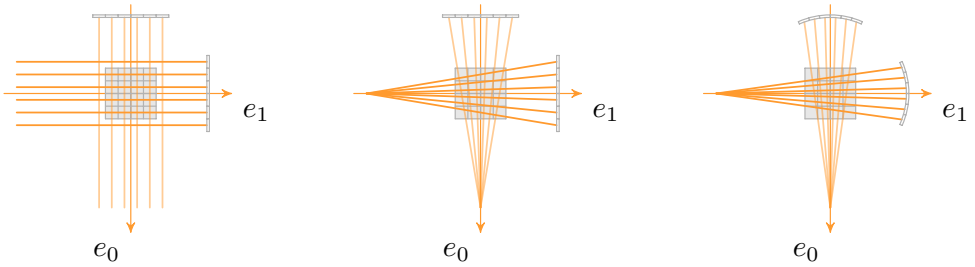

(a) (b) (c)

Figure 3.1 Illustration of the X-ray/Radon transform in 2D for different setup geometries. In (a) we show a parallel beam geometry which is the common scheme for the Radon transform. Further we show two point source based geometries with a flat detector in (b) and a curved one in (c). Both situations can be modeled using the X-ray transform (def. 3.2) and with a suitable parametrization also with the Radon transform (def. 3.1).

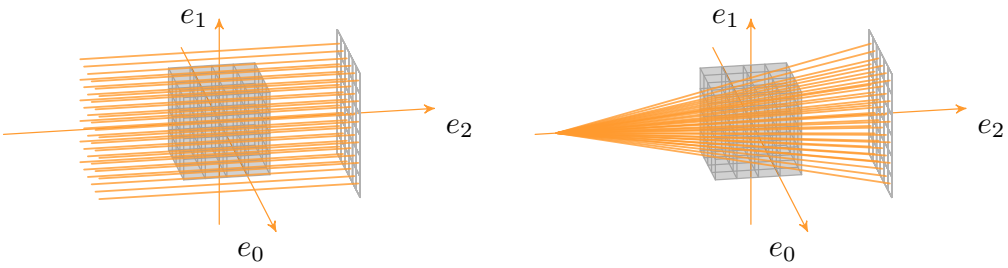

(a) 3D Parallel **(b)** 2D Cone beam

Figure 3.2 Illustration of the X-ray transform in 3D for different setup geometries. In (a) we show a parallel beam geometry while (b) shows a cone-beam setup. Both situations can be modeled using the X-ray transform def. 3.2.

is called **X-ray transform**.

Note: For $N = 2$ the following equality holds: $\mathcal{R}f(s,u) = \mathcal{X}f\left(su, u^{\perp}\right)$. Furthermore, the domain of the transformed function $\mathcal{X}f$ can be restricted to the tangent bundle $\mathbb{T}^N$ as the line definition is unique on this subset of $\mathbb{R}^N \times \mathbb{S}^{N-1}$. However, as we often deal with setups similar to cameras it is often advantageous to use the camera center, i.e. the X-ray source, for x. It should be mentioned that the so-called divergent beam transform is defined in [264] as well, which is similar to the X-ray transform above but operates on half-lines instead. We omit this transform as in the following we will predominantly consider functions f of compact support, for which the two transforms are equal for all $x \notin \operatorname{supp}(f)$, i.e. a source outside of the object.

Please note that both transforms $\mathcal{R}f$ and $\mathcal{X}f$ are linear with respect to f due to the linearity of the integral. This is essential, as the tomographic reconstruction thus falls into the class of linear inverse problems which we will discuss in chapter 4.

Of special interest is the evaluation of these functions for specific ray directions. For parallel beam geometry setups these reflect one detector image/scan (compare figs. 3.1 and 3.2). Therefore we use the shorthand notation $\mathcal{R}_u f(s) = \mathcal{R}f(s,u)$ and $\mathcal{X}_u f(x) = \mathcal{X}f(x,u)$. These

single orientation scans are typically referred to as X-ray projection images within the X-ray imaging community. Further, the computation of this forward model is commonly referred to as *forward projection*.

However, many modern CT machines typically do not operate with parallel geometries but with geometries defined by a point source instead (compare figs. 3.1b, 3.1c and 3.2b). This is known as fan beam geometry in 2D and cone-beam geometry in 3D. In these cases the X-ray projection is typically identified with the direction of the central beam while the relation of the directions for non-central X-rays is defined by the opening angle of the fan/cone. As discussed above, for fan/cone geometries the position of the point source provides a natural choice for the parameter x of $\mathcal{X}f$. The interested reader may consider [78, 205] for further insights into common geometries.

An actual measurement using a CT machine naturally reduces the domain of the transformed function. With respect to the X-ray transform this reduction happens for example for x as the possible poses for the source are limited due to the physical arrangement of the CT system. The same is true for the parameter u as the finite size of the detector in combination with similar physical restrictions to those of x imposes a similar reduction. Additionally, due to the finite amount of pixels on a detector this set is further discretized. We will discuss tools to model this in section 4.1 and will consider the continuous formulation for now.

A very interesting relation exists between the X-ray transform and the Fourier transform which is known as Fourier slice theorem[1]. It basically states that the Fourier transform of a single X-ray projection of f equals the cut through the Fourier transform of the function itself.

Theorem 3.3 **(Fourier slice theorem (N-dimensional))** (c.f. [264]) Let $f \in \mathcal{S}\left(\mathbb{R}^N\right)$ and $u \in \mathbb{S}^{N-1}$, the following equality holds:

$$\mathcal{F}_{N-1}\mathcal{X}_u f\left(\xi\right) = \mathcal{F}_N f(\xi) \quad \forall \xi \in u^\perp \tag{3.4}$$

Note: Natterer uses a different definition of $\mathcal{F}$ which leads to an additional normalization factor.

A key consequence from theorem 3.3 is that it provides a straightforward inversion formula, known as Fourier reconstruction [263]. This formula is inherently given by the invertibility of the Fourier transform. Additionally, theorem 3.3 gives important information on what can be reconstructed in the case of limited-angle CT, i.e. a restriction of u to a wedge of $\mathbb{S}^{N-1}$. Quinto [285] showed that only information on singularities which are hit tangentially is collected by an X-ray projection. Frikel and Quinto further studied the theoretical properties of artifacts caused by this insufficient sampling [152].

A detailed mathematical discussion of these transforms would go far beyond the scope of this thesis and we are therefore going to focus on the essential properties used within this thesis. These will be discussed exemplarily in the following regarding the 2D Radon transform as this provides the clearest picture. However, we point out that similar concepts apply to the other transforms and the 3D case as well. For a more in-depth discussion on these transformations, especially the requirements on f etc., we refer to [116, 178, 204, 264, 284].

[1] A similar theorem holds for the Radon transform [264, p. 11].

We start with the dual of the (2D) Radon transform. The dual is of special interest as in the case of the Hilbert space L^2 it represents the Hilbert-adjoint of the Radon transform.

Definition 3.4 **(Dual Radon transform (2D))** ([263, p. 13]) The dual operator to $\mathcal{R}$ is defined as:

$$\mathcal{R}^* g(x) := \int_{\mathbb{S}^1} g(\langle x, u \rangle, u) \, d\sigma(u) \tag{3.5}$$

with $g : \mathbb{R} \times \mathbb{S}^1 \to \mathbb{R}$ being sufficiently nice.

This operator is commonly referred to as (unfiltered[2]) **back-projection**. This name is based on the fact that an alternative way of interpreting def. 3.4 is that the value at a position (s, u) in the Radon space is back-projected along the ray corresponding to (s, u). In order to illustrate this relation in fig. 3.3 the sinogram of a simple function together with a back-projection of a single X-ray projection as well as a full back-projection is shown[3].

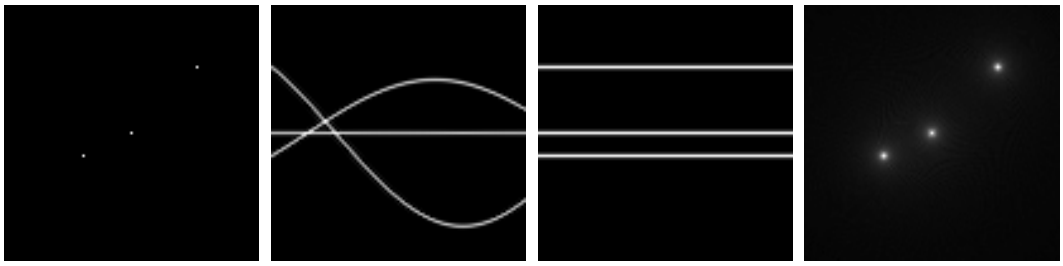

(a) (b) (c) (d)

Figure 3.3 Illustration of the Radon transform of three single pixels (a) and the resulting sinogram (b). Further a back-projection of a single X-ray projection is shown in (c) while the result of the full back-projection of all X-ray projections are displayed in (d).

In order to perform tomographic reconstruction we are interested in inverting eq. (3.1), i.e. in 2D the inversion of the Radon transform $\mathcal{R}f$. Both Radon [286] and Cormack [106, 107] presented inversion formulas for this type of integral transforms. However, in practice these are expensive to compute and a much more elegant method exists today – namely the Filtered Back-Projection (FBP).

As prerequisite we recall the definition of the Riesz potential which states a kind of "integrating" (c.f. [167]) convolution operator.

Definition 3.5 **(Riesz potential)** (c.f. [167, Definition 6.1.1.]) Let $0 < r < N$. The *Riesz potential* of order r is defined as the operator:

$$I_r := (-\triangle)^{-\frac{r}{2}}, \tag{3.6}$$

with the fractional Laplacian operator defined as:

$$(-\triangle)^{-\frac{r}{2}} f := \mathcal{F}^{-1}\left((2\pi |\xi|)^{-r} \mathcal{F} f \right) \tag{3.7}$$

for $f \in \mathcal{S}(\mathbb{R}^N)$.

Note: While the *Riesz potential* is well-defined for r being in the range given above, the concept carries over to other r as well (see [167, pp. 414ff]). However, it is not necessarily guaranteed

[2] Opposed to the Filtered Back-Projection (FBP)
[3] Created with Matlab [on2] *radon()*, *iradon()* procedures.

that the potential is well-defined as the function may not be locally integrable any longer. Additionally, please note that due to the convolution theorem (theorem 2.4) this states a convolution.

The relation of the Radon transform and the Fourier transform now results in a very interesting relation between the Riesz potential, the Radon transform, and its dual. This relation is given in the following theorem.

Theorem 3.6 **(Radon transform and Riesz potential)** (c.f. [263, Theorem 2.1]) (2D) Let $f \in \mathcal{S}\left(\mathbb{R}^2\right)$. The following equality holds,

$$I_r f = \frac{1}{\sigma\left(\mathbb{S}^2\right)} \mathcal{R}^* \left(I_{r-1} \otimes \mathrm{id}\right) \mathcal{R} f \tag{3.8}$$

for all $0 \leq r < n$. With $\otimes$ denoting the tensor product.

Note: For clarification, in theorem 3.6 the tensor product is used to highlight that the second Riesz potential acts only on the variable s in the Radon space.

As a direct result, this theorem provides two major implications (c.f. [264, pp. 18ff]). First, for $r = 1$ one finds that the concatenation of forward and back-projection acts on f like the Riesz potential of order 1 which due to the integrating nature leads to a blurred version of f (see fig. 3.3d). Secondly, for $s = 0$ one obtains the inversion formula of FBP:

$$f = \frac{1}{\sigma\left(\mathbb{S}^2\right)} \mathcal{R}^* \left(I_{-1} \otimes \mathrm{id}\right) \mathcal{R} f \tag{3.9}$$

Thus the inversion of a given sinogram $g = \mathcal{R} f$ can be computed by performing a filtering in the Radon space according to the Riesz potential I_{-1} and a subsequent back-projection.

This closes our discussion of the mathematical model for X-ray imaging. While the method of FBP already provides a first reconstruction method, we want to consider inverse problems from a more general point of view. This allows for an advanced method to deal with restrictions, noise, and other perturbations of measurements. Therefore, we continue with the definition and discussion of inverse problems.

4 Inverse Problems

As discussed above tomographic reconstruction, i.e the computation/reconstruction of a cause from an observed/measured effect, belongs to the problem class of linear inverse problems. In the following we will discuss the mathematical tools used to model, discretize, and solve this specific type of inverse problem. We will strictly focus on linear inverse problems due to the linear forward model. Thus, in the following whenever we write inverse problem we implicitly assume a linear relation between cause and effect (except when stated otherwise).

From an abstract level we can define a linear inverse problem as follows:

Definition 4.1 **(Linear inverse problem)** Let X, Y denote two spaces (e.g. Hilbert or Banach spaces), modeling the space of cause and effect, respectively. Further let $\mathcal{A} : X \to Y$ be a linear operator modeling the relation between cause and effect and finally let $y \in Y$ be a given effect. The (linear) inverse problem consisting of the tuple $(\mathcal{A}, y)$ is to find a $x \in X$ such that

$$\mathcal{A}x = y, \tag{4.1}$$

holds.

Note: If $\mathcal{A}$ is invertible the solution is given by $x = \mathcal{A}^{-1}y$.

The problem of tomographic reconstruction falls into this class as the corresponding forward model, i.e. the Radon/X-ray transform, is linear. For a further reading on inverse problems we refer to [212, 260, 301] on which the following summary is based.

One part project of this thesis was the development of a software framework previously called *CampRecon* [28] which is currently being refactored into an open-source framework called *elsa*. In order to map the functionality to model and solve inverse problems into a software framework it is essential to understand how these problems are modeled mathematically. In the following we will provide all necessary mathematical concepts which enabled us to do exactly that.

4.1 Continuous vs. Discrete Problems

In def. 4.1 we have defined inverse problems in an abstract and continuous fashion. However, in order to be able to make use of modern computer equipments such continuous problems need to be discretized. The most simple way of discretization is sampling on discrete sampling points. While the simplicity is appealing the relation between the continuous and the discrete problem/model is not straightforward. Instead, we want to consider a more general framework of discretization, namely the framework of projection methods.

Within this framework, the process of discretization is understood as projection onto finite subspaces. Therefore a substantial connection between discrete and continuous problem formulation is introduced. For readings which go beyond the following summary we refer to [212, 301] on which this summary is based. The first ingredients which we need are projection operators[1] which are defined as follows.

Definition 4.2 **(Projection)** Let $V \subset X$ of a normed space X. A linear continuous mapping $P : X \to V$ is a **projection operator** if

$$Px \in V, \quad \forall x \in X, \tag{4.2}$$

$$Px = x, \quad \forall x \in V. \tag{4.3}$$

Among others the two most famous representatives of projection operators are the orthogonal projection and the interpolation operators. The orthogonal projection is, as the name already indicates, based on the concept of orthogonality within a Hilbert space.

Definition 4.3 **(Orthogonal projection)** (c.f. [212, example 3.3. a]) Let $V \subset X$ be a complete subspace of a Hilbert space X. The **orthogonal projection** of $x \in X$ is defined as:

$$Px = \arg\min_{v \in V} \|v - x\|_X . \tag{4.4}$$

The solution to eq. (4.4) is characterized by the equation

$$\langle x - Px, u \rangle_X = 0, \quad \forall u \in V, \tag{4.5}$$

i.e. the vector connecting Px and x stands orthogonally on the subspace V.

The second projection operator which will be used throughout this thesis is the interpolation operator. We will later discuss that many discretized versions of the forward model (see chapter 3) which are applied in the context of tomographic reconstruction intrinsically use this operator for discretization.

Definition 4.4 **(Interpolation operator)** (c.f. [212, example 3.3. b]) Let $V \subset C(\Omega)$ with a compact domain Ω. Let further $V = \operatorname{span}\{v_0, \ldots, v_{N-1}\}$ N-dimensional such that for pair-wise distinct sampling points $t_0, \ldots, t_{N-1} \in \Omega$ the corresponding Vandermonde matrix is invertible, i.e. the interpolation problem is uniquely solvable. The **interpolation operator** $P : C(\Omega) \to V, x \mapsto v$ is defined by the mapping of $x \in C(\Omega)$ to its interpolant in $v \in V$, i.e. $v(t_j) = x(t_j)$, $\forall j = 0, \ldots, N-1$.

Note: We have already discussed in case of the forward model (see chapter 3) for CT that the function we want to reconstruct is assumed to be of compact support. This means that one assumes that the function is assumed zero for any position that is not located within a bounding box of the measured object.

Following these definitions, we now discuss projection methods which enable the use of projection operators in order to discretize an inverse problem. The great advantage of

[1] This is not to be confused with the forward projection operator discussed previously.

this approach is that it establishes a direct, linear and continuous connection between the continuous problem and its discretization. The key idea is to use projection operators to project onto finite sub-spaces of both, the domain and the range of the operator $\mathcal{A}$ in def. 4.1.

Definition 4.5 **(Projection method)** (c.f. [212, Def. 3.4.],[301, Sec. 6.1.1]) Let $\mathcal{A} : X \to Y$ be a bounded, linear operator. Further, let $X^N \subset X$ and $Y^M \subset Y$ be finite-dimensional subspaces with $\dim\left(X^N\right) = N$, $\dim\left(Y^M\right) = M$ and the projection operator $Q_M : Y \to Y^M$. The **projection method** for a linear inverse problem $(\mathcal{A}, y)$ with $y \in Y$ is to solve

$$Q_M \mathcal{A} x_N = Q_M y, \tag{4.6}$$

for $x_N \in X^N$.

If one further considers two bases $\{\widetilde{x}_n\}_{n=0}^{N-1}$ and $\{\widetilde{y}_m\}_{m=0}^{M-1}$ of X^N and Y^M it is possible to express $Q_M y$ and $Q_M \mathcal{A} \widetilde{x}_n$, $n = 0, \ldots, N-1$:

$$Q_M y = \sum_{m=0}^{M-1} \mathbf{y}_m \widetilde{y}_m \quad \text{and} \quad Q_M \mathcal{A} \widetilde{x}_n = \sum_{m=0}^{M-1} a_{mn} \widetilde{y}_m, \; n = 0, \ldots, N-1. \tag{4.7}$$

For this discretized formulations, $x_N = \sum_{n=0}^{N-1} \mathbf{x}_n \widetilde{x}_n$ solves eq. (4.6) if and only if $A\mathbf{x} = \mathbf{y}$, with **system matrix** $A = (a_{mn}) \in \mathbb{R}^{M \times N}$ and $\mathbf{x} = (\mathbf{x}_n) \in \mathbb{R}^N$, $\mathbf{y} = (\mathbf{y}_m) \in \mathbb{R}^M$ as:

$$\begin{aligned}
Q_M \mathcal{A} x_n &= Q_M \mathcal{A} \sum_{n=0}^{N-1} \mathbf{x}_n \widetilde{x}_n && (4.8)\\
&= \sum_{n=0}^{N-1} \mathbf{x}_n Q_M \mathcal{A} \widetilde{x}_n && (4.9)\\
&= \sum_{n=0}^{N-1} \mathbf{x}_n \sum_{m=0}^{M-1} a_{mn} \widetilde{y}_m && (4.10)\\
&= \sum_{m=0}^{M-1} \underbrace{\sum_{n=0}^{N-1} a_{mn} \mathbf{x}_n}_{\mathbf{y}_m} \widetilde{y}_m && (4.11)\\
&= Q_M y. && (4.12)
\end{aligned}$$

Thus, by using projection methods we are able to discretize both, the domain and the range of a continuous operator and obtain a finite linear system of equations. The task to solve eq. (4.6) is transformed to solve a system of linear equations $A\mathbf{x} = \mathbf{y}$. Additionally, the choice of X_N and Y_M enables the modeling of properties of the measurement equipment. In case of CT this could e.g. be used to model detector properties such as the point spread function of a detector pixel[2]. In addition, this method enables the use of specific basis function in the domain to enforce/support special characteristics of the solution.

It should be mentioned that both Kirsch [212, Def. 3.4.] and Rieder [301, Sec. 6.1.1] use slightly different definitions of projection methods as they further study properties of

[2] For more on this topic we refer to [78, pp. 410ff]

these methods which require some additional restrictions on $\mathcal{A}$, X^N, and Y^M. Among other properties they e.g. investigate in the regularizing properties of projection methods in the sense of section 4.1. Further stability and convergence towards the continuous problem for increased N, M are investigated and discussed. However, in this work we strictly use this toolset as mathematical framework for discretization. For any discussion beyond this we highly recommend [212, 301] on which the afore given summary is based.

Up until now we did not explicitly formulate the entries a_{mn} of A, but we have discussed that such entries exist. This representation depends on the choice of X^N, Y^M as well as the choice of the projection operators. We are now going to discuss some popular choices.

If X and Y are Hilbert spaces and one chooses $Q_M : Y \to Y^M$ to be the orthogonal projection (def. 4.3) one obtains the **Galerkin method** (c.f. [212, Chap. 3.2]). The explicit formulation of the system matrix A is given by $a_{mn} = \langle \mathcal{A}\widetilde{x}_n, \widetilde{y}_m \rangle_Y$. A sub-class of the Galerkin method is the method of least-squares where $Y^M := \mathcal{A}X^N$ (c.f. [212, Sec. 3.2.1]). The matrix becomes $a_{mn} = \langle \mathcal{A}\widetilde{x}_m, \mathcal{A}\widetilde{x}_n \rangle_Y$ and its solution solves

$$\arg\min_{x_n \in X^N} \|\mathcal{A}x_n - y\|_Y \,. \tag{4.13}$$

Please note that this least-squares problem is formulated with respect to the inner product in Y. We will later also consider discrete least-squares methods where the sequence norm ℓ^2 and therefore the inner product $\langle \cdot, \cdot \rangle_{\ell^2}$ is considered instead. While at this point we did not consider perturbations/statistics of the measurements yet it is worth mentioning that the least-squares approach corresponds to the assumption of a Gaussian noise model. We provide a short discussion in section 4.5.

A second class is given by the *Collocation Method* (c.f. [212, Chap. 3.4]) where $Y = C(\Omega)$ on a compact domain Ω. For the Collocation Method the Y^M is chosen to be the space of linear splines according to the sampling points $t_0, \ldots, t_{M-1} \in \Omega$. Using the interpolation operator for Q_M the system matrix becomes $a_{mn} = (\mathcal{A}\widetilde{x}_n)(t_m)$. This method is predominantly used for tomographic reconstruction, often implicitly.

We are now able to formulate a discrete version of an inverse problem by using the presented methods while maintaining a linear relation to the original/continuous inverse problem.

4.2 Ill-posedness

We have already stated that a solution to an inverse problem $(\mathcal{A}, y)$ is given by $\mathcal{A}^{-1}y$ if the operator is invertible. However, if the operator $\mathcal{A}$ is e.g. only surjective and not bijective a solution may not be unique. If on the other hand $\mathcal{A}$ is purely injective a solution may not even exist. Additionally, it is important to consider how the solution varies with small perturbations of y, as measurements typically contain noise. These three conditions have been postulated by Hadamard [173] and are known as Hadamard conditions on well-posed problems:

Definition 4.6 **(Well-posed problem)** An inverse problem $(\mathcal{A}, y)$ is called *well-posed* if and only if all of the following requirements hold.

- $\forall y \in Y$, $\exists x \in X$ such that $\mathcal{A}x = y$. **(Existence/Surjectivity)**
- $\forall y \in Y$, there exists at most one $x \in X$ such that $\mathcal{A}x = y$. **(uniqueness/Injectivity)**
- The solution x depends continuously on y. **(Stability)**

Otherwise the problem is called *ill-posed*.

Unfortunately, the problems which are considered within this thesis fall into the category of ill-posed linear inverse problems (c.f. [264, chapter. IV]). Due to the Riesz potential the inverse operator to the Radon transform is an unbounded and therefore not continuous operator. Consequently, the stability condition in particular does not hold for our reconstruction problem. This is crucial as we are typically dealing with noisy measurements, i.e. we do not measure the perfect y but a perturbed version y^δ. Thus, from this on if we write inverse problem we implicitly expect this problem to be ill-posed.

4.3 Minimum-norm Solution

A common approach to deal with the first issue of def. 4.6 is to replace the direct problem with an optimization problem solving for a minimum-norm solution. In this context one aims at finding the $x \in \operatorname{dom}(\mathcal{A})$, such that $\mathcal{A}x$ is the "closest" element $y \in \operatorname{ran}(\mathcal{A})$. Consequently, for an inverse problem $\left(\mathcal{A}, y^\delta\right)$ with $y^\delta \in Y$ being a Banach space we solve:

$$\underset{x \in X}{\arg\min} \left\| \mathcal{A}x - y^\delta \right\|_Y . \tag{4.14}$$

Depending on the task there are various possible choices for Y. This choice however is commonly motivated by the underlying physics. However, as we are mainly interested in function spaces and their discrete counterparts common choices are the L^p- and the ℓ^p-spaces.

As we are investigating linear inverse problems for $\left(\mathcal{A}, y^\delta\right)$ we can combine the minimum-norm approach with the previously discussed projection methods (see section 4.1). Consequently the problem is discretized in terms of range and domain of the operator $\mathcal{A}$. This yields the discrete problem $\left(A, \mathbf{y}^\delta\right)$ with $A \in \mathbb{R}^{M \times N}$ and $\mathbf{y}^\delta \in \mathbb{R}^M$ using any of the methods described in section 4.1. A minimum-norm approach can now be stated with respect to the sequence ℓ^p-spaces, i.e.

$$\underset{\mathbf{x} \in \mathbb{R}^N}{\arg\min} \left\| A\mathbf{x} - \mathbf{y}^\delta \right\|_{\ell^p} , \tag{4.15}$$

with $p \geq 1$.

4.4 Regularization

A common approach to control the influence of noise and/or other perturbations which effect measurements is **regularization**. For a general overview we refer to [134]. Assume the

perfect measurements to be given as $y \in Y$ in a Banach space Y. Further, let $y^\delta \in Y$ be the perturbed measurements with $\delta > 0$ such that

$$\left\| y - y^\delta \right\|_Y < \delta. \tag{4.16}$$

Instead of solving $(\mathcal{A}, y)$ we have to stick with what we measured and solve $\left(\mathcal{A}, y^\delta\right)$ instead. Nevertheless we are interested in the solution of $(\mathcal{A}, y)$. Due to the ill-posed nature of the inverse problems considered in this thesis we may face several problems here. First of all, y^δ does not have to be in $\mathrm{ran}\,(\mathcal{A})$, i.e. even though $(\mathcal{A}, y)$ may posses a solution, $\left(\mathcal{A}, y^\delta\right)$ may not. Secondly, a solution to $\left(\mathcal{A}, y^\delta\right)$ may again not be unique. Finally, even if one has an idea about the error caused by the perturbation in the measurements (eq. (4.15)), one has no idea how strongly the perturbation influences the solution if the solution does not depend continuously on the data.

Again for the first issue we may apply minimum-norm approaches as discussed in section 4.3. This leaves us with the two remaining issues, those of uniqueness and stability. Fortunately, in many cases we have an idea about how our solution should look like. This information could e.g. be given by physical facts such as positivity of the physical quantity, tangible models such as anatomic models, or by more abstract assumptions such as smoothness etc. One consequently wants to use this prior knowledge to cope with the remaining two issues of ill-posedness, i.e. the uniqueness and the stability.

Recalling the definition of projection methods def. 4.5 one possibility is to choose X^N such that elements of this space are "favorable". However, this is very restrictive and it is quite complicated to incorporate multiple restrictions. This is where the much more flexible framework of regularization comes into play[3]. Mathematically, regularization is defined as follows.

Definition 4.7 **(Regularization)** (c.f. [212, Def. 2.1.],[301, Def. 3.1.1]) For a perturbed inverse problem $\left(\mathcal{A}, y^\delta\right)$, a family $\{\mathcal{H}_\lambda\}_{\lambda>0}$ of continuous operators $\mathcal{H}_\lambda : Y \to X$ is called a *regularization strategy* with *parameter* λ, if

$$\lim_{\lambda \to 0} \mathcal{H}_\lambda \mathcal{A} x = x, \quad \forall x \in X. \tag{4.17}$$

The key ingredients in this definition are the continuity and the point-wise convergence of $\mathcal{H}_\lambda \mathcal{A}$ to the identity. Again we restrict the provided summary to the concepts that are needed within the scope of this thesis, especially with respect to the development of the software framework presented in part III. For further reading we once again refer to [212, 260, 301].

Based on the abstract def. 4.7 we will now provide an overview on frameworks and common concepts of regularization strategies.

[3] To be precise, the choice of X^N can impose a regularization in the sense of def. 4.7. For further readings on this topic we refer to [212, 262, 301]

4.4.1 Variational Methods

The most prominent regularization methods are based on *variational methods* (c.f [112, p. 375ff] [319, p. 53ff]). These methods develop from optimizing a Tikhonov type of functional composed of a *data term* and possibly multiple *regularization terms* whose influences are controlled via a corresponding *regularization parameters*. Throughout this thesis we will consider the following definition of variational methods.

Definition 4.8 **(Variational method)** (c.f. [319, chap. 3]) For a perturbed inverse problem $\left(\mathcal{A}, y^{\delta}\right)$ a **variational method** is given as an *energy functional*

$$E\left(x\right) := \mathcal{F}_0\left(\mathcal{A}_0 x, y_0\right) + \sum_{k=1}^{K} \lambda_k \mathcal{F}_k\left(\mathcal{A}_k x, y_k\right), \tag{4.18}$$

with linear operators $\mathcal{A}_k$, corresponding reference data y_k for $0 \leq k \leq K$, and mappings $\mathcal{F}_k : \operatorname{ran}\left(\mathcal{A}_k\right) \times \operatorname{ran}\left(\mathcal{A}_k\right) \to \mathbb{R}$. The $\mathcal{F}_0\left(\mathcal{A}_0 x, y_0\right)$ is called **data term** while the $\mathcal{F}_k\left(\mathcal{A}_k x, y_k\right)$, $k \geq 1$ are called **regularization terms** with **regularization parameters** λ_k[4].

Note: An obvious choice for the $\mathcal{F}_k : \operatorname{ran}\left(\mathcal{A}_k\right) \times \operatorname{ran}\left(\mathcal{A}_k\right) \to \mathbb{R}$, $0 \leq k \leq K$ are metrics, if such exist on $\operatorname{ran}\left(\mathcal{A}_k\right)$, as they quantify the "distance" of $\mathcal{A}_k x$ to y_k. In the special case of Banach spaces a natural choice therefore is given by the metric induced by the corresponding norm. In this case the function is composed of a functional $\widetilde{\mathcal{F}}_k : \operatorname{ran}\left(\mathcal{A}_k\right) \to \mathbb{R}$ wrapping the linear residual $\mathcal{R}_k\left(\mathcal{A}_k, x, y_k\right) := \mathcal{A}_k x - y_k$, $0 \leq k \leq K$. In this special case eq. (4.18) becomes

$$E\left(x\right) := \widetilde{\mathcal{F}}_0\left(\mathcal{R}_0\left(\mathcal{A}_0, x, y_0\right)\right) + \sum_{k=1}^{K} \lambda_k \widetilde{\mathcal{F}}_k\left(\mathcal{R}_k\left(\mathcal{A}_k, x, y_k\right)\right). \tag{4.19}$$

In order to compute a solution to the inverse problem $\left(\mathcal{A}, y^{\delta}\right)$ one w.l.o.g aims at finding a minimum of $E\left(x\right)$:

$$\arg\min_{x \in X} E\left(x\right). \tag{4.20}$$

While the aforementioned definition is very generic and universally applicable, we want to highlight some examples using such type of formulations which are of special interest. Of special interest are those functionals $E\left(x\right)$ which are convex and lower semi-continuous functions. These choices ensure that a solution to eq. (4.20) exists (c.f. [103]). This optimum does not need to be unique though. Beside the examples already given in section 4.6.2 we now want to discuss some more advanced methods.

In the note of def. 4.8 we discussed the special form for Banach spaces which uses linear *residuals* $\mathcal{R}_k\left(\mathcal{A}_k, x, y_k\right) = \mathcal{A}_k x - y_k$, where the $\mathcal{A}_k$ are linear mappings which "investigate" a specific property of x and compare it to a reference y_k. The $\widetilde{\mathcal{F}}_k$ measures this residual. Therefore common choices are the p-th power of the L^p-norms and their sequence counter-part, the ℓ^p-norms.

[4] An important question which will not be considered as part of this thesis is how this parameter should be chosen. We refer to e.g. [174, 289, 291, 394].

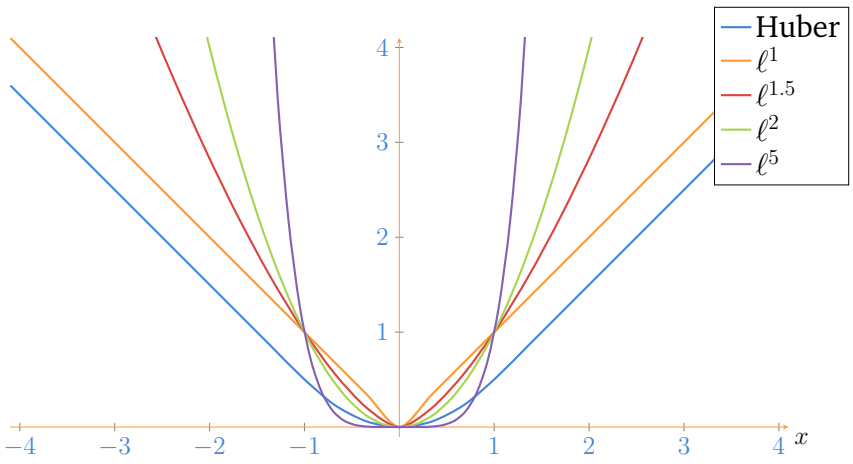

Figure 4.1 Illustration of the $\|\cdot\|_p$ for $p = 1, 1.5, 2, 5$ and the Huber-norm for $x \in \mathbb{R}$.

Another prominent example is the Huber-norm [188], which is a combination of $\|\cdot\|_1$ and $\|\cdot\|_2^2$ such that it becomes continuously differentiable. These choices have in common that they are non-negative and convex which is of special interest as we are aiming at finding an optimum of $E(x)$.

Among the various possibilities given by the framework of variational methods there are some commonly used examples for these type of approaches. Some of these will be described and discussed in the following to showcase the broad applicability which also motivates the design of our framework in part III.

Example 4.9 **(Tikhonov regularization)** The arguably most famous variant of regularization is the (generalized) Tikhonov regularization introduced by Tikhonov [355] (c.f. [319, sec. 3.1]). Here a least-squares approach is chosen for the data term and a L^2-norm regularization is added:

$$E_{\text{tikhonov}}(x) := \frac{1}{2}\left\|\mathcal{A}x - y^\delta\right\|_2^2 + \frac{\lambda}{2}\left\|\mathcal{A}_1 x\right\|_2^2. \tag{4.21}$$

For the classical Tikhonov regularization the operator in the regularization term is set to the identity, i.e. $\mathcal{A}_1 = \mathrm{id}$. Thus it penalizes large x in terms of the L^2-norm.

Example 4.10 **(Total variation regularization)** Another commonly used feature for regularization is variation. Within the method of Total Variation (TV), as introduced by Rudin *et al.* [313], one aims at finding a balance between the data term and the total amount of variation which is given by the derivation/gradient if one assumes $X = C^1(\Omega)$. The corresponding objective function is

$$E_{\text{TV,iso}}(x) := \frac{1}{2}\left\|\mathcal{A}x - y^\delta\right\|_2^2 + \lambda \int_\Omega \left\|\nabla x(\mathbf{x})\right\|_2 d\mathbf{x}. \tag{4.22}$$

Effectively this is the L^1-norm of the Euclidean norm of the gradient in each position. This is also referred to as isotropic Total Variation as the Euclidean norm and therefore the ℓ^2-ball of the gradient is considered.

In order to get rid of the combination of the two norms a minor modification leads to the anisotropic Total Variation (c.f. [60]). Here one uses a pure L^1-norm

$$E_{\text{TV,aniso}}(x) := \frac{1}{2}\left\|\mathcal{A}x - y^\delta\right\|_2^2 + \lambda \left\|\nabla x\right\|_1 . \tag{4.23}$$

TV has been used in the context of X-ray CT for example in [97, 336, 337, 341, 388]. The anisotropic version has been used in e.g. [117, 197]. However, a known side effect of this method is staircasing and loss of fine structures (c.f. [66, 76, 90, 123, 304]).

Example 4.11 **(Sparse regularization)** A method which became increasingly popular in recent years is sparse regularization. Here, the key idea is to express the domain of the inverse problem using special basis functions or over-complete frames (in terms of X^N). A preferable solution can then be assumed to be sparse, i.e. only few coefficients are non-zero with respect to this representation (c.f. [260, Ch. 7]).

Donoho [124] proposed the ℓ^0-"norm"[5] for this purpose which effectively counts the non-zero entries of a coefficient vector. However, this penalty term is hard to optimize and non convex, i.e. uniqueness may not be guaranteed, which is why alternative ways have been investigated. Most common is the substitution with a ℓ^1-penalty term which provides a regularization strategy as shown by Daubechies *et al.* [111], favors sparse solutions [84, 124, 126, 127], and is the smallest p such that the ℓ^p-norm is still a proper norm.

Let a basis or frame (c.f. [99]) transform be given by the analysis operator $\mathcal{C}$ and corresponding synthesis operator operator $\mathcal{C}^*$. This leads to the following two approaches.

The *synthesis* approach aims at recovering a sparse coefficient vector with respect to the given transform $\mathcal{C}^*$. The corresponding objective function is given as:

$$E_{\text{syn}}(c) := \frac{1}{2}\left\|\mathcal{A}\mathcal{C}^* c - y^\delta\right\|_2^2 + \lambda \left\|c\right\|_1 \tag{4.24}$$

and the solution is then given as $x^* = \mathcal{C}^* \arg\min_c E_{\text{syn}}(c)$.

In contrast, the *analysis* approach recovers a x in the original space which is sparse under transformation. This leads to the following formulation:

$$E_{\text{ana}}(x) := \frac{1}{2}\left\|\mathcal{A}x - y^\delta\right\|_2^2 + \lambda \left\|\mathcal{C}x\right\|_1 . \tag{4.25}$$

Elad *et al.* [132] found that these two approaches differ in their solution if an over-complete representation is used. The basis/frames that are used for these kinds of methods are predominantly based on the theory of wavelets. For a further reading on wavelets see e.g. [113, 246]. Common variants are Haar- [172] and Daubechies-wavelets [113] and wavelet-frames [110]. These are defined in the one-dimensional (1D) case and brought to higher dimensions by using the tensor product. Sparse regularization using Haar wavelets for CT has been considered in [157]. The relation between sparse wavelet regularization and TV is studied in [345]. Additionally for the 2D case, dictionaries were proposed which offer

[5] We use the quotation marks to indicate that this is not a true norm as the function is not homogeneous.

special properties for e.g. edge preservation. Ridgelets as proposed by Candes [85] offer an optimal representation for signals with singularities along straight lines. These have been used in [51] for adaptive sampling in the case of CT as X-rays are modeled as straight lines. For optimally sparse representations of C^2-functions with edges, i.e. singularities, along C^2-curves, curvelets[6] [80, 81, 82, 83], and shearlets [169, 219] have been proposed. An alternative approach is given by contourlets [122]. Frikel [149, 151] used curvelet sparse regularization for limited-angle CT. A comparison of TV to shearlets [363] and curvelets [8] has been discussed for CT as well and both proved to recover small line-like structures more reliably when compared to TV. For three and four dimensions tensor framelets have been investigated [121, 155, 156, 393]. The interested reader may refer to [343] for a further insight into sparse signal processing.

Example 4.12 **(Proximity problem)** (c.f. [103, Def. 10.1]) Another very prominent example which gains special attention in the context of splitting methods are **proximity problems**:

$$E_{\text{prox}}(x) := \frac{1}{2}\|x-y\|_2^2 + f(x). \tag{4.26}$$

Let f be convex and lower semicontinuous, then $y \mapsto \arg\min_x E_{\text{prox}}(x)$ has a unique solution. The operator, mapping $y \mapsto \arg\min_x E_{\text{prox}}(x)$ is called **proximity operator** and is written as prox_f [103, Def. 10.1].

We refer to [71, 103, 272] for exceptionally comprehensive discussions of related methods. Tables 10.1 and 10.2 in [103] provide a great overview on common proximity problems and their corresponding operators in particular.

In addition to the aforementioned examples there are many more variants of variational methods which mainly differ in the used functionals.

4.5 Excursus: Statistical Reconstruction

In the context of CT, in contrast to the linearized model given in eq. (3.1) an alternative approach is *statistical reconstruction* (c.f. [145]). Here, the original measurements (see eq. (1.1)), i.e. before applying the logarithm, of the detector are considered to represent realizations of a random variable. This enables incorporation of nonlinear physical effects. The reconstruction becomes another optimization problem similar to def. 4.8 with the "distance" being formulated in terms of the log-likelihood. In contrast to the functions we considered above one aims at maximizing the log-likelihood. However, this is equivalent to the form of variational methods as maximization is equivalent to minimization of the negative function. Therefore, most of the concepts discussed here and especially the framework presented in part III are applicable to this kind of reconstruction as well.

Common approaches for CT assume Poisson noise on the measurements [307][221]. If one considers the problem after taking the logarithm, the ℓ^2-norm based approach corresponds to the assumption of white noise. If strictly Poisson effects are considered the problem can

[6] Also see [239] for a great review.

be expressed in terms of a weighted ℓ^2_w-norm [69]. Taking the logarithm has two major issues, firstly it is not defined for negative readouts and the estimation is biased due to Jensen's inequality (c.f. [145]). Nevertheless, taking the logarithm is very attractive as linear inverse problems are very well understood and we will therefore stick with the linearized problem within this thesis. Beside noting that these more advanced statistical approaches are easily incorporated into the discussed framework part III, we therefore stick to the linearized version[7].

4.6 Solving the Inverse Problem

So far we have focused on the formulation of inverse problems (def. 4.1), their discretization (def. 4.5), the complications we face if this problem is ill-posed (def. 4.6), and regularization (def. 4.7). This has been discussed with respect to the problem formulation so far. Now it is time to face the computational part of our work and discuss methods to actually compute a solution to our inverse problem.

Typically one distinguishes between analytic and iterative[8] methods. For the first kind of methods one considers an analytic inversion $\mathcal{A}^{-1}$ for the forward model $\mathcal{A}$. This analytic inversion formula gets discretized in whole or in parts e.g. using the idea of discretizing $\operatorname{ran}\left(\mathcal{A}^{-1}\right)$ and $\operatorname{dom}\left(\mathcal{A}^{-1}\right)$ as introduced in the context of projection methods. In case of the second class the inverse problem $\left(\mathcal{A}, y^\delta\right)$ is typically discretized using e.g. the method from section 4.1 and the resulting system of linear equations $\left(A, \mathbf{y}^\delta\right)$ is solved in an iterative fashion.

4.6.1 Analytic Inversion for Tomographic Reconstruction

For standard CT multiple analytic methods have been proposed throughout the years. While we focus on iterative methods within this thesis, we want to give a brief overview on analytic methods as well.

The predominant method for analytic inversion is the FBP (c.f. [78, Ch. 5.7]). Recalling the FBP inversion formula for the 2D Radon transform (eq. (3.9)). The inversion formula can be separated into two linear operators which are typically discretized separately. First of all a convolution/filtering operator $(I_{-1} \otimes \mathrm{id})$ acting on the sinogram $g(s,u)$ in the Fourier domain is required. This Fourier convolution operator can be implemented in a discrete fashion using the Fast (discrete) Fourier Transform (FFT)[9]. Secondly, the back-projection is computed by discretizing the adjoint Radon operator $\mathcal{R}^*$ as $R^\top$ and applying it to the filtered version of the sinogram. Thus the analytic inversion formula gets discretized by discretization of its parts.

[7] We have recently presented a statistical approach for AXDT (compare part IV) in [9] based on the work of Chabior [88].

[8] In the context of tomographic reconstruction this is sometimes also referred to as algebraic reconstruction technique. This is easily confused with the algorithm Algebraic Reconstruction Technique (ART) of the same name, therefore we stick to the label *iterative*.

[9] For implementation of FFT based convolution we refer to [283, p. 641ff]

While the direct form of this method is appealing, the incorporation of regularization is less straightforward and mainly evolves around preprocessing and variation of the used filter. The most famous is the Ram-Lak filter proposed in [293]. Here the Riesz potential I_{-1} gets modified by an additional cut-off filter

$$\Theta(\zeta) := \begin{cases} 1 & |\zeta| < \mathrm{T} \\ 0 & \text{else} \end{cases}, \tag{4.27}$$

with cut-off frequency T.

Beside the Ram-Lak filter e.g. the Shepp-Logan filter [332], the Cosine [261], or the Hamming filter [211] have also been proposed. While the original method of FBP is built for 2D and parallel beam geometry, similar filter-based methods for cone-beam setups [142] exist. Additionally, analytic methods based on decompositions have been proposed. E.g. this has been proposed for wavelets [128, 228], curvelets [79], and shearlets [102].

Within the scope of this thesis and especially targeting at Anisotropic X-ray Dark-field Tomography (AXDT) we predominately focus on the much more flexible framework of iterative reconstruction[10].

4.6.2 Iterative Approaches

The second class of solvers is the class of *iterative approaches*. In contrast to analytic methods, here one aims at the iterative improvement of an initial guess. For this kind of algorithm the discretization is performed with respect to the forward model $\mathcal{A}$ of an inverse problem $\left(\mathcal{A}, y^{\delta}\right)$ with e.g. one of the techniques described in section 4.1. A given problem $\left(\mathcal{A}, y^{\delta}\right)$ is discretized and one obtains a discrete representation $\left(A, \mathbf{y}^{\delta}\right)$. Let w.l.o.g the system matrix be denoted as $A \in \mathbb{R}^{M \times N}$ and the discretized measurements as $\mathbf{y}^{\delta} \in \mathbb{R}^{M}$.

In order to cope with ill-posedness, common methods based on the least-squares formulation (see section 4.3) are employed. In the context of tomographic reconstruction the most famous representatives are the ART [165], Simultaneous Iterative Reconstruction Technique (SIRT) [159], and SART [41], which effectively represent reinventions of the Kaczmarz method [201], and the Landweber method [220].

Equivalent Problems

Sometimes a specific solver is built for a special problem formulation but nevertheless other problems might be brought to the required form by equivalence.

As an example, consider the finite linear least-squares problem with objective function

$$E_{\mathrm{ls}}(\mathbf{x}) := \frac{1}{2} \|A\mathbf{x} - \mathbf{y}\|_2^2, \tag{4.28}$$

[10] A comparison of alternating minimization and FBP in the context of CT can be found in [137]

for some linear operator A and a right-hand side $\mathbf{y}$. This objective function is convex and a minimum is characterized as a critical point, i.e. $\nabla E_{\text{ls}} = 0$. Evidently, the gradient is given as

$$\nabla E_{\text{ls}}(\mathbf{x}) = A^\top A\mathbf{x} - A^\top \mathbf{y}. \tag{4.29}$$

Equation (4.29) is commonly referred to as normal equation (c.f. [333]). Consequently the linear least-squares problem is equivalent to the linear problem implicitly stated by setting the gradient to zero. Furthermore, as

$$E_{\text{ls}}(\mathbf{x}) = \underbrace{\frac{1}{2}\mathbf{x}^\top A^\top A\mathbf{x} - \mathbf{x}A^\top \mathbf{y}}_{E_{\text{quad}}} + \underbrace{\frac{1}{2}\mathbf{y}^\top \mathbf{y}}_{const}, \tag{4.30}$$

by simply computing the squared norm explicitly, the linear least-squares problem is moreover equivalent to a quadric problem given by the objective function

$$E_{\text{quad}} = \frac{1}{2}\mathbf{x}^\top A^\top A\mathbf{x} - \mathbf{x}A^\top \mathbf{y}. \tag{4.31}$$

The latter equivalence is e.g. used to apply the Method of Conjugate Gradients (CG), which is meant to solve a quadric objective function with a Symmetric Positive-Definite (SPD) model A [333]. Following the equivalence and the fact that $A^\top A$ is SPD for any given matrix A eq. (4.31) is in fact a quadric function.

Regularization

In order to use the framework of variational methods (def. 4.8) which enables the broad application of regularization methods as discussed before, one considers optimization problems based on $(A, \mathbf{y}^\delta)$ as

$$\underset{\mathbf{x}\in\mathbb{R}^N}{\arg\min}\, E(\mathbf{x}), \tag{4.32}$$

with $E : \mathbb{R}^N \to \mathbb{R}$. Examples are presented in section 4.4.

Some of the most famous methods evolve around gradient descent methods. In this case the algorithm computes an iterative sequence of the following form

$$\mathbf{x}^{k+1} = \mathbf{x}^k - \alpha_k \nabla E(\mathbf{x}^k), \tag{4.33}$$

with α_k denoting the step size[11]. Great introductions to this topic are given in [70, 270, 362]. The main question here is how the step-length is chosen and whether momentum/relaxation terms are employed in addition. Examples for such methods are the Landweber methods [220]. Nesterov [266] presented an improved gradient method by adding an adaptive relaxation to the Landweber method, i.e. the computation of a new iterate based on two previous gradients. In contrast to the Landweber method this leads to a quadratic convergence rate.

Only recently, Kim *et al.* [209][207] have even improved this rate of convergence by adding additional momentum terms. In order to choose the step-length within the Separable Quadratic Surrogate (SQS) as developed by Erdogan *et al.* [136], the step-length is chosen according to

[11] Among others, the Barzilai-Borwein step size is a famous method [52].

a quadratic surrogate such that the matrix D majorizes the Hessian matrix of E. One choice is $D = \operatorname{diag}\{H_E(x)\,\mathbf{1}\}$ which leads to the update

$$\mathbf{x}^{k+1} = \mathbf{x}^k - D^{-1}\nabla E\left(\mathbf{x}^k\right). \tag{4.34}$$

A further discussion would go beyond the scope of this thesis. In particular, we have to omit Ordered Subsets (OS) methods and would like to refer the interested reader to [136]. The important message from this brief summary is that they fit into the framework of variational methods. This motivated the design of the software framework which will be discussed in part III.

One of the probably most famous methods for quadric problems (eq. (4.31)) is the method of CG [182]. Due to its fast convergence and the discussed equivalence of problems (see section 4.6.2) it is one of the most commonly applied methods for quadric, least-squares, and linear problems. We will use the CG for tomographic reconstruction of AXDT in part IV. Therefore, we provide the pseudocode for this method in code 4.1.

Input: $B \in \mathbb{R}^{N\times N}$ a SPD matrix and $\mathbf{y} \in \mathbb{R}^N$, initial guess $\mathbf{x}_0 \in \mathbb{R}^N$, $I \in \mathbb{N}$ and $\epsilon \in \mathbb{R}$.
Output: Minimizer $\mathbf{x} \in \mathbb{R}^N$ of the quadric problem

$$E_{\text{quad}}(\mathbf{x}) = \frac{1}{2}\mathbf{x}^\top B\mathbf{x} - \mathbf{x}^\top\mathbf{y} \tag{4.35}$$

with a relative gradient tolerance of ϵ.
$\mathbf{r} \leftarrow \mathbf{y} - B\mathbf{y}$
$\mathbf{d} \leftarrow \mathbf{r}$
$\delta_{\text{new}} \leftarrow \mathbf{r}^\top\mathbf{r}$
$\delta_0 \leftarrow \delta_{\text{new}}$
while $it \leftarrow 0, 1, 2, \ldots$ and $\delta_{\text{new}}/\delta_0 > \epsilon^2$ **do**
  $\mathbf{q} \leftarrow B\mathbf{d}$
  $\alpha \leftarrow \frac{\delta_{\text{new}}}{\mathbf{d}^\top\mathbf{q}}$
  $\mathbf{x} \leftarrow \mathbf{x} + \alpha\mathbf{d}$
  if $it \mod I == 0$ **then** ▷ The gradient gets reset each I iterations.
    $\mathbf{r} \leftarrow \mathbf{b} - B\mathbf{x}$
  else
    $\mathbf{r} \leftarrow \mathbf{r} - \alpha\mathbf{q}$
  end if
  $\delta_{\text{old}} \leftarrow \delta_{\text{new}}$
  $\delta_{\text{new}} \leftarrow \mathbf{r}^\top\mathbf{r}$
  $\beta \leftarrow \frac{\delta_{\text{new}}}{\delta_{\text{old}}}$
  $\mathbf{d} \leftarrow \mathbf{r} + \beta\mathbf{d}$
end while

Code 4.1 Pseudocode of the CG for quadric problems (c.f. [333, B2])

A special sub-class of methods based on optimization problems are splitting-based methods. Such methods are studied in the framework of proximity operators associated with monotone operators (c.f. [306]). An excellent overview is provided by Combettes and Pesquet [103]. Primal dual splitting for inverse problems is considered in e.g. [89, 91]. Examples are the Iterative Soft-Thresholding Algorithm (ISTA), Fast Iterative Soft-Thresholding Algorithm (FISTA) for sparse regularization, and more general methods such as the split-Bregman [164]

and the Alternating Direction Method of Multipliers (ADMM) [71, 131]. Gabay [154] has shown that the ADMM can be interpreted as a splitting method applied to a dual functional while Eckstein and Bertsekas [131] have established that ADMM is a particular instance of a proximal method. Within the context of CT the ADMM has been applied e.g. in [8, 267, 292, 290]. As an example, we will provide a brief summary of the ADMM as this again will provide an improved insight into the needs of a general software framework for inverse problems.

Case Study: ADMM

The method of ADMM provides a framework to solve a linear combination of two convex functionals via variable splitting. For an excellent overview we refer to [71] and the corresponding website [on5] which provides an extensive collection of example code for various problems.

However, if we investigate this we actually find that a lot of code duplicates are created while the basic procedure is shared. As an illustration consider the following optimization problem with both the data and the regularization term being convex,

$$\arg\min_{\mathbf{x}} \mathcal{F}_0\left(\mathcal{R}_0\left(A_0, \mathbf{x}, \mathbf{y}_0\right)\right) + \lambda_1 \mathcal{F}_1\left(\mathcal{R}_1\left(A_1, \mathbf{x}, \mathbf{y}_1\right)\right). \tag{4.36}$$

Within the ADMM this problem is transformed into an equivalent constrained optimization problem by decoupling data and regularization term as [71, pp. 13ff]

$$\arg\min_{\mathbf{x}} \mathcal{F}_0\left(\mathcal{R}_0\left(A_0, \mathbf{x}, \mathbf{y}_0\right)\right) + \lambda_1 \mathcal{F}_1\left(\mathbf{z}\right) \quad \text{s.t.} \quad \mathcal{R}_1\left(A_1, \mathbf{x}, \mathbf{y}_1\right) = \mathbf{z}. \tag{4.37}$$

Formulating the *augmented Lagrangian* L_ρ in scaled form yields

$$\begin{aligned} L_\rho\left(\mathbf{x}, \mathbf{z}, u\right) &= \mathcal{F}_0\left(\mathcal{R}_0\left(A_0, \mathbf{x}, \mathbf{y}_0\right)\right) + \lambda_1 \mathcal{F}_1\left(\mathbf{z}\right) && (4.38)\\ &\quad + \frac{\rho}{2}\left\|\mathcal{R}_1\left(A_1, \mathbf{x}, \mathbf{y}_1\right) - \mathbf{z} + \mathbf{u}\right\|_2^2 - \frac{\rho}{2}\left\|\mathbf{u}\right\|_2^2, && (4.39) \end{aligned}$$

with the *scaled dual variable* $\mathbf{u} = (1/\rho)\,\mu$, μ denoting the Lagrange multiplier. The parameter ρ couples $\mathcal{R}_1$ and $\mathbf{z}$. Within each iteration of ADMM one computes updates for $\mathbf{x}$, $\mathbf{z}$ and $\mathbf{u}$ via three steps, which involves two optimization problems and one pure update:

$$\begin{aligned} \mathbf{x}^{k+1} &= \arg\min_{\mathbf{x}} L_\rho\left(\mathbf{x}, \mathbf{z}^k, \mathbf{u}^k\right) && (4.40)\\ &= \arg\min_{\mathbf{x}} \left\{\mathcal{F}_0\left(\mathcal{R}_0\left(A_0, \mathbf{x}, \mathbf{y}_0\right)\right) + \frac{\rho}{2}\left\|\mathcal{R}_1\left(A_1, \mathbf{x}, \mathbf{y}_1\right) - \mathbf{z}^k + \mathbf{u}^k\right\|_2^2\right\}, && (4.41)\\ \mathbf{z}^{k+1} &= \arg\min_{\mathbf{z}} L_\rho\left(\mathbf{x}^{k+1}, \mathbf{z}, \mathbf{u}^k\right) && (4.42)\\ &= \arg\min_{\mathbf{z}} \left\{\frac{1}{2}\left\|\mathcal{R}_1\left(A_1, \mathbf{x}^{k+1}, \mathbf{y}_1\right) - \mathbf{z} + \mathbf{u}^k\right\|_2^2 + \frac{\lambda_1}{\rho}\mathcal{F}_1\left(\mathbf{z}\right)\right\}, && (4.43)\\ \mathbf{u}^{k+1} &= \mathcal{R}_1\left(A_1, \mathbf{x}^{k+1}, \mathbf{y}_1\right) - \mathbf{z}^{k+1} + \mathbf{u}^k. && (4.44) \end{aligned}$$

The beauty of this method is that by decoupling the two terms the ADMM provides a framework to solve the initial problem via solving a Tikhonov regularized problem ($\mathbf{x}$ update) and a proximity problem ($\mathbf{z}$ update). Both these problems are very well understood and are typically easier to solve than the initial problem.

With this we conclude the chapter on inverse problems. This chapter serves as motivation for the design of the software framework in part III. Before we move on to this framework, we first want to provide a detailed discussion on the dark-field signal from a mathematical point of view and mathematical tools to model the scattering within an object.

5 Mathematics of Dark-field

Before we move on to the mathematical concepts which will be used to model the scattering in order to reconstruct the scattering information from anisotropic dark-field imaging, we want to take a closer look at the dark-field imaging model. Throughout the recent years multiple explanations for the dark-field contrast have been proposed [238, 384, 385]. The change of the intensity of the dark-field signal when a sample is rotated around the beam direction is commonly modeled by a cosine. This idea was used in directional X-ray dark-field imaging [193, 194], which further led to XVR [55, 280]. Jensen *et al.* [193] discussed that this cosine approximation is valid if Gaussian as well as comparably weak scattering is assumed. Based on the cosine relation, both Malecki *et al.* [243] and Revol *et al.* [299] developed a model for the accumulation of anisotropic scattering along the X-ray beam direction. Please note that the assumption of a Gaussian scattering function has a big advantage, namely the existence of an intrinsic relation of the scattering observed under rotation as above. For this reason we will stick with the principle proposed by Malecki *et al.* [243] throughout part IV. However, only recently Strobl [349] provided a much more complete explanation for the dark-field contrast. Interestingly, these explanations originate from a different scattering imaging modality SESANS (c.f. [295]). For an extensive analysis on SESANS we refer to [40]. The model presented by Strobl [349] has been experimentally validated by Prade *et al.* [282]. However, the direct relation between measurements is partially lost. This, at least with the current setup configuration, poses a nearly unsolvable problem. Nevertheless, for completeness we want to provide this model together with a brief summary, as this is one of the most promising starting points for further improvements to the methods proposed in part IV. For any insight which goes beyond this summary we refer to [40, 160, 282, 349] on which this summary is based.

Recalling eq. (1.4), the scattering intensity of the diffraction pattern is given as (c.f. [160, pp. 19ff])

$$I_{\text{SAXS}}(q) = \left| \int \rho(x)\, e^{iqx} dx \right|^2 = \mathcal{F}_3(\rho * \rho)(q), \tag{5.1}$$

with $\rho : \mathbb{R}^3 \to \mathbb{R}$ denoting the electron density. The last equality follows from the convolution theorem (theorem 2.4). To simplify this equation further the autocorrelation function $\gamma = \rho * \rho$ is introduced.[1]

Following the approximation for SAXS in eq. (1.5), we recall that the following approximation holds

$$\theta \approx \frac{\lambda}{2\pi} |q|, \tag{5.2}$$

with θ denoting the scattering angle, λ the wavelength of the X-ray and q the scattering vector. Further, the offset on the detector that is caused by a scattering with angle θ leads to a shift

[1] As mentioned before we use a slightly different form of the Fourier transform (see section 2.1) but nevertheless use the $\mathcal{F}$ symbol in this context.

$\triangle x_g$ of the interference pattern. This shift relates to θ and the distance between sample and detector d_s, i.e.

$$\theta \approx \frac{\triangle x_g}{d_s}. \tag{5.3}$$

Recall the intensity approximation eq. (1.10)

$$I\left(x_g\right) = a_0 + a_1 \cos\left(\varphi + \frac{2\pi}{p_2} x_g\right), \tag{5.4}$$

with p_2 denoting the period of the grating G_2. The shift $\triangle x_g$ relates to a phase-shift $\triangle\varphi$

$$\triangle\varphi = \frac{2\pi}{p_2}\triangle x_g \approx \underbrace{\frac{\lambda d_s}{p_2}}_{\xi_{GI}} |q|, \tag{5.5}$$

with ξ_{GI} denoting the autocorrelation length [238]. This effectively establishes a connection between scattering vector and introduced phase-shift using eq. (5.2) and eq. (5.3).

According to Friedel's law, scattering results in an equal amount of scattering in positive and negative direction, i.e. x_g and $-x_g$, effectively resulting in a reduction of the amplitude. Considering the accumulation for all scattering vectors q[2] and taking multiple scattering into account leads to a dark-field signal for autocorrelation length ξ_{GI} of [349],

$$d\left(\xi_{GI}\right) = \exp\Big(\sigma_t z\big(\mathcal{X}_l\gamma\left(\xi_{GI}\cdot t\right) - 1\big)\Big), \tag{5.6}$$

with z giving the sample thickness, l denoting the X-ray beam direction, and t denoting the grating direction. For clarification we break down the term $\mathcal{X}_l\gamma\left(\xi_{GI}\cdot t\right)$. First, this takes the X-ray projection of the autocorrelation function in beam direction l. Second, it maps to the explicit evaluation at the point given by $\xi_{GI}\cdot t$. The constant σ_t is the total scattering probability [282, A.4],

$$\sigma_t = \int_{\mathbb{L}(t)} I_{\text{SAXS}}\left(q\right) dq. \tag{5.7}$$

While this provides a highly complete description of the dark-field signal, this formula has been derived with isotropic scattering in mind thus far. Consequently, throughout these isotropic considerations $\mathcal{X}_l\gamma\left(\xi_{GI}\cdot t\right)$ and σ_t are constant within the sample and under rotation, i.e. rotation of l, t. Nevertheless, it gives some great insight into the imaging process. An overview of the mathematical relationships between SAXS and dark-field imaging in this case are given in fig. 5.1. As the model in [349] is stated with pure imaging in mind we will provide the relation with respect to the tomographic setup. While the relationships on the left side correspond to SAXS imaging, the right side represents the image formation of dark-field using GBI. For convenience we quickly walk through fig. 5.1. The intensity observed for a scattering vector q is given by the Fourier transform of the autocorrelation function γ (see **reciprocal space**). The splitting-based method effectively leads to a slicing through the reciprocal space as one assumes that the observed q vectors are orthogonal to the ray direction l (see **SAXS**). According to the Fourier slice theorem (see theorem 3.3) this is equivalent to an X-ray projection (see def. 3.2) of the autocorrelation function (see **X-ray projection**) and a subsequent Fourier transform. The sensitivity of the grating leads to a projection of the scattering function I_{SAXS} along the axis orthogonal to X-ray beam direction

[2] According to the SAXS approximation.

l and grating direction t (see **grating projection**). Furthermore, the most interesting effect is that the analyzer grating inverts the Fourier relation between autocorrelation γ and I_{SAXS} relation (see **correlation function**). Alternatively, once more due to the Fourier slice theorem this is equivalent to the Fourier transform of the slice of the reciprocal space and restricting the evaluation to the line defined by the direction t of the grating (see **Fourier SAXS**). The resulting function is sampled at the setup specific quantity ξ_{GI}. Thus the measured dark-field signal relates to the explicit evaluation of the projection (in the sense of the X-ray transform – compare def. 3.2) evaluated at $\xi_{GI} \cdot t$.

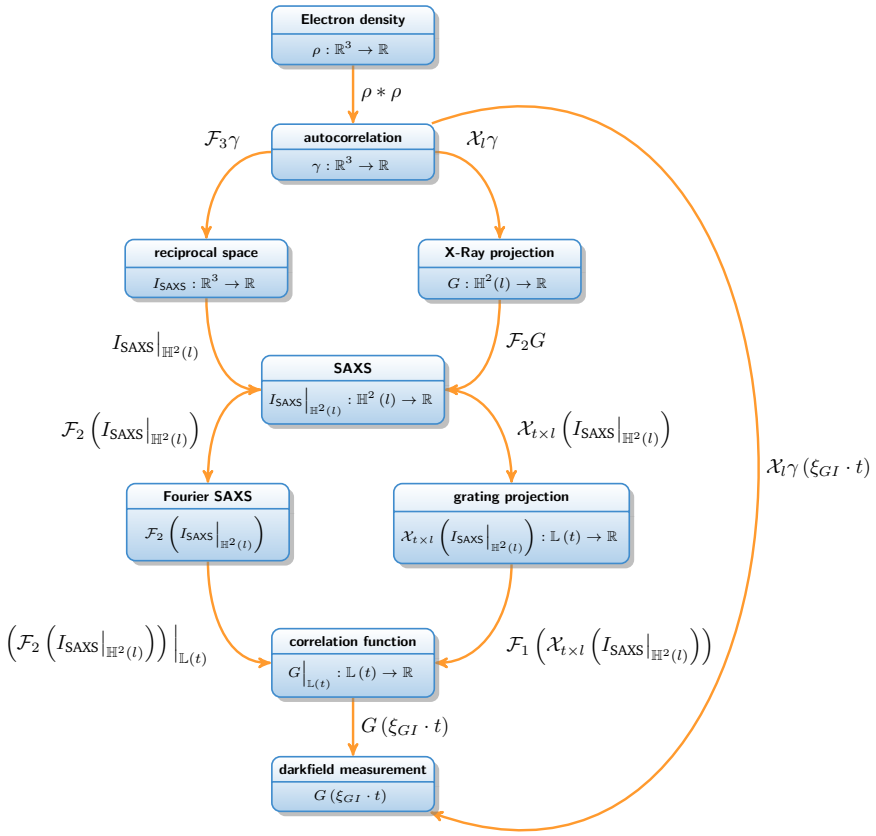

Figure 5.1 Relation between the dark-field signal and SAXS. With $l, t \in \mathbb{S}^2$ denoting the beam direction and the grating orientation.[3]

We want to conclude with the summary of further ideas and starting points for future work and possible applications to AXDT[4]. The formula derived by Strobl [349] states that for a single X-ray projection we actually sample the projection of the autocorrelation function only at one single point. This single point is defined by the grating orientation t and the autocorrelation length ξ_{GI}. If the sample can be rotated freely in 3D, as is the case for the Euler cradle, this means that we only collect integral values along lines which are tangential to the sphere with radius ξ_{GI}. By moving the sample on the connection between the gratings one effectively samples the projection space by increasing/decreasing this radius (c.f. [282]). Alternatively, the grating period p_2 or the wavelength could be varied. For the latter, one could build upon the idea of spectroscopic dark-field imaging [56]. This, however, results in an additional

[3] Credits for this illustration go to F. Schaff. The only change that has been performed within the scope of this thesis is the addition of the tomography parameter l and t.
[4] This summary is the result of many discussions within our XTT/AXDT group.

and more complicated imaging process. Further, in order to apply this model to anisotropic dark-field tomography, the autocorrelation function becomes position dependent, which also affects the σ_t. For this purpose one could replace the autocorrelation function in eq. (5.6) by a position dependent equivalent $\eta : \mathbb{R}^3 \rightarrow \left(\mathbb{R}^3 \rightarrow \mathbb{R}\right)\ ,\ x \mapsto \gamma_x$, with γ_x denoting the autocorrelation at position x. With this definition eq. (5.6) becomes

$$d\left(\xi_{GI}\right) = \exp\left(\mathcal{X}_l\left(\sigma_{t,\text{aniso}}\left(x\right)\left(\mathcal{X}_l\big(\eta(x)\big)\left(\xi_{GI}\cdot t\right) - 1\right)\right)\right), \tag{5.8}$$

with $\sigma_{t,\text{aniso}}\left(x\right) = \sigma_{t,x}$ denoting the total scattering probability at the location x corresponding to $\eta\left(x\right)$.

At present we are not aware of a reconstruction based on this model. Nevertheless, as this model offers a possible link between the theory of SAXS and the method of AXDT, which will be discussed in part IV, we consider this one of the most interesting starting points for further improvements to AXDT.

We are going to continue with the elements and related mathematical concepts which are used to model the scattering within the object within part IV.

6 Tensors and Spherical Functions

In this chapter we will consider a special kind of function, namely spherical functions in $\mathbb{R}^3$, i.e. functions defined on $\mathbb{S}^2$. As the quantity to be reconstructed in part IV is anisotropic in contrast to X-ray attenuation and phase-contrast, a scalar function is not sufficient to describe the physical process influencing the X-ray beam at a specific position within the measured object. Instead, in part IV we will see that the scattering process in each position can be modeled as spherical function $f : \mathbb{S}^2 \to \mathbb{R}$ with f mapping a scattering direction $u \in \mathbb{S}^2$ to a corresponding scattering strength $f(u)$.

With this motivation in mind we will first discuss a special class of spherical functions based on rank-2 tensors. This forms the basis for XTT. Furthermore, generic spherical functions, a basis for $L^2\left(\mathbb{S}^2\right)$, as well as useful theorems for such functions will be discussed. This will lead to the development of AXDT in part IV.

The first class which is based on rank-2 tensors is well-known from its application for DTI (c.f. [54, 277, 374, 375]). For a symmetric rank-2 tensor, i.e. $A \in \mathrm{Pos}_3$, we define the spherical function $f : \mathbb{S}^2 \to \mathbb{R}_+$

$$f_A(u) := \frac{1}{\sqrt{u^\top A u}}. \tag{6.1}$$

This kind of function is of special interest, as the radial projection of a 3D Gaussian distribution results in eq. (6.1) (up to a factor). This is the motivation behind using tensors to model the diffusivity in DTI [54]. This relation is presented in the following lemma.

Lemma 6.1 **(Radial projection of a Gaussian distribution)** Let $f : \mathbb{R}^3 \to \mathbb{R}, x \mapsto e^{-\frac{1}{2}x^\top A x}$ denote a Gaussian distribution and with A denoting the inverse of the covariance matrix, then the radial projection for $u \in \mathbb{S}^2$ is:

$$\int_0^\infty e^{-\frac{1}{2}ru^\top Aru} dr = \int_0^\infty e^{-\frac{1}{2}r^2 u^\top Au} dr, \tag{6.2}$$

$$= \lim_{x\to\infty} \sqrt{\frac{\pi}{2}} \frac{1}{\sqrt{u^\top Au}} \operatorname{erf}\left(\sqrt{\frac{1}{2}u^\top Aux}\right), \tag{6.3}$$

$$= \sqrt{\frac{\pi}{2}} \frac{1}{\sqrt{u^\top Au}}. \tag{6.4}$$

In the equation above erf denotes the error function and the final step results from A being SPD and $\lim_{x\to\infty} \operatorname{erf}(cx) = 1, \forall c > 0$.

The graph of a function as given in eq. (6.1) is an ellipsoid which can be naturally analyzed using an eigenvalue decomposition of A, i.e.

$$A = \begin{pmatrix} \vdots & & \\ v_0 & v_1 & v_2 \\ \vdots & & \end{pmatrix} \begin{pmatrix} \lambda_0 & & \\ & \lambda_1 & \\ & & \lambda_2 \end{pmatrix} \begin{pmatrix} \vdots & & \\ v_0 & v_1 & v_2 \\ \vdots & & \end{pmatrix}^\top, \tag{6.5}$$

with $v_0, v_1, v_2 \in \mathbb{R}^3$ denoting the eigenvectors and $\lambda_0, \lambda_1, \lambda_2 \in \mathbb{R}$ the corresponding eigenvalues of A, which describe the half-axis and their corresponding reciprocal squared lengths $\frac{1}{\sqrt{\lambda_0}}, \frac{1}{\sqrt{\lambda_1}}, \frac{1}{\sqrt{\lambda_2}}$ respectively.

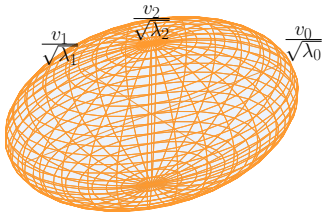

Figure 6.1 Ellipsoid given by a tensor with eigenvectors v_0, v_1, v_2 and eigenvalues $\lambda_0, \lambda_1, \lambda_2$. The chosen values are $\lambda_0 = 1^{-2}$, $\lambda_1 = 0.7^{-2}$ and $\lambda_2 = 0.5^{-2}$.

Consequently, eq. (6.1) gives a parametric version of the ellipsoid:

$$\left\{x \in \mathbb{R}^3 \ : \ x^\top A x = 1\right\} \tag{6.6}$$

The space of tensors is referred to as Pos_3 and in chapter 7 we are going to discuss that this space provides a Riemannian manifold. Modeling the scattering process in each position using a rank-2 tensor has lead to the method of XTT. We are going to provide an overview/review of this method together with a discussion of its advantages and disadvantages in chapter 16.

Minor spoiler: We will see that the simplicity of the tensor model turns out to be too basic and general spherical functions enable improved reconstructions. For this purpose we will consider the space $L^2\left(\mathbb{S}^2\right)$ and one of its bases, the **spherical harmonics**.

The set of **spherical harmonics** $\{V_k^m\}_{k\geq 0, -k\leq m\leq k}$ provides an orthonormal basis for $L^2\left(\mathbb{S}^2\right)$. Similar to the Fourier transform, multiple definitions using different scalings exist. Within this thesis we are going to use the orthonormal version which also conforms to the support provided by boost [on4] and the Matlab [on2] toolbox by Politis [on15]. For $u = (u_0, u_1, u_2) \in \mathbb{S}^2$ let θ, φ denote the corresponding spherical coordinates[1], then the basis functions are defined as

$$V_k^m(u) = \sqrt{\frac{(2k+1)}{4\pi}\frac{(k-m)!}{(k+m)!}} P_k^m(\cos(\theta))\, e^{im\varphi}, \tag{6.7}$$

with P_k^m denoting the associated Legendre polynomials.

[1] With the convention $\theta = \frac{\pi}{2} + \operatorname{atan2}\left(u_2, \sqrt{u_0^2 + u_1^2}\right)$, $\varphi = \operatorname{atan2}(u_1, u_0)$.

For a detailed discussion we refer the interested reader to [49]. Mohlenkamp provides an overview in [on14] as well. He also introduced a fast spherical harmonics transform in [254] which uses similar techniques to the ones used for the FFT.

As this set provides a basis, for any $f \in L^2\left(\mathbb{S}^2\right)$ there exists an expansion with respect to the V_k^m, i.e.

$$f = \sum_{k=0}^{\infty} \sum_{m=-k}^{k} f_k^m V_k^m, \tag{6.8}$$

with f_k^m denoting the coefficients corresponding to V_k^m. Due to the orthonormality the coefficients are computed as

$$f_k^m = \langle f, V_k^m \rangle_{L^2(\mathbb{S}^2)} = \int_{\mathbb{S}^2} f(u)\, V_k^m(u)\, d\sigma(u). \tag{6.9}$$

In the equation above the σ denotes the standard Lebesque measure on the sphere.

With respect to this expansion there exists a similar theorem to Parseval's theorem [49], i.e. for $f, g \in L^2\left(\mathbb{S}^2\right)$ the following equality holds,

$$\langle f, g \rangle_{L^2(\mathbb{S}^2)} = \left\langle \left(f_k^m\right)_{k\geq 0, -k\leq m\leq k}, \left(g_k^m\right)_{k\geq 0, -k\leq m\leq k} \right\rangle_{\ell^2}. \tag{6.10}$$

According to eq. (6.9), computing the transformation in the discrete case is reduced to the task of numerical integration on the sphere. Within the scope of this thesis, we will omit the discussion of methods to numerically compute the spherical harmonics transform and refer to Mohlenkamp [254] for an efficient transform. Nevertheless we will rely on concepts to compute surface integrals on the sphere. A common scheme to numerically approximate integrals is quadrature. Here, an integral is replaced by a finite sum over weighted function evaluations. Quadrature in the context of surface integrals on the sphere $\mathbb{S}^2$ is also referred to as cubature (c.f. [181]) and we will provide a corresponding definition in the following.

Definition 6.2 **(Quadrature/Cubature on sphere)** (c.f. [49][181]) Let $f : \mathbb{S}^2 \to \mathbb{R}$ be a spherical function. A **cubature** rule is defined by a set of K tuples $U = \{(u_0, w_0), \ldots, (u_{K-1}, w_{K-1})\}$ with $u_k \in \mathbb{S}^2$ denoting sampling points and $w_k \in \mathbb{R}$ denoting corresponding quadrature weights with $\sum_{k=0}^{K-1} w_k = \sigma(\mathbb{S}^2)$, such that the integral over f is approximated by:

$$\int_{\mathbb{S}^2} f(u)\, d\sigma(u) \approx \sum_{k=0}^{K-1} w_k f(u_k) \tag{6.11}$$

Note: For a discussion of approximation bounds we refer to [181].

While there are various techniques to choose the sampling/weighting pairs in case of a cubature rule, we will focus on two specific ones – partition and t-design based cubature. For an in depth overview we refer to [49, 181], on which the following summary is based.

For partition based cubature, one chooses a partition $\{T_0, \ldots, T_{K-1}\}$ (see def. 2.1) of $\mathbb{S}^2$. The corresponding cubature rule is given as (u_k, w_k) with $u_k \in T_k$ and $w_k = \sigma(T_k)$ according to def. 6.2. The remaining task is to compute an according partition of $\mathbb{S}_2$. Possible methods are

spherical Delauney triangulation/Voronoi diagrams [296], which compute a partitioning based on given sampling points u_k [2]. Centroidal Voronoi tesselation [129] in contrast is an iterative process based on Voronoi diagrams, which aims at finding K pairs (u_k, w_k), $0 \leq k \leq K-1$ such that the u_k are the center of mass of the corresponding Voronoi cell[3]. Finally, in case of equal-area partitions [288] the partitions are chosen such that $\sigma(T_k) = \frac{\sigma(\mathbb{S}^2)}{K}$, $0 \leq k \leq K-1$ holds.

Another class of special sampling schemes are spherical t-designs [119]. A t-design consist of sampling directions $\{u_k, \ldots, u_{K-1}\}$ which provide accurate integration, i.e. equality holds in eq. (6.11), with $w_k := \frac{\sigma(\mathbb{S}^2)}{K}$, $\forall 0 \leq i \leq K-1$ for any polynomial function $p \in \mathbb{P}_k(\mathbb{S}^2)$ of degree $k \leq t$, i.e.

$$\int_{\mathbb{S}^2} f(u)\, d\sigma(u) = \sum_{k=0}^{K-1} \underbrace{\frac{\sigma(\mathbb{S}^2)}{K}}_{w_k} f(u_k). \tag{6.12}$$

In [176] t-designs up to $t = 21$ are provided.

Finally we want to discuss a special transform similar to the aforementioned Radon transform on spherical functions. This transform is the Funk-Radon transform [153]. While the Radon transform maps functions to integral values over hyperplanes, the Funk-Radon transform performs something similar on functions on $\mathbb{S}^{N-1}$, i.e. mapping a function $f : \mathbb{S}^{N-1} \to \mathbb{R}$ to integral values along great circles. The definition for N dimensions is as follows.

Definition 6.3 **(Funk-Radon transform (N-dimensional))** (c.f. [153]) Let $f : \mathbb{S}^{N-1} \to \mathbb{R}$ be sufficiently nice. The mapping $\mathcal{P}f : \left(f : \mathbb{S}^{N-1} \to \mathbb{R}\right) \to \left(\mathcal{P}f : \mathbb{S}^{N-1} \to \mathbb{R}\right)$ of f to integrals over great circles $\mathbb{C}(u) := \left\{u' \in \mathbb{S}^{N-1} \;:\; \langle u, u' \rangle = 0\right\}$:

$$\mathcal{P}f(u) = \int_{\mathbb{C}(u)} f(u')\, ds(u') \tag{6.13}$$

is called **Funk-Radon transform**, with s denoting the Lebesque measure on $\mathbb{S}^{N-2}$.

Note: Due to the accumulation along great circles, this, in the case of positive functions, maps extrema located along great circles to extrema orthogonal to the great circle. We will make special use of this property in chapter 19.

With respect to the afore-discussed basis for spherical functions $f \in L^2(\mathbb{S}^2)$, the Funk-Radon transform can be computed in a very convenient way. This has already been proposed in the original publication by Funk [153] and the relation is summarized in the following theorem.

Theorem 6.4 **(Funk-Radon transform (3D) the spherical harmonics way)** (c.f. [153]) Let $f \in L^2(\mathbb{S}^2)$ be expanded via spherical harmonics, such that $f = \sum_{k=0}^{\infty} \sum_{m=-k}^{k} f_k^m V_k^m$. Then the Funk-Radon transform (def. 6.3) of f is given as [153]:

$$\mathcal{P}f = \sum_{k=0}^{\infty} \sum_{m=-k}^{k} \underbrace{P_k(0)\, f_k^m}_{(\mathcal{P}f)_k^m} V_k^m \tag{6.14}$$

[2] Matlab [on2] code is available from Burkardt *et al.* [on7, on8].
[3] Matlab [on2] code is available from Burkardt *et al.* [on6].

with P_k denoting the Legendre polynomial. Explicitly the factors are given as:

$$P_{2n+1}(0) = 0 \tag{6.15}$$

$$P_{2n}(0) = (-1)^n \frac{1 \cdot 3 \cdot 5 \cdots 2n-1}{2 \cdot 4 \cdot 6 \cdots 2n} \tag{6.16}$$

This concludes our discussion of spherical functions. In the following chapter, we are going to discuss the special case of Pos_3, as already mentioned above, in the context of spherical functions based on symmetric rank-2 tensors. While the Euclidean space provides an intrinsic concept of distance, this is not as straightforward for Pos_3. The reason why we are nevertheless interested in quantifying distances is that we again use this space to model the domain of an inverse problem (see chapter 4) in part IV. We are therefore interested in how the concept of variational methods translates to Pos_3.

7 Manifolds

In the previous chapter (chapter 6) we have already mentioned the space of Pos_3. This space, in contrast to the Euclidean space which is used for CT, does not provide a straightforward concept of "distance". In order to establish a similar concept nonetheless, we need to consider another mathematical concept, i.e. manifolds. This chapter will provide a brief discussion of manifolds in general and the manifold Pos_3 in particular. For an overview on the topic of manifolds we refer to the books of Lee [229, 230, 231] and to Pennec *et al.* for Pos_3 [277], on which this summary is based.

An N-dimensional manifold M is a topological space which locally, i.e. in the neighborhood of each point $p \in M$, provides similar features as the Euclidean space $\mathbb{R}^N$. Thus, a manifold is defined as a topological space M, which $\forall p \in M$ possesses a neighborhood which is homeomorphic to $\mathbb{R}^N$ (c.f. [229, p. 38]). If in addition the manifold is smooth, one can define a tangential space at each $p \in M$ denoted by $T_p(M)$. This brings the concept of direction to the manifold. Further, a Riemannian manifold additionally enables the concept of distances in form of a Riemannian metric, i.e. an inner product on the tangent space $d_p : T_p(M) \times T_p(M) \to \mathbb{R}$. With this bilinear form it is possible to introduce concepts of distances and angles to the manifold. This enables the concept of geodesics, i.e. informally spoken, the shortest connection between two elements of the manifold. For this purpose one introduces the exponential map $\exp_p : T_p(M) \to M$. The result of $q = \exp_p(v)$ with $v \in T_p(v)$ is the element $q \in M$ if one moves along the geodesic starting from point p in direction v[1]. Accordingly one defines its inverse, sometimes also referred to as logarithmic map, $\exp_p^{-1} : M \to T_p(M)$. Thus the mapping $v = \exp_p^{-1}(q)$ provides the tangent element $v \in T_p(M)$ pointing from p in direction of q[2]. With these two mappings, the geodesic between two elements $p, q \in M$ is given as [277] (c.f. [374]):

$$[p, q]_t = \exp_p^{-1}\left(t \exp_p^{-1}(q)\right) \tag{7.1}$$

for $t \in [0, 1]$. This further enables the concept of distance between two elements $p, q \in M$ by using the Riemannian metric:

$$d(p, q) = d_p\left(\exp_p^{-1}(q), \exp_p^{-1}(q)\right). \tag{7.2}$$

One of the most famous Riemannian manifolds is $\mathbb{S}^2$, for which the concepts above are illustrated in fig. 7.1.

A discussion of the mathematical requirements would go far beyond the scope of this thesis but the important information here is that the concept of tangents, directions, distances, and angles can be introduced for Riemannian manifolds.

[1] The Euclidean equivalent is $q = p + v$.
[2] The Euclidean equivalent is $v = q - p$.

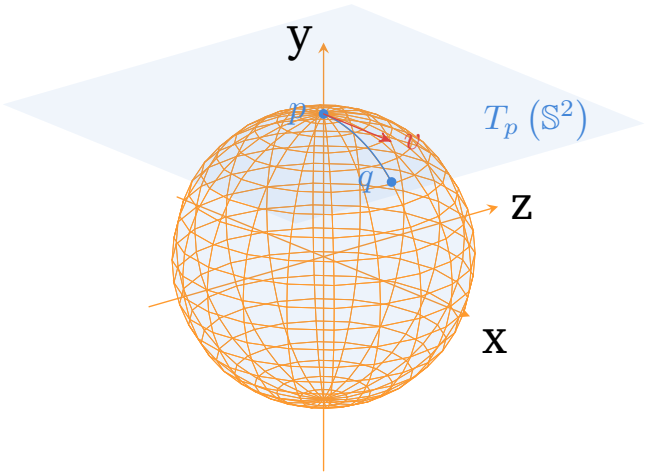

Figure 7.1 Illustration of the manifold on $\mathbb{S}^2$, the tangent space at the point $p \in \mathbb{S}^2$ and the element of the tangent space $v = \exp_p^{-1}(q)$ as well as the geodesic connecting p and q.

The manifold of Pos_3 has been introduced by Pennec *et al.* [277] mainly with DTI in mind, who imposes a Riemannian manifold on the space of SPD matrices[3]. In contrast to alternative approaches, such as those based on the space of matrices $\mathbb{R}^{3\times3}$, this manifold allows for a more meaningful form of interpolation. Pennec *et al.* [277] presented an example of interpolation between two tensors using both the matrix space as well as the manifold. Using this example, they illustrated that the matrix interpretation leads to e.g. non-convex transitions in terms of the volume of the corresponding ellipsoid. The definitions of the Riemannian metric $d_D : T_D(\text{Pos}_3) \times T_D(\text{Pos}_3) \to \mathbb{R}$,[4], the exponential map $\exp_D : T_D(\text{Pos}_3) \to \text{Pos}_3$, and its inverse[5] $\exp_D^{-1} : \text{Pos}_3 \to T_D(\text{Pos}_3)$ are as follows:

$$
\begin{aligned}
d_D(W,V) &= \operatorname{trace}\left(D^{-\frac{1}{2}} W D^{-1} V D^{-\frac{1}{2}}\right), \\
\exp_D(W) &= D^{\frac{1}{2}} \exp\left(D^{-\frac{1}{2}} W D^{\frac{1}{2}}\right) D^{-\frac{1}{2}}, \\
\exp_D^{-1}(E) &= D^{\frac{1}{2}} \exp^{-1}\left(D^{-\frac{1}{2}} E D^{-\frac{1}{2}}\right) D^{\frac{1}{2}},
\end{aligned}
$$

with $D, E \in \text{Pos}_3$ denoting elements of the manifold, and $W, V \in T_D(\text{Pos}_3)$ denoting elements of the tangent space at the point D. The distance can be reduced to (c.f. [277, 374])

$$
d(D,E) = d_D\left(\exp_D^{-1}(E), \exp_D^{-1}(E)\right) = \sum_{i=0}^{2} \left(\exp^{-1}(\kappa_i)\right)^2, \tag{7.3}
$$

with κ_i denoting the i-th eigenvalue of $D^{-\frac{1}{2}} E D^{-\frac{1}{2}}$.

[3] This is a subspace of the Euclidean space $\mathbb{R}^{3\times3}$.
[4] The tangent space of Pos_3, i.e. $T_D(\text{Pos}_3)$ is the space of symmetric matrices.
[5] Sometimes also referred to as logarithmic map.

Part III

Reconstruction Software Framework

8 Motivation

> *Endless wonder*
>
> — **Mrs. Irene Frederic**
> Warehouse 13

Throughout our projects we require a flexible and adaptive software framework for large-scale, ill-posed, linear inverse problems[1] $(\mathcal{A}, y^\delta)$, called *CampRecon*[2] [28]. For a great overview on the theory of optimization and numerical optimization we refer to [70, 362], and [270]. While other frameworks such as CONRAD [240] and ASTRA [31, 109] exist, these frameworks are typically strictly targeted towards a special application (e.g. tomographic reconstruction). However, as we discussed previously within the mathematical part (part II), we found that the problem formulation is commonly independent of the modeling operator itself. The same holds true for multiple methods of regularization. We have therefore aimed at the development of a software framework which revolves around the problem formulation instead of the approach used to compute a solution. By doing so we have created a framework that enables the user to flexibly apply methods, regularization strategies, and solvers to his specific problem. The only thing that has to be provided is the linear[3] forward model for the specific imaging modality. Examples reach from tomographic reconstruction to image denoising [313, 348], superresolution reconstruction [133] and of course regularized tomographic reconstruction such as total variation regularization or sparse regularization [363, 8].

With this goal in mind, we have followed the mathematical modeling of such problems as discussed previously in sections 4.1, 4.4 and 4.6.

Recalling section 4.1 we have discussed that discretization of a linear inverse problem $(\mathcal{A}, y^\delta)$ can be achieved in form of projection methods def. 4.5. These methods establish a direct connection of the continuous and the discrete problem via projection onto finite dimensional subsets of the range and the domain of the operator $\mathcal{A}$ (compare def. 4.2).

In fig. 8.1 we illustrate the pipeline of modeling a Tikhonov regularized linear least-squares problem (compare example 4.9), i.e.

$$\arg\min_{\mathbf{x}} \frac{1}{2} \left\| A\mathbf{x} - \mathbf{y}^\delta \right\|_2^2 + \frac{\lambda}{2} \left\| \mathbf{x} \right\|_2^2, \tag{8.1}$$

for a given discretized forward model A and a given discrete measurement $\mathbf{y}^\delta$.

[1] According to defs. 4.1 and 4.6.
[2] At current, the project is refactored into the *elsa* project which we plan to make publicly available as an Open Source project.
[3] Within the scope of this thesis we stick to the linearity of the forward model. However, as we support non-linearity in terms of functionals, non-linear optimization problems could be mapped as well.

In this part we are going to discuss the way our framework maps the mathematical properties of an inverse problem, regularization, and the numerical computation of a solution into the framework. With this in mind, in the following we will present both the idea as well as the abstract formulations of base classes for the most important components of this framework.

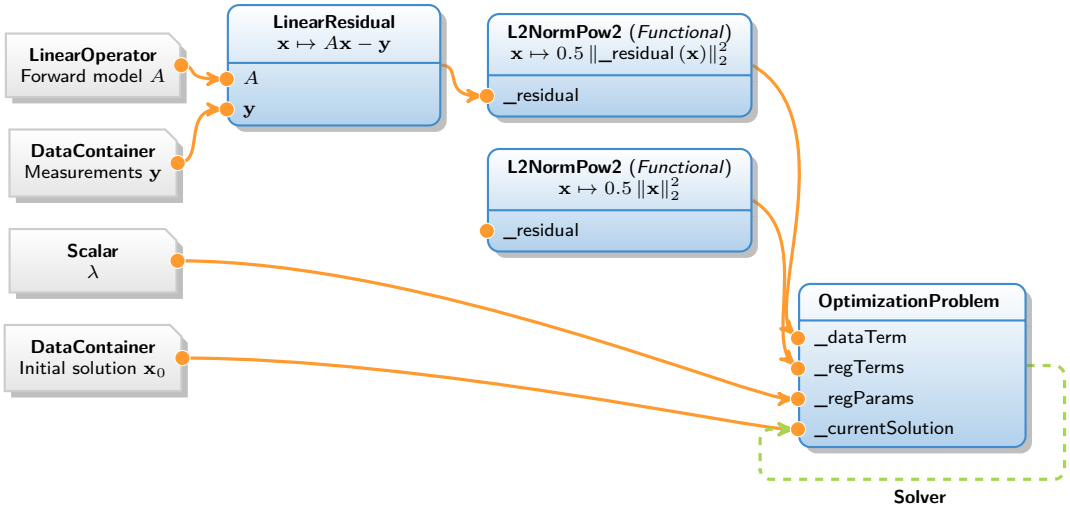

Figure 8.1 Illustration of the pipeline of modeling an inverse problem within our CampRecon framework. Additionally we illustrate how a *Solver* acts on the *OptimizationProblem*. In this case a Tikhonov regularized linear least-squares problem is modeled.

9 DataContainer and DataDescriptor

The first and foremost task for a framework of the type that we are about to present is the handling of data representation. Therefore, we first have a look at a specific example on how discretization in terms of projection methods is performed in a practical case.

Case Study: Pixel/Voxel Basis

Let us consider the mathematical representation of an image in 2D. An image is typically represented as a function $f \in L^2(V)$ with compact support $\mathrm{supp}(f) = V \subset \mathbb{R}^2$ and it is evident that the dimensionality used in natural language is the dimensionality of the domain of f. Next one needs to choose a finite dimensional basis for V. As modern digital camera detectors are commonly partitioned into a regular grid, it is a natural choice to follow this idea. W.l.o.g.[1] let the support be the rectangle with edge size s, i.e. $V = [0, s]^2$.

Based on the intuition of a regular grid, we consider the space of piece-wise constant functions on a regular grid as a finite dimensional[2] subset of $L^2(V)$. For this purpose, a partition (compare def. 2.1) of V is created via subdividing both dimensions of V as

$$A_{m,n} = \left(m\frac{s}{N}, (m+1)\frac{s}{N}\right) \times \left(n\frac{s}{N}, (n+1)\frac{s}{N}\right), \tag{9.1}$$

for $0 \leq m, n \leq N-1$ (see fig. 9.1). Obviously, this partition results in N^2 regular grid cells[3]. With this partition, an orthonormal basis[4] for the space of piece-wise constant functions on it is given by

$$\widetilde{x}_{k=m+N\cdot n} = \widetilde{x}_{m,n} := \frac{N^2}{s^2}\chi_{A_{m,n}}. \tag{9.2}$$

Please note the implicit serialization via the index k. It is important to notice that this is a convention and this choice is not unique. In the 2D case one obvious alternative exists, i.e. $k = n + N \cdot m$.[5] However, the number of possibilities strongly increases with the number of dimensions of V, i.e. by the factorial of $\dim(V)$.

Now, for any $f \in L^2(V)$ the orthogonal projection can be computed as

$$\mathbf{x}_{k=m+N\cdot n} = \left\langle f, \widetilde{x}_{k=m+N\cdot n}\right\rangle_{L^2(V)}, \tag{9.3}$$

[1] If f is of compact support there is always a containing rectangle fulfilling the necessary characteristics.
[2] Careful: This dimension refers to the dimension of the function space. This should not be confused with the dimension of the domain of f.
[3] Referred to as *pixel* (2D) or *voxel* (3D) in analogy to the camera metaphor.
[4] Typically referred to as *pixel* (2D) or *voxel* (3D) basis.
[5] It is worth mentioning that beside linear indexing also memory optimized approaches have been considered.

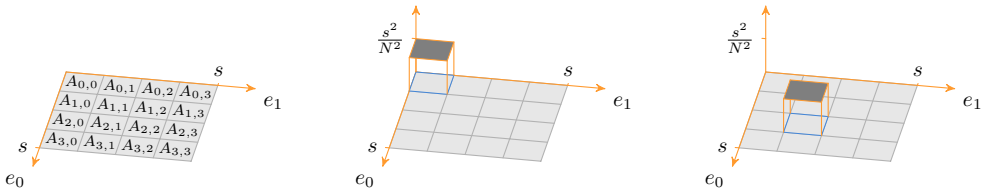

(a) $A_{m,n}$ (b) $\widetilde{x}_{0,0}$ (c) $\widetilde{x}_{2,1}$

Figure 9.1 Illustration of the partitioning of a 2D image (a) with $N = 4$. (b), (c) illustration of the graph of two basis functions of the corresponding discrete subspace.

resulting in the coefficient vector[6] $\mathbf{x} := \{\mathbf{x}_k\}_{k=0}^{N^2-1}$. We therefore conclude with a complete description of the discretization of f using the piece-wise constant functions on V paired with the orthogonal projection.

In order to map this idea onto our software framework, we implemented two classes *DataDescriptor* (see code 9.2) and *DataContainer* (see code 9.1). The former describes the underlying structure, e.g. the original function space, the dimension of its domain, the finite dimensional subset and its basis as well as the projection operator used for discretization. The latter exclusively contains the coefficient vector $\mathbf{x}$ accompanied by an object of *DataDescriptor* describing how the coefficients are to be interpreted. In addition, this class overloads arithmetic operators based on the arithmetics of vectors.

The decoupling of data and its interpretation also serves an additional purpose: the implementation of specializations of *DataContainer* for e.g. Open Graphics Library (OpenGL) [on13] textures, Compute Unified Device Architecture (CUDA) [on1], and Open Computing Language (OpenCL) [on3] in order to enable computation on modern Graphics Processing Units (GPUs). As the *DataContainer* class also defines the implementation of the arithmetic operations, these can be overwritten for the according architecture. This enabled us to reduce the synchronization operations between host and device memory, which are typically a bottleneck for high-performance computing. For our implementation of *DataContainer* for the Central Processing Unit (CPU), and therefore the memory storage on the standard Random Access Memory (RAM), we use the Eigen3[7] library [168] which offers a large and flexible implementation for linear algebra operations. On the other hand, the interpretation is independent of the location where the data is stored on the computer. Specializations of *DataDescriptor* furthermore enable the support of various discretization and basis functions. E.g we used this flexibility in the past to use curvelets [8], tensor fields [7] and fields of spherical functions [6]. In addition to the aforementioned, many different basis functions have been proposed for tomographic reconstruction. Among others: B-splines [135, 267, 268], triangulation [27, 72], blobs [215, 234], Shearlets [363] and curvelets [8, 151, 150, 29, 149] as well as tensor framelets [155, 156, 393]. As this purely covers research for the field of tomographic reconstruction, one gets a clear impression that wide variety of possibilities exists.

[6] Additionally we use the notation $\mathbf{x}_{i,j}$ for the coefficients corresponding to $\widetilde{x}_{m,n}$ if we want to refer to the underlying 2D structure. Nevertheless the coefficients are treated as vectors.

[7] For the sake of simplicity we use the Standard Template Library (STL) vector in the example code 9.1 instead of the Eigen3 vector.

Again we want to consider an explicit example based on the example of 2D images and the approximation via piece-wise constant functions used above.

```
/**
 * \brief Container class for data paired with a descriptor.
 */
class DataContainer {
public:
    DataContainer(const DataDescriptor& dataDescriptor)
    : _dataDescriptor(dataDescriptor.clone())
    : _data(dataDescriptor.getNumberOfCoefficients())
    {}

    // In this example we omit addtional constructors as well as in-place operators.
    . . .
    // getter for_dataDescriptor
    const DataDescriptor& getDataDescriptor() const { return *_dataDescriptor; }
    // getter for _data
    std::vector<float>& getData() { return _data; }
    // reinterpete the DataContainer with a different DataDescriptor
    void reinterpret(const DataDescriptor& dataDescriptor);
    // We omit e.g. the const getters to keep things clean.
    . . .
private:
    std::vector<float> _data;
    std::unique_ptr<DataDescriptor> _dataDescriptor;
};
DataContainer operator+(const DataContainer& lhs, const DataContainer& rhs) {
    // perform elementwise addition of lhs._data and rhs._data
}
DataContainer operator-(const DataContainer& lhs, const DataContainer& rhs) {
    // perform elementwise substraction of rhs._data from lhs._data
}
DataContainer operator*(float lhs, const DataContainer& rhs) {
    // perform scalar multiplication of lhs and rhs._data
}
```

Code 9.1 Lightweight version of our *DataContainer* class. This class wraps a pair of *_data* and an according *_dataDescriptor*. As the wrapped data is interpreted as coefficient vector, the binary arithmetic operators have been overloaded accordingly. We omit anything that goes beyond this illustration to focus on the key features. Additionally, the version we present has been restricted to *float* to omit any template parameters.

In order to map the discretization based on the pixel basis onto our framework, we summarize the necessary parts to achieve a full representation in our software. We start with the original function space, i.e. in the example above $L^2(V)$. The important part here is the dimension of V as this describes the underlying dimension of the object. For example in the case of an image this dimension is 2. Next, we consider the finite-dimensional subspace. We subdivide V along each dimension resulting in a specific *number of coefficients in each dimension*. Trivially, the total *number of coefficients* in $\mathbf{x}$ is given as the product of the amount of coefficients in each dimension. Additionally, the resulting basis functions have a specific expansion, i.e. the distance between the center of one pixel and the next one. This is commonly referred to as *spacing*. In our example we choose an isotropic spacing as well as an isotropic number of

coefficients in each dimension. Finally, we need to provide an interpretation of the *serialization convention* and the projection operator we used.

```cpp
/**
 * \brief Descriptor providing all information on the discretization
 *        and the original spaces.
 */
class DataDescriptor {
public:
    DataDescriptor(const std::vector<std::size_t>& numberOfCoefficientsPerDimension)
    : _numDim(numberOfCoefficientsPerDimension.size())
    , _numberOfCoefficients(std::accumulate(v.begin(), v.end(), 1,
                                            std::multiplies<std::size_t>()))
    , _numberOfCoefficientsPerDimension(numberOfCoefficientsPerDimension)
    {}

    // In this example we omit addtional constructors as well as in-place operators.
    . . .
    // factory method
    virtual std::unique_ptr<DataDescriptor> clone() const
    { return std::make_unique<DataDescriptor>(_numberOfCoefficientsPerDimension) };
    // getter for the dimension of the domain of the original function
    // e.g. 2D for an image
    int getNumDim() const { return _numDim; }
    // getter for the total number of coefficients
    std::size_t getNumberOfCoefficients() const { return _numberOfCoefficients; }
    // getter for the number of coefficients per dimension
    const std::vector<std::size_t>& getNumberOfCoefficientsPerDimension() const
    { return _numberOfCoefficientsPerDimension; }
    . . .
private:
    int _numDim;
    std::size_t _numberOfCoefficients;
    std::vector<std::size_t> _numberOfCoefficientsPerDimension;
    // Additional members containing information on the discretization process
    // as well as the basis functions.
    . . .
};
```

Code 9.2 Lightweight version of our *DataDescriptor* class. The *DataDescriptor* contains all information on the underlying function space, the dimensionality and the discretization that was used. In this example we only consider the number of dimensions and the individual number of coefficients as well as the total amount.

Obviously this concept carries over to N-dimensional fields. As a side note we want to mention several cases where one is interested in exchanging the way data is interpreted exist. A straightforward example from image processing is interpolation. Here, given a specific coefficient vector $\mathbf{x}$, we are interested in the function values in between the chosen grid. Evidently, the result varies depending on the chosen basis functions. Thus, if we want to move from a nearest neighbor interpolation, which would be the result using the piece-wise constant basis from above, we easily incorporate linear interpolation by *reinterpret()* the coefficient vector with the according *DataDescriptor*.

Now that we have a proper description of the data itself (*DataContainer*) paired with a suitable interpretation of the underlying function space, the dimensionality of the field as well as the

discretization process (*DataDescriptor*), we move on to the next part of an inverse problem: the linear operator mapping from model to measurement space.

10 LinearOperator

Above we have already stated that this software framework is especially developed with large-scale inverse problems $(\mathcal{A}, y^\delta)$ in mind. However, so far we have not specified what large-scale means in this context. Large-scale refers to a linear operator $\mathcal{A}$ which matrix representation A is too large to be stored in memory. Again, we will use the case of tomographic reconstruction as an example. If we use the Collocation Method (compare section 4.1) we find that the corresponding matrix A has one entry per voxel and measurement pair each. Further, consider single floating point precision (i.e. $32Bit$), an isotropic number of detector pixels N, an isotropic number of voxels of N as well, and a total number of 360 detector positions/X-ray projection. In this case we find the size of the matrix in the 3D case to accumulate to $360 \cdot N^5 \cdot 32Bit$. With e.g. $N = 256$ this already results in a matrix size of approximately $1.4PiB$. In conclusion, it is typically impractical to fully pose and store the matrix. Instead, one considers on-the-fly executions of the matrix. For this purpose two methods are implemented, *apply()* which computes the matrix-vector product $A\mathbf{x}$ for a given vector $\mathbf{x}$ and *applyAdjoint()* which computes the matrix-vector product $A^*\mathbf{x}$ of the Hilbert-adjoint of A and a vector $\mathbf{x}$. In the case of the real-valued Euclidean space the Hilbert-adjoint is the transposed matrix $A^\top$.

Again, we consider the discretization of the operator $\mathcal{A}$ using the idea of projection methods. Thus we need the information on how the range and the domain of $\mathcal{A}$ are supposed to be discretized and which projection operators are used. This is exactly the information that is contained in the *DataDescriptor*. Thus, we figured that a *LinearOperator* (see code 10.1) within our software framework is defined by two *DataDescriptor*s – one for the range of $\mathcal{A}$ and one for the domain of $\mathcal{A}$.

```
/**
 * \brief Class providing large scale linear operators with in-place apply/applyAdjoint.
 */
class LinearOperator {
public:
    LinearOperator(const DataDescriptor& domainDescriptor,
                   const DataDescriptor& rangeDescriptor)
    : _domainDescriptor(domainDescriptor.clone())
    , _rangeDescriptor(rangeDescriptor.clone())
    {}
    // In this example we omit addtional constructors.
    . . .
    // abstract method to apply the operator to x
    virtual DataContainer apply(const DataContainer& x) const = 0;
    // abstract method to apply the adjoint operator to x
    virtual DataContainer applyAdjoint(const DataContainer& x) const = 0;
    // factory method
    virtual std::unique_ptr<LinearOperator> clone() const = 0;
    // get transposed operator
    std::unique_ptr<LinearOperator> adjoint() const {
        /* return an adjoint version of this operator */
```

```
    }
    // getter for _domainDescriptor
    const DataDescriptor& getDomainDescriptor() const { return *_domainDescriptor; }
    // getter for _rangeDescriptor
    const DataDescriptor& getRangeDescriptor() const { return *_rangeDescriptor; }
    ...
private:
    std::unique_ptr<DataDescriptor> _domainDescriptor;
    std::unique_ptr<DataDescriptor> _rangeDescriptor;
};
```

Code 10.1 Lightweight version of our *LinearOperator* class. A *LinearOperator* receives a *_rangeDescriptor* and a *_domainDescriptor* providing the essential information on these two spaces and their discretization. The *LinearOperator* only requires the implementation of two methods *apply()* and *applyAdjoint()*. Please note that this class is purely abstract.

With respect to CT we find many methods which share this intuition. As mentioned in section 4.1 the most common approach is the Collocation Method. Siddon *et al.* [339] proposed a method which is a Collocation Method that uses a voxel basis for the domain. This method is also known as intersection weighted. If instead one considers piece-wise linear functions, this leads to a method similar to those proposed in [140, 199, 236, 248]. Collocation Methods with respect to more complicated basis functions are considered e.g. in [149, 151, 155, 156, 215, 234, 267, 268, 363, 27, 8, 393]. Galerkin type methods again with voxel basis in both, the range and the domain, are considered in [171, 236, 248] and are typically referred to as area weighted. The group of Brankov *et al.* studied adaptive triangulation of the domain and Collocation Methods for SPECT in [72, 73, 380].

Since the computation of this operation is very expensive the exact formulation is sometimes replaced by a faster but less precise formulation. Also, while sharing the intuition most of these methods were not developed with projection methods in mind and therefore differ slightly.

Most of the aforementioned methods evolve around ray oriented voxel traversal. In fig. 10.1 we illustrate the Collocation Method for the Radon transform R for the case of a pixel basis used in the domain. For each detector pixel a ray is computed and the intersections (blue circles) of this ray and the voxel along the ray are computed. For efficient algorithms related to voxel traversal and box intersection we refer the interested reader to [38, 377].

10.1 EvalTreeNode – a Composite Pattern

If we think about the matrix analogy we figure that we miss a key part in flexibility. The feature we lack is the composition of linear operators in form of forming sums and products with matrices as well as scalars. As we well know from linear algebra, the results of these operations again form linear operations/matrices.

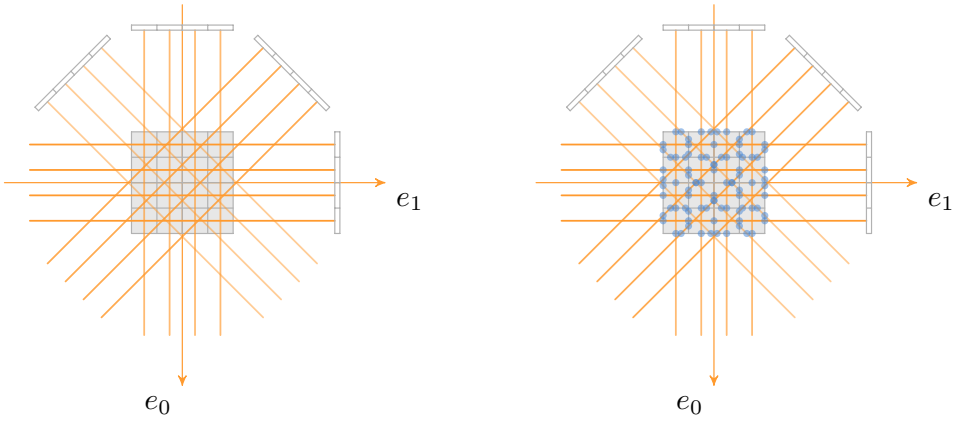

(a) Discrete partition/sampling **(b)** Intersections

Figure 10.1 Illustration of the Collocation Method of the Radon transform R. From the discrete number of rays illustrated in (a) one computes the intersection of the rays with the pixel boundaries. The entries of the system matrix are now given by the length of the intersection with the basis function.

As an example we consider three matrices $A \in \mathbb{R}^{N\times M}, B \in \mathbb{R}^{M\times N}, C \in \mathbb{R}^{N\times K}$ and a scalar $a \in \mathbb{R}$. Further we want to formulate a *LinearOperator* $D \in \mathbb{R}^{N\times N}$ that is composed of these elements as:

$$D = A \cdot B + a \cdot \left(C \cdot C^\top\right) \tag{10.1}$$

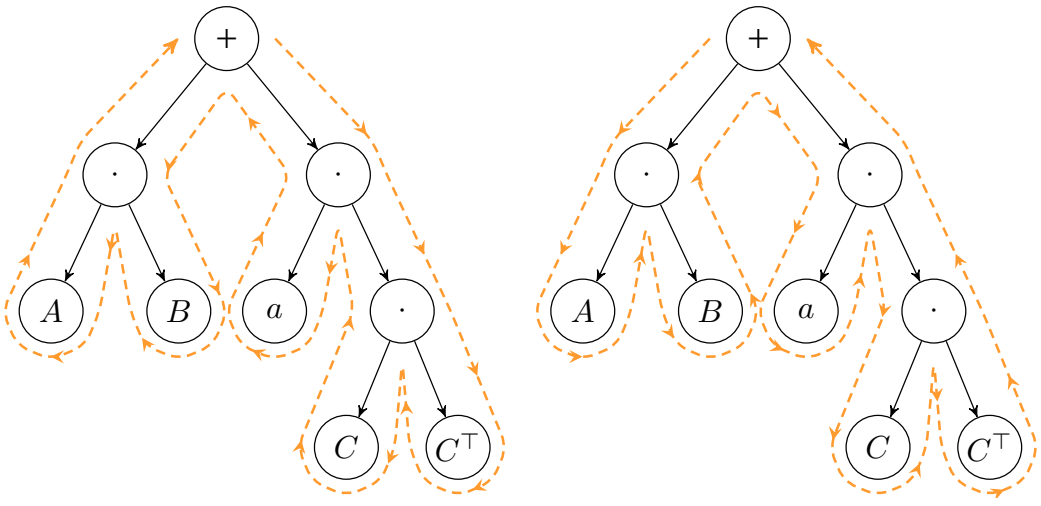

(a) *apply()* **(b)** *applyAdjoint()*

Figure 10.2 Illustration of one *EvalTreeNode* for eq. (10.1). (a) shows the tree traversal for *apply()* while in (b) the traversal for *applyAdjoint()* is shown.

Aiming at a large scale representation in the form as we defined *LinearOperator*, we want to implement the two methods *apply()* and *applyAdjoint()*. Starting from a formula as given in eq. (10.1), we built a corresponding evaluation tree as illustrated in fig. 10.2. This is represented within our framework by the *EvalTreeNode* class (see code 10.2) and the overloaded operators of *LinearOperator* (see code 10.3). Now the implementation of the *apply()* method is straightforward via a depth-first pre-order traversal with a right to left rule

and consequent calls of the *apply()* method of the components (compare fig. 10.2a). While the *applyAdjoint()* might seem more complicated at first, it actually is not. Due to the linearity of the Hilbert-adjoint and the fact that

$$(A \cdot B)^\top = B^\top \cdot A^\top \tag{10.2}$$

holds, we can implement this method by simply performing a depth-first pre-order traversal, but this time with a left to right rule, while calling *applyAdjoint()* of each operator (compare fig. 10.2b).

```
/**
 * \brief Class providing arithmetic composition of LinearOperator.
 */
class EvalTreeNode : public LinearOperator {
public:
    enum CompositionMode {
        PLUS,
        MULT
    };

    EvalTreeNode(const LinearOperator& lhs,
                 const LinearOperator& rhs,
                 CompositionMode mode)
    : LinearOperator(rhs.getDomainDescriptor(), lhs.getRangeDescriptor())
    , _lhs(lhs.clone())
    , _rhs(rhs.clone())
    , _mode(mode)
    {}

    // In this example we omit addtional constructors.
    . . .
    // apply operator to x via tree traversal
    DataContainer apply(const DataContainer& x) const override final {
        switch(_mode) {
            case PLUS:
                return _lhs->apply(x) + _rhs->apply(x);
                break;
            case MULT:
                return _lhs->apply(_rhs->apply(x));
                break;
        }
    }
    // apply adjoint operator to x via tree traversal
    DataContainer applyAdjoint(const DataContainer& x) const override final {
        switch(_mode) {
            case PLUS:
                return _rhs->applyAdjoint(x) + _lhs->applyAdjoint(x);
                break;
            case MULT:
                return _rhs->applyAdjoint(_lhs->applyAdjoint(x));
                break;
        }
    }
    // We omit e.g. getters to keep things clean.
    . . .
private:
    // We omit members inherited from LinearOperator
    . . .
```

```
    std::unique_ptr<LinearOperator> _lhs;
    std::unique_ptr<LinearOperator> _rhs;
    CompositionMode _mode;
};
```

Code 10.2 Lightweight version of our *EvalTreeNode* class. As described, the methods *apply()* and *applyAdjoint()* are implicitly defined by an according depth-first tree traversal.

```
// Binary addition of two LinearOperators
std::unique_ptr<LinearOperator> operator+(const LinearOperator& lhs,
                                          const LinearOperator& rhs) {
    return std::make_unique<EvalTreeNode>(lhs, rhs, EvalTreeNode::PLUS);
}
// Binary multiplication of two LinearOperators
std::unique_ptr<LinearOperator> operator*(const LinearOperator& lhs,
                                          const LinearOperator& rhs) {
    return std::make_unique<EvalTreeNode>(lhs, rhs, EvalTreeNode::MULT);
}
// Scalar multiplication with a LinearOperator
std::unique_ptr<LinearOperator> operator*(float lhs,
                                          const LinearOperator& rhs) {
    // create a diag operator from lhs, i.e. an implementation of LinearOperator
    // this creates the equivalent of a diagonal matrix with lhs on the diagonal.
    auto scalingOp = DiagOperator(rhs.getRangeDescriptor(), lhs);
    return std::make_unique<EvalTreeNode>(scalingOp, rhs, EvalTreeNode::MULT);
}
```

Code 10.3 Overloaded addition and multiplication operators for *LinearOperator*. For large-scale operators this is achieved via the *EvalTreeNode*.

In conclusion, the composite is fully described by its parts as well as the formula with no additional information needed. This composition of linear operators has been used especially for the following publications [6, 7, 8].

10.2 BlockOperator – another Composite Pattern

An additional way of forming compositions of linear operators is forming *BlockOperators*. Again this is something we are completely used to when working with Matlab [on2] or NumPy [on11], but to our knowledge is not covered in any framework. E.g. in the context of AXDT we present a tomographic problem which is composed as a column block operator. In order to cover the composition of block operators we implemented the class *BlockOperator* (see code 10.4). For multiple *LinearOperators* A_1, A_2, A_3 consider the column block C, the row block D and the diagonal composition E,

$$C = \begin{pmatrix} A_0 & A_1 & A_2 \end{pmatrix}, \quad D = \begin{pmatrix} A_0 \\ A_1 \\ A_1 \end{pmatrix}, \quad E = \begin{pmatrix} A_0 & & \\ & A_1 & \\ & & A_2 \end{pmatrix}. \tag{10.3}$$

Again we find the composition to be completely described by its parts. This reaches from *_domainDescriptor* and *_rangeDescriptor* to *apply()* as well as *applyAdjoint()*. For completeness, we here explicitly give the formulation for the *applyAdjoint()* form, i.e

$$C^\top = \begin{pmatrix} {A_0}^\top \\ {A_1}^\top \\ {A_2}^\top \end{pmatrix}, \quad D^\top = \begin{pmatrix} {A_0}^\top & {A_1}^\top & {A_2}^\top \end{pmatrix}, \quad E^\top = \begin{pmatrix} {A_0}^\top & & \\ & {A_1}^\top & \\ & & {A_2}^\top \end{pmatrix}. \tag{10.4}$$

In the next chapter we will consider how we map a linear inverse problem onto our framework.

```
/**
 * \brief Class providing block-wise composition of LinearOperator.
 */
class BlockOperator : public LinearOperator {
public:
    enum CompositionMode {
        COL,
        ROW,
        DIAG
    };

    BlockOperator(const std::list<const LinearOperator&>& oplist,
                  CompositionMode mode)
    : LinearOperator(/*We omit the computation of the descriptors here*/)
    , _mode(mode)
    {
        for(const auto& op : oplist)
            _oplist.push_back(op.clone());
    }

    // In this example we omit addtional constructors.
    . . .
    // apply the operator block-wise to x
    DataContainer apply(const DataContainer& x) const override final {
        DataContainer ret(_rangeDescriptor);

        switch(_mode){
            case COL: {
                std::size_t offset = 0;
                for(const auto& op : _oplist) {
                    ret += op->apply(x.getBlock(offset,op->getDomainDescriptor()));
                    offset += op->getDomainDescriptor().getNumberOfCoefficients();
                }
                break;
            } case ROW: {
                std::size_t offset = 0;
                for(const auto& op : _oplist) {
                    ret.getBlock(offset,op->getRangeDescriptor()) = op.apply(x);
                    offset += op->getRangeDescriptor().getNumberOfCoefficients();
                }
                break;
            } case DIAG: {
                std::size_t offsetdomain = 0;
```

```
                std::size_t offsetrange = 0;
                for(const auto& op : _oplist) {
                    ret.getBlock(offsetrange,op->getRangeDescriptor())
                        = op->apply(x.getBlock(offsetdomain,op->getDomainDescriptor()));
                    offsetdomain += op->getDomainDescriptor().getNumberOfCoefficients();
                    offsetrange += op->getRangeDescriptor().getNumberOfCoefficients();
                }
                break;
            }
        }
        return ret;
    }
    // apply the adjoint operator block-wise to x
    DataContainer applyAdjoint(const DataContainer& x) const override final {
        // just like apply but applyAdjoint() is called and COL, ROW are switched
    }
    // We omit e.g. getters to keep things clean.
    . . .
private:
    // We omit members inherited from LinearOperator
    . . .
    std::list<std::unique_ptr<LinearOperator>> _oplist;
    CompositionMode _mode;
};
```

Code 10.4 Lightweight version of our *BlockOperator* class. As described, the methods *apply()* and *applyAdjoint()* are implicitly defined by linearity. Please note the method *getBlock()* which we did not describe in the text. Its purpose is to extract the according block from the *DataContainer* corresponding to a specific *op*.

11 LinearResidual

In the previous two chapters we have described the classes *DataDescriptor*, *DataContainer* and *LinearOperator*. These are sufficient to fully describe a linear inverse problem $(\mathcal{A}, y^\delta)$ and its discretized version $(A, \mathbf{y}^\delta)$. All information on how the continuous problem is translated into its discrete version is contained in the two *DataDescriptors* of the *LinearOperator* A, i.e. the *_rangeDescriptor* and the *_domainDescriptor*. Obviously, the *DataDescriptor* of $\mathbf{y}^\delta$ needs to match the *_rangeDescriptor*. In order to create a representation of the discrete linear inverse problem $(A, \mathbf{y}^\delta)$ we implemented the class *LinearResidual* (see code 11.1).

```
/**
 * \brief Container class for the residual of an inverse problem,
 * i.e measurements paired with a forward model.
 */
class LinearResidual : public Problem {
public:
    LinearResidual(const LinearOperator& A, const DataContainer& y)
    : Problem(A.getDomainDescriptor())
    , _A(A.clone())
    , _y(y)
    {}

    // In this example we omit addtional constructors
    // as well as simplifications for identity operator A and zero y.
    . . .
    // evaluate residual
    DataContainer eval(const DataContainer& x) const {
        return _A->apply(x) - _y;
    }
    // getter for the domainDescriptor of _A
    const DataContainer& getDomainDescriptor() const { return _A->getDomainDescriptor(); }
    // getter for the rangeDescriptor of _A
    const DataContainer& getRangeDescriptor() const { return _A->getRangeDescriptor(); }
    // get the Jacobian matrix
    LinearOperator& getJacobian() { return *_A; }
    // getter for _y
    const DataContainer& getValues() { return _y; }
    // We omit e.g. inherited parts to keep things clean.
    . . .
private:
    std::unique_ptr<LinearOperator> _A;
    const DataContainer& _y;
};
```

Code 11.1 Lightweight version of our *LinearResidual* class. This class wraps a linear inverse problem in terms of its residual. The most important methods are *eval()* and *getJacobian()* which we will use in the following implementation of *Functional* code 12.1. Please note that the range and the domain of the residual are implicitly defined by the *LinearOperator*.

This class first and foremost holds the tuple A and $\mathbf{y}^\delta$ and further expresses the residual of the problem, i.e. the error vector $A\mathbf{x} - \mathbf{y}^\delta$ for a given $\mathbf{x}$. The linear problem is equivalent to finding an $\mathbf{x}$ such that the residual becomes zero. Additionally to the pure representation, we implemented two additional methods. First, *eval()* returns the results $A\mathbf{x} - \mathbf{y}^\delta$ for a provided $\mathbf{x}$. Second, the method *getJacobian()* returns the first order derivative, i.e. the Jacobian matrix, which for a linear function is trivially given by the operator A.

At this point we have everything we need to map the linear inverse problem onto our software framework. Next we consider how to cope with the ill-posedness.

12 Functional

We have discussed that the inverse problem does not need to possess a solution due to its ill-posedness during chapter 4 and section 4.4. A common approach is to replace the problem with an optimization problem. Such an optimization problem is given in form of a functional wrapping around the residual that quantifies the error. This goes hand in hand with the framework of variational methods described in section 4.4.1. Within these methods, prior knowledge/assumptions of a solution are incorporated via regularization terms (compare def. 4.8). In each of these regularization terms, a specific characteristic of a current estimate to the solution $\mathbf{x}$ is analysed (e.g. in the form of a linear residual $\mathcal{R}_k\left(A_k, \mathbf{x}, \mathbf{y}_k\right)$) and quantified via a wrapping functional $\mathcal{F}_k$.

The only component we are missing at this point is the software representation of the functionals. Consequently, we implemented a class called *Functional* (see code 12.1). This class wraps a *LinearResidual* and quantifies the residual. Specific implementations are e.g. the ℓ^p-norms and their weighted versions ℓ^p_w as well as the Huber-norm [188]. In the example in fig. 8.1 we already used the *L2NormPow2* which represents the squared Euclidean norm, i.e.

$$\frac{1}{2}\left\|\cdot\right\|_2^2. \tag{12.1}$$

With optimization, i.e. the search for a local/global optimum in mind, we implemented the methods *eval()*, *evalGradient()* and *evalHessian()*. These methods evaluate the functional as a whole, meaning the composition of *Functional* and *LinearResidual*. For computation of the gradient as well as the Hessian matrix we use the fact, that the residuals are purely linear. This allows us to use the multi-dimensional chain rule, i.e. for

$$E_i\left(\mathbf{x}\right) = \mathcal{F}_k\left(\mathcal{R}_k\left(A_k, \mathbf{x}, \mathbf{y}_k\right)\right) \tag{12.2}$$

the gradient evaluates to

$$\nabla E_i\left(\mathbf{x}\right) = J_{\mathcal{R}_k}^{\top}(\mathbf{x}) \cdot \nabla \mathcal{F}_k\left(A_k\mathbf{x} - \mathbf{y}_k\right), \tag{12.3}$$

and the Hessian matrix becomes

$$H_{E_k}\left(\mathbf{x}\right) = J_{\mathcal{R}_k}^{\top}\left(\mathbf{x}\right) \cdot H_{\mathcal{F}_k}\left(A_k\mathbf{x} - \mathbf{y}_k\right) \cdot J_{\mathcal{R}_k}\left(\mathbf{x}\right), \tag{12.4}$$

respectively. In fact, the Hessian matrix again represents a *LinearOperator*, and as we overloaded the arithmetic operations, we are able to directly compose the operator according to the formula above. This turns out to be especially useful if one considers Newton's method or Quasi-Newton methods. Here, the search direction for a descent is computed via solving a linear equation system composed of the Hessian matrix. Evidently this turns out to be a large-scale problem in our case again, as the original large-scale operator A_k is contained

in the formulation of the Hessian matrix. For a great overview on optimization we refer to [270].

```
/**
 * \brief Container class for the residual of an inverse problem,
 * i.e measurements paired with a forward model.
 */
class Functional {
public:
    Functional(const LinearResidual& residual)
    : _residual(residual)
    {}

    // In this example we omit addtional constructors
    // as well as simplifications for identity residuals.
    . . .
    // evalute the functional at position x
    float eval(const DataContainer& x) const {
        return evalImpl(_residual.eval(x));
    }
    virtual float evalImpl(const DataContainer& x) const = 0;

    // evalute gradient at position x
    DatanContainer evalGradient(const DataContainer& x) const {
        return _residual.getJacobian().applyAdjoint(evalGradientImpl(_residual.eval(x)));
    }
    virtual DatanContainer evalGradientImpl(const DataContainer& x) const = 0;

    // evalute Hessian matrix at position x
    std:unique_ptr<LinearOperator> evalHessian(const DataContainer& x) const {
        auto hessian = *(_residual.getJacobian().transposed()) *
        *(evalHessianImpl(_residual.eval(x))) *
        *(_residual.getJacobian());

        return std::move(hessian);
    }
    virtual std:unique_ptr<LinearOperator>
    evalHessianImpl(const DataContainer& x) const = 0;

    // get domain descriptor
    const DataDescriptor& getDomainDescriptor() const {
        return _residual.getDomainDescriptor();
    }
    // We omit e.g. the getters to keep things clean.
    . . .
private:
    LinearResidual _residual;
};
```

Code 12.1 Lightweight version of our *Functional* class. This class wraps a functional around a *LinearResidual* providing access to the first and second order derivatives using the multi-dimensional chain rule.

13 Problem

Next in line is the modeling of the *Problem* (see code 13.1) to be solved, i.e. in this context a linear inverse problem. Following our previous discussion we distinguish between a pure *LinearProblem*, which is already represented by a *LinearResidual* (see code 11.1), and an *OptimizationProblem* (see code 13.2), which provides an interface to an objective function as presented in the scope of variational methods (compare def. 4.8). The abstract *Problem* class only contains one member, i.e. the *_currentSolution* providing the current estimate to a solution.

```
/**
 * \brief Abstract class for inverse problems
 */
class Problem {
public:
    Problem(const DataDescriptor& domainDescriptor)
    : _currentSolution(domainDescriptor)
    {}

    // In this example we omit addtional constructors
    . . .
    // The class is abstract
    virtual ~Problem() = 0;
    // getter for _currentSolution
    DataContainer& getCurrentSolution() { return _currentSolution; }
    // We omit e.g. the const getters to keep things clean.
    . . .
private:
    DataContainer _currentSolution;
};
```

Code 13.1 Lightweight version of our *Problem* class. This class provides an abstract representation of an inverse problem.

13.1 LinearProblem

For the *LinearProblem* we already have everything in place, i.e. the *LinearResidual*. This is why in code 11.1 we derived from *Problem*. We therefore directly move on to the optimization based approach.

13.2 OptimizationProblem

Recalling the definition of variational methods (compare def. 4.8) we further introduce a class wrapping optimization problems. These problems consist of a data term $\mathcal{F}_0\left(\mathcal{R}_0\left(A_0, \mathbf{x}, \mathbf{y}_0\right)\right)$ and multiple weighted regularization terms $\mathcal{F}_k\left(\mathcal{R}_k\left(A_k, \mathbf{x}, \mathbf{y}_k\right)\right)$ with regularization parameter λ_k, for $k \geq 1$. These terms are linearly combined to an objective function $E : \mathbb{R}^N \to \mathbb{R}$ stating an *OptimizationProblem* (see code 13.2) with K being the number of regularization terms, and

$$E\left(\mathbf{x}\right) := \mathcal{F}_0\left(\mathcal{R}_0\left(A_0, \mathbf{x}, \mathbf{y}_0\right)\right) + \sum_{k=1}^{K} \lambda_k \mathcal{F}_k\left(\mathcal{R}_k\left(A_k, \mathbf{x}, \mathbf{y}_k\right)\right). \tag{13.1}$$

Due to the linearity and our definition of *Functional* and *LinearResidual* the gradient and the Hessian matrix of E are directly provided by the parts of the *OptimizationProblem*. The *OptimizationProblem* therefore describes an objective function,

$$\arg\min_{\mathbf{x}} E\left(\mathbf{x}\right). \tag{13.2}$$

```
/**
 * \brief Wraps an optimization problem
 */
class OptimizationProblem : public Problem {
public:
    OptimizationProblem(const Functional& dataTerm,
        const std::list<std::pair<float, const Functional&>>& regTerms)
    : Problem(dataTerm.getDomainDescriptor())
    , _dataTerm(dataTerm.clone())
    {
        for(const auto& regTerm : regTerms)
            _regTerms.emplace_back({regTerm.first, regTerm.second.clone()});
    }

    // In this example we omit addtional constructors
    // as well as inherited methods
    . . .
    // evaluate the objective function
    float eval(const DataContainer& x) const {
        float ret = _dataTerm->eval(x);
        for( const auto& regTerm : _regTerms )
            ret += regTerm.first * regTerm.second->eval(x);
        return ret;
    }
    float eval() const { return eval(_currentSolution); }

    // evaluate the gradient of the objective function
    DataContainer evalGradient(const DataContainer& x) const {
        DataContainer ret = _dataTerm->evalGradient(x);
        for( const auto& regTerm : _regTerms )
            ret += regTerm.first * regTerm.second->evalGradient(x);
        return ret;
    }
    DataContainer evalGradient() const { return evalGradient(_currentSolution); }

    // formulate the Hessian of the objective function
    std:unique_ptr<LinearOperator> evalHessian(const DataContainer& x) const {
```

```
        auto ret = dataTerm->evalHessian(x);
        for( const auto& regTerm : _regTerms )
            ret = *ret + regTerm.first * *(regTerm.second->evalHessian(x));
        return std::move(ret);
    }
    std:unique_ptr<LinearOperator> evalHessian() const
    { return std::move(evalHessian(_currentSolution)); }
    // We omit additional methods e.g. to partially evaluate the involved terms.
    . . .
private:
    std::unique_ptr<Functional> _dataTerm;
    std::list<std::pair<float,std::unique_ptr<Functional>>> _regTerms;
};
```

Code 13.2 Lightweight version of our *OptimizationProblem* class. This class provides a representation of an objective function as given in eq. (13.1). The class also provides means to evaluate the derivatives.

Case Study: Equivalent Problems

At this point we have realized that we had actually created a framework that was able to pose an equivalent problem (compare section 4.6.2) from a given one (providing such exists) by using the composition feature of *LinearOperator*.

Recalling the equivalent quadric formulation from a given linear least-squares problem, i.e.

$$E_{\text{ls}}(\mathbf{x}) := \frac{1}{2} \|A\mathbf{x} - \mathbf{y}\|_2^2 , \tag{13.3}$$

is equivalent to the quadric problem

$$E_{\text{quad}}(\mathbf{x}) = \frac{1}{2}\mathbf{x}^\top A^\top A\mathbf{x} - \mathbf{x}A^\top \mathbf{y} \tag{13.4}$$

for a linear operator A and a right-hand side $\mathbf{y}$. We see that the original least-squares problem already contains all information that is needed to formulate the equivalent quadric problem. Thus, the aforementioned composite pattern allows our framework to do exactly this without the need to do so by the user.

This is especially useful if algorithms crafted to solve a specific type of problem are considered. We have already mentioned the CG as being one of those. This brings us to the final part of our framework – *Solver*.

14 Solver

From an abstract point of view, the task of a *Solver* is reduced to updating the *_currentSolution* of a given *Problem* in order to improve the estimate. Following the distinction between *LinearProblem* and *OptimizationProblem* we again distinguish in *LinearSolver* and *OptimizationSolver*. Additionally, a *Solver* is able to decide if it is suitable to solve a specific *Problem*. Again, this aims at the model-oriented approach as we have stated initially, for a specific modeled problem the framework is able to create a list of suitable solvers. As we mentioned previously this also extends to equivalent problem formulations.

```
/**
 * \brief Interface class for solver
 */
class Solver {
public:
    // In this example we omit the constructors
    // as this is a pure interface
    . . .
    // returns true if a Solver is able to solve problem
    virtual bool isSolvable(const Problem& problem) const = 0;
    // solve the Problem by updating _currentSolution
    virtual void solve(Problem& problem) const = 0;
};
```

Code 14.1 Lightweight version of our *Solver* class. This is a pure interface class. Implementations are only required to implement the *solve()* and the *isSuitable()* method. The *solve()* method solves a *Problem* and updates its *_currentSolution*.

Examples for implementations for pure linear problems are e.g. general methods like Gaussian elimination (c.f. [270, Algorithm A.1]) and the Singular Value Decomposition (SVD) (c.f. [260, Chapter 4]) as well as specific methods such as the FBP (compare chapter 3). However, in most cases the general methods are not applicable as they require a complete representation of the system matrix, and the problem might not possess a solution at all. Therefore, the portion of iterative methods which considers an optimization type of problem is much larger in our framework.

Examples reach from methods which solve the linear least-squares problem, such as Kaczmarz method [201] and the Landweber method [220]. These methods or specializations have also been considered for tomographic reconstruction, i.e. ART [165], SIRT [159] and SART [41]. Furthermore this includes Nesterov's method [266] as well as the improved version developed by Kim *et al.* [207, 209]. Additionally, the method of SQS is included as proposed in [136] (c.f. [145]). Please note that ordered subset methods (c.f. [136, 208]) can be easily incorporated via the *BlockOperator*.

For proximity problems as discussed in example 4.12 corresponding solvers are given by the according proximity operators. A great overview is given in [103].

For non-linear optimization problems we feature gradient methods and the Non-Linear CG (NLCG) (c.f. [333]).

For a further discussion on solvers see section 4.6.

Case Study: ADMM

As another showpiece we will consider the method of ADMM. Recalling section 4.6.2, consider the following optimization problem with both, the data and the regularization term to be convex,

$$\arg\min_{\mathbf{x}} \mathcal{F}_0\left(\mathcal{R}_0\left(A_0, \mathbf{x}, \mathbf{y}_0\right)\right) + \lambda_1 \mathcal{F}_1\left(\mathcal{R}_1\left(A_1, \mathbf{x}, \mathbf{y}_1\right)\right). \tag{14.1}$$

We have discussed that this method translates eq. (14.1) problem into three much simpler optimization problems. Thus, within each iteration of ADMM one computes updates for $\mathbf{x}$, $\mathbf{z}$ and $\mathbf{u}$ via three steps which involve two optimization problems and one pure update:

$$\mathbf{x}^{k+1} = \arg\min_{\mathbf{x}} \left\{ \mathcal{F}_0\left(\mathcal{R}_0\left(A_0, \mathbf{x}, \mathbf{y}_0\right)\right) + \frac{\rho}{2} \left\| \mathcal{R}_1\left(A_1, \mathbf{x}, \mathbf{y}_1\right) - \mathbf{z}^k + \mathbf{u}^k \right\|_2^2 \right\}, \tag{14.2}$$

$$\mathbf{z}^{k+1} = \arg\min_{\mathbf{z}} \left\{ \frac{1}{2} \left\| \mathcal{R}_1\left(A_1, \mathbf{x}^{k+1}, \mathbf{y}_1\right) - \mathbf{z} + \mathbf{u}^k \right\|_2^2 + \frac{\lambda_1}{\rho} \mathcal{F}_1\left(\mathbf{z}\right) \right\}, \tag{14.3}$$

$$\mathbf{u}^{k+1} = \mathcal{R}_1\left(A_1, \mathbf{x}^{k+1}, \mathbf{y}_1\right) - \mathbf{z}^{k+1} + \mathbf{u}^k. \tag{14.4}$$

We again find that a given suitable problem (compare eq. (14.1)) already contains all information needed to formulate the subproblems. Consequently, we were able to implement a version of the ADMM using the structure above to automatically perform the necessary splitting. This functionality proved to be highly useful and was used in [1, 12, 13, 8] Additionally, as we are able to detect if a *Solver* is suitable we can even provide suggestions which *Solvers* are suitable for the subproblems.

While this case study considered ADMM it is worth mentioning that similar model independent implementations have been added for other splitting-based methods, e.g. ISTA [111], FISTA [61] and Parallel ProXimal Algorithm (PPXA) [103]. For a great overview on these type of methods we refer to [103].

Case Study: Line Search

A final case study considers *LineSearch*[1]. Searching along a line is of particular interest in non-linear optimization. Here one chooses a direction of descent, e.g. the gradient, and one aims at moving in this direction to maximally decrease the objective function. Mathematically this is described by the following optimization problem:

$$\arg\min_{\alpha} E\left(\mathbf{x} + \alpha \mathbf{d}\right), \tag{14.5}$$

[1] As we focused on linear optimization within this summary, we omit code for *LineSearch*.

where $\mathbf{x}$ is the current position and $\mathbf{d}$ is the search direction. Evidently, the required information on the function E is already fully provided by an object of *OptimizationProblem*. The only missing part to perform a line search is the direction vector $\mathbf{d}$. Thus, we added *LineSearch* by inheriting from *Solver* and passing the search direction as a parameter on construction.

15 Conclusion

In this part we presented a flexible software framework for inverse problems. Within this implementation we have paid special attention to a model oriented implementation, i.e. we wanted to enable prospective users to be able to quickly apply different methods, e.g. in terms of regularization, to their specific inverse problem. This should ideally be realized with as little overhead and code duplication as possible, such that researchers are able to apply and compare various methods even among the borders of specific modalities. The composition functionality proved to be of high value in particular. This mechanism, for example, enabled us to provide a problem-independent implementation of the ADMM, which has been used in [1, 12, 13, 8], and the incorporation of the XTT and the AXDT model [6, 7], which is integrated as *BlockOperator*. As mentioned initially, we currently perform a refactoring combined with streamlining and plan to provide open source access to this framework in the future. We are positive that the presented concepts can be of high value for any framework targetting tomographic reconstruction.

Part IV

Anisotropic X-ray Dark-field Tomography

16 X-ray Tensor Tomography

> *Science is so amazing*
>
> — **Ash Ketchum**
> (c.f. Pokémon XY, episode 32)

For the final part of this thesis we return to the problem of Anisotropic X-ray Dark-field Tomography.

The very first attempt at tomographic reconstruction of the anisotropic dark-field signal has been presented by Malecki *et al.* [242, 244] – namely X-ray Tensor Tomography (XTT). This method was further improved by Vogel *et al.* [20, 366, 7]. In this chapter we will provide a summary and a discussion, especially of the limitations of this method which lead to the development of Anisotropic X-ray Dark-field Tomography (AXDT).

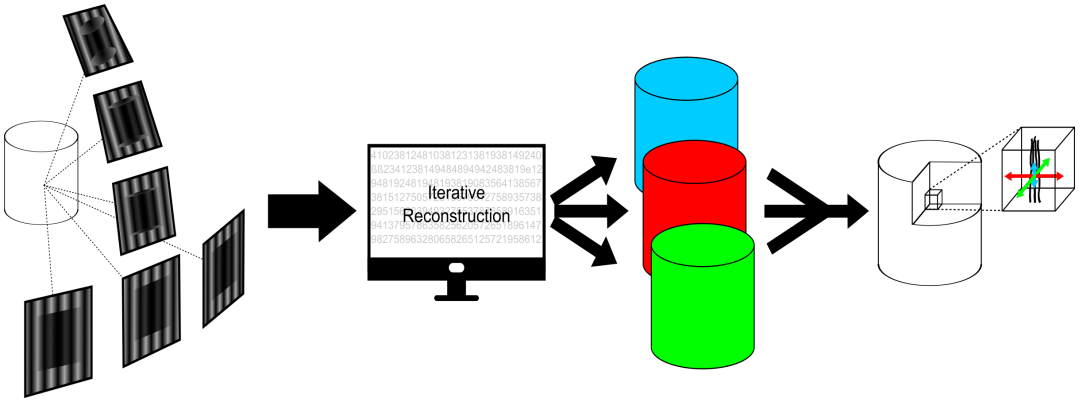

Figure 16.1 Illustration of the reconstruction of the directional dark-field signal. The sample is measured from many different orientations. Multiple parts of the scattering profile are reconstructed simultaneously and are finally merged into the full representation of the scattering in each location. From M. **Wieczorek**, F. Schaff, F. Pfeiffer, and T. Lasser. "Anisotropic X-Ray Dark-Field Tomography: A Continuous Model and its Discretization". English. In: *Physical Review Letters* 117.15 (Oct. 2016), p. 158101
DOI: 10.1103/PhysRevLett.117.158101
URL: http://link.aps.org/doi/10.1103/PhysRevLett.117.158101, with the permission of APS (©2016 American Physical Society)

As discussed in chapter 4 one requires a forward model in order to perform tomographic reconstruction for the directional dark-field component. This forward model provides a tool to simulate measurements. In order to formulate such, Malecki *et al.* [243] derived a model for thick samples with multiple microstructures and therefore multiple dominant scattering directions based on simulations, which have been supported by follow-up experiments. The key result of this work is that if $K \in \mathbb{N}$ dominant scattering directions $u_k \in \mathbb{S}^2$ are present in a sample, the dark-field measurement can be modeled by a line integral over the sums

of the scattering η_k occurring in the direction of u_k weighted by their relative orientation to the grating. Based on this finding, Malecki *et al.* [244] further refined this forward model and provided an approximative formula for the detectability in form of a function of u_k, the grating orientation $t \in \mathbb{S}^2$, and the beam direction $l \in \mathbb{S}^2$ (see fig. 16.2). This resulted in the following forward model of the dark-field signal d for a single X-ray beam L with direction l and a relative[1] grating orientation t:

$$d = \exp\left(-\int_L \sum_{k=0}^{K-1} \left(|l \times u_k| \langle u_k, t\rangle\right)^2 \eta_k(x)\, dx\right), \tag{16.1}$$

with $\eta_k : \mathbb{R}^3 \to \mathbb{R}$ denoting the scattering strength[2] at each position in the direction u_k.

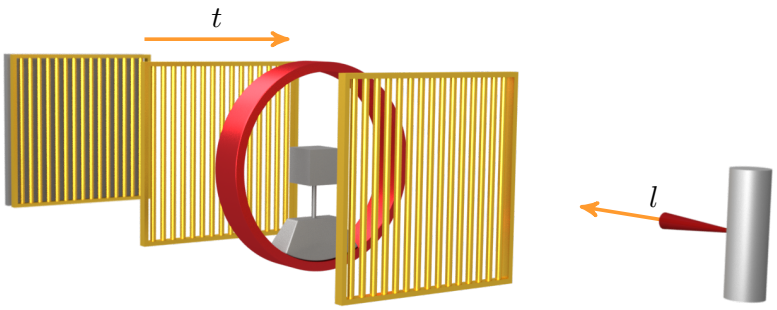

Figure 16.2 Illustration of the direction of the beam l and the grating orientation t.

This, for the first time, enabled the tomographic reconstruction of the local scattering profiles and subsequently the local microstructure orientation within the measured sample.

For an unknown object the dominant scattering directions are unknown. Thus, the first step for XTT is to choose a well-distributed sampling scheme on the unit sphere for the u_k. Malecki *et al.* [244] decided to use the three main axes as well as the cubic diagonals, resulting in a total of $K = 7$ (see fig. 16.3b) sampling direction which have later been extended to $K = 13$ (see fig. 16.3a) directions by Vogel *et al.* [7]. For the computation of the reconstruction Malecki modified the SART method to fit eq. (16.1). The reconstruction process is illustrated in fig. 16.1. However, a formulation of the problem such that other solvers could be applied had not been derived at this point.

In a second step, in order to retrieve a close representation of the scattering a rank-2 tensor field $T : \mathbb{R}^3 \to \mathrm{Pos}_3$ (see chapter 6) has been fitted to the scattering data (η_k, u_k) at each volume element $x \in \mathbb{R}^3$. The corresponding inverse problem is implicitly given by eq. (6.1), i.e.

$$f_{T(x)}(u_k) = \frac{1}{\sqrt{u_k^\top T(x)\, u_k}} := \eta_k(x), \tag{16.2}$$

[1] In-plane and orthogonal to the grating bars.
[2] To be precise, the η_k correspond to the squared scattering strength according to Malecki *et al.* [244].

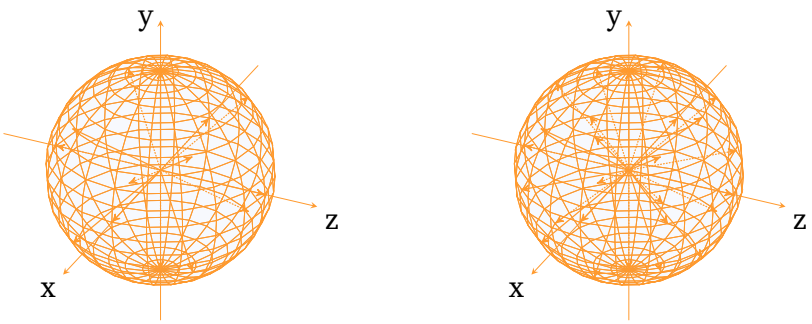

(a) $K = 7$ (b) $K = 13$

Figure 16.3 Illustration of the sampling direction u_k as used by Malecki *et al.* [244] (a) and Vogel *et al.* [7] (b).

for all $x \in \mathbb{R}^3$. Malecki *et al.* [244] initially used a least-squares fit to fit the tensors, which was replaced by a Principal Component Analysis (PCA) (c.f. [183, 275]) by Vogel *et al.* [7].

Further, based on the observation that scattering is strongest when orthogonal to a microstructure, the direction of the microstructure within one voxel can be extracted in a third and final step by computing the direction of the smallest half-axis of the tensor. Vogel *et al.* [7] proposed to perform a streamline algorithm, similar to what is done for DTI (c.f. [365]), on these directions in order to visualize these directions. The result of each phase is illustrated in fig. 16.4 for a carbon fiber sample.

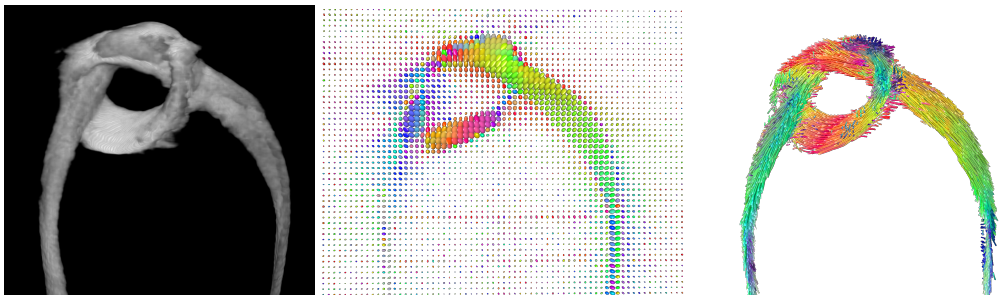

(a) (b) (c)

Figure 16.4 Illustration of XTT as developed by Malecki *et al.* [244] and the refinements from Vogel *et al.* [7] for a carbon fiber sample. (a) shows a Volume Rendering (VR), (b) shows the reconstructed tensors and in (c) the streamline visualization is shown. Visualizations (a),(c) were created with CampVis [324, 327].

Vogel *et al.* [7] pointed out that due to the linearity of the integral and the fact that the weighting is independent of the position within the sample, the order of integral and sum can be swapped. This led to the following improved formulation of the forward model given by Malecki.

Definition 16.1 **(XTT forward model)** (c.f. [7, 244]) Let $t \in \mathbb{S}^2$ denote the grating direction and $l \in \mathbb{S}^2$ the direction of an X-ray beam L. Further let a finite set of K scattering directions $u_k \in \mathbb{S}^2$ and

the corresponding squared scattering strengths $\eta_k : \mathbb{R}^3 \to \mathbb{R}$ be given. Then the relation of η_k and the dark-field measurement is modeled by

$$d = \exp\left(- \sum_{k=0}^{K-1} h\left(u_k, t, l\right) \int_L \eta_k\left(x\right) dx \right), \tag{16.3}$$

with $h : \mathbb{S}^2 \times \mathbb{S}^2 \times \mathbb{S}^2 \to \mathbb{R}$ denoting the detectability weighting.

Note: Effectively eq. (16.3) assembles a weighted sum of the standard CT model (compare chapter 3) applied individually to each component. The weighting can be formulated as function $h : (u, t, l) \mapsto \left(|l \times u| \left\langle u, t \right\rangle\right)^2$.

These considerations led to the formulation of the corresponding inverse problem in a whole-system fashion, i.e. the formulation of it as one large linear inverse problem [7]. Consider a specific number of J measurements d_j with corresponding pairs of beam and beam direction L_j, l_j and the relative grating orientation t_j. Further, let $P \in \mathbb{R}^{J \times I}$ denote the projection matrix, i.e. the discretization of the projection operator mapping from I voxel to the J measurements (see for example [199, 339]). Additionally, by taking the negative logarithm of the discrete measurements $\mathbf{p} = (-\ln d_j)$ a linearization and discretization[3] is given by

$$\mathbf{p} = \underbrace{\begin{pmatrix} W_0 P & \dots & W_{K-1} P \end{pmatrix}}_{A} \underbrace{\begin{pmatrix} \boldsymbol{\eta}_0 \\ \vdots \\ \boldsymbol{\eta}_{K-1} \end{pmatrix}}_{\boldsymbol{\eta}}, \tag{16.4}$$

with $\boldsymbol{\eta}_k$ denoting the discretization of the field $\eta_k : \mathbb{R}^3 \to \mathbb{R}$. The weighting matrices are given by $W_k = \operatorname{diag}\left(h\left(u_k, t_0, l_0\right), \dots, h\left(u_k, t_J, l_J\right)\right) \in \mathbb{R}^{J \times J}$. In contrast to the model provided by Malecki, this whole-system approach can be solved using any of the methods we have discussed in section 4.6, including the application of regularization.

By simply using this whole-system with a CG instead of the previously used SART-type [244] or SIRT-type algorithm [7] we were able to achieve a strong improvement in computation time on our hardware. From the initial hours of computation we are now down to a scale of minutes for the carbon knot dataset (201^3 voxel) [16, 17] while achieving the same residual error.

Except for the speedup in form of the more efficient PCA, the tensor fitting and the extraction of the microstructure direction in form of the smallest half-axis remained the same in principle.

XTT provided the very first method to perform tomographic reconstruction of the anisotropic dark-field signal. This marks a significant impact for modern X-ray imaging. In the following we want to provide a discussion/review of the XTT method and especially its shortcomings, which led to the development of AXDT which we are going to present in chapter 18.

[3] This assembles a composition of a discretization of the weighting operator using the Collocation Method and the discretization of the projection operator using one of the common methods.

Discussion: Before we go into the depths of the forward model itself, we first stick with the tensor approach. The main issue is that the tensor fit is performed after the actual reconstruction took place, meaning that the tensor information, especially the information on the orientation, is inaccessible during the reconstruction and in consequence can not be incorporated within a regularization term. However, as one of the most interesting pieces of information gained from this approach is the orientation, a regularization taking this into account would be highly interesting. On the other hand, as the tensors live on the manifold (compare chapter 7) Pos_3, reconstruction within the manifold was unavailable prior to our work in 2016 [4]. The same holds for the direction, as $\mathbb{S}^2$ is a manifold as well. Due to this limitation, Vogel *et al.* [7] decided to use soft/hard constraints which push/force the reconstructed quantities to form a tensor. While both methods provided visual improvements, we were not able to prove that these operations are linear and therefore projections. As an alternative, Seyyedi *et al.* [1, 12, 13] considered component-wise total variation regularization treating the components individually. Still, a focus on the orientation rather than the scattering magnitude seems favorable and we will discuss a manifold oriented denoising approach in chapter 17.

Now we want to provide a closer look at the forward model. Returning to eq. (16.3) we realize that the reconstructed quantities are not invariant with the number of sampling direction, meaning that the reconstructed scattering strengths η_k get smaller the more sampling direction are chosen. This is something one wants to avoid. An increased number of directions should only lead to a more dense representation of the scattering profile but not to a change of the quantity itself. The important part that is missing is a form of normalization with the number of scattering directions K. Recalling the discussion on cubature (see def. 6.2) we realize that the inner sum of eq. (16.1) is already very similar to a cubature rule, but lacking the weightings. We will come back to this in section 18.1.

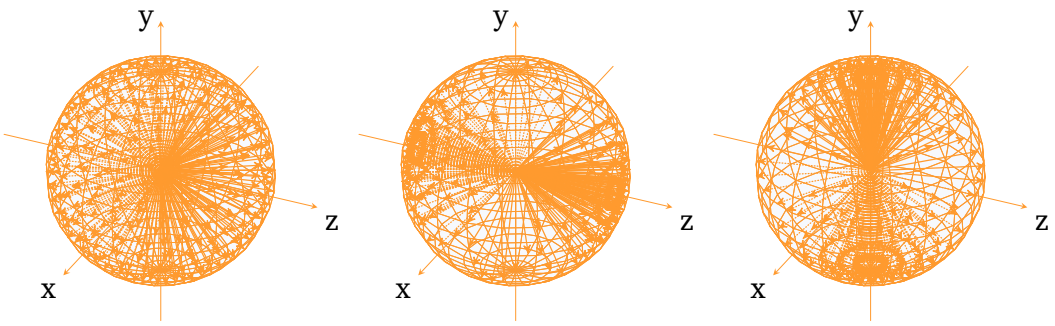

(a) $K = 147$ **(b)** $K = 148$ **(c)** $K = 148$

Figure 16.5 Illustration of a well-distributed sampling scheme (a) and two less well-distributed sampling schemes (b),(c) with nearly the same amount of directions.

The second issue is directly linked to this observation as well. In the previous discussion we have mentioned that the u_k should provide a good sampling of the sphere. However, we did not further describe what this is supposed to mean. In fig. 16.5 we show[4] a well-distributed sampling (fig. 16.5a) for $K = 147$ and two less well-distributed ones (figs. 16.5b and 16.5c) with $K = 148$ each. While using nearly the same amount of directions, the first sampling provides a roughly uniform sampling of the sphere while the other two samplings show a

[4] Credits for these examples go to Florian Schaff.

more dense sampling along the z axis (fig. 16.5b) and the y axis (fig. 16.5c), respectively. The main issue is that in the formula eq. (16.3) the contributions from each sampling direction are counted the same. In the examples presented, this means that we obtain a stronger influence from the regions that are sampled more densely. Again, these are effects we have already discussed in the context of the cubature rules, and as the u_k live on $\mathbb{S}^2$ we were motivated to replace def. 16.1 by a surface integral based version. This will be discussed in chapter 18.

The final limitation is due to the rank-2 tensors. A tensor can only represent one single direction, which is easy to see if one considers the ellipsoid analogy. A minimum is either a single point, a great circle or the whole sphere. This would be of no harm if we could assume that we only have one single microstructure crossing a voxel. However, as discussed earlier the microstructures that cause the SAXS, which results in the dark-field signal, are much smaller than the detector resolution, which is why this seems to be a troubling assumption. For more complex samples, we expected multiple directions crossing a single voxel, which can not be retrieved with this method. These considerations led to the development of AXDT, which proved to be capable to overcome these limitations of XTT. Interestingly, we were able to show that the presented method enables optimal reconstruction for the currently used weighting function while achieving a complexity that is equal to the XTT reconstruction with a sampling of $K = 15$.

In the following, we firstly present a method to perform total variation denoising of the tensor field. This is linked to the idea of joint regularization of the components. Afterwards, we will focus on the main limitations of XTT, discussed above, and we will introduce the improved method called AXDT. As this method will enable retrieving multiple directions in each location, we will further present means to extract the microstructure directions in each location, i.e. those directions which have the highest accumulated scattering orthogonal to them.

17 Denoising of XTT

As mentioned above, we have started our investigation while preserving the tensor model. The method in the following chapter has been partially presented in [21]. Simultaneously to the work of Vogel *et al.* [7], we have investigated methods to denoise/regularize the reconstructed tensors. The key challenge here is that either one performs the regularized fitting/denoising in the space of matrices, for which it is not guaranteed that one stays in the subspace Pos_3, or one has to deal with the manifold structure.

Due to the similarity to DTI, i.e. the rank-2 tensor model, we investigated which methods have been developed for denoising/regularization for this imaging model. In fact, if we identify the u_k in def. 16.1 with the gradient directions from DTI and the η_k with the Diffusion Weighted Images (DWIs), we are able to utilize many of the methods developed in the context of DTI to the XTT problem.

Consequently, we have investigated related methods for DTI[1]. Throughout this investigation we identified four types of methods for regularized/denoised tensor fitting[2]:

- Denoising of the DWIs, i.e. the input data, prior to the fitting (c.f. [50, 53, 237]),
- Constrained tensor fitting, i.e. enforcing the positive definiteness (c.f. [214, 367]),
- Regularized fitting (c.f. [4, 146, 265, 46, 273, 359, 93]) and
- Denoising of the fitted tensors/directions posterior to the fitting (c.f. [45, 86, 94, 170, 258, 277, 358]).

At the time we investigated this field, Weinmann *et al.* [374] had only recently proposed their *proximal point algorithm* for total variation denoising manifold data. This algorithm showed very promising results for DTI data in only few iterations, which motivated us to apply this method to XTT. We therefore decided to apply this algorithm paired with the manifold Pos_3 as proposed by Pennec *et al.* [277] (see chapter 7 for a detailed discussion) to XTT data.

In order to apply the aforementioned method, let us assume $\boldsymbol{\eta}_0, \ldots, \boldsymbol{\eta}_{K-1}$, with $\boldsymbol{\eta}_k \in \mathbb{R}^{n\times n\times n}$ denotes a solution to eq. (16.4). We further assume an a-priori performed tensor fit to be given, i.e. a field of tensors $\mathbf{T} \in \mathrm{Pos}_3^{n\times n\times n}$, such that the tensor $T_{x,y,z}$ fits the value pairs $\left(u_k, (\boldsymbol{\eta}_k)_{x,y,z}\right)$.

[1] This literature research was performed in the scope of [4]

[2] As a side note, it is important to mention that the term "reconstruction" in the scope of this thesis is predominantly used in the sense of "tomographic reconstruction" while the community of DTI typically refers to the tensor fit as "reconstruction".

Recalling the definition (compare chapter 7) of the Riemannian metric $d_D : T_D(\mathrm{Pos}_3) \times T_D(\mathrm{Pos}_3) \to \mathbb{R}$, the exponential map $\exp_D : T_D(\mathrm{Pos}_3) \to \mathrm{Pos}_3$ and its inverse[3] $\exp_D^{-1} : \mathrm{Pos}_3 \to T_D(\mathrm{Pos}_3)$ are

$$\begin{aligned} d_D(W,V) &= \operatorname{trace}\left(D^{-\frac{1}{2}} W D^{-1} V D^{-\frac{1}{2}}\right), \\ \exp_D(W) &= D^{\frac{1}{2}} \exp\left(D^{-\frac{1}{2}} W D^{\frac{1}{2}}\right) D^{-\frac{1}{2}}, \\ \exp_D^{-1}(E) &= D^{\frac{1}{2}} \exp^{-1}\left(D^{-\frac{1}{2}} E D^{-\frac{1}{2}}\right) D^{\frac{1}{2}}, \end{aligned}$$

with $D, E \in \mathrm{Pos}_3$ denoting two elements of the manifold, and $W, V \in T_D(\mathrm{Pos}_3)$ denoting elements of the tangent space at the point D. The distance between two points $D, E \in \mathrm{Pos}_3$ is given as

$$d(D,E) = \sum_{i=0}^{2} \exp^{-1}(\kappa_i)^2, \tag{17.1}$$

with κ_i denoting the i-th eigenvalue of $D^{-\frac{1}{2}} E D^{-\frac{1}{2}}$. This definition of distances further allows for a discrete formulation of the ℓ^2-total variation problem using finite differences, as we have discussed for the Euclidean case in example 4.10. The corresponding optimization problem, i.e. the manifold version of a TV regularized least-squares problem, is given as:

$$\begin{aligned} \arg\min_{\widehat{T}} \quad & \frac{1}{2} \sum d^2\left(\widehat{T}_{x,y,z}, T_{x,y,z}\right) \\ & + \lambda \sum d\left(\widehat{T}_{x,y,z}, \widehat{T}_{x+1,y,z}\right) \\ & + \lambda \sum d\left(\widehat{T}_{x,y,z}, \widehat{T}_{x,y+1,z}\right) \\ & + \lambda \sum d\left(\widehat{T}_{x,y,z}, \widehat{T}_{x,y,z+1}\right). \end{aligned} \tag{17.2}$$

This problem can be iteratively solved by the cyclic proximal point algorithm proposed by Weinmann *et al.* [374] (see code 17.1). Additionally, they have proved global convergence for particular manifolds, including Pos_3.

17.1 Experiments and Results

For our experiments, we used a sample of carbon fibers which were inter-looped to form a knot, fixated by hot glue and mounted to a sample holder via adhesive tape (see fig. 17.1). This dataset is referred to as *carbon knot* or *knot* in the following. As stated previously, as we consider post-reconstruction denoising we require a reconstruction to be performed a-priori. We therefore used the reconstruction of the carbon knot computed by Vogel *et al.* [7].

The dark-field signal has been recorded via a setup as illustrated in fig. 16.2 as proposed in [244, 279]. The acceleration voltage was set to $60\,\mathrm{kV\,p}$. Images/X-ray projections have been recorded with a (Varian) flat panel detector with isotropic pixel size of $127\,\mu\mathrm{m}$ and a total of 800×800 pixels. In total 732 X-ray projections were recorded and for each X-ray projections eight phase steps with $1\,\mathrm{s}$ exposure time each were recorded. The $\pi/2$ phase grating (**G1**)

[3] Sometimes also referred to as logarithmic map.

Input: The manifold data $T \in \mathrm{Pos}_3^{n\times n\times n}$, regularization parameter $\lambda > 0$, parameter sequence $\alpha = (\alpha_0, \dots) \in \ell^2 \setminus \ell^1$.
Output: Minimizer $\widehat{T}$ of ℓ^2-total variation problem eq. (17.2)

$\widehat{T} \leftarrow T$
for $it \leftarrow 0, 1, 2, \dots$ **do**
▷ proximal mapping of the data term
for $x \leftarrow 0, \dots, n-1; y \leftarrow 0, \dots, n-1; z \leftarrow 0, \dots, n-1$ **do**
$t \leftarrow \frac{\alpha_{it}}{1+\alpha_{it}} d\left(\widehat{T}_{x,y,z}, T_{x,y,z}\right)$
$\widehat{T}_{x,y,z} \leftarrow \left[\widehat{T}_{x,y,z}, T_{x,y,z}\right]_t$
end for
▷ proximal mapping of the regularization term
for $x \leftarrow 0, \dots, n-2; y \leftarrow 0, \dots, n-1; z \leftarrow 0, \dots, n-1$ **do**
$t \leftarrow \min\left(\alpha_{it}\lambda, \frac{1}{2} d\left(\widehat{T}_{x,y,z}, \widehat{T}_{x+1,y,z}\right)\right)$
$\widehat{T}'_{x,y,z} \leftarrow \left[\widehat{T}_{x,y,z}, \widehat{T}_{x+1,y,z}\right]_t$
$\widehat{T}'_{x+1,y,z} \leftarrow \left[\widehat{T}_{x+1,y,z}, \widehat{T}_{x,y,z}\right]_t$
$\widehat{T}_{x,y,z} \leftarrow \widehat{T}'_{x,y,z}; \widehat{T}_{x+1,y,z} \leftarrow \widehat{T}'_{x+1,y,z}$
end for
for $x \leftarrow 0, \dots, n-1; y \leftarrow 0, \dots, n-2; z \leftarrow 0, \dots, n-1$ **do**
$t \leftarrow \min\left(\alpha_{it}\lambda, \frac{1}{2} d\left(\widehat{T}_{x,y,z}, \widehat{T}_{x,y+1,z}\right)\right)$
$\widehat{T}'_{x,y,z} \leftarrow \left[\widehat{T}_{x,y,z}, \widehat{T}_{x,y+1,z}\right]_t$
$\widehat{T}'_{x,y+1,z} \leftarrow \left[\widehat{T}_{x,y+1,z}, \widehat{T}_{x,y,z}\right]_t$
$\widehat{T}_{x,y,z} \leftarrow \widehat{T}'_{x,y,z}; \widehat{T}_{x,y+1,z} \leftarrow \widehat{T}'_{x,y+1,z}$
end for
for $x \leftarrow 0, \dots, n-1; y \leftarrow 0, \dots, n-1; z \leftarrow 0, \dots, n-2$ **do**
$t \leftarrow \min\left(\alpha_{it}\lambda, \frac{1}{2} d\left(\widehat{T}_{x,y,z}, \widehat{T}_{x,y,z+1}\right)\right)$
$\widehat{T}'_{x,y,z} \leftarrow \left[\widehat{T}_{x,y,z}, \widehat{T}_{x,y,z+1}\right]_t$
$\widehat{T}'_{x,y,z+1} \leftarrow \left[\widehat{T}_{x,y,z+1}, \widehat{T}_{x,y,z}\right]_t$
$\widehat{T}_{x,y,z} \leftarrow \widehat{T}'_{x,y,z}; \widehat{T}_{x,y,z+1} \leftarrow \widehat{T}'_{x,y,z+1}$
end for
end for

Code 17.1 Cyclic proximal point algorithm ([374, Algorithm 1]). We recall eq. (7.1) for the definition of $[\cdot,\cdot]_t$.

had a period of $5\,\mu\mathrm{m}$ while the two absorption gratings (**G0**, **G2**) had a period of $10\,\mu\mathrm{m}$. The distance between the gratings was chosen symmetrically and set to $92.7\,\mathrm{cm}$.

The reconstruction has been computed using our CampRecon framework [28] (see chapter 8). For the forward and the back-projection, i.e. P in eq. (16.4), we are using the OpenCL based projectors proposed by Fehringer *et al.* [140]. The scattering sampling direction u_k where chosen according to the scheme illustrated in fig. 16.3b with $K = 13$. The tomographic reconstruction was computed via 50 iterations of the SIRT-type algorithm (see [7, Alg. 1]). In total, the reconstruction of the carbon knot with 201^3 voxels took approximately $2\,\mathrm{h}$. Following the reconstruction, a tensor has been fitted to each voxel (compare eq. (16.2)).

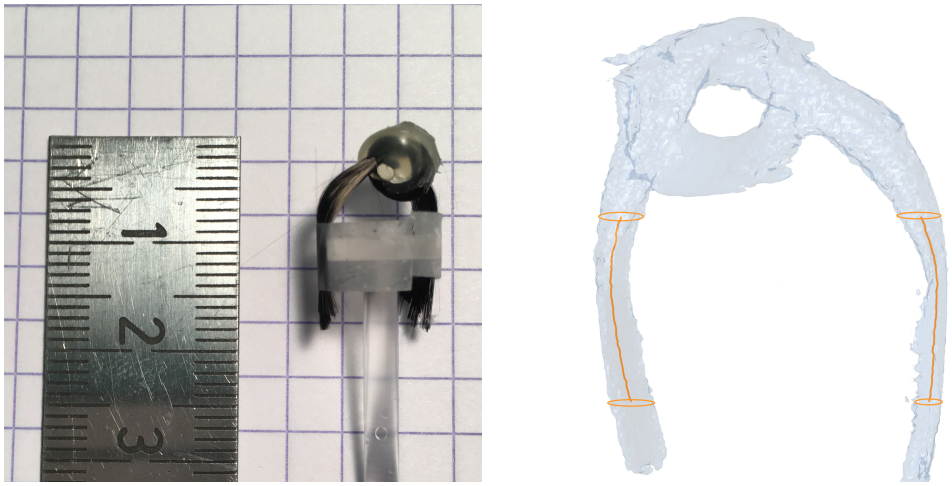

(a) (b)

Figure 17.1 A picture of the carbon knot (a). The illustration (b) shows a rendering of the surface of the segmentation as well as two Regions Of Interest (ROIs) with the extracted centerlines. The left arm is referred to as ROI 1 while the right arm is referred to as ROI 2.

The denoising algorithm (code 17.1) has been implemented in a C++ toolbox developed by Maximilian Baust[4]. This toolbox offers an abstract formulation of the algorithm given above, and we only needed to add the support for Pos_3, i.e. the implementation of the metric/distance, the exponential map, and its inverse. As all these implementations require eigenvalue decompositions of the matrices (i.e. the tensors as well as the elements of the tangent space) we decided to use Eigen [168].

We ran 10 iterations of code 17.1 with $\lambda = 1$ and $\alpha_{it} = 3\,(it+1)^{-0.95}$ ($\in \ell^2 \setminus \ell^1$ as proposed in [374]). The denoising took $\approx 20\,\mathrm{min}$[5].

In fig. 17.2 we present the original data (figs. 17.2a and 17.2c) and the results of the denoising (figs. 17.2b and 17.2d) for the center slice of the dataset. For the visualization we chose to display every fifth tensor/direction within this plane in both directions. Additionally, the data has been scaled by a factor of 100. The upper row (figs. 17.2a and 17.2b) shows the tensors, while the lower row (figs. 17.2c and 17.2d) shows the smallest half-axis projected onto the plane. In both cases, the coloring has been chosen by the projection of the smallest half-axis onto the plane according to the color-wheel depicted at the right side of each row.

Further, in fig. 17.3 we present a 3D visualization of streamlines along the extracted smallest half-axis of the tensors. This visualization is computed using a Runge-Kutta [218, 314] (RK4) method to track streamlines along a vector field as proposed in [7]. This visualization paradigm is also well known from the DTI context.

Aiming at a quantitative evaluation one requires a directional reference. As the carbon fibers in this dataset (see fig. 17.1a) point mostly into the same direction, we considered the centerline

[4] This toolbox was used for several contributions, including [4, 21].
[5] In [21] we originally only performed a 2D version of this algorithm, which was applied slice-wise. The 2D version of the algorithm took $\approx 4\,\mathrm{s}$ for a single slice using the same parameters.

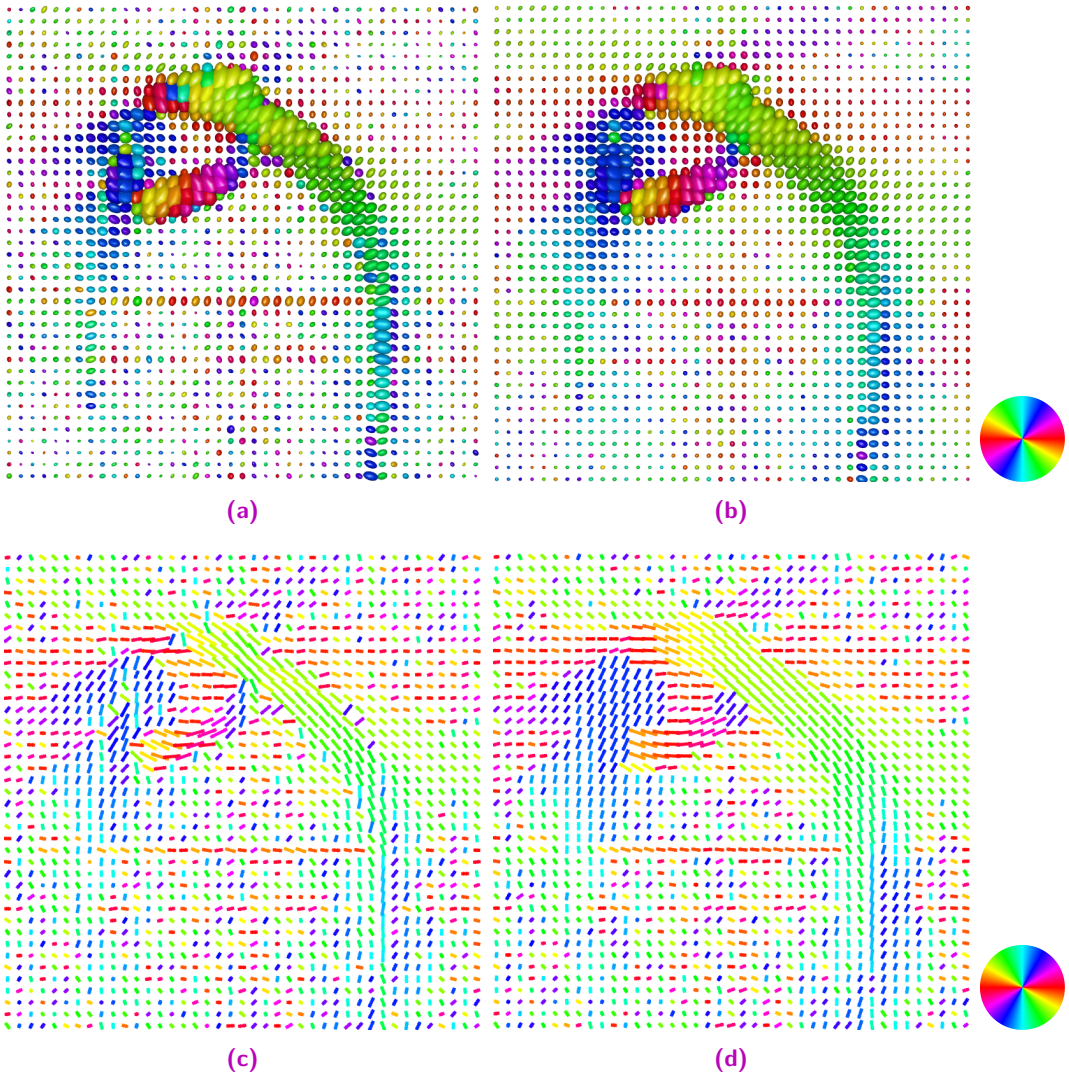

Figure 17.2 Results for the denoising algorithm applied to the carbon knot dataset. In order to increase the visibility we chose to display every fifth voxel in each direction and to scale the data isotropically by a factor of 100. The upper row shows the original tensors (a) and the denoised tensors (b) after the algorithm was applied. In the lower row we extracted the smallest half-axis of the tensors above and display the original data in (c) and their denoised counterparts in (d). For all images, the direction of the smallest half-axis has been encoded in the visualization by choosing the color according to the color-wheel on the right.

of the arms of the carbon knot as a ground-truth for the surrounding directions. This is motivated by the fact that carbon fibers bend very smoothly. With this in mind, we segmented the carbon knot from the reconstruction via simple thresholding. The resulting segmentation is shown in fig. 17.1b. This segmentation is processed slice by slice from bottom to top (we illustrate the limits of the chosen slices with rings in fig. 17.1b). For each slice we computed the center of the circle-like cross-section through the segmentation. The direction between two slices was computed via finite differences. The similarity of the resulting direction vector and every element of the corresponding ROI within this slice has been evaluated in terms of the angle between these two vectors.

In fig. 17.4 we present the quantitative results for both the original dataset and the denoised dataset. The plots show the normalized histogram and corresponding box-plots for the angle between the reference direction from the centerline and each corresponding tensor direction located in the same slice and ROI.

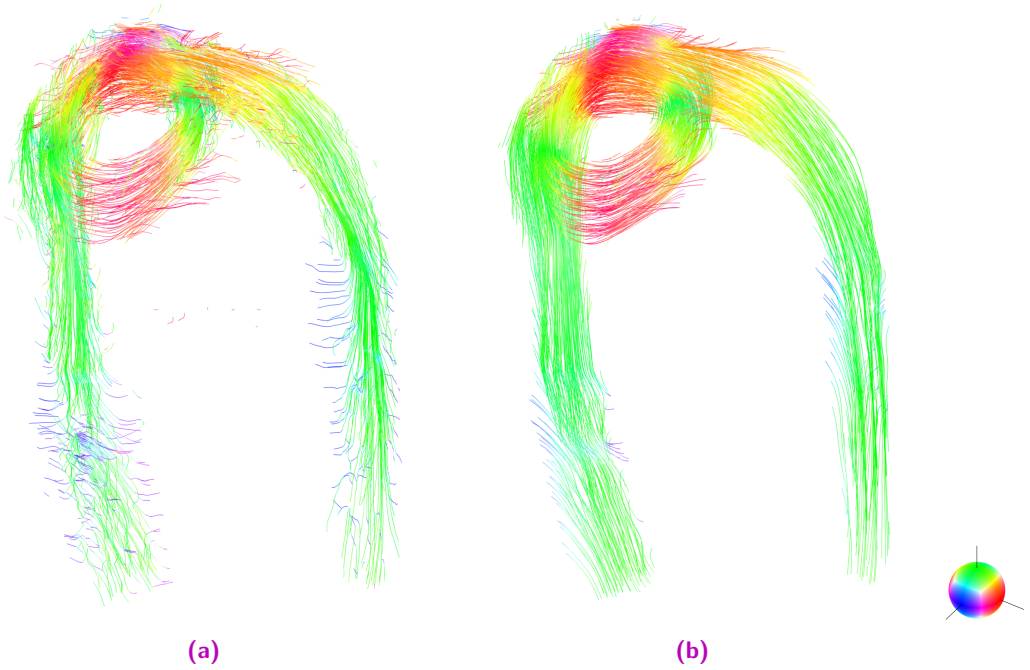

Figure 17.3 3D results of the denoising algorithm displayed via streamlines along the vector field defined by the smallest half-axis of the tensor field. The coloring again displays the direction using the symmetric color-ball depicted on the right side. In (a) we show the streamlines computed on the original data, while (b) shows the streamlines of the denoised data. Seeding and stopping criterias for the RK4 algorithm have been chosen the same in both cases.

Both the 2D as well as the 3D visual results presented in figs. 17.2 and 17.3 clearly show much smoother directional information. Additionally, we find the streamline visualization to trace more, longer, and smoother streamlines. These visual results are supported by the natural behavior of carbon fibers themselves, which due to their composition bend very smoothly.

Considering the quantitative evaluation using the centerline as reference, we can quantify the improvement in terms of a shift of the median toward $0°$. For ROI 1 the median was $\approx 24.5°$ in case of the original data which improved to $\approx 16.48°$. In the case of ROI 2 the improvement was from $\approx 25.31°$ to $\approx 17.05°$.

17.2 Conclusion

In this chapter we presented a manifold-based method for a-posteriori denoising of XTT reconstructions. Both the visual as well as the quantitative evaluation paired with the physical nature of carbon fibers support the claim that we successfully denoised the tensor valued data set and increased the information quality.

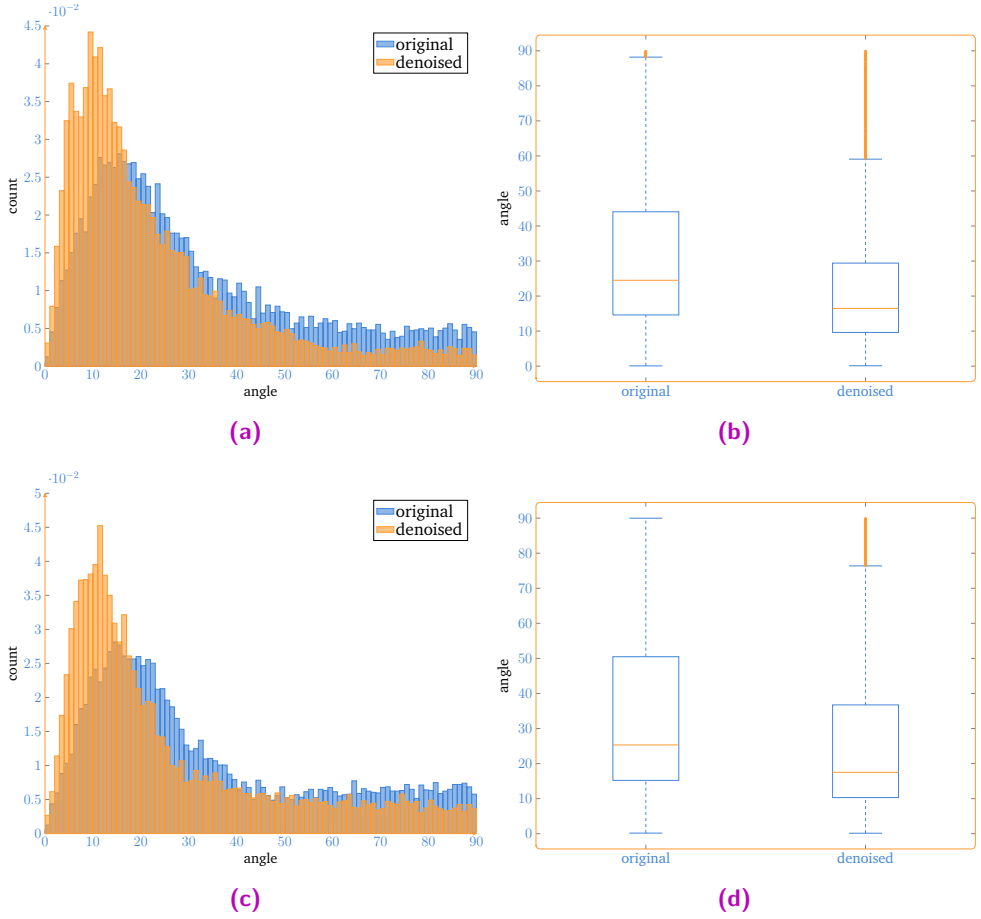

Figure 17.4 Evaluation of the denoising algorithm of the original data compared to the denoised data for the ROIs 1 (a),(b) and 2 (c),(d). The plots (a),(c) show the normalized histograms of the angle between the direction of the smallest half-axis and the reference given by the centerline direction in the same slice. Additionally in (b),(d) we present the corresponding box plots.

This method considered the denoising after an actual reconstruction including the tensor fit is performed. The natural question that arises is if it is possible to compute a regularized reconstruction of the tensors directly within the manifold. As a follow-up to this work we have therefore investigated the regularized tensor fit in the context of DTI in [4]. In this work Baust *et al.* [4] presented a forward-backward splitting algorithm to compute a TV-regularized tensor fit. The algorithm has been validated for DTI data and shows promising improvements in terms of Signal-to-Noise Ratios (SNRs).

However, while this algorithm in general can be applied to the XTT problem as a whole, it turned out that the least-squares data term is not convex within the manifold Pos_3. Consequently the optimization involves a line-search along the gradient direction. As the computation of the gradient would involve the large-scale forward model from eq. (16.4) and as the pure denoising results already proved very promising, we did not follow this path for XTT.

Beside this manifold-based approach, Seyyedi *et al.* [1, 12, 13] have investigated multiple alternative regularization methods based on regularization of the single components η_k.

On a final note we want to mention that Weinmann *et al.* [375] have additionally presented algorithms for different problems such as Mumford-Shah and Potts regularization.

While the previously presented method provides strong improvements, we did not take the actual reconstruction into account at this point. Thus, the following chapter is dedicated to the remaining restriction imposed by the tensor model as well as the forward model for XTT.

18 Anisotropic X-ray Dark-field Tomography

Now we want to investigate the limitations linked to the tensor model as well as the XTT model as discussed in chapter 16. In the following, we will develop a fully continuous forward model. We will see that this continuous formulation enables us to apply all methods we have discussed in the scope of cubature (compare chapter 6). Additionally, we will present a special version of discretization using spherical harmonics, which provides strongly improved reconstruction results. This spherical harmonics-based approach has been presented in [6] and is termed Anisotropic X-ray Dark-field Tomography (AXDT), as opposed to X-ray Tensor Tomography (XTT).

Let's recall the remaining two issues. First is a missing weighting/normalization depending on the number of sampling direction u_k, as well as the actual sampling scheme. Second the fact that the tensor model is limited to a single microstructure direction. As mentioned before, the assumption of a single direction is assumed to be restrictive for more complicated samples, as the dark-field signal relates to structures with a size far below the detector resolution. Thus, the case of multiple structures crossing the same voxel is likely.

For a detailed analysis, we recall the form of the original forward model developed by Malecki *et al.* [244] given in eq. (16.1), i.e.

$$d = \exp\left(-\int_L \sum_{k=0}^{K-1} h\left(u_k, t, l\right) \eta_k\left(x\right) dx\right), \tag{18.1}$$

with the weighting function $h : \mathbb{S}^2 \times \mathbb{S}^2 \times \mathbb{S}^2 \to \mathbb{R}$ as given in eq. (16.1) and the K fields $\eta_k : \mathbb{R}^3 \to \mathbb{R}$ denoting the scattering strength in the direction u_k. We observe that the finite sum can already be interpreted as a form of discretization. Both the weighting function as well as the scattering profile are discretely sampled at the u_k. While for the weighting function this is obvious, for the η_k it can be seen by identifying the η_k with discrete samplings of a scattering function $\eta : \mathbb{S}^2 \times \mathbb{R}^3 \to \mathbb{R}$. The mapping η therefore can be seen as the function mapping a sampling direction $u_k \in \mathbb{S}^2$ and a position in 3D space $x \in \mathbb{R}^3$ to the corresponding scattering strength $\eta_k\left(x\right) := \eta\left(u_k, x\right)$. As mentioned previously, this is exactly what we discussed in the scope of cubature methods in chapter 6 with one major difference – namely the missing weighting used for cubature rules. This, however, is exactly what prevents the XTT model from providing invariant reconstruction quantities and also leads to major issues if the sampling scheme is not well-distributed on the sphere[1].

[1] Beside the pure domination of more densely sampled regions, which can be adjusted by using an appropriate weighting, the sampling also effects the approximation quality of the cubature rule. Effects related to this are not subject of this thesis but might pose an interesting question for further research.

Based on these observations, we have proposed a fully continuous model for AXDT in [6] by replacing the sum with a surface integral on $\mathbb{S}^2$ as follows.

Definition 18.1 **(AXDT continuous forward model)** (c.f. [6, Definition 2]) Let $t \in \mathbb{S}^2$ denote the grating direction and $l \in \mathbb{S}^2$ the direction of an X-ray beam L. Further let the spherical scattering profile $\eta : \mathbb{S}^2 \times \mathbb{R}^3 \to \mathbb{R}$ be given. The forward model relating η and the dark-field measurement is defined as

$$d = \exp\left(- \int_L \int_{\mathbb{S}^2} h\left(u,t,l\right) \eta\left(u,x\right) \frac{d\sigma\left(u\right)}{\sigma\left(\mathbb{S}^2\right)} dx \right), \tag{18.2}$$

with $h : \mathbb{S}^2 \times \mathbb{S}^2 \times \mathbb{S}^2 \to \mathbb{R}$ denoting the detectability weighting.

Note: Please note the normalization of the surface integral with the Lebesque measure σ of the unit sphere, i.e. 4π in case of the standard measure on $\mathbb{S}^2$.

With this definition in place, we are once again faced with the task of discretization. However, in contrast to the original XTT model, we are now able to build upon a fully continuous formulation. We will focus on the discretization of the inner, i.e. the surface integral on $\mathbb{S}^2$, as the outer integral can be discretized in exactly the same fashion as is done for standard CT. In fact, we will find that the resulting discrete models can be rewritten in a similar fashion as proposed by Vogel *et al.* [7] for the XTT model (compare eq. (16.4)).

18.1 Discretization using cubature

Previously we observed that the XTT model (see def. 16.1) is very similar to what one would expect in case of a cubature rule. Consequently, a straightforward approach to discretize the inner integral is to use a cubature rule (see def. 6.2).

Theorem 18.2 **(AXDT discrete cubature based forward model)** Let $U = \{(u_0, w_0), \ldots, (u_{K-1}, w_{K-1})\}$, with $u_k \in \mathbb{S}^2, w_k \in \mathbb{R}$, denote a cubature rule according to def. 6.2. Then a discretization of eq. (18.2) is given by

$$d \approx \exp\left(- \frac{1}{\sigma\left(\mathbb{S}^2\right)} \sum_{k=0}^{K-1} w_k h\left(u_k,t,l\right) \int_L \eta\left(u_k,x\right) dx \right), \tag{18.3}$$

with h, t, l, η as defined in def. 18.1.

Proof: Consider the inner integral in eq. (18.2). By applying the cubature rule U to the product of $h\left(u,t,l\right)$ and $\eta\left(u,x\right)$ we obtain the approximation

$$\int_{\mathbb{S}^2} h\left(u,t,l\right) \eta\left(u,x\right) \frac{d\sigma\left(u\right)}{\sigma\left(\mathbb{S}^2\right)} \approx \frac{1}{\sigma\left(\mathbb{S}^2\right)} \sum_{k=0}^{K-1} w_k h\left(u_k,t,l\right) \eta\left(u_k,x\right). \tag{18.4}$$

As neither the w_k nor $h\left(u_k,t,l\right)$ depend on the position within the volume, i.e. x, eq. (18.3) follows directly from eq. (18.4) by using the linearity of the integral. We therefore exchange sum and integral just as Vogel *et al.* [7] proposed for the original XTT model (compare def. 16.1). □

Interestingly, we find the model to become a weighted sum of the standard CT problem once again. Further, if we consider a cubature rule with equal weights for all sampling directions[2], e.g. spherical t-designs (see eq. (6.12)), we can make a very interesting discovery. Consider $U = \left\{\left(u_0, \frac{1}{K}\right), \ldots, \left(u_{K-1}, \frac{1}{K}\right)\right\}$, then eq. (18.3) becomes

$$d \approx \exp\left(-\frac{1}{K}\sum_{k=0}^{K-1} h\left(u_k, t, l\right) \int_L \eta\left(u_k, x\right) dx\right). \tag{18.5}$$

This model is equal to eq. (16.3) up to the factor $\frac{1}{K}$. The factor is exactly what is needed to yield a normalization, leading to reconstructed scattering strengths invariant to the number of sampling direction.

However, the key strength of this approach can be seen if a non-uniform scheme is applied and consequently the weights of the sampling points differ. This could e.g. be used to use adaptive sampling schemes to refine regions on the sphere, which show more variation than regions which are mostly homogeneous. The incorporated weights enable the prevention of domination of the problem by more densely sampled regions, which was one key issue with the XTT model (def. 16.1).

Following the whole-system approach discussed previously (compare eq. (16.4)) and in [16, 17, 7], we consider J measurements d_j. Further let L_j, l_j denote the corresponding X-ray beams and the relative grating orientation t_j. Given a discretization of the standard modeling operator for CT by a projection matrix $P \in \mathbb{R}^{J\times I}$, we obtain a large scale linear inverse problem by taking the negative logarithm of the measurements $\mathbf{p} = (-\ln d_j)$. The discretization of theorem 18.2 is now given as

$$\mathbf{p} = \underbrace{\begin{pmatrix} W_0 P & \ldots & W_{K-1} P \end{pmatrix}}_{A} \underbrace{\begin{pmatrix} \boldsymbol{\eta}_0 \\ \vdots \\ \boldsymbol{\eta}_{K-1} \end{pmatrix}}_{\boldsymbol{\eta}}, \tag{18.6}$$

with $\boldsymbol{\eta}_k$ denoting the discretization of the field $\eta_k := \eta\left(u_k, \cdot\right) : \mathbb{R}^3 \to \mathbb{R}$. The only change in comparison to the whole-system approach for the XTT model is within the weighting matrices, i.e. $W_k = \frac{w_k}{\sigma(\mathbb{S}^2)} \operatorname{diag}\left(h\left(u_k, t_0, l_0\right), \ldots, h\left(u_k, t_{J-1}, l_{J-1}\right)\right) \in \mathbb{R}^{J\times J}$.

In summary, the proposed continuous forward model def. 18.1 first enables the detailed, mathematical investigation of the model. Further, we find that the discretization of this forward model coincides with the original XTT model def. 16.1 up to a normalization constant if an appropriate cubature rule is chosen. Additionally, this in principle enables the use of any cubature rule[3], which especially in the scope of adaptive sampling might be a very interesting topic for further investigations. Altogether, we therefore subsumed all previous findings related to XTT under this new model.

[2] As discussed in chapter 6 a suitable choice is based on the Voronoi tesselation.
[3] For an excellent overview on this topic we refer to [181].

18.2 Discretization using Spherical Harmonics

While discretization based on cubature already provides a strong improvement over the original XTT model, the continuous model enables an even more versatile approach. This approach uses the set of spherical harmonics and was presented in [6]. A closer look at the inner integral of eq. (18.2) reveals that this integral actually constitutes an inner product in $L^2\left(\mathbb{S}^2\right)$, i.e.

$$\int_{\mathbb{S}^2} h\left(u,t,l\right)\eta\left(u,x\right)d\sigma\left(u\right) = \left\langle h\left(\cdot,t,l\right),\eta\left(\cdot,x\right)\right\rangle_{L^2\left(\mathbb{S}^2\right)}, \tag{18.7}$$

for fixed $t,l \in \mathbb{S}^2$ and $x \in \mathbb{R}^3$. Thus, the integral of the inner product can be replaced by a countable sum by using Parseval's theorem eq. (6.10) for spherical harmonics. This leads to the following discrete forward model.

Theorem 18.3 **(AXDT discrete spherical harmonics based forward model)** (c.f. [6, Theorem 1]) Assuming $\eta\left(\cdot,x\right), h\left(\cdot,t,l\right) \in L^2\left(\mathbb{S}^2\right)$, let $\{h_k^m\left(t,l\right)\}$ and $\{\eta_k^m\left(x\right)\}$ denote the spherical harmonics coefficients of η, h with respect to the variable u (compare chapter 6). Further consider a truncation degree $K \in \mathbb{N}$. Then a discrete approximation of eq. (18.2) in terms of the spherical harmonics coefficients of $\eta\left(\cdot,x\right)$ is given by

$$d \approx \exp\left(-\frac{1}{\sigma\left(\mathbb{S}^2\right)}\sum_{k=0}^{K}\sum_{m=-k}^{k} h_k^m\left(t,l\right)\int_L \eta_k^m\left(x\right)dx\right). \tag{18.8}$$

Proof: Again consider the inner integral and use Parseval's theorem (eq. (6.10)):

$$\begin{aligned}
\int_{\mathbb{S}^2} h\left(u,t,l\right)\eta\left(u,x\right)\frac{d\sigma\left(u\right)}{\sigma\left(\mathbb{S}^2\right)} &= \frac{1}{\sigma\left(\mathbb{S}^2\right)}\left\langle h\left(\cdot,t,l\right),\eta\left(\cdot,x\right)\right\rangle_{L^2\left(\mathbb{S}^2\right)} && (18.9)\\
&= \frac{1}{\sigma\left(\mathbb{S}^2\right)}\left\langle h_k^m\left(t,l\right),\eta_k^m\left(x\right)\right\rangle_{\ell^2} && (18.10)\\
&= \frac{1}{\sigma\left(\mathbb{S}^2\right)}\sum_{k\geq 0}\sum_{m=-k}^{k} h_k^m\left(t,l\right)\eta_k^m\left(x\right) && (18.11)\\
&\approx \frac{1}{\sigma\left(\mathbb{S}^2\right)}\sum_{k=0}^{K}\sum_{m=-k}^{k} h_k^m\left(t,l\right)\eta_k^m\left(x\right) && (18.12)
\end{aligned}$$

As due to the truncating and the fact that the $h_k^m\left(t,l\right)$ are independent from the position within the volume, i.e. x, eq. (18.8) follows directly from eq. (18.9) by using the linearity of the integral. We therefore again exchange sum and integral just as Vogel *et al.* [7] proposed for the original XTT model (compare def. 16.1). □

Note: It is worth mentioning that the approximation imposed by the truncation is actually exact for $K = 4$ in the case of the weighting function proposed by Malecki *et al.* [244], i.e. $h : (u,t,l) \mapsto \left(|l \times u|\,\langle u,t\rangle\right)^2$. The reason is that this function represents a product of four functions that can be expressed with spherical harmonics of degree one. Consequently $h_k^m = 0, \forall k > 4$ holds[4].

Besides the fact that this method used for the discretization is essentially different, we again find the resulting model (theorem 18.3) to constitute a weighted sum of the standard CT

[4] Thanks to Referee A of [6] for pointing this out.

model. This time the standard CT model is applied to the 3D scalar fields of spherical harmonics coefficients. The similarity in the forward model further allows us to once again formulate a large scale inverse problem in a similar fashion as performed for both the XTT model eq. (16.4) as well as the AXDT model using cubature eq. (18.6):

Once again, we consider J measurements d_j corresponding to X-ray beams with L_j, l_j and a relative grating orientation t_j. Further denote the projection matrix as $P \in \mathbb{R}^{J \times I}$ and take the negative logarithm of the measurements $\mathbf{p} = (-\ln d_j)$. This leads to the following large scale inverse problem

$$\mathbf{p} = \underbrace{\begin{pmatrix} W_0^0 P & \dots & W_K^{-K} P & \dots & W_K^K \end{pmatrix}}_{A} \underbrace{\begin{pmatrix} \boldsymbol{\eta}_0^0 \\ \vdots \\ \boldsymbol{\eta}_K^{-K} \\ \vdots \\ \boldsymbol{\eta}_K^K \end{pmatrix}}_{\boldsymbol{\eta}}, \tag{18.13}$$

with $\boldsymbol{\eta}_k^m$ denoting the discretization of the coefficient field $\eta_k^m : \mathbb{R}^3 \to \mathbb{R}$ corresponding to the spherical harmonic V_k^m. The entries of the weighting matrices are given by the spherical harmonics coefficients of the function h, i.e. $W_k^m = \frac{1}{\sigma(\mathbb{S}^2)} \operatorname{diag}\left(h_k^m\left(t_0, l_0\right), \dots, h_k^m\left(t_{J-1}, l_{J-1}\right)\right) \in \mathbb{R}^{J \times J}$.

As the process of scattering is symmetric, we actually benefit from an additional property of spherical harmonics. The symmetry directly affects the function h and is reflected in a point symmetry with respect to the origin, i.e. $h\left(u, t, l\right) = h\left(-u, t, l\right)$, $\forall u, t, l \in \mathbb{S}^2$. This symmetry leads to the elimination of all coefficients with odd degree, meaning that $h_k^m\left(t_j, l_j\right) = 0$ for $k = 1, 3, \dots$. Consequently, we limit the computation to even degrees. As the forward model links the weighting and the coefficients of the scattering profile $\eta_k^m\left(x\right)$ in a multiplicative way, this implicitly imposes a symmetry constraint on the reconstructed scattering function.
Note: In combination with the fact that a truncation with $K = 4$ is exact for the currently employed weighting function, this results in a total of 15 relevant η_k^m. The complexity of the whole-system approach depends linearly on the number of volumes to be reconstructed. This means that we are in a similar complexity domain as the XTT approach with $K = 13$ directions from Vogel *et al.* [7].

In summary, the continuous forward model (def. 18.1) enabled us to massively enlarge the body of applicable methods which can be used for discretization. Most notably, the spherical harmonics based approach (theorem 18.3) proved to be of high value as it provides accurate discretization for the currently applied weighting function while requiring similar computational complexity as the XTT approach. We will later see (in chapter 19) that the spherical harmonics based approach has yet another advantage when it comes to the extraction of the microstructure orientations. In addition, we have also eliminated the rank-2 tensor model. In the following we will focus on the evaluation of the spherical harmonics approach.

18.3 Experiments and Results

In order to evaluate the methods discussed above, we were explicitly interested in a sample consisting of well-defined microstructure orientations which at some points are likely to cross the same voxel in the final reconstruction. With this in mind, we considered a dataset of two wooden sticks forming a cross (see fig. 18.1 for an overview on the dataset). The key property with natural wood is that similar to the carbon fiber dataset used in chapter 17, the orientation of the microstructures can be very well predicted. In the case of wood, one finds microstructures in the direction of growth (compare fig. 18.1c for a μCT of the dataset[5]). Please note that the microstructures are not visible in the isotropic dark-field reconstruction of lesser resolution (fig. 18.1b), as opposed to the high-resolution μCT (fig. 18.1c). Also, the sample holder is rendered invisible in the dark-field reconstruction as is does not scatter. Further, these two wooden sticks touch each other in the center of the cross and we expect to find voxels containing directional information from both wooden sticks in this center region. As mentioned before, we assume to find the strongest scattering orthogonal to the microstructures shown in fig. 18.1c. We will refer to this dataset by the term *crossed sticks* in the following.

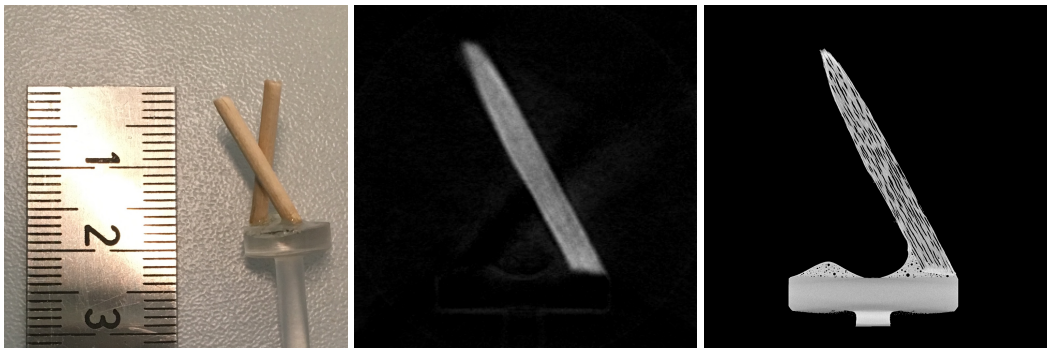

(a) (b) (c)

Figure 18.1 Overview of the crossed sticks dataset. (a) shows an actual photography, (b) shows the center slice of the isotropic part of the dark-field reconstruction (320×320 pixel) and (c) shows a μCT of the dataset (1280×1280 pixel).

In fig. 18.2 we show a VR of the dataset along with two ROIs **A** and **B** each consisting of a single voxel. The point **A** is chosen such that we expect the voxel to consist of one single orientation. The point **B** is chosen exactly in the region where the two wooden sticks touch each other.

The sample was again measured with a setup as illustrated in fig. 16.2, as proposed in [244, 279]. The inter-grating distance was chosen symmetrically and set to $91\,\mathrm{cm}$. Generation of X-rays was performed with a tungsten-target X-ray tube operated at $60\,\mathrm{kV\,p}$ with a current of $13.3\,\mathrm{mA}$. Three gratings (**G0**, **G1**, **G2**) were used, with a period of $5\,\mu\mathrm{m}$ in case of the phase grating (**G1**) and $10\,\mu\mathrm{m}$ in case of the two absorption gratings (**G0**, **G2**). The spectrum was

[5] Credits for providing the μCT go to Christoph Jud. The dataset was measured with a GE phoenix|X-ray v|tome|x using a tube voltage of $60\,\mathrm{kV}$ with a current of $200\,\mu\mathrm{A}$. In total the scan consists of 1000 X-ray projections recorded with an exposure time of $2\,\mathrm{s}$ each. The reconstruction was computed using the built-in tool datos|x 2.0. The final reconstruction provides a voxel size of isotropic $17.5\,\mu\mathrm{m}$ and a total of 1280^3 voxel.

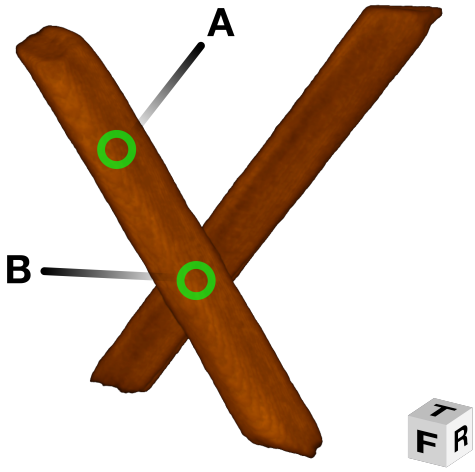

Figure 18.2 VR of the crossed sticks dataset. The point **A** is located in the front stick, while the point **B** is located in the center region where the wooden sticks touch. The cube on the right shows the sample orientation (T=Top, F=Front and R=Right). From M. **Wieczorek**, F. Schaff, F. Pfeiffer, and T. Lasser. "Anisotropic X-Ray Dark-Field Tomography: A Continuous Model and its Discretization". English. In: *Physical Review Letters* 117.15 (Oct. 2016), p. 158101
DOI: 10.1103/PhysRevLett.117.158101
URL: http://link.aps.org/doi/10.1103/PhysRevLett.117.158101, with the permission of APS (©2016 American Physical Society)

filtered with $2\,\mathrm{mm}$ aluminum. We recorded a total of 1200 X-ray projections from various viewpoints sampling the unit sphere using the Euler cradle. For each viewpoint we recorded eight phase-stepping images with an exposure time of $1\,\mathrm{s}$ each. Images were recorded with a Varian PaxScan 2520D flat-panel detector equipped with a CsI scintillator. Each image consists of 800×800 pixels with an isotropic pixel size of $127\,\mu\mathrm{m}$. Prior to any processing, the raw data has been rebinned by a factor of 2 in order to reduce the computational requirements. In total, the measurement took $345\,\mathrm{min}$.

All reconstructions have been computed using our CampRecon framework [28] (see chapter 8). As projector, i.e. the standard CT model, we used the ray-driven multi-GPU projector of Fehringer *et al.* [140] which is written in OpenCL. For each reconstruction we performed 20 iterations of CG using the according whole-system formulation. Any computations were performed using a compute server with a dual Intel Xeon E5-2687W v2 CPU equipped with $128\,\mathrm{GB}$ RAM and dual Nvidia GeForce GTX 980Ti GPUs. The weighting function h was chosen according to the formulation of Malecki *et al.* [244], i.e. $h : (u, t, l) \mapsto (|l \times u| \langle u, t \rangle)^2$. Due to the rebinning and a nearly parallel beam geometry, the resulting reconstructions offer an isotropic voxel size of $254\,\mu\mathrm{m}$ with a total number of 320^3 voxels.

For the spherical harmonics transform and visualization of spherical harmonics we used the excellent Matlab [on2] toolbox provided in [on15][6]. The entries of the weighting matrices W_k^m were precomputed using this toolbox. Exploiting both the symmetry of the scattering and the aforementioned fact that a truncation of degree 4 is optimal, the whole system eq. (18.13) was formulated using $K = 4$ and $k = 0, 2, 4$. Thus the reconstruction effectively constitutes of 15 volumes η_k^m. In total, the computation took $50\,\mathrm{min}$.

[6] Since [6] we incorporated the support for spherical harmonics directly into our CampRecon framework. However we still use the excellent toolbox of [on15] for visualization purposes.

For comparison, the same data was reconstructed using eq. (16.4) with the sampling scheme $K = 13$ (see fig. 18.3a). The corresponding tomographic reconstruction took $45\,\mathrm{min}$. The resulting reconstruction was scaled by a factor of K in order to obtain comparable scattering strengths as discussed above. To the resulting 13 η_k we fitted rank-2 tensors using the PCA based method as proposed in [7].

Additionally, we performed a reconstruction using the cubature based method eq. (18.6) with $K = 50$ directions (see fig. 18.3b) generated with a Voronoi tesselation (c.f. [129])[7]. This reconstruction took $192\,\mathrm{min}$.

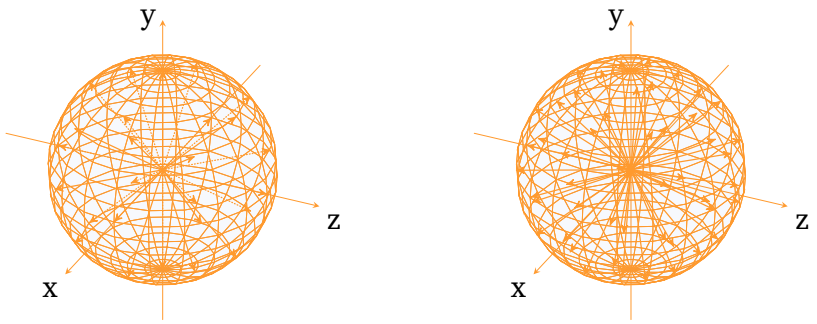

(a) $K = 13$ **(b)** $K = 50$

Figure 18.3 Illustration of the sampling direction used for the reconstruction. (a) shows the sampling scheme with $K = 13$ used for the XTT approach as proposed by Vogel *et al.* [7]. (b) shows the scheme with $K = 50$ directions created with Voronoi tesselation (c.f. [129]).

Figure 18.4 shows plots of the residual norm δ_{new} and its normalization δ_{new}/δ_0 (compare code 4.1). Especially the latter is commonly used as convergence measure. In fig. 18.4a we see that the residual norm is much higher for the original XTT method, which is mainly linked to the missing normalization. The normalized residual norm fig. 18.4b shows that all algorithms reached a similar value after 20 iterations and it is therefore reasonable to consider these results to be comparable. We also see that the update already flattened out, which also indicates that the results are not expected to change essentially in further iterations.

The reconstructed scattering profiles for the two voxels **A** and **B** (see fig. 18.2) are displayed[8] in fig. 18.5 for voxel **A** and in fig. 18.6 for **B**. Positive function values are colored blue while red color was chosen for negative entries.

Additionally, in fig. 18.7 we present slice views for the slices containing the voxel **A** and **B**. We focus on comparing the XTT results with those obtained by using the spherical harmonics based AXDT method.

For the voxel **A**, which is located in the front stick, we expect only one single microstructure orientation. This orientation aligns with the direction of growth, i.e. the main direction of the stick itself. Consequently, for all methods we find similar orientations. We also see that while the XTT method using the scheme with $K = 13$ provides a very coarsely sampled result

[7] Matlab [on2] code is available from Burkardt *et al.* [on6].

[8] In case of the scattering profiles using discrete sampling direction we utilized a Delauney triangulation in order to display the corresponding graph of the spherical function. For the spherical harmonics we employed the tools provided in [on15].

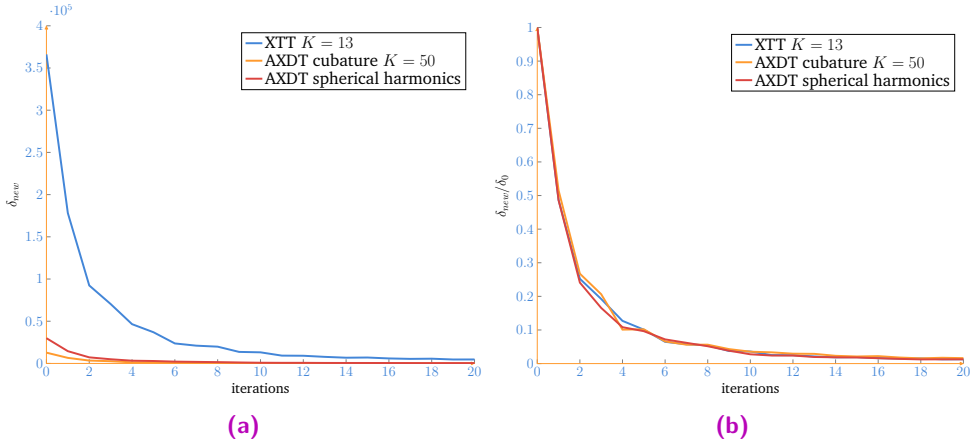

Figure 18.4 (a) shows the absolute norm of δ_{new} while (b) shows the normalized residual norm $\frac{\delta_{new}}{\delta_0}$.

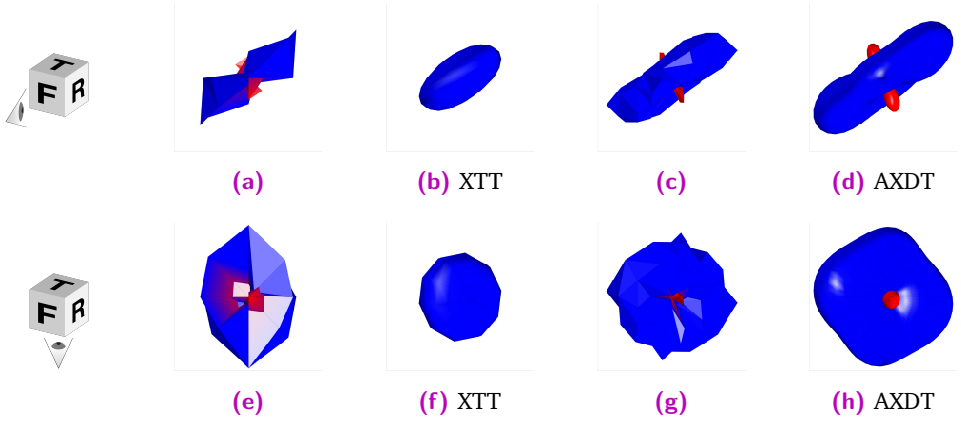

Figure 18.5 Scattering profiles of the results for the voxel **A** in fig. 18.2. Positive function values are rendered in blue while red color is chosen for negative values. The images show the results obtained by the XTT reconstruction with $K = 13$ (a), (e), the fitted rank-2 tensors to this reconstruction (b), (f), the cubature based AXDT reconstruction with $K = 50$ (c), (g) and finally the spherical harmonics based AXDT reconstruction (d), (h). The upper row shows the profiles from a front (F) view, while the lower row shows the same profiles but from a bottom (B) view as illustrated by the corresponding viewpoint cube on the left side. (b), (d), (f), (h) are from M. **Wieczorek**, F. Schaff, F. Pfeiffer, and T. Lasser. "Anisotropic X-Ray Dark-Field Tomography: A Continuous Model and its Discretization". English. In: *Physical Review Letters* 117.15 (Oct. 2016), p. 158101
DOI: 10.1103/PhysRevLett.117.158101
URL: http://link.aps.org/doi/10.1103/PhysRevLett.117.158101, with the permission of APS (©2016 American Physical Society)

the orientation represented by the tensor aligns very well with the one obtained by the other methods. Further, the cubature method with $K = 50$ provides much more densely sampled results. Consequently, the computational effort is roughly five times higher. Finally, the spherical harmonic based result shows a similar profile as obtained by the cubature method. This method however only slightly differs in terms of computational effort from the XTT method.

The situation, however, changes drastically for the voxel **B** where the two wooden sticks touch. Directly considering the spherical harmonics AXDT results we actually find that two structure

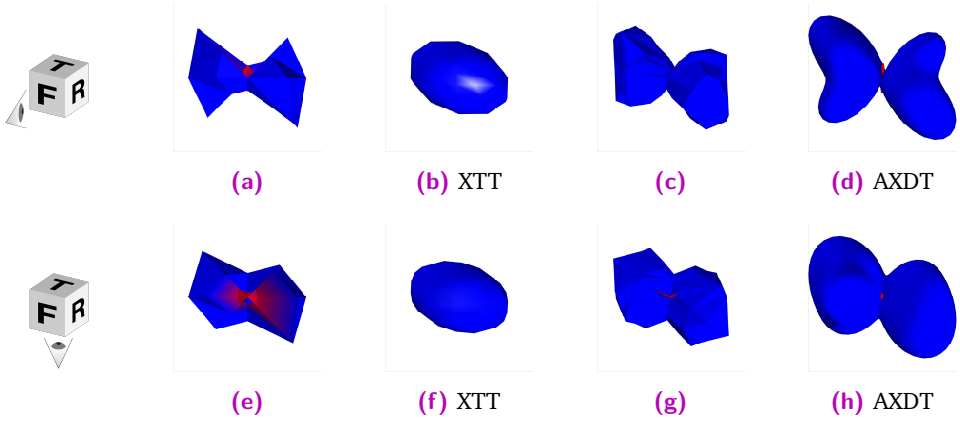

Figure 18.6 Scattering profiles of the results for the voxel **B** in fig. 18.2. Positive function values are rendered in blue while red color is chosen for negative values. The images show the results obtained by the XTT reconstruction with $K = 13$ (a), (e), the fitted rank-2 tensors to this reconstruction (b), (f), the cubature based AXDT reconstruction with $K = 50$ (c), (g) and finally the spherical harmonics based AXDT reconstruction (d), (h). The upper row shows the profiles from a front (F) view, while the lower row shows the same profiles but from a bottom (B) view as illustrated by the corresponding viewpoint cube on the left side. (b), (d), (f), (h) are from M. **Wieczorek**, F. Schaff, F. Pfeiffer, and T. Lasser. "Anisotropic X-Ray Dark-Field Tomography: A Continuous Model and its Discretization". English. In: *Physical Review Letters* 117.15 (Oct. 2016), p. 158101
DOI: 10.1103/PhysRevLett.117.158101
URL: http://link.aps.org/doi/10.1103/PhysRevLett.117.158101, with the permission of APS (©2016 American Physical Society)

orientations are reconstructed within the scattering profile. These two directions can be clearly distinguished from the visual results of the spherical harmonics reconstruction. However, this is neither the case for the XTT reconstruction nor for the cubature based AXDT reconstruction. While the cubature method with $K = 50$ already tends towards the spherical harmonics based result, the orientations are not visually distinguishable. This again may be explained by the optimality of the spherical harmonics discretization. Finally, considering the fitted XTT tensors we find the tensors to suffer from the two existing directions and falsely orient orthogonally to these two orientations.

All raw reconstructions show "negative" function values, especially along the direction of the expected microstructures. Currently we hypothesize that this is linked to the weighting function h which does not perfectly model the measurement in case of a microstructure pointing in a similar direction as the X-ray (see chapter 5 for a detailed discussion).

18.4 Conclusion

In summary, we have presented a fully continuous forward model for Anisotropic X-ray Dark-field Tomography (AXDT).

It is worth mentioning that due to the similarity of dark-field imaging and SESANS (compare chapter 5), the presented methods might be applicable to this imaging modality in a similar fashion. Unfortunately, a corresponding investigation goes beyond the scope of this thesis.

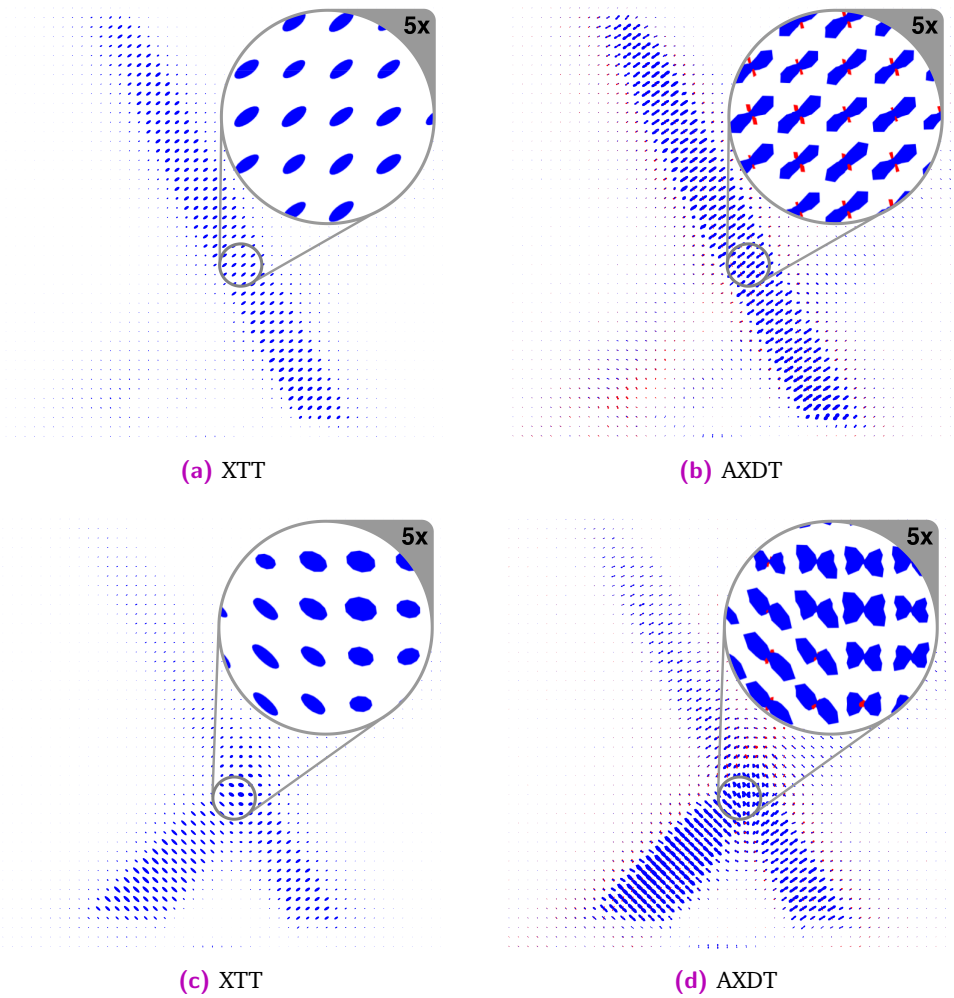

(a) XTT (b) AXDT

(c) XTT (d) AXDT

Figure 18.7 Slice visualization of every fifth tensor/scattering profile. The XTT tensors are displayed in (a), (c) while the spherical harmonics based AXDT results are shown in (b), (d). The upper row shows the slice containing the voxel **A**, while the bottom row shows the one containing voxel **B** (see fig. 18.2). Positive function values are rendered in blue while red color is chosen for negative values. From M. **Wieczorek**, F. Schaff, F. Pfeiffer, and T. Lasser. "Anisotropic X-Ray Dark-Field Tomography: A Continuous Model and its Discretization". English. In: *Physical Review Letters* 117.15 (Oct. 2016), p. 158101
DOI: 10.1103/PhysRevLett.117.158101
URL: http://link.aps.org/doi/10.1103/PhysRevLett.117.158101, with the permission of APS (©2016 American Physical Society)

The presented model has been crafted independently of the explicit formulation of the weighting function h, which enables further adjustments in this domain in the future. Due to its fully continuous fashion, this model can in future be used to analyze its mathematical properties, such as its null space or error estimates which can be used to create simplified acquisition protocols. A first investigation in this scope has been performed by Sharma *et al.* [3]. We additionally presented two ways to discretize this forward model, i.e. the cubature based approach (see section 18.1) and the spherical harmonics based approach (see section 18.2). The cubature base approach turned out to provide a formula very similar to the original XTT model, which enabled us to subsume the former XTT method as a special case of the novel AXDT approach. In case of the current weighting function h, we found the discretization using the spherical harmonics to be exact for $K = 4$.

For both discretization approaches, we were able to derive a large scale inverse problem eqs. (18.6) and (18.13), enabling us to actually reconstruct the scattering profiles at each position within the sample from a given dark-field measurement.

Finally, the experimental results show that for single microstructure orientations these novel methods yield comparable orientations. For multiple microstructures crossing the same voxel, however, we find the previous method to fail in successfully retrieving both directions. In contrast, the spherical harmonics AXDT method successfully retrieved both directions in our sample in these cases. This is again of particular interest with the considered microstructure being far smaller than the detector resolution, which makes multiple orientations crossing the same voxel very likely in more complicated samples. The experiments presented in this chapter support these findings.

For future investigation, a highly interesting field of research is to further continue the work of Sharma *et al.* [10, 3, 15, 5] and investigate the basic mathematical properties of eq. (18.2). In addition, to the standard tomographic axis, AXDT requires the rotation in a fully 3D fashion. It is therefore of high interest to investigate what really needs to be measured and how the simplification of the acquisition protocol affects the reconstructed results.

Besides these theoretical fields of research in order to reduce the computational effort, block based algorithms (c.f. [342]) or ordered subset approaches (c.f. [136]) might be investigated.

We also observe a certain amount of noise in our reconstructions and the positive effect of denoising on XTT in chapter 17 raises the interest to include regularization. A straightforward method would be to independently regularize the coefficient fields corresponding to a specific degree k and order m as done for XTT by Seyyedi *et al.* [1, 12, 13].

However, as we are mainly interested in the orientation of the scattering profiles, it is worth to consider how the spherical harmonics coefficients change under rotation. A recursive method was presented by Ivanic *et al.* [190] and an implementation is supported in [on15]. One important observation is that we are dealing with axisymmetric functions, i.e. the reconstructed scattering profiles can be seen as a rotation of a function expressed by spherical harmonics with $\eta_k^m = 0$ for $m \neq 0$. This property has been e.g. used in the scope of SAXS to obtain the orientations of collagen fibrils within bone tissue [235]. An additional interesting fact about rotations is that the coefficients of degree k of the rotated function are only affected by the coefficients of degree k of the original function. This means that there is no information transfer between degrees, and the ℓ^2-norm of the coefficients of a degree k is invariant under rotation. This has been used by Kazhdan *et al.* [206] to develop rotationally invariant descriptors for 3D shapes. Consequently, this might be an interesting way of regularization, as it enables imposing a constraint on the strength, while imposing no constraint on the orientation.

Additionally, in order to regularize the orientations one might investigate a similar method to what is presented in chapter 17. For the orientations of q-ball imaging, Cheng *et al.* [95] and Goh *et al.* [162, 163] independently proposed to consider the normalized coefficient vector

as element of $\mathbb{S}^{(K+1)^2}$. $\mathbb{S}^{(K+1)^2}$ again forms a manifold, meaning that the manifold based approach could directly be applied to denoise these normalized coefficients.

As physically positive values make sense only, it also is reasonable to employ a positivity constraint in addition to regularization.

In addition to these considerations, within the scope of q-ball imaging as proposed by Tuch *et al.* [361], many metrics and quality measures have been proposed (c.f. [101, 361]). Among these one famous measure is Generalized Fractional Anisotropy (GFA) defined as (c.f. [100, 101]),

$$\mathrm{GFA} = \sqrt{\frac{\left(1 - \left(\eta_0^0\right)^2\right)}{\sum_{k\geq 0}\sum_{m=-k}^{k}\left(\eta_k^m\right)^2}}. \tag{18.14}$$

These can be directly transferred to AXDT.

Recently, we have also proposed a first attempt to statistical reconstruction based AXDT in [9]. A detailed discussion would go beyond the scope of this thesis, but as a rough summary we have presented a statistical model for AXDT which allows for a joint statistical reconstruction of all three signals, attenuation, phase-contrast, and AXDT all at once. Statistical joint reconstruction approaches with an isotropic scattering assumption have already been presented in [75, 305].

Besides these predominantly reconstruction-oriented considerations, the actual application to specific imaging tasks is of high interest for further research. Following the already presented advantages of XTT in the past we are positive that this imaging modality will provide a great complementary insight not available through other modalities.

Recalling the XTT tensor model, we again mention that the microstructure orientation is related to the smallest half-axis of the corresponding tensor. While we found this method to work well for a single microstructure, this approach failed in the case of multiple directions. We are therefore interested in the extraction of microstructure orientation from a given AXDT reconstruction. As a simple minimum extraction does not work in the presence of multiple directions either, we have to come up with a more versatile approach. In the following chapter, we are going to present a method to extract these directions using AXDT.

19 Microstructure Orientation Extraction for AXDT

The original method of XTT provided an insight into microstructure orientation in form of the smallest half-axis of the tensor. However, as discussed in chapter 18, this is only applicable if the considered voxel is crossed by microstructures pointing in the same direction. A sort of minima detection does not apply either in case one faces multiple directions crossing the same voxel. Thus, a more versatile method has to be developed. Luckily, in q-ball imaging [120, 180, 361] one faces a similar setting. Consequently, we have investigated whether a similar approach can be applied to the method of AXDT. The following has been partially presented in [11].

For the following investigation we consider a tomographic reconstruction in terms of the spherical harmonics based AXDT model theorem 18.3, to be given, i.e. $\eta : \mathbb{S}^2 \times \mathbb{R}^3 \to \mathbb{R}$, with $\eta_k^m : \mathbb{R}^3 \to \mathbb{R}$ denoting the corresponding spherical harmonics coefficients at each location within the volume. Further, as only positive scattering is physically meaningful, we denote the positivity constrained version as $\eta_+(u,x) = \max(\eta(u,x),0)$, for all $x \in \mathbb{R}^3, u \in \mathbb{S}^2$. The corresponding spherical harmonics coefficients are denoted by $(\eta_+)_k^m$. For a fiber-like structure, one finds the scattering to be strongest in the plane orthogonal to the orientation of the microstructure. Considering our reconstruction, we thus expect the peak scattering to be located on the great circle orthogonal to this direction. The task is now to transform a scattering profile such that a peak along a great circle is translated into a peak corresponding to a single direction. If we consider the positivity constrained version, such a transform is naturally given by the Funk-Radon transform [153] def. 6.3. This integral transform maps a spherical function to integral values over all great circles. Following theorem 6.4, we find that we additionally benefit from the spherical harmonics based AXDT approach, as the transform $\mathcal{P}\eta_+(\cdot,x)$ for any $x \in \mathbb{R}^3$ is given in terms of the spherical harmonics coefficients by

$$(\mathcal{P}\eta_+)_k^m = P_k(0)(\eta_+)_k^m \tag{19.1}$$

with P_k denoting the Legendre polynomials (compare theorem 6.4). The only remaining task is to detect the peaks on the result of the transform. For this task, we choose a discrete method based on a finite sampling of the unit sphere[1]. In order to detect local maxima/peaks of $\mathcal{P}\eta_+(\cdot,x)$ at a specific location $x \in \mathbb{R}^3$, the function is sampled at N sampling direction $u_n \in \mathbb{S}^2$, $0 \leq n \leq N-1$. Further, we impose a neighborhood relation by computing a spherical Delauney triangulation [118] D on these directions [296][2]. The resulting triangulation imposes a neighborhood for a direction u_n in terms of each direction that is connected with u_n via

[1] Similar methods can be found in the *dipy* package [158].
[2] Matlab [on2] code is available from Burkardt *et al.* [on7].

an edge in D. We denote the neighborhood of u_n by $\mathcal{N}(u_n) := \{u_m \ : \ n \neq m, \ \{u_n, u_m\} \in D\}$. With this neighborhood relation we can further characterize a local maximum u_n, i.e.

$$\mathcal{P}\eta_+(u_n, x) \geq \mathcal{P}\eta_+(u_m, x), \quad \forall u_l \in \mathcal{N}(u_n), \tag{19.2}$$

holds for a specific position $x \in \mathbb{R}^3$.

Note: The explicit evaluation of the Funk-Radon transformed scattering profile at position $x \in \mathbb{R}^3$ is given as

$$\mathcal{P}\eta_+(u_n, x) = \sum_{k \geq 0} \sum_{m=-k}^{k} (\mathcal{P}\eta_+)_k^m(x) \, V_k^m(u_n). \tag{19.3}$$

These considerations lead to the pseudocode version of the microstructure orientation extraction in code 19.1. Subsequent to the actual detection, we sort the directions which have been detected to be maxima by their corresponding accumulated scattering orthogonally to them, i.e. $\mathcal{P}\eta_+(u_n, x)$.

Input:
Output:
for all Voxel $x \in \mathbb{R}^3$ **do**
▷ Initialize set of peaks
$M \leftarrow \emptyset$
for $k \leftarrow 0, \ldots, K$ **do**
for $m \leftarrow -k, \ldots, k$ **do**
▷ Compute Funk-Radon transform
$(\mathcal{P}\eta_+)_k^m \leftarrow P_k(0)\,(\eta_+)_k^m$
end for
end for
for $n \leftarrow 0, \ldots, N-1$ **do**
if $\mathcal{P}\eta_+(u_n, x) \geq \mathcal{P}\eta_+(u_m, x), \quad \forall u_m \in \mathcal{N}(u_n)$ **then**
$M \leftarrow M \cup \{u_n\}$
end if
end for
Sort M by $\mathcal{P}\eta_+(u_n, x)$
end for

Code 19.1 Pseudocode of the microstructure orientation extraction.

An efficient implementation written in C++ is presented in code 19.2. As the number of edges increases linearly with the number of chosen directions (c.f. [331]), the dominant element in this code is the evaluation of the Funk-Radon transformed scattering function at the sampling direction. In our implementation the values of $V_k^m(u_n)$ as well as the triangulation are precomputed and thus the evaluation (*delauney()* and *sphTransform.inverse()*) happen in constant time (with respect to N). Thus, the algorithm's complexity depends linearly on the number of chosen directions N.

```
/**
 * \brief Computes local maxima of a function f : S^2 -> R given
 *        by its coefficients with respect to spherical harmonics f_k^m.
 *
 * \param[in] coeffs The f_k^m
 * \param[in] sphere A sampling on the unit sphere given as a list of unit 3D vectors.
```

```
 *
 * \return sorted index list such that for each entry i, sphere[i] is a local maxima
 *         of f and f[sphere[i]] ≤ f[sphere[j]], ∀sphere[j] ∈ 𝒩(sphere[i])
 *
 */
std::list<int> computeLocalMaxima(DataContainer& coeffs,
                                  SphericalFunctionDescriptor& sphere){
    // local maxima index list
    std::list<int> localMaxima;
    // index list of the edges within the Delauney triangulation
    std::list<std::pair<int,int>> edgeList;
    // compute a spherical Delauney triangulation on the sampling sphere
    delauney(sphere, edgeList);
    // sample the spherical function f at the sampling points given by sphere
    // this is an inverse discrete spherical harmonics transform
    auto sphTransform = SphericalHarmonicsTransform(sphere, coeffs.getDataDescriptor());
    DataContainer f = sphTransform.inverse(coeffs);

    // initialize flag vector for all sampling points
    // the flags are set to:
    // - -1 if there is at least one neighbor (of all so far considered)
    //      with a higher function value
    // -  0 if the function value equals the function value
    //      of all so far considered neighbors
    // -  1 if not -1 and there is at least one neighbor with a lower
    //      function value of all so far considered neighbors
    std::vector<int> flags(sphere.size(),0);

    // process all edges and update the flags
    for( auto edge : edgeList ){
        // get edge indices
        int index1 = edge.first;
        int index2 = edge.second;
        // obtain function values at the vertices of the edge
        float val1 = f[index1];
        float val2 = f[index2];
        // update flags
        if(val1 < val2){
            // flag index1 to be no candidate any longer
            flags[index1] = -1;
            // if index2 is still a candidate, i.e. flags[index2] == 0,
            // set the local maximaFlag
            if(!flags[index2])
                flags[index2] = 1;
        }
        else if(val1 > val2){
            // flag index2 to be no candidate any longer
            flags[index2] = -1;
            // if index1 is still a candidate, i.e. flags[index1] == 0,
            // set the local maximaFlag
            if(!flags[index1])
                flags[index1] = 1;
        }
    }

    // all remaining vertices flagged with 1 are local maxima
    for( int i = 0; i < sphere.size(); ++i)
        if(flags[i] > 0)
            localMaxima.push_back(sphere[i]);
```

```
    // finally sort localMaxima by the corresponding function value
    std::sort(localMaxima.begin(), localMaxima.end(), [f](int i1, int i2) {
        return f(i1) > f(i2);
    });

    return localMaxima;
}
```

Code 19.2 C++ style pseudocode for the maxima detection on spherical functions. A similar method can be found in [158].

19.1 Experiments and Results

For evaluation we have once again employed the crossed sticks dataset. Furthermore we have used the reconstruction results of the spherical harmonics AXDT approach discussed in section 18.3. For the maxima detection we used a sampling scheme with $N = 750$ directions u_n. These directions were computed via a Voronoi tesselation[3]. A neighborhood relation was computed using a spherical Delauney triangulation[4].

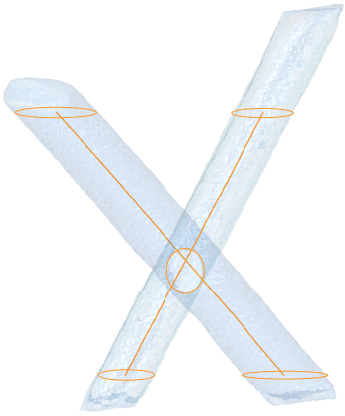

Figure 19.1 Rendering of the surface of the segmentation for the crossed sticks dataset. Additionally, the ROIs used for the evaluation are illustrated. The stick from bottom left to top right is referred to as ROI 1 while the stick from bottom right to top left is referred to as ROI 2. The segmented region in the center where the two wooden sticks touch is referred to as ROI 3.

In fig. 19.2 we present the same two slices used in section 18.3 corresponding to the two voxels of interest denoted in fig. 18.2. This figure shows the originally reconstructed scattering profiles in figs. 19.2a and 19.2b. The corresponding Funk-Radon transforms are shown in figs. 19.2c and 19.2d and the extracted peaks in figs. 19.2e and 19.2f.

Additionally, in order to provide a quantitative evaluation we follow the idea used for evaluation in section 17.1. The μCT image in fig. 18.1c shows that the microstructures align with the orientation of the wooden sticks. For comparison we have used the smallest half-axis orientation of the XTT tensor results from section 18.3.

[3] Matlab [on2] code is available from Burkardt *et al.* [on6].
[4] Matlab [on2] code is available from Burkardt *et al.* [on7].

First, a segmentation of both wooden sticks was computed by pure thresholding (see fig. 19.1). From the segmentation we have extracted three ROIs, one ROI per stick and a special ROI in the center region where the two wooden sticks touch. Again we processed the slices of the dataset from bottom to top within a certain range. This range is illustrated in fig. 19.1 in addition to the segmentation and the ROIs. For the slices where the two wooden sticks were separable, i.e. do not touch, we again computed the centroids of the ROIs 1 and 2. For those slices for which the wooden sticks were not separable, we linearly interpolated the diameters as well as the centroids from the neighboring slices above and below. Within this slice region, ROI 3 was then computed by the intersection of the two circles around the centroids with a diameter enlarged by 3 voxels. Subtraction of the resulting region from the segmentation again provides a well-separated segmentation for each stick providing ROIs 1 and 2 in this region, too.

For each slice within the region marked by the circles in fig. 19.1 we compared the extracted microstructure orientations to the direction of the corresponding centerline. For the special case ROI 3, the minimum of the two angles to both centerlines corresponding to ROIs 1 and 2 is chosen. The results for each ROI are presented in fig. 19.3.

The results in fig. 19.2 indicate that the presented method is capable of retrieving the microstructure orientation even in the situations where multiple directions are present. However, we also observe that we do not detect two directions for all voxels in fig. 19.2b which visually indicate the presence of two directions. We assume that this is linked to the fact that similar to other integral transforms the Funk-Radon transform leads to a certain amount of smoothing. Consequently, the peaks are not clearly separated in the transformed version even if this is visually indicated in the original scattering profile.

The quantitative evaluation in fig. 19.3 shows very similar results in case of the single orientation regions, i.e. ROI 1, 2. Nevertheless, we see a certain variation. For ROI 1 the presented method provides improved results, while for ROI 2 the XTT method shows higher counts in the histogram for $1°$ and $2°$. This could be explained if we recall that the proposed method only considers the directions u_k for possible peak candidates while the XTT method enables a continuous representation of the orientation. A rough approximation based on equal partition of the sphere and approximation of the Voronoi cells of each direction by a circle yields an approximate tolerance T of:

$$T \approx \sin^{-1}\left(\underbrace{\sqrt{\frac{4\pi}{K}\Big/\pi}}_{\text{radius}}\right) \approx 4.2° \tag{19.4}$$

This approximation gives a rough estimate for the expected variation when this method is applied. For ROI 3 we find strong improvements using the presented methods, which is shown by a considerable increase of the counts for low angular variations in fig. 19.3e as well as a strong shift of the median in the boxplot fig. 19.3f. However, we still find many voxels which show a orientation very different from what is expected. We assume this to be linked to falsely undetected multiple directions as discussed above.

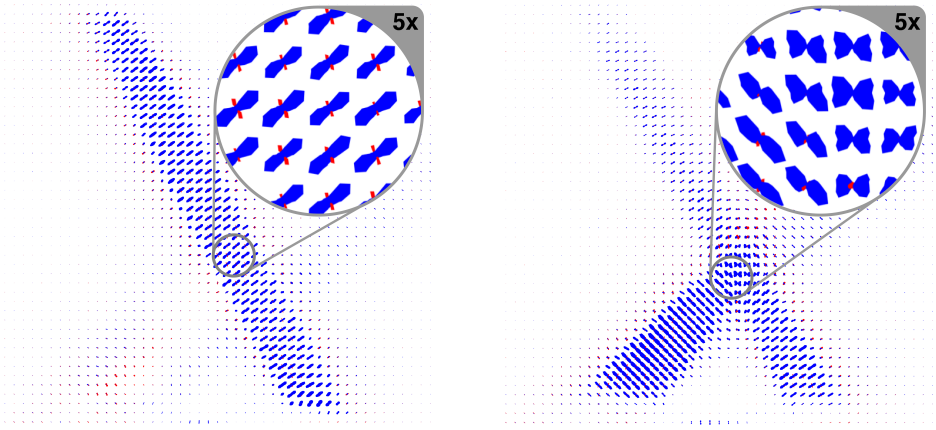

(a) AXDT (b) AXDT

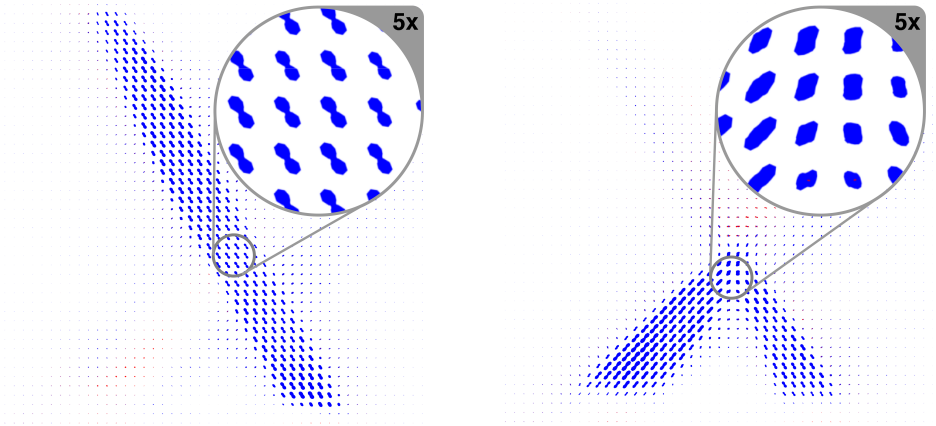

(c) AXDT Funk-Radon (d) AXDT Funk-Radon

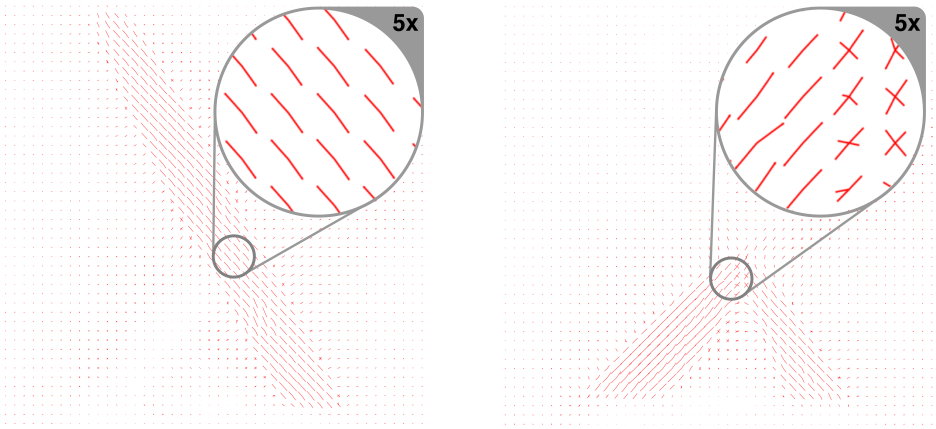

(e) AXDT directions (f) AXDT directions

Figure 19.2 Slice visualizations of the results for the crossed sticks dataset. (a), (b) show a visualization of every fifth scattering profile, (c), (d) the corresponding Funk-Radon transform, and (e), (f) the extracted maxima (i.e. the extracted microstructure orientation). (a), (b) are from M. **Wieczorek**, F. Schaff, F. Pfeiffer, and T. Lasser. "Anisotropic X-Ray Dark-Field Tomography: A Continuous Model and its Discretization". English. In: *Physical Review Letters* 117.15 (Oct. 2016), p. 158101
DOI: 10.1103/PhysRevLett.117.158101
URL: http://link.aps.org/doi/10.1103/PhysRevLett.117.158101, with the permission of APS (©2016 American Physical Society)

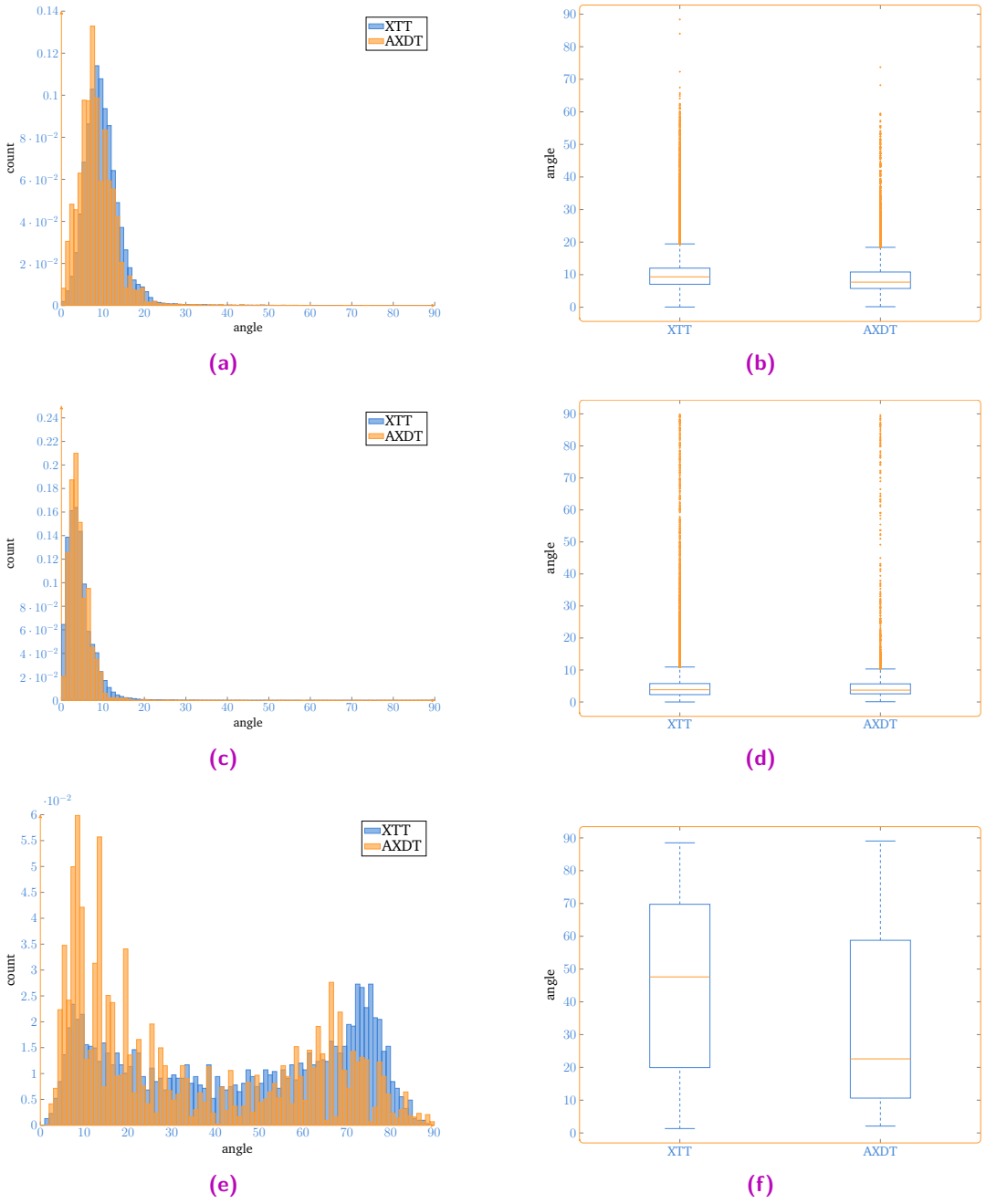

Figure 19.3 Evaluation of the microstructure orientation extraction algorithm. The results for the XTT approach in comparison to the proposed AXDT method, (a), (b) ROI 1 and (c), (d) ROI 2, and finally the results for the center region ROI 3 where the two wooden sticks touch each other in (e), (f). The plots (a), (c), (e) show the normalized histograms of the angle between the direction of the smallest half-axis and the reference given by the centerline direction in the same slice. Additionally in (b), (d), (f) we present the corresponding box plots.

19.2 Conclusion

In this chapter, we have presented a method to extract microstructure orientations based on the spherical harmonics AXDT approach. We found that in addition to the advantages discussed in chapter 18, we benefit from the representation of the scattering profiles using spherical harmonics as the computation of the Funk-Radon transform is particularly efficient with this representation. With this approach, we are now able to fully assimilate the former method of XTT by the novel method of AXDT. Most prominently the capability of extracting multiple directions as supported by our quantitative evaluation in this chapter is likely to strongly improve future applications for more complex samples.

Beside the presented method, multiple alternative additional methods to extract peaks on spherical functions exist. Many of these methods originate from the community of D-MRI. Particularly with respect to the observed problem of smoothing, Descoteaux *et al.* [120] have proposed an interesting approach based on deconvolution. Additionally, other approaches from this domain might be considered – see e.g. [32, 33, 357]. A review is provided in [35]. A great starting point for further advancements of AXDT are the methods developed for D-MRI.

As a final remark we would like to draw the reader's attention to an effect that is not covered within the scope of this thesis but might be worth additional investigation as well: edge scattering. We have focused on fiber-like structures that cause a horn torus type of scattering profile. Scattering on edges, however, leads to a scattering profile that looks similar to a dumbbell. Consequently, it could be interesting to compute a peak detection directly on the scattering profile to detect edges in addition to fibers.

In the following and final chapter we will provide a first biomedical experiment for AXDT, which illustrates possible fields of application of AXDT in the future.

20 AXDT for Human Cerebellum

The following chapter presents a first preclinical experiment on the applicability of AXDT for tomographic imaging of the human CNS. Additionally, it will serve as a summary and closure for this part and is therefore going to conclude this thesis. The combination of the spherical harmonics based AXDT approach combined with the proposed microstructure orientation extraction from chapter 19 as well as the methods of this chapter have been presented in [2].

Connections within the human CNS are related to axons/nerve fibers connecting neurons. These axons have a diameter on the μm scale (c.f. [191, 369]), which renders them invisible in standard attenuation CT. Currently, the already established method for clinical application is D-MRI [54]. The key concept of D-MRI based imaging is that for a nerve fiber, also known as *tract*, diffusion predominantly happens in direction of the fiber. Since its introduction this method led to a great improvement of the understanding of the CNS and related clinical procedures. We have provided a brief overview on some of these applications in section 1.4.

However, the additional investigation in CT-based methods for the application to imaging of the CNS is reasonable despite the existence of D-MRI for mainly two reasons. First, CT is typically superior to MRI in terms of resolution. Second, and even more importantly, X-ray based imaging provides a fundamentally different imaging modality which might provide complementary information/insights in the future. For a SAXS based study we refer to [195]. In [311] a phase-contrast μCT study is presented. Further, in [317] a μCT with contrast agent study is presented. While μCT can resolve these structures, the limitation of the Field Of View (FOV) renders this method impossible for larger samples including an entire brain. This is where AXDT could provide the missing link, as this method is capable of resolving structures far below the voxel resolution, as discussed previously in chapter 18.

We have therefore investigated the application of AXDT in combination with the fiber extraction as discussed in chapter 19 to a sample from a human brain. This sample was from a human cerebellum[1]. In fig. 20.1 (B) (left) we illustrate the location of the cerebellum within the human brain. Further, a zoom in form of a schematic histology slice showing the white matter and the contained fiber tracts is displayed fig. 20.1 (B) (center). Finally, fig. 20.1 (B) (right) shows an illustration of a further zoom to a single fiber (purple) along with the illustration of diffusion (golden) and AXDT scattering (blue). In order to image this sample we used the same GBI based system as used throughout the previous experiments (see fig. 20.1 (A)). Finally, in fig. 20.1 (C) we show the expected outcome[2]. In addition to the attenuation CT

[1] The sample is part of the ethics applicant 319/13, which was approved by the ethics commission of the TUM School of Medicine. Thanks to Dr. M. Willner, Dr. J. Herzen and L. Birnbacher, Dr. med. A. Fingerle, PD Dr. Peter Noël and Dr. med. C. Braun for organization of the cerebellum and the corresponding ethics applicant.

[2] The used images are actual reconstructions computed AXDT.

(left), which is not able to resolve for the fiber tracts, we assume to obtain the fiber tract directions from the AXDT reconstruction.

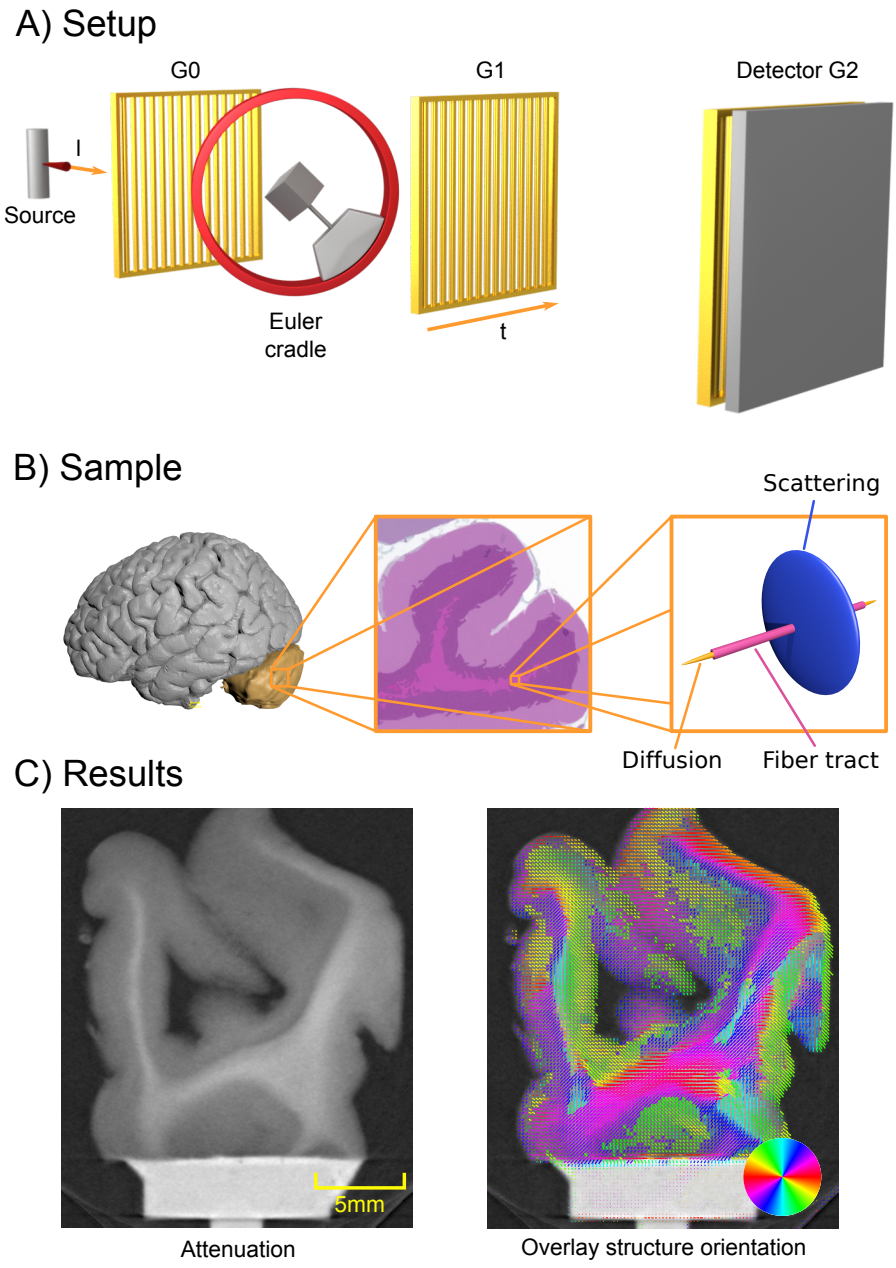

Figure 20.1 Illustration of the GBI setup (A), the sample[3] (B), and the expected results (C). The sample is of a human cerebellum whose location is shown in (B) (left). The cerebellum consists (among others) of fiber tracts located within the white matter (B) (center). Finally, the expected diffusion (golden) and scattering (blue) for such a fiber (mangenta) is illustrated in (B) (right). From M. **Wieczorek**, F. Schaff, C. Jud, D. Pfeiffer, F. Pfeiffer, and T. Lasser. "Brain connectivity exposed by Anisotropic X-ray Dark-field Tomography". In: *Scientific reports* 8.1 (2018), p. 14345
DOI: 10.1038/s41598-018-32023-y
URL: https://www.nature.com/articles/s41598-018-32023-y.

[3] The brain image is created using the Brainder project with kind permission of A. Winkler [on17]. The data is publicly available under the Creative Commons Attribution-ShareAlike 3.0 License (https://creativecommons.org/licenses/by-sa/3.0/). For a great histology database we refer to [on9, on10, sample 77].

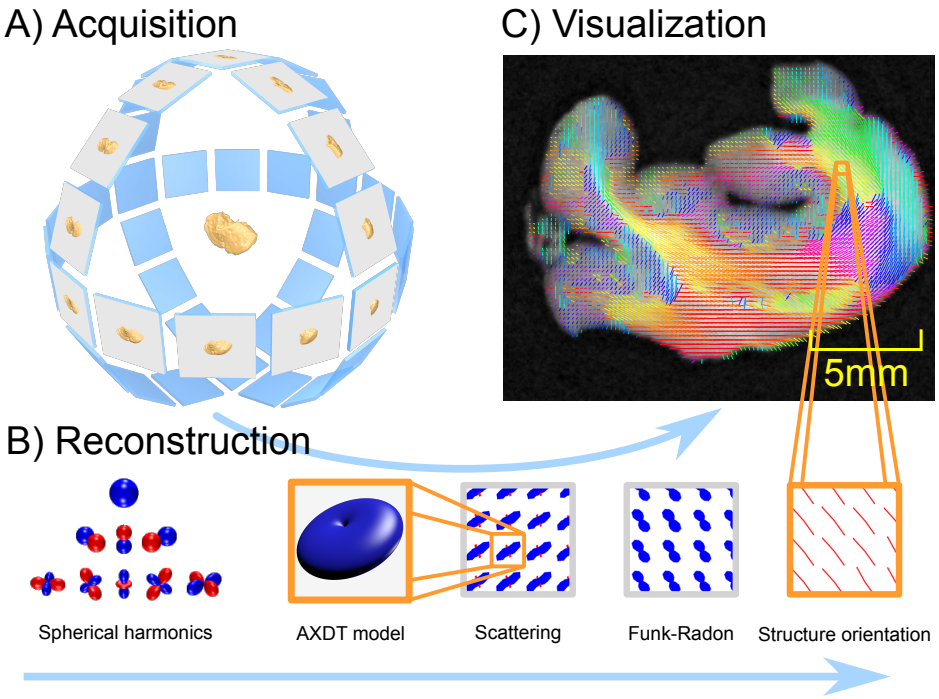

Figure 20.2 Illustration of the whole procedure. Firstly, the sample is imaged from various positions using the Euler cradle (A)[4]. The reconstruction (B) uses spherical harmonics to model the scattering in each location, the reconstruction is performed with the AXDT method and finally the orientations are obtained by the Funk-Radon based approach discussed in chapter 19. Finally, in (C) a visualization is presented, showing the obtained directions overlaid on-top of the attenuation CT (C). From M. **Wieczorek**, F. Schaff, C. Jud, D. Pfeiffer, F. Pfeiffer, and T. Lasser. "Brain connectivity exposed by Anisotropic X-ray Dark-field Tomography". In: *Scientific reports* 8.1 (2018), p. 14345
DOI: 10.1038/s41598-018-32023-y
URL: https://www.nature.com/articles/s41598-018-32023-y.

Figure 20.2 shows an illustration of the entire procedure. Firstly, the acquisition (A), where the Euler cradle is used to obtain dark-field measurements from various orientations. This step is followed by the reconstruction (B) using the spherical harmonics based AXDT approach, where the scattering is modeled using spherical harmonics. Subsequent to the reconstruction of the scattering profiles the microstructure orientations in each location are extracted by computing the Funk-Radon transform and a maxima detection on the result (compare chapter 19). Finally, the attenuation CT result is visualized together with the directions obtained from AXDT (C).

[4]The brain image is created using the Brainder project with kind permission of A. Winkler [on17]. The data is publicly available under the Creative Commons Attribution-ShareAlike 3.0 License (https://creativecommons.org/licenses/by-sa/3.0/).

20.1 Experiments and Results

The measurements and the reconstructions were performed with the same GBI setup and parameters as given in chapter 18 and chapter 19 with few exceptions. Thus, we limit the discussion of the experiments to those parameters that differ from the previous settings.

Firstly, the sample of the human cerebellum was dried with a critical point method. The drying was performed to fix the probe and increase visibility as the sensitivity of the setup is fixed at current[5].

In total, we have recorded 1404 viewpoints from various orientations providing a well-sampled unit sphere. The measurements took approximately $11\,\mathrm{h}$. The attenuation CT was reconstructed from the original absorption measurements, yielding an effective voxel resolution of isotropic $0.127\,\mathrm{mm}$. Due to the additional computational demands for the AXDT reconstruction, the raw dark-field measurements were rebinned by a factor of 4 prior to any processing. This leads to a voxel resolution of $0.508\,\mathrm{mm}$ for the AXDT reconstruction.

The reconstruction was performed on the very same machine and with the same parameters as we have already used in chapters 18 and 19. The AXDT reconstruction took $18\,\mathrm{min}$ while the linear attenuation CT took $85\,\mathrm{min}$ due to the higher resolution. While the other parameters remained unchanged, we have used $N = 1500$ directions of a Voronoi tesselation for the directions extraction.

In fig. 20.3 (A), (B) and (C) we show the results for the three central slices of the volume. The reconstructed fiber orientations extracted from AXDT are overlaid on top of the attenuation reconstruction and colored according to the given color-wheel. The vectors have been scaled by the value of the Funk-Radon transformed scattering function in this direction. Figure 20.3 (D) shows a streamline visualization of the fiber tracts of the white matter between three slices parallel to the main planes.

The white matter regions show strong scattering magnitudes as well as directionality. Closer to the border of the sample, less of these effects are observed. The streamline visualization in particular strongly supports the premise that the fiber tracts are aligned within the white matter, which fits the knowledge e.g. from histology (compare the schematic image in fig. 20.2 (B)).

20.2 Conclusion

In this chapter, we have summarized the developed methods subsumed under the term Anisotropic X-ray Dark-field Tomography (AXDT). Furthermore, we have presented a first, preclinical application to tomographic imaging of the human CNS.

[5] Recent advancements by Birnbacher *et al.* [67] showed that GBI setups are able to reach sensitivity comparable to synchrotrons. However, this requires multiple changes to the setup which at current is not applicable to the setup with the Euler cradle.

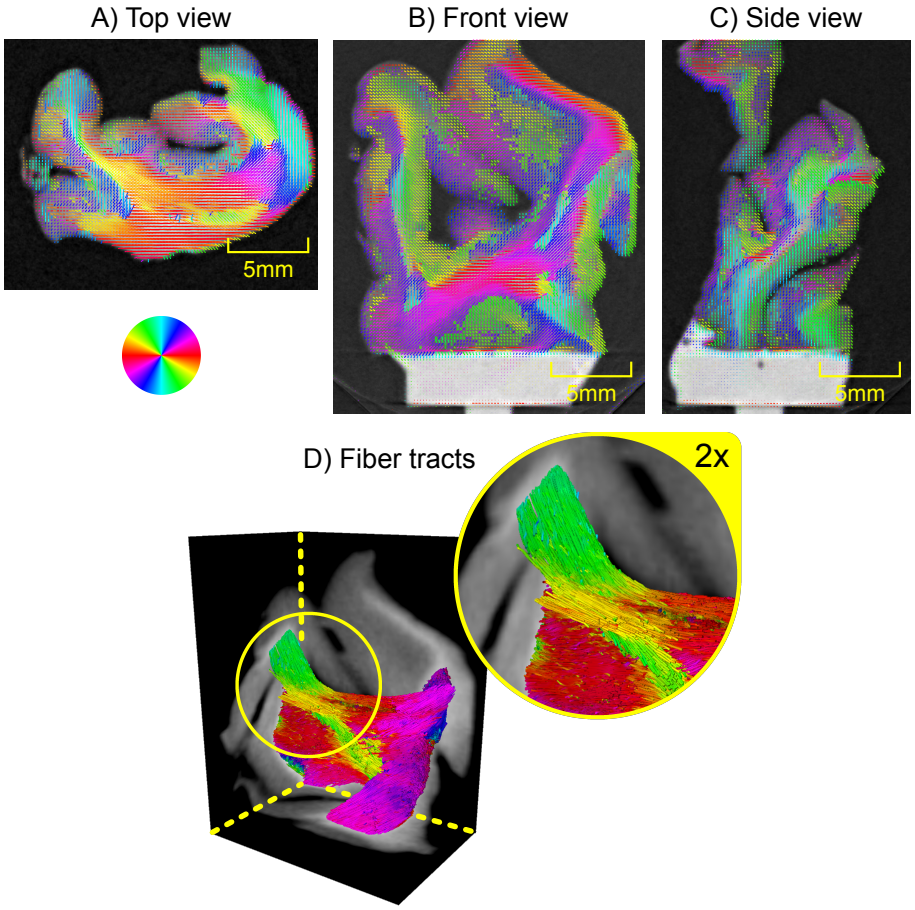

Figure 20.3 Visualization of the results. (A)-(C) show the three center slices of the results. The attenuation CT is overlaid with the directions obtained from AXDT. (D) shows three slices, each parallel to one of the main planes, and a fiber tract visualization of the directions within the white matter. The streamline visualization was created with the ImFusion Suite [on12]. The yellow lines illustrate the intersections of the slices. The directions are color-coded according to the color-wheel. From M. **Wieczorek**, F. Schaff, C. Jud, D. Pfeiffer, F. Pfeiffer, and T. Lasser. "Brain connectivity exposed by Anisotropic X-ray Dark-field Tomography". In: *Scientific reports* 8.1 (2018), p. 14345
DOI: 10.1038/s41598-018-32023-y
URL: https://www.nature.com/articles/s41598-018-32023-y.

While due to the lack of a ground truth, the evaluation is limited to interpretation of the visual results, these results strongly indicate the successful reconstruction of fiber tracts orientations using AXDT. This is supported by knowledge from histology as well as D-MRI. This is particularly interesting as this method is capable of resolving these structures despite being much smaller than the detector resolution. The complementary nature of X-ray imaging to D-MRI imaging supports the assumption that this imaging modality will be capable to provide additional information in the future. While the sample for this experiment was dried, recent advances by Birnbacher *et al.* [67] render the imaging of raw brain material realistic in the future.

This concludes this thesis and as the chapter itself already summarizes everything developed in this part we will omit another summary.

> *We're all stories, in the end. Just make it a good one, eh?*

— The Doctor
Doctor Who

Part V

Appendix

(Co-)Authored Publications

A

Journal Articles

[1] S. Seyyedi, M. **Wieczorek**, F. Pfeiffer, and T. Lasser. "Incorporating Total Variation Noise Reduction in X-ray Tensor Tomography". In: *IEEE Transactions on Computational Imaging* PP.99 (2018), pp. 1–1. (Cited on pp. 88, 91, 99, 107, 120)
DOI: 10.1109/TCI.2018.2794740
URL: http://ieeexplore.ieee.org/document/8260830/.

[2] M. **Wieczorek**, F. Schaff, C. Jud, D. Pfeiffer, F. Pfeiffer, and T. Lasser. "Brain connectivity exposed by Anisotropic X-ray Dark-field Tomography". In: *Scientific reports* 8.1 (2018), p. 14345. (Cited on pp. 131–133, 135)
DOI: 10.1038/s41598-018-32023-y
URL: https://www.nature.com/articles/s41598-018-32023-y.

[3] Y. Sharma, F. Schaff, M. **Wieczorek**, F. Pfeiffer, and T. Lasser. "Design of Acquisition Schemes and Setup Geometry for Anisotropic X-ray Dark-Field Tomography (AXDT)". In: *Scientific reports* 7.1 (2017), p. 3195. (Cited on pp. 15, 119, 120)
DOI: 10.1038/s41598-017-03329-0
URL: http://www.nature.com/articles/s41598-017-03329-0.

[4] M. Baust, A. Weinmann, M. **Wieczorek**, T. Lasser, M. Storath, and N. Navab. "Combined Tensor Fitting and TV Regularization in Diffusion Tensor Imaging Based on a Riemannian Manifold Approach." In: *IEEE Transactions on Medical Imaging* 35.8 (Aug. 2016), pp. 1972–1989. (Cited on pp. 99, 101, 104, 107)
DOI: 10.1109/TMI.2016.2528820
URL: http://ieeexplore.ieee.org/lpdocs/epic03/wrapper.htm?arnumber=7460232.

[5] Y. Sharma, M. **Wieczorek**, F. Schaff, S. Seyyedi, F. Prade, F. Pfeiffer, and T. Lasser. "Six dimensional X-ray Tensor Tomography with a compact laboratory setup". In: *Applied physics letters* 109.13 (Sept. 2016), p. 134102. (Cited on pp. 15, 120)
DOI: 10.1063/1.4963649
URL: http://scitation.aip.org/content/aip/journal/apl/109/13/10.1063/1.4963649.

[6] M. **Wieczorek**, F. Schaff, F. Pfeiffer, and T. Lasser. "Anisotropic X-Ray Dark-Field Tomography: A Continuous Model and its Discretization". In: *Physical Review Letters* 117.15 (Oct. 2016), p. 158101. (Cited on pp. 66, 75, 91, 95, 109, 110, 112, 115, 117–119, 128)
DOI: 10.1103/PhysRevLett.117.158101
URL: http://link.aps.org/doi/10.1103/PhysRevLett.117.158101.

[7] J. Vogel, F. Schaff, A. Fehringer, C. Jud, M. **Wieczorek**, F. Pfeiffer, and T. Lasser. "Constrained X-ray tensor tomography reconstruction." In: *Optics Express* 23.12 (June 2015), pp. 15134–15151. (Cited on pp. 15, 66, 75, 91, 95–99, 101–104, 110–113, 116)
DOI: 10.1364/OE.23.015134
URL: https://www.osapublishing.org/abstract.cfm?URI=oe-23-12-15134.

[8] M. **Wieczorek**, J. Frikel, J. Vogel, E. Eggl, F. Kopp, P. B. Noël, F. Pfeiffer, L. Demaret, and T. Lasser. "X-ray computed tomography using curvelet sparse regularization." In: *Medical Physics* 42.4 (Apr. 2015), pp. 1555–1565. (Cited on pp. 40, 45, 63, 66, 72, 75, 88, 91)
DOI: 10.1118/1.4914368
URL: http://scitation.aip.org/content/aapm/journal/medphys/42/4/10.1118/1.4914368.

Conference Proceedings

[9] N. Schilling, M. **Wieczorek**, and T. Lasser. "Statistical Models for Anisotropic X-Ray Dark-field Tomography". In: *International Meeting on Fully Three-Dimensional Image Reconstruction in Radiology and Nuclear Medicine*. June 2017. (Cited on pp. 41, 121).

[10] Y. Sharma, F. Schaff, M. **Wieczorek**, F. Pfeiffer, and T. Lasser. "Acquisition Schemes for Directional Dark-Field Tomographic Modalities". In: *International Meeting on Fully Three-Dimensional Image Reconstruction in Radiology and Nuclear Medicine*. June 2017. (Cited on pp. 15, 120).

[11] M. **Wieczorek**, F. Pfeiffer, and T. Lasser. "Micro-structure orientation extraction for Anisotropic X-Ray Dark-Field Tomography". In: *International Meeting on Fully Three-Dimensional Image Reconstruction in Radiology and Nuclear Medicine*. June 2017. (Cited on p. 123).

[12] S. Seyyedi, M. **Wieczorek**, C. Jud, F. Pfeiffer, and T. Lasser. “A Regularized X-ray Tensor Tomography Reconstruction Technique”. In: *International Conference on Image Formation in X-Ray Computed Tomography*. July 2016. (Cited on pp. 88, 91, 99, 107, 120).

[13] S. Seyyedi, M. **Wieczorek**, Y. Sharma, F. Schaff, C. Jud, F. Pfeiffer, and T. Lasser. “Component-based TV regularization for X-ray tensor tomography”. In: *IEEE International Symposium on Biomedical Imaging*. IEEE, Apr. 2016, pp. 581–584. ISBN: 978-1-4799-2349-6. (Cited on pp. 88, 91, 99, 107, 120)
DOI: 10.1109/isbi.2016.7493335
URL: http://ieeexplore.ieee.org/document/7493335/.

[14] Y. Sharma, M. **Wieczorek**, C. Jud, F. Schaff, F. Pfeiffer, and T. Lasser. “X-ray Tensor Tomography: How much to measure?” In: *International Conference on Image Formation in X-Ray Computed Tomography*. July 2016.

[15] Y. Sharma, M. **Wieczorek**, F. Schaff, C. Jud, F. Pfeiffer, and T. Lasser. “Acquisition Geometry for X-Ray Tensor Tomography”. In: *International Symposium on BioMedical Applications of X-Ray Phase Contrast Imaging (IMXP)*. Jan. 2016. (Cited on pp. 15, 120).

[16] M. **Wieczorek**, C. Jud, F. Schaff, F. Pfeiffer, and T. Lasser. “An optimization oriented approach to X-ray tensor tomogprahy”. In: *International Symposium on BioMedical Applications of X-Ray Phase Contrast Imaging (IMXP)*. Jan. 2016. (Cited on pp. 98, 111).

[17] M. **Wieczorek**, C. Jud, F. Schaff, F. Pfeiffer, and T. Lasser. “X-ray tensor tomography – a linear system approach to reconstruction”. In: *International Conference on Image Formation in X-Ray Computed Tomography*. **(Oral presentation.)** July 2016. (Cited on pp. 98, 111).

[18] J. Gardiazabal, J. Vogel, P. Matthies, M. **Wieczorek**, B. Frisch, N. Navab, S. Ziegler, and T. Lasser. “Fully 3D thyroid imaging with mini gamma cameras”. In: *International Meeting on Fully Three-Dimensional Image Reconstruction in Radiology and Nuclear Medicine*. June 2015.

[19] T. Lasser, J. Gardiazabal, M. **Wieczorek**, P. Matthies, J. Vogel, B. Frisch, and N. Navab. “Towards 3D Thyroid Imaging Using Robotic Mini Gamma Cameras.” In: *Bildverarbeitung für die Medizin*. Mar. 2015.

[20] J. Vogel, M. **Wieczorek**, C. Jud, F. Schaff, F. Pfeiffer, and T. Lasser. “X-ray Tensor Tomography Reconstruction”. In: *International Meeting on Fully Three-Dimensional Image Reconstruction in Radiology and Nuclear Medicine*. June 2015. (Cited on p. 95).

[21] M. **Wieczorek**, J. Vogel, A. Weinmann, C. Jud, F. Schaff, M. Storath, F. Pfeiffer, M. Baust, and T. Lasser. “Total Variation Regularization for X-Ray Tensor Tomography”. In: *International Meeting on Fully Three-Dimensional Image Reconstruction in Radiology and Nuclear Medicine*. June 2015. (Cited on pp. 101, 104).

[22] A. Aichert, M. **Wieczorek**, J. Wang, M. Kreiser, L. Wang, P. Fallavollita, and N. Navab. “The Colored X-Rays”. In: *International Conference on Medical Image Computing and Computer-Assisted Intervention*. Ed. by C. A. Linte, E. C. S. Chen, M.-O. Berger, J. T. Moore, and D. R. Holmes. Workshop on Augmented Environments for Computer-Assisted Interventions. Berlin, Heidelberg: Springer, 2013, pp. 45–54. ISBN: 978-3-642-38085-3
DOI: 10.1007/978-3-642-38085-3_6
URL: http://link.springer.com/10.1007/978-3-642-38085-3_6.

[23] M. **Wieczorek**, J. Frikel, J. Vogel, F. Pfeiffer, L. Demaret, and T. Lasser. “Curvelet sparse regularization for differential phase-contrast X-ray imaging”. In: *International Meeting on Fully Three-Dimensional Image Reconstruction in Radiology and Nuclear Medicine*. June 2013.

[24] M. **Wieczorek**, A. Aichert, P. Fallavollita, O. Kutter, A. Ahmadi, L. Wang, and N. Navab. “Interactive 3D Visualization of a Single-View X-Ray Image”. In: *International Conference on Medical Image Computing and Computer-Assisted Intervention*. Ed. by G. Fichtinger, A. Martel, and T. Peters. Berlin, Heidelberg: Springer, 2011, pp. 73–80. ISBN: 978-3-642-23623-5
DOI: 10.1007/978-3-642-23623-5_10
URL: http://link.springer.com/chapter/10.1007%2F978-3-642-23623-5_10.

[25] T. Blum, M. **Wieczorek**, A. Aichert, R. Tibrewal, and N. Navab. “The effect of out-of-focus blur on visual discomfort when using stereo displays”. In: *IEEE International Symposium on Mixed and Augmented Reality*. IEEE, 2010, pp. 13–17. ISBN: 978-1-4244-9343-2
DOI: 10.1109/ISMAR.2010.5643544
URL: http://ieeexplore.ieee.org/document/5643544/.

[26] M. **Wieczorek**, A. Aichert, O. Kutter, C. Bichlmeier, J. Landes, S. M. Heining, E. Euler, and N. Navab. “GPU-accelerated Rendering for Medical Augmented Reality in Minimally-Invasive Procedures”. In: *Bildverarbeitung für die Medizin*. Mar. 2010.

Other

[27] M. **Wieczorek**. “Inversion of the Radon transform using adaptive triangulation”. BA thesis. München, Aug. 2014. (Cited on pp. 66, 72).

[28] M. **Wieczorek**, J. Vogel, and T. Lasser. *CampRecon*. Tech. rep. Technische Universität München, 2014. (Cited on pp. 31, 63, 103, 115)
URL: http://mediatum.ub.tum.de/node?id=1191442.

[29] M. **Wieczorek**. “Curvelet sparse regularization for differential phase-contrast X-ray imaging ”. MA thesis. München, Dec. 2012. (Cited on p. 66).

[30] M. **Wieczorek**. “Evaluation of Advanced real-time Visualization Techniques for Medical Augmented Reality”. BA thesis. München, June 2009.

B

Abstract of a Publication not discussed in this Thesis

X-ray computed tomography using curvelet sparse regularization.

Matthias Wieczorek, Jürgen Frikel, Jakob Vogel, Elena Eggl, Felix Kopp, Peter B. Noël, Franz Pfeiffer, Laurent Demaret, and Tobias Lasser

Purpose. Reconstruction of x-ray computed tomography (CT) data remains a mathematically challenging problem in medical imaging. Complementing the standard analytical reconstruction methods, sparse regularization is growing in importance, as it allows inclusion of prior knowledge. The paper presents a method for sparse regularization based on the curvelet frame for the application to iterative reconstruction in x-ray computed tomography. *Methods*. In this work, the authors present an iterative reconstruction approach based on the alternating direction method of multipliers using curvelet sparse regularization. *Results*. Evaluation of the method is performed on a specifically crafted numerical phantom dataset to highlight the method's strengths. Additional evaluation is performed on two real datasets from commercial scanners with different noise characteristics, a clinical bone sample acquired in a micro-CT and a human abdomen scanned in a diagnostic CT. The results clearly illustrate that curvelet sparse regularization has characteristic strengths. In particular, it improves the restoration and resolution of highly directional, high contrast features with smooth contrast variations. The authors also compare this approach to the popular technique of total variation and to traditional filtered backprojection. *Conclusion*. The authors conclude that curvelet sparse regularization is able to improve reconstruction quality by reducing noise while preserving highly directional features.

Medical Physics, 42.4, (2015)

Bibliography

[31] W. van Aarle, W. J. Palenstijn, J. De Beenhouwer, T. Altantzis, S. Bals, K. J. Batenburg, and J. Sijbers. "The ASTRA Toolbox: A platform for advanced algorithm development in electron tomography". In: *Ultramicroscopy* 157 (Oct. 2015), pp. 35–47. (Cited on p. 63)
DOI: 10.1016/j.ultramic.2015.05.002
URL: http://linkinghub.elsevier.com/retrieve/pii/S0304399115001060.

[32] I. Aganj, C. Lenglet, and G. Sapiro. "ODF Maxima Extraction in Spherical Harmonic Representation via Analytical Search Space Reduction". In: *Medical Image Computing and Computer-Assisted Intervention – MICCAI 2010*. Berlin, Heidelberg: Springer, Sept. 2010, pp. 84–91. ISBN: 978-3-642-15744-8. (Cited on p. 130)
DOI: 10.1007/978-3-642-15745-5_11
URL: http://link.springer.com/10.1007/978-3-642-15745-5_11.

[33] I. Aganj, C. Lenglet, G. Sapiro, E. Yacoub, K. Ugurbil, and N. Harel. "Reconstruction of the orientation distribution function in single- and multiple-shell q-ball imaging within constant solid angle." In: *Magnetic Resonance in Medicine* 64.2 (Aug. 2010), pp. 554–566. (Cited on p. 130)
DOI: 10.1002/mrm.22365
URL: http://doi.wiley.com/10.1002/mrm.22365.

[34] A. L. Alexander, K. M. Hasan, M. Lazar, J. S. Tsuruda, and D. L. Parker. "Analysis of partial volume effects in diffusion-tensor MRI". In: *Magnetic Resonance in Medicine* 45.5 (2001), pp. 770–780. (Cited on p. 16)
DOI: 10.1002/mrm.1105
URL: http://doi.wiley.com/10.1002/mrm.1105.

[35] D. C. Alexander. "Multiple-Fiber Reconstruction Algorithms for Diffusion MRI". In: *Annals of the New York Academy of Sciences* 1064.1 (Dec. 2005), pp. 113–133. (Cited on p. 130)
DOI: 10.1196/annals.1340.018
URL: http://doi.wiley.com/10.1196/annals.1340.018.

[36] A. L. Alexander, J. E. Lee, M. Lazar, R. Boudos, M. B. DuBray, T. R. Oakes, J. N. Miller, J. Lu, E.-K. Jeong, W. M. McMahon, E. D. Bigler, and J. E. Lainhart. "Diffusion tensor imaging of the corpus callosum in Autism". In: *NeuroImage* 34.1 (Jan. 2007), pp. 61–73. (Cited on p. 16)
DOI: 10.1016/j.neuroimage.2006.08.032
URL: http://linkinghub.elsevier.com/retrieve/pii/S1053811906008901.

[37] J. Als-Nielsen and D. McMorrow. *Elements of Modern X-ray Physics*. Als-Nielsen/Elements. Hoboken, NJ, USA: John Wiley & Sons, Inc., Mar. 2011. ISBN: 9780470973950. (Cited on pp. 5, 8)
DOI: 10.1002/9781119998365
URL: http://doi.wiley.com/10.1002/9781119998365.

[38] J. Amanatides and A. Woo. "A fast voxel traversal algorithm for ray tracing". In: *Eurographics* (1987). (Cited on p. 72)
DOI: 10.2312/egtp.19871000
URL: https://diglib.eg.org/handle/10.2312/egtp19871000.

[39] M. Ando, K. Yamasaki, F. Toyofuku, H. Sugiyama, C. Ohbayashi, G. Li, L. Pan, X. Jiang, W. Pattanasiriwisawa, D. Shimao, E. Hashimoto, T. Kimura, M. Tsuneyoshi, E. Ueno, K. Tokumori, A. Maksimenko, Y. Higashida, and M. Hirano. "Attempt at Visualizing Breast Cancer with X-ray Dark Field Imaging". In: *Japanese Journal of Applied Physics* 44.4L (Apr. 2005), pp. L528–L531. (Cited on p. 13)
DOI: 10.1143/JJAP.44.L528
URL: http://stacks.iop.org/1347-4065/44/L528.

[40] R. Andersson, L. F. v. Heijkamp, I. M. d. Schepper, W. G. Bouwman, and IUCr. "Analysis of spin-echo small-angle neutron scattering measurements". In: *Journal of Applied Crystallography* 41.5 (Oct. 2008), pp. 868–885. (Cited on pp. 15, 47)
DOI: 10.1107/S0021889808026770
URL: http://scripts.iucr.org/cgi-bin/paper?S0021889808026770.

[41] A. Andersen. "Simultaneous Algebraic Reconstruction Technique (SART): A superior implementation of the ART algorithm". In: *Ultrasonic Imaging* 6.1 (Jan. 1984), pp. 81–94. (Cited on pp. 15, 42, 87)
DOI: 10.1016/0161-7346(84)90008-7
URL: http://linkinghub.elsevier.com/retrieve/pii/0161734684900087.

[42] G. Anton, F. Bayer, M. W. Beckmann, J. Durst, P. A. Fasching, W. Haas, A. Hartmann, T. Michel, G. Pelzer, M. Radicke, C. Rauh, J. Rieger, A. Ritter, R. Schulz-Wendtland, M. Uder, D. L. Wachter, T. Weber, E. Wenkel, and L. Wucherer. "Grating-based darkfield imaging of human breast tissue". In: *Zeitschrift für Medizinische Physik* 23.3 (Sept. 2013), pp. 228–235. (Cited on p. 13)
DOI: 10.1016/j.zemedi.2013.01.001
URL: http://linkinghub.elsevier.com/retrieve/pii/S0939388913000032.

[43] F. Arfelli, V. Bonvicini, A. Bravin, G. Cantatore, E. Castelli, L. D. Palma, M. Di Michiel, M. Fabrizioli, R. Longo, R. H. Menk, A. Olivo, S. Pani, D. Pontoni, P. Poropat, M. Prest, A. Rashevsky, M. Ratti, L. Rigon, G. Tromba, A. Vacchi, E. Vallazza, and F. Zanconati. "Mammography with Synchrotron Radiation: Phase-Detection Techniques". In: *Radiology* 215.1 (2000), pp. 286–293
DOI: 10.1148/radiology.215.1.r00ap10286
URL: http://pubs.rsna.org/doi/abs/10.1148/radiology.215.1.r00ap10286.

[44] F. Arfelli, L. Rigon, and R. H. Menk. "Microbubbles as x-ray scattering contrast agents using analyzer-based imaging". In: *Physics in Medicine and Biology* 55.6 (Feb. 2010), pp. 1643–1658. (Cited on pp. 10, 14)
DOI: 10.1088/0031-9155/55/6/008
URL: http://stacks.iop.org/0031-9155/55/i=6/a=008?key=crossref.1ab98b0e6c7a0997e98cb7bc2033badb.

[45] V. Arsigny, P. Fillard, X. Pennec, and N. Ayache. "Fast and Simple Calculus on Tensors in the Log-Euclidean Framework". In: *Medical Image Computing and Computer-Assisted Intervention – MICCAI 2005*. Berlin, Heidelberg: Springer, Oct. 2005, pp. 115–122. ISBN: 978-3-540-29327-9. (Cited on p. 101)
DOI: 10.1007/11566465_15
URL: https://link.springer.com/chapter/10.1007/11566465_15.

[46] V. Arsigny, P. Fillard, X. Pennec, and N. Ayache. "Log-Euclidean metrics for fast and simple calculus on diffusion tensors." In: *Magnetic Resonance in Medicine* 56.2 (2006), pp. 411–421. (Cited on p. 101)
DOI: 10.1002/mrm.20965
URL: http://doi.wiley.com/10.1002/mrm.20965.

[47] Y. Assaf and O. Pasternak. "Diffusion Tensor Imaging (DTI)-based White Matter Mapping in Brain Research: A Review". In: *Journal of Molecular Neuroscience* 34.1 (Sept. 2007), pp. 51–61. (Cited on p. 16)
DOI: 10.1007/s12031-007-0029-0
URL: http://link.springer.com/10.1007/s12031-007-0029-0.

[48] H.-E. Assemlal, D. Tschumperlé, L. Brun, and K. Siddiqi. "Recent advances in diffusion MRI modeling: Angular and radial reconstruction". In: *Medical Image Analysis* 15.4 (Apr. 2017), pp. 369–396. (Cited on p. 16)
DOI: 10.1016/j.media.2011.02.002
URL: http://dx.doi.org/10.1016/j.media.2011.02.002.

[49] K. Atkinson and W. Han. *Spherical Harmonics and Approximations on the Unit Sphere: An Introduction*. Vol. 2044. Lecture Notes in Mathematics. Berlin, Heidelberg: Springer, 2012. ISBN: 978-3-642-25982-1. (Cited on p. 53)
DOI: 10.1007/978-3-642-25983-8
URL: http://link.springer.com/10.1007/978-3-642-25983-8.

[50] L. J. Bao, Y. M. Zhu, W. Y. Liu, P. Croisille, Z. B. Pu, M. Robini, and I. E. Magnin. "Denoising human cardiac diffusion tensor magnetic resonance images using sparse representation combined with segmentation". In: *Physics in Medicine and Biology* 54.6 (Mar. 2009), pp. 1435–1456. (Cited on p. 101)
DOI: 10.1088/0031-9155/54/6/004
URL: http://iopscience.iop.org/article/10.1088/0031-9155/54/6/004.

[51] O. Barkan, J. Weill, A. Averbuch, and S. Dekel. "Adaptive Compressed Tomography Sensing". In: *2013 IEEE Conference on Computer Vision and Pattern Recognition (CVPR)*. IEEE, June 2013, pp. 2195–2202. ISBN: 978-0-7695-4989-7. (Cited on p. 40)
DOI: 10.1109/CVPR.2013.285
URL: http://ieeexplore.ieee.org/lpdocs/epic03/wrapper.htm?arnumber=6619129.

[52] J. Barzilai and J. Borwein. "Two-point step size gradient methods". In: *IMA Journal of Numerical Analysis* 8.1 (1988), pp. 141–148. (Cited on p. 43)
DOI: 10.1093/imanum/8.1.141
URL: http://imajna.oxfordjournals.org/content/8/1/141.short.

[53] S. Basu, T. Fletcher, and R. Whitaker. "Rician Noise Removal in Diffusion Tensor MRI". In: *Medical Image Computing and Computer-Assisted Intervention – MICCAI 2006*. Berlin, Heidelberg: Springer, Oct. 2006, pp. 117–125. ISBN: 978-3-540-44707-8. (Cited on pp. 16, 101)
DOI: 10.1007/11866565_15
URL: https://link.springer.com/chapter/10.1007/11866565_15.

[54] P. J. Basser, J. Mattiello, and D. LeBihan. "MR diffusion tensor spectroscopy and imaging." In: *Biophysical journal* 66.1 (Jan. 1994), pp. 259–267. (Cited on pp. 16, 51, 131)
DOI: 10.1016/S0006-3495(94)80775-1
URL: http://linkinghub.elsevier.com/retrieve/pii/S0006349594807751.

[55] T. Baum, E. Eggl, A. Malecki, F. Schaff, G. Potdevin, O. Gordijenko, E. G. Garcia, R. Burgkart, E. J. Rummeny, P. B. Noël, J. S. Bauer, and F. Pfeiffer. "X-ray Dark-Field Vector Radiography—A Novel Technique for Osteoporosis Imaging". In: *Journal of Computer Assisted Tomography* 39.2 (2015), pp. 286–289. (Cited on pp. 14, 47)
DOI: 10.1097/RCT.0000000000000192
URL: http://content.wkhealth.com/linkback/openurl?sid=WKPTLP:landingpage&an=00004728-201503000-00026.

[56] F. Bayer, K. Gödel, W. Haas, J. Rieger, A. Ritter, T. Weber, L. Wucherer, J. Durst, T. Michel, and G. Anton. "Spectroscopic dark-field imaging using a grating-based Talbot-Lau interferometer". In: *SPIE Medical Imaging*. Ed. by N. J. Pelc, R. M. Nishikawa, and B. R. Whiting. SPIE, Feb. 2012, pp. 83135I–83135I–7. (Cited on p. 49)
DOI: 10.1117/12.911640
URL: http://proceedings.spiedigitallibrary.org/proceeding.aspx?doi=10.1117/12.911640.

[57] F. Bayer, S. Zabler, C. Brendel, G. Pelzer, J. Rieger, A. Ritter, T. Weber, T. Michel, and G. Anton. "Projection angle dependence in grating-based X-ray dark-field imaging of ordered structures". In: *Optics Express* 21.17 (Aug. 2013), pp. 19922–19933. (Cited on p. 14)
DOI: 10.1364/OE.21.019922
URL: http://www.opticsinfobase.org/vjbo/fulltext.cfm?uri=oe-21-17-19922&id=260341.

[58] F. L. Bayer, S. Hu, A. Maier, T. Weber, G. Anton, T. Michel, and C. P. Riess. “Reconstruction of scalar and vectorial components in X-ray dark-field tomography.” In: *Proceedings of the National Academy of Sciences of the United States of America* 111.35 (Sept. 2014), pp. 12699–12704. (Cited on p. 15)
DOI: 10.1073/pnas.1321080111
URL: http://www.pnas.org/cgi/doi/10.1073/pnas.1321080111.

[59] M. Bech. “X-ray imaging with a grating interferometer”. PhD thesis. Copenhagen, July 2009. (Cited on p. 12).

[60] A. Beck and M. Teboulle. “Fast Gradient-Based Algorithms for Constrained Total Variation Image Denoising and Deblurring Problems”. In: *IEEE Transactions on Image Processing* 18.11 (Nov. 2009), pp. 2419–2434. (Cited on p. 39)
DOI: 10.1109/TIP.2009.2028250
URL: http://ieeexplore.ieee.org/lpdocs/epic03/wrapper.htm?arnumber=5173518.

[61] A. Beck and M. Teboulle. “A fast iterative shrinkage-thresholding algorithm for linear inverse problems”. In: *SIAM Journal on Imaging Sciences* 2.1 (Jan. 2009), pp. 183–202. (Cited on p. 88)
DOI: 10.1137/080716542
URL: http://epubs.siam.org/doi/abs/10.1137/080716542.

[62] M. Bech, O. Bunk, T. Donath, R. Feidenhans’l, C. David, and F. Pfeiffer. “Quantitative x-ray dark-field computed tomography”. In: *Physics in Medicine and Biology* 55.18 (Aug. 2010), pp. 5529–5539. (Cited on p. 13)
DOI: 10.1088/0031-9155/55/18/017
URL: http://stacks.iop.org/0031-9155/55/i=18/a=017?key=crossref.698954954add6a39544b554436f99ede.

[63] M. Bech, S. Schleede, G. Potdevin, K. Achterhold, O. Bunk, T. H. Jensen, R. Loewen, R. Ruth, and F. Pfeiffer. “Experimental validation of image contrast correlation between ultra-small-angle X-ray scattering and grating-based dark-field imaging using a laser-driven compact X-ray source”. In: *Photonics and Lasers in Medicine* 1.1 (2012). (Cited on p. 13)
DOI: 10.1515/plm-2011-0012
URL: http://www.degruyter.com/view/j/plm.2012.1.issue-1/plm-2011-0012/plm-2011-0012.xml.

[64] M. Bech, A. Tapfer, A. Velroyen, A. Yaroshenko, B. Pauwels, J. Hostens, P. Bruyndonckx, A. Sasov, and F. Pfeiffer. “In-vivo dark-field and phase-contrast x-ray imaging.” In: *Scientific reports* 3 (2013), p. 3209. (Cited on p. 13)
DOI: 10.1038/srep03209
URL: http://www.nature.com/doifinder/10.1038/srep03209.

[65] L. Bello, A. Gambini, A. Castellano, G. Carrabba, F. Acerbi, E. Fava, C. Giussani, M. Cadioli, V. Blasi, A. Casarotti, C. Papagno, A. K. Gupta, S. Gaini, G. Scotti, and A. Falini. “Motor and language DTI Fiber Tracking combined with intraoperative subcortical mapping for surgical removal of gliomas”. In: *NeuroImage* 39.1 (Jan. 2008), pp. 369–382. (Cited on p. 16)
DOI: 10.1016/j.neuroimage.2007.08.031
URL: http://linkinghub.elsevier.com/retrieve/pii/S1053811907007549.

[66] M. Benning, C. Brune, M. Burger, and J. Müller. “Higher-Order TV Methods—Enhancement via Bregman Iteration”. In: *Journal of Scientific Computing* 54.2-3 (Oct. 2012), pp. 269–310. (Cited on p. 39)
DOI: 10.1007/s10915-012-9650-3
URL: http://link.springer.com/10.1007/s10915-012-9650-3.

[67] L. Birnbacher, M. Willner, A. Velroyen, M. Marschner, A. Hipp, J. Meiser, F. Koch, T. Schröter, D. Kunka, J. Mohr, F. Pfeiffer, and J. Herzen. “Experimental Realisation of High-sensitivity Laboratory X-ray Grating-based Phase-contrast Computed Tomography.” In: *Scientific reports* 6 (Apr. 2016), p. 24022. (Cited on pp. 134, 135)
DOI: 10.1038/srep24022
URL: http://eutils.ncbi.nlm.nih.gov/entrez/eutils/elink.fcgi?dbfrom=pubmed&id=27040492&retmode=ref&cmd=prlinks.

[68] U. Bonse and M. Hart. “AN X-RAY INTERFEROMETER”. In: *Applied physics letters* 6.8 (Apr. 1965), pp. 155–156. (Cited on pp. 4, 10)
DOI: 10.1063/1.1754212
URL: http://aip.scitation.org/doi/10.1063/1.1754212.

[69] C. Bouman and K. Sauer. “A generalized Gaussian image model for edge-preserving MAP estimation”. In: *IEEE Transactions on Image Processing* 2.3 (July 1993), pp. 296–310. (Cited on p. 41)
DOI: 10.1109/83.236536
URL: http://ieeexplore.ieee.org/document/236536/.

[70] S. Boyd and L. Vandenberghe. *Convex Optimization*. New York, NY, USA: Cambridge University Press, 2004. ISBN: 0521833787. (Cited on pp. 43, 63)
URL: http://portal.acm.org/citation.cfm?id=993483&coll=DL&dl=GUIDE&CFID=424121886&CFTOKEN=62934953.

[71] S. Boyd. “Distributed Optimization and Statistical Learning via the Alternating Direction Method of Multipliers”. In: *Foundations and Trends® in Machine Learning* 3.1 (July 2011), pp. 1–122. (Cited on pp. 40, 45)
DOI: 10.1561/2200000016
URL: http://www.nowpublishers.com/product.aspx?product=MAL&doi=2200000016.

[72] J. G. Brankov, Y. Yang, and M. N. Wernick. “Tomographic Image Reconstruction Based on a Content-Adaptive Mesh Model”. In: *IEEE Transactions on Medical Imaging* 23.2 (Feb. 2004), pp. 202–212. (Cited on pp. 66, 72)
DOI: 10.1109/TMI.2003.822822
URL: http://ieeexplore.ieee.org/lpdocs/epic03/wrapper.htm?arnumber=1263610.

[73] J. G. Brankov, Y. Yang, and M. N. Wernick. “Spatiotemporal processing of gated cardiac SPECT images using deformable mesh modeling”. In: *Medical Physics* 32.9 (2005), pp. 2839–2849. (Cited on p. 72)
DOI: 10.1118/1.2013027
URL: http://scitation.aip.org/content/aapm/journal/medphys/32/9/10.1118/1.2013027.

[74] R. N. Bracewell. “Strip Integration in Radio Astronomy”. In: *Aust. J. Phys.* 9.2 (1956), pp. 198–217. (Cited on p. 9)
DOI: 10.1071/PH560198
URL: http://www.publish.csiro.au/ph/PH560198.

[75] B. Brendel, M. von Teuffenbach, P. B. Noël, F. Pfeiffer, and T. Koehler. “Penalized maximum likelihood reconstruction for x-ray differential phase-contrast tomography”. In: *Medical Physics* 43.1 (Dec. 2015), pp. 188–194. (Cited on p. 121)
DOI: 10.1118/1.4938067
URL: http://doi.wiley.com/10.1118/1.4938067.

[76] A. Buades, B. Coll, and J. M. Morel. “The staircasing effect in neighborhood filters and its solution”. In: *IEEE Transactions on Image Processing* 15.6 (June 2006), pp. 1499–1505. (Cited on p. 39)
DOI: 10.1109/TIP.2006.871137
URL: http://ieeexplore.ieee.org/lpdocs/epic03/wrapper.htm?arnumber=1632203.

[77] O. Bunk, M. Bech, T. H. Jensen, R. Feidenhans’l, T. Binderup, A. Menzel, and F. Pfeiffer. “Multimodal x-ray scatter imaging”. In: *New Journal of Physics* 11.12 (Dec. 2009), p. 123016. (Cited on p. 10)
DOI: 10.1088/1367-2630/11/12/123016
URL: http://iopscience.iop.org/1367-2630/11/12/123016/fulltext/.

[78] T. M. Buzug. *Computed Tomography*. From Photon Statistics to Modern. Berlin, Heidelberg: Springer, 2008. ISBN: 978-3-540-39407-5. (Cited on pp. 5, 6, 8, 9, 25, 27, 33, 41)
DOI: 10.1007/978-3-540-39408-2
URL: http://www.springer.com/us/book/9783642072574.

[79] E. J. Candès and D. L. Donoho. “Curvelets and reconstruction of images from noisy radon data”. In: *Wavelet Applications in Signal and Image Processing VIII*. Ed. by A. Aldroubi, A. F. Laine, and M. A. Unser. SPIE, 2000, p. 108. (Cited on p. 42)
DOI: 10.1117/12.408569
URL: http://proceedings.spiedigitallibrary.org/proceeding.aspx?doi=10.1117/12.408569.

[80] E. J. Candès and D. Donoho. “Recovering edges in ill-posed inverse problems: Optimality of curvelet frames”. In: *Annals of statistics* 30.3 (2002), pp. 784–842. (Cited on p. 40)
DOI: 10.1214/aos/1028674842
URL: http://www.jstor.org/stable/10.2307/2699979.

[81] E. J. Candès and D. Donoho. “New tight frames of curvelets and optimal representations of objects with piecewise C2 singularities”. In: *Communications on pure and applied mathematics* 57.2 (2004), pp. 219–266. (Cited on p. 40)
URL: http://onlinelibrary.wiley.com/doi/10.1002/cpa.10116/abstract.

[82] E. J. Candès and D. L. Donoho. “Continuous Curvelet Transform: II. Discretization and Frames”. In: *Applied and Computational Harmonic Analysis* 19.2 (Mar. 2005), pp. 198–222. (Cited on p. 40)
DOI: 10.1016/j.acha.2005.02.004
URL: http://www.sciencedirect.com/science/article/pii/S1063520305000205.

[83] E. J. Candès and D. Donoho. “Continuous Curvelet Transform: I. Resolution of the wavefront set”. In: *Applied and Computational Harmonic Analysis* 19.2 (Mar. 2005), pp. 162–197. (Cited on p. 40)
DOI: 10.1016/j.acha.2005.02.003
URL: http://linkinghub.elsevier.com/retrieve/pii/S1063520305000199.

[84] E. J. Candès, J. Romberg, and T. Tao. “Robust uncertainty principles: exact signal reconstruction from highly incomplete frequency information”. In: *IEEE Transactions on Information Theory* 52.2 (Feb. 2006), pp. 489–509. (Cited on p. 39)
DOI: 10.1109/TIT.2005.862083
URL: http://ieeexplore.ieee.org/lpdocs/epic03/wrapper.htm?arnumber=1580791.

[85] E. J. Candès. “Ridgelets: Theory and Applications”. PhD thesis. 1998. (Cited on p. 40).

[86] C. A. Castaño-Moraga, C. Lenglet, R. Deriche, and J. Ruiz-Alzola. “A Riemannian approach to anisotropic filtering of tensor fields”. In: *Signal Processing* 87.2 (Feb. 2007), pp. 263–276. (Cited on p. 101)
DOI: 10.1016/j.sigpro.2006.02.049
URL: http://linkinghub.elsevier.com/retrieve/pii/S0165168406001708.

[87] A. Cedola, M. Mastrogiacomo, S. Lagomarsino, R. Cancedda, C. Giannini, A. Guagliardi, M. Ladisa, M. Burghammer, F. Rustichelli, and V. Komlev. “Orientation of mineral crystals by collagen fibers during in vivo bone engineering: An X-ray diffraction imaging study”. In: *Spectrochimica Acta Part B: Atomic Spectroscopy* 62.6-7 (July 2007), pp. 642–647. (Cited on p. 10)
DOI: 10.1016/j.sab.2007.02.015
URL: http://linkinghub.elsevier.com/retrieve/pii/S058485470700047X.

[88] M. Chabior, T. Donath, C. David, M. Schuster, C. Schroer, and F. Pfeiffer. “Signal-to-noise ratio in x ray dark-field imaging using a grating interferometer”. In: *Journal of Applied Physics* 110.5 (Sept. 2011), p. 053105. (Cited on pp. 16, 41)
DOI: 10.1063/1.3630051
URL: http://scitation.aip.org/content/aip/journal/jap/110/5/10.1063/1.3630051.

[89] A. Chambolle and T. Pock. “A First-Order Primal-Dual Algorithm for Convex Problems with Applications to Imaging”. In: *Journal of Mathematical imaging and vision* 40.1 (May 2011), pp. 120–145. (Cited on p. 44)
DOI: 10.1007/s10851-010-0251-1
URL: http://dx.doi.org/10.1007/s10851-010-0251-1.

[90] A. Chambolle and P.-L. Lions. “Image recovery via total variation minimization and related problems”. In: *Numerische Mathematik* 76.2 (Apr. 1997), pp. 167–188. (Cited on p. 39)
DOI: 10.1007/s002110050258
URL: http://link.springer.com/10.1007/s002110050258.

[91] T. F. Chan, G. H. Golub, and P. Mulet. “A nonlinear primal-dual method for total variation-based image restoration”. In: *SIAM Journal on Scientific Computing* 20.6 (1999), pp. 1964–1977. (Cited on p. 44)
URL: http://epubs.siam.org/doi/abs/10.1137/S1064827596299767.

[92] D. Chapman, W. Thomlinson, R. E. Johnston, D. Washburn, E. Pisano, N. Gmür, Z. Zhong, R. Menk, F. Arfelli, and D. Sayers. “Diffraction enhanced x-ray imaging”. In: *Physics in Medicine and Biology* 42.11 (Jan. 1999), pp. 2015–2025. (Cited on p. 10)
DOI: 10.1088/0031-9155/42/11/001
URL: http://stacks.iop.org/0031-9155/42/i=11/a=001?key=crossref.5f0bd0c952047e87f82b88cf73a2bde4.

[93] C. Chefd'hotel, D. Tschumperle, R. Deriche, and O. Faugeras. "Constrained Flows of Matrix-Valued Functions: Application to Diffusion Tensor Regularization". In: *Computer Vision — ECCV 2002*. Berlin, Heidelberg: Springer, May 2002, pp. 251–265. ISBN: 978-3-540-43745-1. (Cited on p. 101)
DOI: 10.1007/3-540-47969-4_17
URL: https://link.springer.com/chapter/10.1007/3-540-47969-4_17.

[94] C. Chefd'hotel, D. Tschumperle, R. Deriche, and O. Faugeras. "Regularizing Flows for Constrained Matrix-Valued Images". In: *Journal of Mathematical imaging and vision* 20.1-2 (2004), pp. 147–162. (Cited on p. 101)
DOI: 10.1023/B:JMIV.0000011920.58935.9c
URL: https://link.springer.com/article/10.1023/B:JMIV.0000011920.58935.9c.

[95] J. Cheng, A. Ghosh, T. Jiang, and R. Deriche. "A Riemannian Framework for Orientation Distribution Function Computing". In: *Medical Image Computing and Computer-Assisted Intervention – MICCAI 2011*. Berlin, Heidelberg: Springer, 2009, pp. 911–918. ISBN: 978-3-642-04267-6. (Cited on p. 120)
DOI: 10.1007/978-3-642-04268-3_112
URL: http://link.springer.com/10.1007/978-3-642-04268-3_112.

[96] G.-H. Chen, N. Bevins, J. Zambelli, and Z. Qi. "Small-angle scattering computed tomography (SAS-CT) using a Talbot-Lau interferometer and a rotating anode x-ray tube: theory and experiments". In: *Optics Express* 18.12 (2010), p. 12960. (Cited on p. 13)
DOI: 10.1364/OE.18.012960
URL: http://www.opticsinfobase.org/abstract.cfm?URI=oe-18-12-12960.

[97] G.-H. Chen, J. Tang, and S. Leng. "Prior image constrained compressed sensing (PICCS): A method to accurately reconstruct dynamic CT images from highly undersampled projection data sets". In: *Medical Physics* 35.2 (Nov. 2016), pp. 660–663. (Cited on p. 39)
DOI: 10.1118/1.2836423
URL: http://doi.wiley.com/10.1118/1.2836423.

[98] C.-Y. Chou, M. A. Anastasio, J. G. Brankov, M. N. Wernick, E. M. Brey, D. M. Connor Jr, and Z. Zhong. "An extended diffraction-enhanced imaging method for implementing multiple-image radiography". In: *Physics in Medicine and Biology* 52.7 (Mar. 2007), pp. 1923–1945. (Cited on p. 10)
DOI: 10.1088/0031-9155/52/7/011
URL: http://stacks.iop.org/0031-9155/52/i=7/a=011?key=crossref.d16f946be21a8f2d14963ec571998b04.

[99] O. Christensen. *An Introduction to Frames and Riesz Bases*. Applied and Numerical Harmonic Analysis. Boston, MA: Birkhäuser Boston, 2003. ISBN: 978-1-4612-6500-9. (Cited on p. 39)
DOI: 10.1007/978-0-8176-8224-8
URL: http://link.springer.com/10.1007/978-0-8176-8224-8.

[100] J. Cohen-Adad, M. Descoteaux, S. Rossignol, R. D. Hoge, R. Deriche, and H. Benali. "Detection of multiple pathways in the spinal cord using q-ball imaging". In: *NeuroImage* 42.2 (Aug. 2008), pp. 739–749. (Cited on p. 121)
DOI: 10.1016/j.neuroimage.2008.04.243
URL: http://linkinghub.elsevier.com/retrieve/pii/S1053811908005119.

[101] J. Cohen-Adad, M. Descoteaux, and L. L. Wald. "Quality assessment of high angular resolution diffusion imaging data using bootstrap on Q-ball reconstruction." In: *Journal of magnetic resonance imaging : JMRI* 33.5 (May 2011), pp. 1194–1208. (Cited on p. 121)
DOI: 10.1002/jmri.22535
URL: http://doi.wiley.com/10.1002/jmri.22535.

[102] F. Colonna, G. Easley, K. Guo, and D. Labate. "Radon transform inversion using the shearlet representation". In: *Applied and Computational Harmonic Analysis* 29.2 (2010), pp. 232–250. (Cited on p. 42)
URL: http://www.sciencedirect.com/science/article/pii/S106352030900116X.

[103] P. L. Combettes and J.-C. Pesquet. "Proximal Splitting Methods in Signal Processing". In: *Fixed-Point Algorithms for Inverse Problems in Science and Engineering*. Ed. by H. H. Bauschke, R. S. Burachik, P. L. Combettes, V. Elser, D. R. Luke, and H. Wolkowicz. New York, NY: Springer, May 2011, pp. 185–212. ISBN: 978-1-4419-9568-1. (Cited on pp. 37, 40, 44, 88)
DOI: 10.1007/978-1-4419-9569-8_10
URL: http://link.springer.com/10.1007/978-1-4419-9569-8_10.

[104] W. Cong, F. Pfeiffer, M. Bech, and G. Wang. "X-ray dark-field imaging modeling". In: *Journal of the Optical Society of America A* 29.6 (June 2012), pp. 908–912. (Cited on p. 13)
DOI: 10.1364/JOSAA.29.000908
URL: http://www.opticsinfobase.org/josaa/abstract.cfm?uri=josaa-29-6-908.

[105] D. M. Connor and Z. Zhong. "Diffraction-Enhanced Imaging". In: *Current Radiology Reports* 2.7 (2014), pp. 1–11. (Cited on p. 10)
DOI: 10.1007/s40134-014-0055-y
URL: http://link.springer.com/article/10.1007/s40134-014-0055-y/fulltext.html.

[106] A. M. Cormack. "Representation of a Function by Its Line Integrals, with Some Radiological Applications". In: *Journal of Applied Physics* 34.9 (1963), p. 2722. (Cited on pp. 4, 9, 28)
DOI: 10.1063/1.1729798
URL: http://scitation.aip.org/content/aip/journal/jap/34/9/10.1063/1.1729798.

[107] A. M. Cormack. "Representation of a Function by Its Line Integrals, with Some Radiological Applications. II". In: *Journal of Applied Physics* 35.10 (1964), pp. 2908–2913. (Cited on pp. 4, 9, 28)
DOI: 10.1063/1.1713127
URL: http://scitation.aip.org/content/aip/journal/jap/35/10/10.1063/1.1713127.

[108] A. M. Cormack. "EARLY TWO-DIMENSIONAL RECONSTRUCTION AND RECENT TOPICS STEMMING FROM IT". In: *Nobel Lecture* (Dec. 1979). (Cited on p. 4).

[109] A. Dabravolski, E. Janssens, F. Bleichrodt, J. De Beenhouwer, J. Sijbers, J. Cant, K. J. Batenburg, W. J. Palenstijn, and W. van Aarle. “Fast and flexible X-ray tomography using the ASTRA toolbox”. In: *Optics Express* 24.22 (Oct. 2016), pp. 25129–25147. (Cited on p. 63)
DOI: 10.1364/OE.24.025129
URL: https://www.osapublishing.org/viewmedia.cfm?uri=oe-24-22-25129&seq=0&html=true.

[110] I. Daubechies, B. Han, A. Ron, and Z. Shen. “Framelets: MRA-based constructions of wavelet frames”. In: *Applied and Computational Harmonic Analysis* 14.1 (Jan. 2003), pp. 1–46. (Cited on p. 39)
DOI: 10.1016/S1063-5203(02)00511-0
URL: http://linkinghub.elsevier.com/retrieve/pii/S1063520302005110.

[111] I. Daubechies, M. Defrise, and C. De Mol. “An iterative thresholding algorithm for linear inverse problems with a sparsity constraint”. In: *Communications on pure and applied mathematics* 57.11 (2004), pp. 1413–1457. (Cited on pp. 39, 88)
URL: http://onlinelibrary.wiley.com/doi/10.1002/cpa.20042/abstract (Visited on May 27, 2017).

[112] R. Dautray and J.-L. Lions. *Mathematical Analysis and Numerical Methods for Science and Technology*. Volume 2 Functional and Variational Methods. Berlin, Heidelberg: Springer, 1988. ISBN: 978-3-540-66098-9. (Cited on p. 37)
DOI: 10.1007/978-3-642-61566-5
URL: http://link.springer.com/10.1007/978-3-642-61566-5.

[113] I. Daubechies. *Ten lectures on wavelets*. Philadelphia, PA, USA: Society for Industrial and Applied Mathematics, 1992. ISBN: 0-89871-274-2. (Cited on p. 39)
URL: http://portal.acm.org/citation.cfm?id=130655&coll=DL&dl=GUIDE&CFID=474859817&CFTOKEN=43080706.

[114] T. J. Davis, D. Gao, T. E. Gureyev, A. W. Stevenson, and S. W. Wilkins. “Phase-contrast imaging of weakly absorbing materials using hard X-rays”. In: 373.6515 (Feb. 1995), pp. 595–598. (Cited on p. 10)
DOI: 10.1038/373595a0
URL: http://www.nature.com.eaccess.ub.tum.de/nature/journal/v373/n6515/abs/373595a0.html.

[115] M. De Felici, R. Felici, C. Ferrero, A. Tartari, M. Gambaccini, and S. Finet. “Structural characterization of the human cerebral myelin sheath by small angle x-ray scattering”. In: *Physics in Medicine and Biology* 53.20 (Sept. 2008), pp. 5675–5688. (Cited on p. 10)
DOI: 10.1088/0031-9155/53/20/007
URL: http://stacks.iop.org/0031-9155/53/i=20/a=007?key=crossref.42bed42e9b98a922aca088a30bb43dcf.

[116] S. R. Deans. “Radon and Abel Transforms”. In: *The Transforms and Applications Handbook*. CRC Press, Mar. 2000. ISBN: 978-0-8493-8595-7. (Cited on pp. 25, 27)
DOI: 10.1201/9781420036756.ch8
URL: http://www.crcnetbase.com/doi/abs/10.1201/9781420036756.ch8.

[117] M. Debatin, P. Zygmanski, D. Stsepankou, and J. Hesser. “CT reconstruction from few-views by Anisotropic Total Variation minimization”. In: *Nuclear Science Symposium, 1998. Conference Record. 1998 IEEE*. IEEE, 2012, pp. 2295–2296. ISBN: 978-1-4673-2029-0. (Cited on p. 39)
DOI: 10.1109/NSSMIC.2012.6551521
URL: http://ieeexplore.ieee.org/lpdocs/epic03/wrapper.htm?arnumber=6551521.

[118] B. Delaunay. “Sur la sphere vide”. In: *Bulletin de l’Académie des Sciences de l’URSS* 7.793-800 (1934), pp. 1–2. (Cited on p. 123).

[119] P. Delsarte, J. M. Goethals, and J. J. Seidel. “Spherical codes and designs”. In: *Geometriae Dedicata* 6.3 (Sept. 1977), pp. 363–388. (Cited on p. 54)
DOI: 10.1007/BF03187604
URL: http://link.springer.com/10.1007/BF03187604.

[120] M. Descoteaux, E. Angelino, S. Fitzgibbons, and R. Deriche. “Regularized, fast, and robust analytical Q-ball imaging”. In: *Magnetic Resonance in Medicine* 58.3 (2007), pp. 497–510. (Cited on pp. 123, 130)
DOI: 10.1002/mrm.21277
URL: http://doi.wiley.com/10.1002/mrm.21277.

[121] H. Ding, H. Gao, B. Zhao, H.-M. Cho, and S. Molloi. “A high-resolution photon-counting breast CT system with tensor-framelet based iterative image reconstruction for radiation dose reduction”. In: *Physics in Medicine and Biology* 59.20 (Sept. 2014), pp. 6005–6017. (Cited on p. 40)
DOI: 10.1088/0031-9155/59/20/6005
URL: http://stacks.iop.org/0031-9155/59/i=20/a=6005?key=crossref.ac71168281b6353baf0ebf18433c53d8.

[122] M. N. Do and M. Vetterli. “The contourlet transform: an efficient directional multiresolution image representation”. In: *IEEE Transactions on Image Processing* 14.12 (2005), pp. 2091–2106. (Cited on p. 40)
URL: http://ieeexplore.ieee.org/document/1532309/.

[123] D. C. Dobson and F. Santosa. “Recovery of Blocky Images from Noisy and Blurred Data”. In: *SIAM Journal on Applied Mathematics* 56.4 (Aug. 1996), pp. 1181–1198. (Cited on p. 39)
DOI: 10.1137/S003613999427560X
URL: http://epubs.siam.org/doi/10.1137/S003613999427560X.

[124] D. Donoho. “Compressed sensing”. In: *IEEE Transactions on Information Theory* 52.4 (Apr. 2006), pp. 1289–1306. (Cited on p. 39)
DOI: 10.1109/TIT.2006.871582
URL: http://ieeexplore.ieee.org/document/1614066/.

[125] T. Donath, M. Chabior, F. Pfeiffer, O. Bunk, E. Reznikova, J. Mohr, E. Hempel, S. Popescu, M. Hoheisel, M. Schuster, J. Baumann, and C. David. “Inverse geometry for grating-based x-ray phase-contrast imaging”. In: *Journal of Applied Physics* 106.5 (Sept. 2009), p. 054703. (Cited on p. 11)
DOI: 10.1063/1.3208052
URL: http://scitation.aip.org/content/aip/journal/jap/106/5/10.1063/1.3208052.

[126] D. Donoho and I. M. Johnstone. “Threshold selection for wavelet shrinkage of noisy data”. In: *Proceedings of 16th Annual International Conference of the IEEE Engineering in Medicine and Biology Society IS - SN - VO - VL -*. IEEE, Nov. 1994, A24–A25 vol.1. ISBN: 0-7803-2050-6. (Cited on p. 39)
DOI: 10.1109/IEMBS.1994.412133
URL: http://ieeexplore.ieee.org/document/412133/.

[127] D. L. Donoho. “De-noising by soft-thresholding”. In: *IEEE Transactions on Information Theory* 41.3 (1995), pp. 613–627. (Cited on p. 39)
DOI: 10.1109/18.382009
URL: http://ieeexplore.ieee.org/document/382009/.

[128] D. L. Donoho. “Nonlinear Solution of Linear Inverse Problems by Wavelet–Vaguelette Decomposition”. In: *Applied and Computational Harmonic Analysis* 2.2 (1995), pp. 101–126. (Cited on p. 42)
DOI: 10.1006/acha.1995.1008
URL: http://www.sciencedirect.com/science/article/pii/S1063520385710081.

[129] Q. Du, V. Faber, and M. Gunzburger. “Centroidal Voronoi Tessellations: Applications and Algorithms”. In: *SIAM review* 41.4 (Aug. 2006), pp. 637–676. (Cited on pp. 54, 116)
DOI: 10.1137/S0036144599352836
URL: http://epubs.siam.org/doi/abs/10.1137/S0036144599352836.

[130] J. Dubois, L. Hertz-Pannier, G. Dehaene-Lambertz, Y. Cointepas, and D. Le Bihan. “Assessment of the early organization and maturation of infants’ cerebral white matter fiber bundles: A feasibility study using quantitative diffusion tensor imaging and tractography”. In: *NeuroImage* 30.4 (May 2006), pp. 1121–1132. (Cited on p. 16)
DOI: 10.1016/j.neuroimage.2005.11.022
URL: http://linkinghub.elsevier.com/retrieve/pii/S1053811905024535.

[131] J. Eckstein and D. P. Bertsekas. “On the Douglas—Rachford splitting method and the proximal point algorithm for maximal monotone operators”. In: *Mathematical Programming* 55.1-3 (Apr. 1992), pp. 293–318. (Cited on p. 45)
DOI: 10.1007/BF01581204
URL: http://link.springer.com/10.1007/BF01581204.

[132] M. Elad, P. Milanfar, and R. Rubinstein. “Analysis versus synthesis in signal priors”. In: *Inverse problems* 23.3 (June 2007), pp. 947–968. (Cited on p. 39)
DOI: 10.1088/0266-5611/23/3/007
URL: http://stacks.iop.org/0266-5611/23/i=3/a=007?key=crossref.96b0bf91086dfef74be06e66b3ad3a59.

[133] M. Elad and A. Feuer. “Restoration of a single superresolution image from several blurred, noisy, and undersampled measured images”. In: *IEEE Transactions on Image Processing* 6.12 (1997), pp. 1646–1658. (Cited on p. 63)
URL: http://ieeexplore.ieee.org/xpls/abs_all.jsp?arnumber=650118.

[134] H. W. Engl, M. Hanke, and A. Neubauer. *Regularization of Inverse Problems*. Dordrecht, Netherlands: Springer, 1996. ISBN: 978-0-7923-6140-4. (Cited on p. 35)
DOI: 10.1007/978-94-009-1740-8
URL: http://link.springer.com/10.1007/978-94-009-1740-8.

[135] A. Entezari, M. Nilchian, and M. Unser. “A Box Spline Calculus for the Discretization of Computed Tomography Reconstruction Problems”. In: *IEEE Transactions on Medical Imaging* 31.8 (Mar. 2012), pp. 1532–1541. (Cited on p. 66)
DOI: 10.1109/TMI.2012.2191417
URL: http://ieeexplore.ieee.org/lpdocs/epic03/wrapper.htm?arnumber=6172241.

[136] H. Erdogan and J. A. Fessler. “Ordered subsets algorithms for transmission tomography”. In: *Physics in Medicine and Biology* 44.11 (Nov. 1999), pp. 2835–2851. (Cited on pp. 43, 44, 87, 120)
DOI: 10.1088/0031-9155/44/11/311
URL: http://stacks.iop.org/0031-9155/44/i=11/a=311?key=crossref.1892acaed0d44600d53a3c4e81c1b745.

[137] J. D. Evans, D. G. Politte, B. R. Whiting, J. A. O’Sullivan, and J. F. Williamson. “Noise-resolution tradeoffs in x-ray CT imaging: A comparison of penalized alternating minimization and filtered backprojection algorithms”. In: *Medical Physics* 38.3 (Mar. 2011), pp. 1444–1458. (Cited on p. 42)
DOI: 10.1118/1.3549757
URL: http://scitation.aip.org/content/aapm/journal/medphys/38/3/10.1118/1.3549757.

[138] G. Falzon, S. Pearson, R. Murison, C. Hall, K. Siu, A. Evans, K. Rogers, and R. Lewis. “Wavelet-based feature extraction applied to small-angle x-ray scattering patterns from breast tissue: a tool for differentiating between tissue types”. In: *Physics in Medicine and Biology* 51.10 (Apr. 2006), pp. 2465–2477. (Cited on p. 10)
DOI: 10.1088/0031-9155/51/10/007
URL: http://stacks.iop.org/0031-9155/51/i=10/a=007?key=crossref.d5372cc11d86d20e4e54f822088bea41.

[139] G. Falzon, S. Pearson, R. Murison, C. Hall, K. Siu, A. Round, E. Schültke, A. H. Kaye, and R. Lewis. “Myelin structure is a key difference in the x-ray scattering signature between meningioma, schwannoma and glioblastoma multiforme”. In: *Physics in Medicine and Biology* 52.21 (Oct. 2007), pp. 6543–6553. (Cited on p. 10)
DOI: 10.1088/0031-9155/52/21/014
URL: http://stacks.iop.org/0031-9155/52/i=21/a=014?key=crossref.b737ed7373e89a4faf975d65467807ef.

[140] A. Fehringer, T. Lasser, I. Zanette, P. B. Noël, and F. Pfeiffer. “A versatile tomographic forward- and back-projection approach on multi-GPUs”. In: *SPIE Medical Imaging*. Ed. by S. Ourselin and M. A. Styner. SPIE, Mar. 2014, 90344F. (Cited on pp. 72, 103, 115)
DOI: 10.1117/12.2043860
URL: http://proceedings.spiedigitallibrary.org/proceeding.aspx?doi=10.1117/12.2043860.

[141] J. M. Feldkamp, M. Kuhlmann, S. V. Roth, A. Timmann, R. Gehrke, I. Shakhverdova, P. Paufler, S. K. Filatov, R. S. Bubnova, and C. G. Schroer. “Recent developments in tomographic small-angle X-ray scattering”. In: *physica status solidi (a)* 206.8 (Aug. 2009), pp. 1723–1726. (Cited on p. 10)
DOI: 10.1002/pssa.200881615
URL: http://doi.wiley.com/10.1002/pssa.200881615.

[142] L. A. Feldkamp, L. C. Davis, and J. W. Kress. “Practical cone-beam algorithm”. In: *Journal of the Optical Society of America A* 1.6 (1984), pp. 612–619. (Cited on p. 42)
DOI: 10.1364/JOSAA.1.000612
URL: http://www.opticsinfobase.org/abstract.cfm?URI=josaa-1-6-612.

[143] M. Fernández, J. Keyriläinen, R. Serimaa, M. Torkkeli, M.-L. Karjalainen-Lindsberg, M. Tenhunen, W. Thomlinson, V. Urban, and P. Suortti. “Small-angle x-ray scattering studies of human breast tissue samples”. In: *Physics in Medicine and Biology* 47.4 (Jan. 2002), pp. 577–592. (Cited on p. 10)
DOI: 10.1088/0031-9155/47/4/303
URL: http://stacks.iop.org/0031-9155/47/i=4/a=303?key=crossref.ad35193d727d51058119c79073fb0181.

[144] M. Fernández, J. Keyriläinen, R. Serimaa, M. Torkkeli, M.-L. Karjalainen-Lindsberg, M. Leidenius, K. v. Smitten, M. Tenhunen, S. Fiedler, A. Bravin, T. M. Weiss, and P. Suortti. “Human breast cancer in vitro: matching histo-pathology with small-angle x-ray scattering and diffraction enhanced x-ray imaging”. In: *Physics in Medicine and Biology* 50.13 (June 2005), pp. 2991–3006. (Cited on p. 10)
DOI: 10.1088/0031-9155/50/13/002
URL: http://stacks.iop.org/0031-9155/50/i=13/a=002?key=crossref.3299903c2b15d66d23c77b69dafe8399.

[145] J. A. Fessler. “Statistical Image Reconstruction Methods for Transmission Tomography ”. In: *Handbook of Medical Imaging, Volume 2. Medical Image Processing and Analysis*. Ed. by M. Sonka and J. M. Fitzpatrick. Bellingham, WA, USA: SPIE, June 2000, pp. 1–70. ISBN: 9780819477606. (Cited on pp. 40, 41, 87)
DOI: 10.1117/3.831079
URL: http://ebooks.spiedigitallibrary.org/book.aspx?doi=10.1117/3.831079.

[146] P. Fillard, X. Pennec, V. Arsigny, and N. Ayache. “Clinical DT-MRI Estimation, Smoothing, and Fiber Tracking With Log-Euclidean Metrics”. In: *IEEE Transactions on Medical Imaging* 26.11 (2007), pp. 1472–1482. (Cited on pp. 16, 101)
DOI: 10.1109/TMI.2007.899173
URL: http://ieeexplore.ieee.org/lpdocs/epic03/wrapper.htm?arnumber=4359024.

[147] J. Foong, M. Maier, C. A. Clark, G. J. Barker, D. H. Miller, and M. A. Ron. “Neuropathological abnormalities of the corpus callosum in schizophrenia: a diffusion tensor imaging study”. In: *Journal of Neurology, Neurosurgery & Psychiatry* 68.2 (Feb. 2000), pp. 242–244. (Cited on p. 16)
DOI: 10.1136/jnnp.68.2.242
URL: http://jnnp.bmj.com/cgi/doi/10.1136/jnnp.68.2.242.

[148] E. Förster, K. Goetz, and P. Zaumseil. “Double crystal diffractometry for the characterization of targets for laser fusion experiments”. In: *Crystal Research and Technology* 15.8 (Jan. 1980), pp. 937–945. (Cited on p. 10)
DOI: 10.1002/crat.19800150812
URL: http://doi.wiley.com/10.1002/crat.19800150812.

[149] J. Frikel. “A new framework for sparse regularization in limited angle x-ray tomography”. In: *Biomedical Imaging: From Nano to Macro, 2010 IEEE International Symposium on* (2010), pp. 824–827. (Cited on pp. 40, 66, 72)
DOI: 10.1109/ISBI.2010.5490113
URL: http://ieeexplore.ieee.org/lpdocs/epic03/wrapper.htm?arnumber=5490113.

[150] J. Frikel. “Reconstructions in limited angle x-ray tomography: Characterization of classical reconstructions and adapted curvelet sparse regularization”. PhD thesis. Oct. 2012. (Cited on p. 66).

[151] J. Frikel. “Sparse regularization in limited angle tomography”. In: *Applied and Computational Harmonic Analysis* 34.1 (Jan. 2013), pp. 117–141. (Cited on pp. 40, 66, 72)
DOI: 10.1016/j.acha.2012.03.005
URL: http://linkinghub.elsevier.com/retrieve/pii/S1063520312000449.

[152] J. Frikel and E. T. Quinto. “Characterization and reduction of artifacts in limited angle tomography”. In: *Inverse problems* 29.12 (Nov. 2013), p. 125007. (Cited on p. 27)
DOI: 10.1088/0266-5611/29/12/125007
URL: http://stacks.iop.org/0266-5611/29/i=12/a=125007?key=crossref.9dcb5ea3e029b45f86a06a88dc29f95a.

[153] P. Funk. “Über Flächen mit lauter geschlossenen geodätischen Linien”. In: *Mathematische Annalen* 74.2 (June 1913), pp. 278–300. (Cited on pp. 54, 123)
DOI: 10.1007/BF01456044
URL: http://link.springer.com/article/10.1007/BF01456044.

[154] D. Gabay. “Chapter IX applications of the method of multipliers to variational inequalities”. In: *Studies in mathematics and its applications* 15 (1983), pp. 299–331. (Cited on p. 45)
DOI: 10.1016/S0168-2024(08)70034-1
URL: http://www.sciencedirect.com/science/article/pii/S0168202408700341.

[155] H. Gao, R. Li, Y. Lin, and L. Xing. “4D cone beam CT via spatiotemporal tensor framelet”. In: *Medical Physics* 39.11 (Oct. 2012), pp. 6943–6946. (Cited on pp. 40, 66, 72)
DOI: 10.1118/1.4762288
URL: http://doi.wiley.com/10.1118/1.4762288.

[156] H. Gao, X. S. Qi, Y. Gao, and D. A. Low. “Megavoltage CT imaging quality improvement on TomoTherapy via tensor framelet”. In: *Medical Physics* 40.8 (Nov. 2016), p. 081919. (Cited on pp. 40, 66, 72)
DOI: 10.1118/1.4816303
URL: http://doi.wiley.com/10.1118/1.4816303.

[157] E. Garduño, G. T. Herman, and R. Davidi. “Reconstruction from a few projections by ℓ1-minimization of the Haar transform”. In: *Inverse problems* 27.5 (May 2011), p. 055006. (Cited on p. 39)
DOI: 10.1088/0266-5611/27/5/055006
URL: http://stacks.iop.org/0266-5611/27/i=5/a=055006?key=crossref.152ec98289f27ccd25e85b719e98ddba.

[158] E. Garyfallidis, M. Brett, B. Amirbekian, A. Rokem, S. van der Walt, M. Descoteaux, I. Nimmo-Smith, and Dipy Contributors. "Dipy, a library for the analysis of diffusion MRI data". In: *Frontiers in Neuroinformatics* 8.175 (Feb. 2014), p. 554. (Cited on pp. 123, 126)
DOI: 10.3389/fninf.2014.00008
URL: http://journal.frontiersin.org/article/10.3389/fninf.2014.00008/abstract.

[159] P. Gilbert. "Iterative methods for the three-dimensional reconstruction of an object from projections". In: *Journal of Theoretical Biology* 36.1 (July 1972), pp. 105–117. (Cited on pp. 42, 87)
DOI: 10.1016/0022-5193(72)90180-4
URL: http://linkinghub.elsevier.com/retrieve/pii/0022519372901804.

[160] O. Glatter and O. Kratky. *Small Angle X-ray Scattering*. Academic Press, 1982. ISBN: 0122862805. (Cited on pp. 5, 7, 47)
URL: http://www.worldcat.org/title/small-angle-x-ray-scattering/oclc/797419465.

[161] B. Gleich and J. Weizenecker. "Tomographic imaging using the nonlinear response of magnetic particles". In: *Nature* 435.7046 (June 2005), pp. 1214–1217. (Cited on p. 16)
DOI: 10.1038/nature03808
URL: http://www.nature.com/doifinder/10.1038/nature03808.

[162] A. Goh, C. Lenglet, P. M. Thompson, and R. Vidal. "A nonparametric Riemannian framework for processing high angular resolution diffusion images (HARDI)". In: *2009 IEEE Computer Society Conference on Computer Vision and Pattern Recognition Workshops (CVPR Workshops)*. IEEE, 2009, pp. 2496–2503. ISBN: 978-1-4244-3992-8. (Cited on p. 120)
DOI: 10.1109/CVPR.2009.5206843
URL: http://ieeexplore.ieee.org/lpdocs/epic03/wrapper.htm?arnumber=5206843.

[163] A. Goh, C. Lenglet, P. M. Thompson, and R. Vidal. "A nonparametric Riemannian framework for processing high angular resolution diffusion images and its applications to ODF-based morphometry". In: *NeuroImage* 56.3 (June 2011), pp. 1181–1201. (Cited on p. 120)
DOI: 10.1016/j.neuroimage.2011.01.053
URL: http://linkinghub.elsevier.com/retrieve/pii/S1053811911000899.

[164] T. Goldstein and S. Osher. "The split Bregman method for L1-regularized problems". In: *SIAM Journal on Imaging Sciences* 2.2 (Jan. 2009), pp. 323–343. (Cited on p. 44)
DOI: 10.1137/080725891
URL: http://epubs.siam.org/doi/10.1137/080725891.

[165] R. Gordon, R. Bender, and G. T. Herman. "Algebraic Reconstruction Techniques (ART) for three-dimensional electron microscopy and X-ray photography". In: *Journal of Theoretical Biology* 29.3 (Dec. 1970), pp. 471–481. (Cited on pp. 42, 87)
DOI: 10.1016/0022-5193(70)90109-8
URL: http://linkinghub.elsevier.com/retrieve/pii/0022519370901098.

[166] A. Gourrier, W. Wagermaier, M. Burghammer, D. Lammie, H. S. Gupta, P. Fratzl, C. Riekel, T. J. Wess, and O. Paris. "Scanning X-ray imaging with small-angle scattering contrast". In: *Journal of Applied Crystallography* 40.s1 (Apr. 2007), s78–s82. (Cited on p. 10)
DOI: 10.1107/S0021889807006693
URL: http://scripts.iucr.org/cgi-bin/paper?S0021889807006693.

[167] L. Grafakos. *Classical and Modern Fourier Analysis*. Prentice Hall, 2004. ISBN: 9780130353993. (Cited on pp. 22–24, 28)
URL: http://books.google.de/books?id=MToZAQAAIAAJ&q=intitle:Classical+and+Modern+Fourier+Analysis+grafakos&dq=intitle:Classical+and+Modern+Fourier+Analysis+grafakos&hl=&cd=1&source=gbs_api.

[168] G. Guennebaud, B. Jacob, *et al. Eigen v3*. Tech. rep. 2010. (Cited on pp. 66, 104)
URL: http://eigen.tuxfamily.org.

[169] K. Guo and D. Labate. "Optimally sparse multidimensional representation using shearlets". In: *SIAM J. Math. Anal.* 39.1 (Jan. 2007), pp. 298–318. (Cited on p. 40)
URL: http://epubs.siam.org/doi/abs/10.1137/060649781.

[170] Y. Gur and N. Sochen. "Fast Invariant Riemannian DT-MRI Regularization". In: *2007 IEEE 11th International Conference on Computer Vision*. IEEE, Oct. 2007, pp. 1–7. ISBN: 978-1-4244-1630-1. (Cited on p. 101)
DOI: 10.1109/ICCV.2007.4409142
URL: http://ieeexplore.ieee.org/document/4409142/.

[171] S. Ha, H. Li, and K. Mueller. "Efficient area-based ray integration using summed area tables and regression models". In: *International Conference on Image Formation in X-Ray Computed Tomography*. June 2016. (Cited on p. 72).

[172] A. Haar. "Zur Theorie der orthogonalen Funktionensysteme". In: *Mathematische Annalen* 71.1 (Mar. 1911), pp. 38–53. (Cited on p. 39)
DOI: 10.1007/BF01456927
URL: http://link.springer.com/10.1007/BF01456927.

[173] J. Hadamard. "Sur les problèmes aux dérivés partielles et leur signification physique". In: *Princeton University Bulletin* 13 (1902), pp. 49–52. (Cited on p. 34).

[174] P. C. Hansen. "Analysis of discrete ill-posed problems by means of the L-curve". In: *SIAM review* 34.4 (1992), pp. 561–580. (Cited on p. 37)
DOI: 10.1137/1034115
URL: http://epubs.siam.org/doi/10.1137/1034115.

[175] P. C. Hansen and D. P. O'Leary. "The use of the L-curve in the regularization of discrete ill-posed problems". In: *SIAM Journal on Scientific Computing* 14.6 (1993), pp. 1487–1503
DOI: 10.1137/0914086
URL: http://epubs.siam.org/doi/10.1137/0914086.

[176] R. H. Hardin and N. J. A. Sloane. “McLaren’s improved snub cube and other new spherical designs in three dimensions”. In: *Discrete & Computational Geometry* 15.4 (Apr. 1996), pp. 429–441. (Cited on p. 54)
DOI: 10.1007/BF02711518
URL: http://link.springer.com/10.1007/BF02711518.

[177] N. Hauser, Z. Wang, R. A. Kubik-Huch, M. Trippel, G. Singer, M. K. Hohl, E. Roessl, T. Köhler, U. van Stevendaal, N. Wieberneit, and M. Stampanoni. “A Study on Mastectomy Samples to Evaluate Breast Imaging Quality and Potential Clinical Relevance of Differential Phase Contrast Mammography”. In: *Investigative Radiology* 49.3 (Mar. 2014), pp. 131–137. (Cited on p. 13)
DOI: 10.1097/RLI.0000000000000001
URL: http://content.wkhealth.com/linkback/openurl?sid=WKPTLP:landingpage&an=00004424-201403000-00002.

[178] S. Helgason. *The Radon Transform*. 2nd ed. Vol. 5. Progress in Mathematics. Boston, MA, USA: Springer, 1999. ISBN: 978-1-4757-1465-4. (Cited on pp. 25, 27)
DOI: 10.1007/978-1-4757-1463-0
URL: http://link.springer.com/10.1007/978-1-4757-1463-0.

[179] G. T. Herman. *Fundamentals of Computerized Tomography*. Image Reconstruction from Projections. London: Springer, Nov. 2009. ISBN: 9781852336172. (Cited on pp. 9, 25)
DOI: 10.1007/978-1-84628-723-7
URL: http://link.springer.com/10.1007/978-1-84628-723-7.

[180] C. P. Hess, P. Mukherjee, E. T. Han, D. Xu, and D. B. Vigneron. “Q-ball reconstruction of multimodal fiber orientations using the spherical harmonic basis”. In: *Magnetic Resonance in Medicine* 56.1 (July 2006), pp. 104–117. (Cited on p. 123)
DOI: 10.1002/mrm.20931
URL: http://onlinelibrary.wiley.com/doi/10.1002/mrm.20931/full.

[181] K. Hesse, I. H. Sloan, and R. S. Womersley. “Numerical Integration on the Sphere”. In: *Handbook of Geomathematics*. Berlin, Heidelberg: Springer, 2010, pp. 1185–1219. ISBN: 978-3-642-01545-8. (Cited on pp. 53, 111)
DOI: 10.1007/978-3-642-01546-5_40
URL: http://link.springer.com/10.1007/978-3-642-01546-5_40.

[182] M. R. Hestenes and E. Stiefel. “Methods of conjugate gradients for solving linear systems”. In: *Journal of Research of the National Bureau of Standards* 49.6 (1952), p. 409. (Cited on p. 44)
DOI: 10.6028/jres.049.044
URL: http://nvlpubs.nist.gov/nistpubs/jres/049/jresv49n6p409_A1b.pdf.

[183] H. Hotelling. “Analysis of a complex of statistical variables into principal components.” In: *Journal of Educational Psychology* 24.6 (1933), pp. 417–441. (Cited on p. 97)
DOI: 10.1037/h0071325
URL: http://content.apa.org/journals/edu/24/6/417.

[184] G. N. Hounsfield. “Computerized transverse axial scanning (tomography): Part 1. Description of system”. In: *The British Journal of Radiology* 46.552 (Dec. 1973), pp. 1016–1022. (Cited on p. 4)
DOI: 10.1259/0007-1285-46-552-1016
URL: http://www.birpublications.org./doi/abs/10.1259/0007-1285-46-552-1016.

[185] G. N. HOUNSFIELD. “COMPUTED MEDICAL IMAGING”. In: *Nobel Lecture* (Dec. 1979). (Cited on p. 4)
URL: http://www.nobelprize.org/nobel_prizes/medicine/laureates/1979/hounsfield-lecture.pdf.

[186] J. Hsieh. *Computed Tomography: Principles, Design, Artifacts, and Recent Advances*. 2nd ed. SPIE Press, Dec. 2009. ISBN: 9780819475336. (Cited on pp. 9, 25)
URL: http://spie.org/Publications/Book/2049426.

[187] S. Hu, C. Riess, J. Hornegger, P. Fischer, F. Bayer, T. Weber, G. Anton, and A. Maier. “3D Tensor Reconstruction in X-Ray Dark-Field Tomography”. In: *Bildverarbeitung für die Medizin 2015*. Berlin, Heidelberg: Springer, Feb. 2015, pp. 492–497. ISBN: 978-3-662-46223-2. (Cited on p. 15)
DOI: 10.1007/978-3-662-46224-9_84
URL: http://link.springer.com/10.1007/978-3-662-46224-9_84.

[188] P. J. Huber. “Robust Estimation of a Location Parameter”. In: *The Annals of Mathematical Statistics* 35.1 (Mar. 1964), pp. 73–101. (Cited on pp. 38, 81)
DOI: 10.1214/aoms/1177703732
URL: http://projecteuclid.org/euclid.aoms/1177703732.

[189] V. N. Ingal and E. A. Beliaevskaya. “X-ray plane-wave topography observation of the phase contrast from a non-crystalline object”. In: *Journal of Physics D: Applied Physics* 28.11 (Nov. 1995), pp. 2314–2317. (Cited on p. 10)
DOI: 10.1088/0022-3727/28/11/012
URL: http://iopscience.iop.org.eaccess.ub.tum.de/article/10.1088/0022-3727/28/11/012.

[190] J. Ivanic and K. Ruedenberg. “Rotation Matrices for Real Spherical Harmonics. Direct Determination by Recursion”. In: *The Journal of Physical Chemistry* 100.15 (Jan. 1996), pp. 6342–6347. (Cited on p. 120)
DOI: 10.1021/jp953350u
URL: http://pubs.acs.org/doi/abs/10.1021/jp953350u.

[191] M. R. Jayachandra, N. Rehbein, C. Herweh, and S. Heiland. “Fiber tracking of human brain using fourth-order tensor and high angular resolution diffusion imaging.” In: *Magnetic Resonance in Medicine* 60.5 (Nov. 2008), pp. 1207–1217. (Cited on p. 131)
DOI: 10.1002/mrm.21775
URL: http://doi.wiley.com/10.1002/mrm.21775.

[192] T. H. Jensen. “Refraction and scattering based x-ray imaging”. PhD thesis. Copenhagen, Nov. 2008. (Cited on p. 13).

[193] T. H. Jensen, M. Bech, O. Bunk, T. Donath, C. David, R. Feidenhans’l, and F. Pfeiffer. “Directional x-ray dark-field imaging”. In: *Physics in Medicine and Biology* 55.12 (May 2010), pp. 3317–3323. (Cited on pp. 13, 14, 47)
DOI: 10.1088/0031-9155/55/12/004
URL: http://stacks.iop.org/0031-9155/55/i=12/a=004?key=crossref.4ec71389347760a735c02bcc6746b8ac.

[194] T. H. Jensen, M. Bech, I. Zanette, T. Weitkamp, C. David, H. Deyhle, S. Rutishauser, E. Reznikova, J. Mohr, R. Feidenhans'l, and F. Pfeiffer. "Directional x-ray dark-field imaging of strongly ordered systems ". In: *Physical Review B* 82.21 (Dec. 2010), p. 214103. (Cited on pp. 13, 14, 47)
DOI: 10.1103/PhysRevB.82.214103
URL: http://link.aps.org/doi/10.1103/PhysRevB.82.214103.

[195] T. H. Jensen, M. Bech, O. Bunk, A. Menzel, A. Bouchet, G. Le Duc, R. Feidenhans'l, and F. Pfeiffer. "Molecular X-ray computed tomography of myelin in a rat brain". In: *NeuroImage* 57.1 (July 2011), pp. 124–129. (Cited on pp. 10, 131)
DOI: 10.1016/j.neuroimage.2011.04.013
URL: http://linkinghub.elsevier.com/retrieve/pii/S1053811911003910.

[196] T. H. Jensen, M. Bech, O. Bunk, M. Thomsen, A. Menzel, A. Bouchet, G. Le Duc, R. Feidenhans'l, and F. Pfeiffer. "Brain tumor imaging using small-angle x-ray scattering tomography". In: *Physics in Medicine and Biology* 56.6 (Feb. 2011), pp. 1717–1726. (Cited on p. 10)
DOI: 10.1088/0031-9155/56/6/012
URL: http://stacks.iop.org/0031-9155/56/i=6/a=012?key=crossref.bb9241bbc2cc92708568641b99b816a3.

[197] X. Jin, L. Li, Z. Chen, L. Zhang, and Y. Xing. "Anisotropic total variation for limited-angle CT reconstruction". In: *IEEE Nuclear Science Symposium Conference Record*. IEEE, 2010, pp. 2232–2238. ISBN: 978-1-4244-9106-3. (Cited on p. 39)
DOI: 10.1109/NSSMIC.2010.5874180
URL: http://ieeexplore.ieee.org/lpdocs/epic03/wrapper.htm?arnumber=5874180.

[198] H. Johansen-Berg and T. E. J. Behrens, eds. *Diffusion MRI*. 1st ed. From Quantitative Measurement to In vivo Neuroanatomy. San Diego: Academic Press, Apr. 2009. ISBN: 978-0-12-374709-9. (Cited on p. 16)
URL: https://www.elsevier.com/books/diffusion-mri/johansen-berg/978-0-12-374709-9.

[199] P. M. Joseph. "An Improved Algorithm for Reprojecting Rays through Pixel Images". In: *IEEE Transactions on Medical Imaging* 1.3 (1982), pp. 192–196. (Cited on pp. 72, 98)
DOI: 10.1109/TMI.1982.4307572
URL: http://ieeexplore.ieee.org/document/4307572/.

[200] C. Jud, F. Schaff, I. Zanette, J. Wolf, A. Fehringer, and F. Pfeiffer. "Dentinal tubules revealed with X-ray tensor tomography". In: *Dental Materials* 32.9 (Sept. 2016), pp. 1189–1195. (Cited on p. 15)
DOI: 10.1016/j.dental.2016.06.021
URL: http://www.demajournal.com/article/S0109564116301129/fulltext.

[201] S. Kaczmarz. "Angenäherte Auflösung von Systemen linearer Gleichungen". In: *Bulletin International de lAcadémie Polonaise des Sciences et des Lettres. Classe des Sciences Mathématiques et Naturelles. Série A, Sciences Mathématiques* 35 (June 1937), pp. 355–357. (Cited on pp. 42, 87).

[202] S. Kaeppler, F. Bayer, T. Weber, A. Maier, G. Anton, J. Hornegger, M. Beckmann, P. A. Fasching, A. Hartmann, F. Heindl, T. Michel, G. Oezguel, G. Pelzer, C. Rauh, J. Rieger, R. Schulz-Wendtland, M. Uder, D. Wachter, E. Wenkel, and C. Riess. *Signal Decomposition for X-ray Dark-Field Imaging*. Springer International Publishing. Cham, 2014. (Cited on p. 13)
DOI: 10.1007/978-3-319-10404-1_22
URL: http://link.springer.com/10.1007/978-3-319-10404-1_22.

[203] M. Kagias, Z. Wang, P. Villanueva-Perez, K. Jefimovs, and M. Stampanoni. "2D-Omnidirectional Hard-X-Ray Scattering Sensitivity in a Single Shot". In: *Physical Review Letters* 116.9 (Mar. 2016), p. 093902. (Cited on p. 13)
DOI: 10.1103/PhysRevLett.116.093902
URL: https://link.aps.org/doi/10.1103/PhysRevLett.116.093902.

[204] A. Kak and M. Slaney. *Principles of Computerized Tomographic Imaging*. Classics in Applied Mathematics. Society for Industrial and Applied Mathematics, Jan. 2001. ISBN: 978-0-89871-494-4. (Cited on pp. 9, 25, 27)
DOI: 10.1137/1.9780898719277
URL: http://epubs.siam.org/doi/book/10.1137/1.9780898719277.

[205] W. A. Kalender. "X-ray computed tomography". In: *Physics in Medicine and Biology* 51.13 (June 2006), R29–R43. (Cited on pp. 9, 27)
DOI: 10.1088/0031-9155/51/13/R03
URL: http://stacks.iop.org/0031-9155/51/i=13/a=R03?key=crossref.f85b1f73720b2de19220650ca2ba40f8.

[206] M. Kazhdan, T. Funkhouser, and S. Rusinkiewicz. "Rotation invariant spherical harmonic representation of 3D shape descriptors". In: *Eurographics Symposium on Geometry Processing*. Eurographics Association, 2003, pp. 156–164. ISBN: 1-58113-687-0. (Cited on p. 120)
URL: http://gfx.cs.princeton.edu/pubs/Kazhdan_2003_RIS/index.php.

[207] D. Kim and J. A. Fessler. "Optimized first-order methods for smooth convex minimization". In: *Mathematical Programming* 159.1-2 (Oct. 2015), pp. 81–107. (Cited on pp. 43, 87)
DOI: 10.1007/s10107-015-0949-3
URL: http://link.springer.com/10.1007/s10107-015-0949-3.

[208] D. Kim, S. Ramani, and J. A. Fessler. "Combining Ordered Subsets and Momentum for Accelerated X-Ray CT Image Reconstruction". In: *IEEE Transactions on Medical Imaging* 34.1 (2015), pp. 167–178. (Cited on p. 87)
DOI: 10.1109/TMI.2014.2350962
URL: http://ieeexplore.ieee.org/lpdocs/epic03/wrapper.htm?arnumber=6882248.

[209] D. Kim and J. A. Fessler. "On the Convergence Analysis of the Optimized Gradient Method". In: *Journal of Optimization Theory and Applications* 172.1 (Oct. 2016), pp. 187–205. (Cited on pp. 43, 87)
DOI: 10.1007/s10957-016-1018-7
URL: http://link.springer.com/10.1007/s10957-016-1018-7.

[210] J. H. Kinney, J. A. Pople, G. W. Marshall, and S. J. Marshall. "Collagen Orientation and Crystallite Size in Human Dentin: A Small Angle X-ray Scattering Study". In: *Calcified Tissue International* 69.1 (July 2001), pp. 31–37. (Cited on p. 10)
DOI: 10.1007/s00223-001-0006-5
URL: http://link.springer.com/10.1007/s00223-001-0006-5.

[211] P. E. Kinahan and J. G. Rogers. “Analytic 3D image reconstruction using all detected events”. In: *IEEE Transactions on Nuclear Science* 36.1 (1989), pp. 964–968. (Cited on p. 42)
DOI: 10.1109/23.34585
URL: http://ieeexplore.ieee.org/document/34585/.

[212] A. Kirsch. *An Introduction to the Mathematical Theory of Inverse Problems*. 2nd ed. Vol. 120. Applied Mathematical Sciences. New York, NY: Springer, 2011. ISBN: 978-1-4419-8474-6. (Cited on pp. 31–34, 36)
DOI: 10.1007/978-1-4419-8474-6
URL: http://link.springer.com/10.1007/978-1-4419-8474-6.

[213] M. Z. Kiss, D. E. Sayers, Z. Zhong, C. Parham, and E. D. Pisano. “Improved image contrast of calcifications in breast tissue specimens using diffraction enhanced imaging”. In: *Physics in Medicine and Biology* 49.15 (Aug. 2004), pp. 3427–3439. (Cited on p. 10)
DOI: 10.1088/0031-9155/49/15/008
URL: http://stacks.iop.org/0031-9155/49/i=15/a=008?key=crossref.a2766d8a93f336847f9b180ce4848a6c.

[214] C. G. Koay, L.-C. Chang, J. D. Carew, C. Pierpaoli, and P. J. Basser. “A unifying theoretical and algorithmic framework for least squares methods of estimation in diffusion tensor imaging”. In: *Journal of Magnetic Resonance* 182.1 (Sept. 2006), pp. 115–125. (Cited on pp. 16, 101)
DOI: 10.1016/j.jmr.2006.06.020
URL: http://linkinghub.elsevier.com/retrieve/pii/S1090780706001790.

[215] T. Köhler, B. Brendel, and E. Roessl. “Iterative reconstruction for differential phase contrast imaging using spherically symmetric basis functions”. In: *Medical Physics* 38.8 (2011), p. 4542. (Cited on pp. 66, 72)
DOI: 10.1118/1.3608906
URL: http://link.aip.org/link/MPHYA6/v38/i8/p4542/s1&Agg=doi.

[216] M. Kubicki, R. McCarley, C.-F. Westin, H.-J. Park, S. Maier, R. Kikinis, F. A. Jolesz, and M. E. Shenton. “A review of diffusion tensor imaging studies in schizophrenia”. In: *Journal of Psychiatric Research* 41.1–2 (Jan. 2007), pp. 15–30. (Cited on p. 16)
DOI: 10.1016/j.jpsychires.2005.05.005
URL: http://www.sciencedirect.com/science/article/pii/S0022395605000671.

[217] D. E. Kuhl and R. Q. Edwards. “Image Separation Radioisotope Scanning”. In: *Radiology* 80.4 (Apr. 1963), pp. 653–662. (Cited on p. 16)
DOI: 10.1148/80.4.653
URL: http://pubs.rsna.org/doi/10.1148/80.4.653.

[218] M. W. Kutta. “Beitrag zur näherungsweisen Integration totaler Differentialgleichungen”. In: *Zeitschrift für Mathematik und Physik* 46 (1901), pp. 435–453. (Cited on p. 104).

[219] D. Labate, W.-Q. Lim, G. Kutyniok, and G. Weiss. “Sparse multidimensional representation using shearlets”. In: *Optics & Photonics 2005*. Ed. by M. Papadakis, A. F. Laine, and M. A. Unser. SPIE, Aug. 2005, 59140U. (Cited on p. 40)
DOI: 10.1117/12.613494
URL: http://proceedings.spiedigitallibrary.org/proceeding.aspx?doi=10.1117/12.613494.

[220] L. Landweber. “An Iteration Formula for Fredholm Integral Equations of the First Kind”. In: *American Journal of Mathematics* 73.3 (July 1951), p. 615. (Cited on pp. 42, 43, 87)
DOI: 10.2307/2372313
URL: http://www.jstor.org/stable/2372313?origin=crossref.

[221] K. Lange and R. Carson. “EM reconstruction algorithms for emission and transmission tomography.” In: *Journal of Computer Assisted Tomography* 8.2 (Apr. 1984), pp. 306–316. (Cited on p. 40)
URL: http://eutils.ncbi.nlm.nih.gov/entrez/eutils/elink.fcgi?dbfrom=pubmed&id=6608535&retmode=ref&cmd=prlinks.

[222] T. Lasser. “Tomographic Reconstruction Methods for Optical and Intra–operative Functional Imaging”. PhD thesis. Technische Universität München, 2011. (Cited on p. 16).

[223] P. C. LAUTERBUR. “All science is interdisciplinary-from magnetic moments to molecules to men”. In: *Nobel Lecture* (Dec. 2003). (Cited on p. 16)
URL: https://www.nobelprize.org/nobel_prizes/medicine/laureates/2003/lauterbur-lecture.pdf.

[224] T. Lauridsen, M. Willner, M. Bech, F. Pfeiffer, and R. Feidenhans’l. “Detection of sub-pixel fractures in X-ray dark-field tomography”. In: *Applied Physics A* 121.3 (Sept. 2015), pp. 1243–1250. (Cited on p. 14)
DOI: 10.1007/s00339-015-9496-2
URL: http://link.springer.com/10.1007/s00339-015-9496-2.

[225] P. C. LAUTERBUR. “Image Formation by Induced Local Interactions: Examples Employing Nuclear Magnetic Resonance”. In: *Nature* 242.5394 (Mar. 1973), pp. 190–191. (Cited on p. 16)
DOI: 10.1038/242190a0
URL: http://dx.doi.org/10.1038/242190a0.

[226] D. Le Bihan, J. F. Mangin, C. Poupon, C. A. Clark, S. Pappata, N. Molko, and H. Chabriat. “Diffusion tensor imaging: concepts and applications.” In: *Journal of magnetic resonance imaging : JMRI* 13.4 (Apr. 2001), pp. 534–546. (Cited on p. 16)
DOI: 10.1002/jmri.1076
URL: http://doi.wiley.com/10.1002/jmri.1076.

[227] D. Le Bihan, E. Breton, D. Lallemand, P. Grenier, E. Cabanis, and M. Laval-Jeantet. “MR imaging of intravoxel incoherent motions: application to diffusion and perfusion in neurologic disorders.” In: *Radiology* 161.2 (Nov. 1986), pp. 401–407. (Cited on p. 16)
DOI: 10.1148/radiology.161.2.3763909
URL: http://pubs.rsna.org/doi/10.1148/radiology.161.2.3763909.

[228] N.-Y. Lee and B. J. Lucier. “Wavelet methods for inverting the Radon transform with noisy data”. In: *IEEE Transactions on Image Processing* 10.1 (2001), pp. 79–94. (Cited on p. 42)
DOI: 10.1109/83.892445
URL: http://ieeexplore.ieee.org/document/892445/.

[229] J. M. Lee. *Introduction to Topological Manifolds*. Vol. 202. Graduate Texts in Mathematics. New York, NY: Springer, 2011. ISBN: 978-1-4419-7939-1. (Cited on p. 57)
DOI: 10.1007/978-1-4419-7940-7
URL: http://link.springer.com/10.1007/978-1-4419-7940-7.

[230] J. M. Lee. *Introduction to Smooth Manifolds*. Vol. 218. Graduate Texts in Mathematics. New York, NY: Springer, 2012. ISBN: 978-1-4419-9981-8. (Cited on p. 57)
DOI: 10.1007/978-1-4419-9982-5
URL: http://link.springer.com/10.1007/978-1-4419-9982-5.

[231] J. M. Lee. *Riemannian Manifolds*. Vol. 176. Graduate Texts in Mathematics. New York, NY: Springer, 1997. ISBN: 978-0-387-98322-6. (Cited on p. 57)
DOI: 10.1007/b98852
URL: http://link.springer.com/10.1007/b98852.

[232] L. E. Levine and G. G. Long. "X-ray imaging with ultra-small-angle X-ray scattering as a contrast mechanism". In: *Journal of Applied Crystallography* 37.5 (Sept. 2004), pp. 757–765. (Cited on p. 10)
DOI: 10.1107/S0021889804016073
URL: http://scripts.iucr.org/cgi-bin/paper?S0021889804016073.

[233] R. A. Lewis, K. D. Rogers, C. J. Hall, E. Towns-Andrews, S. Slawson, A. Evans, S. E. Pinder, I. O. Ellis, C. R. M. Boggis, A. P. Hufton, and D. R. Dance. "Breast cancer diagnosis using scattered X-rays". In: *Journal of synchrotron radiation* 7.5 (Sept. 2000), pp. 348–352. (Cited on p. 10)
DOI: 10.1107/S0909049500009973
URL: http://scripts.iucr.org/cgi-bin/paper?S0909049500009973.

[234] R. M. Lewitt. "Multidimensional digital image representations using generalized Kaiser-Bessel window functions". In: *Journal of the Optical Society of America A* 7.10 (1990), pp. 1834–1846. (Cited on pp. 66, 72)
DOI: 10.1364/JOSAA.7.001834
URL: http://www.opticsinfobase.org/abstract.cfm?URI=josaa-7-10-1834.

[235] M. Liebi, M. Georgiadis, A. Menzel, P. Schneider, J. Kohlbrecher, O. Bunk, and M. Guizar-Sicairos. "Nanostructure surveys of macroscopic specimens by small-angle scattering tensor tomography." In: *Nature* 527.7578 (Nov. 2015), pp. 349–352. (Cited on pp. 10, 120)
DOI: 10.1038/nature16056
URL: http://www.nature.com/doifinder/10.1038/nature16056.

[236] Y. Long, J. A. Fessler, and J. M. Balter. "3D forward and back-projection for X-ray CT using separable footprints." In: *IEEE Transactions on Medical Imaging* 29.11 (Nov. 2010), pp. 1839–1850. (Cited on p. 72)
DOI: 10.1109/TMI.2010.2050898
URL: http://ieeexplore.ieee.org/document/5482021/.

[237] J. Luo, Y. Zhu, and I. E. Magnin. "Denoising by Averaging Reconstructed Images: Application to Magnetic Resonance Images". In: *IEEE Transactions on Biomedical Engineering* 56.3 (Apr. 2009), pp. 666–674. (Cited on p. 101)
DOI: 10.1109/TBME.2009.2012256
URL: http://ieeexplore.ieee.org/document/4838933/.

[238] S. K. Lynch, V. Pai, J. Auxier, A. F. Stein, E. E. Bennett, C. K. Kemble, X. Xiao, W.-K. Lee, N. Y. Morgan, and H. H. Wen. "Interpretation of dark-field contrast and particle-size selectivity in grating interferometers." In: *Applied Optics* 50.22 (Aug. 2011), pp. 4310–4319. (Cited on pp. 13, 14, 47, 48)
DOI: 10.1364/AO.50.004310
URL: http://www.opticsinfobase.org/abstract.cfm?URI=ao-50-22-4310.

[239] J. Ma and G. Plonka. "The Curvelet Transform". In: *IEEE Signal Processing Magazine* 27.2 (2010), pp. 118–133. (Cited on p. 40)
DOI: 10.1109/MSP.2009.935453
URL: http://ieeexplore.ieee.org/lpdocs/epic03/wrapper.htm?arnumber=5438971.

[240] A. Maier, H. G. Hofmann, M. Berger, P. Fischer, C. Schwemmer, H. Wu, K. Müller, J. Hornegger, J.-H. Choi, C. Riess, A. Keil, and R. Fahrig. "CONRAD—A software framework for cone-beam imaging in radiology". In: *Medical Physics* 40.11 (2013), p. 111914. (Cited on p. 63)
DOI: 10.1118/1.4824926
URL: http://link.aip.org/link/MPHYA6/v40/i11/p111914/s1&Agg=doi.

[241] A. Malecki, G. Potdevin, and F. Pfeiffer. "Quantitative wave-optical numerical analysis of the dark-field signal in grating-based X-ray interferometry". In: *EPL (Europhysics Letters)* 99.4 (Aug. 2012), p. 48001. (Cited on p. 14)
DOI: 10.1209/0295-5075/99/48001
URL: http://iopscience.iop.org/0295-5075/99/4/48001/article/.

[242] A. D. Malecki. "X-Ray Tensor Tomography". PhD thesis. München, 2013. ISBN: 859395887. (Cited on p. 95)
URL: http://books.google.de/books?id=9y6IngEACAAJ&dq=intitle:X+Ray+Tensor+Tomography&hl=&cd=1&source=gbs_api.

[243] A. Malecki, G. Potdevin, T. Biernath, E. Eggl, E. G. Garcia, T. Baum, P. B. Noël, J. S. Bauer, and F. Pfeiffer. "Coherent Superposition in Grating-Based Directional Dark-Field Imaging". In: *PLOS ONE* 8.4 (2013), e61268. ISSN: 1932-6203. (Cited on pp. 14, 15, 47, 95)
DOI: 10.1371/journal.pone.0061268
URL: http://dx.plos.org/10.1371/journal.pone.0061268.

[244] A. Malecki, G. Potdevin, T. Biernath, E. Eggl, K. Willer, T. Lasser, J. Maisenbacher, J. Gibmeier, A. Wanner, and F. Pfeiffer. "X-ray tensor tomography". In: *EPL (Europhysics Letters)* 105.3 (2014), p. 38002. (Cited on pp. 15, 17, 95–98, 102, 109, 112, 114, 115)
DOI: 10.1209/0295-5075/105/38002
URL: http://stacks.iop.org/0295-5075/105/i=3/a=38002?key=crossref.19d752da6c24e2272ae7184e6d0278ab.

[245] A. Malecki, E. Eggl, F. Schaff, G. Potdevin, T. Baum, E. G. Garcia, J. S. Bauer, and F. Pfeiffer. “Correlation of X-Ray Dark-Field Radiography to Mechanical Sample Properties”. In: *Microscopy and Microanalysis* 20.05 (July 2014), pp. 1528–1533. (Cited on p. 14)
DOI: 10.1017/S1431927614001718
URL: http://www.journals.cambridge.org/abstract_S1431927614001718.

[246] S. Mallat. *A wavelet tour of signal processing*. 2nd ed. Academic Press, 1999. ISBN: 978-0-12-466606-1. (Cited on p. 39)
URL: http://dblp.org/rec/books/daglib/0098272.

[247] P. Mansfield. “SNAP-SHOT MRI”. In: *Nobel Lecture* (Dec. 2003). (Cited on p. 16)
URL: https://www.nobelprize.org/nobel_prizes/medicine/laureates/2003/mansfield-lecture.pdf.

[248] B. D. Man and S. Basu. “Distance-driven projection and backprojection in three dimensions”. In: *Physics in Medicine and Biology* 49.11 (May 2004), pp. 2463–2475. (Cited on p. 72)
DOI: 10.1088/0031-9155/49/11/024
URL: http://stacks.iop.org/0031-9155/49/i=11/a=024?key=crossref.2e1f59bde38dad5612138294d5039469.

[249] F. G. Meinel, F. Schwab, S. Schleede, M. Bech, J. Herzen, K. Achterhold, S. Auweter, F. Bamberg, A. Ö. Yildirim, A. Bohla, O. Eickelberg, R. Loewen, M. Gifford, R. Ruth, M. F. Reiser, F. Pfeiffer, and K. Nikolaou. “Diagnosing and Mapping Pulmonary Emphysema on X-Ray Projection Images: Incremental Value of Grating-Based X-Ray Dark-Field Imaging”. In: *PLOS ONE* 8.3 (Mar. 2013), e59526. ISSN: 1932-6203. (Cited on p. 13)
DOI: 10.1371/journal.pone.0059526
URL: http://dx.plos.org/10.1371/journal.pone.0059526.

[250] F. G. Meinel, F. Schwab, A. Yaroshenko, A. Velroyen, M. Bech, K. Hellbach, J. Fuchs, T. Stiewe, A. Ö. Yildirim, F. Bamberg, M. F. Reiser, F. Pfeiffer, and K. Nikolaou. “Lung tumors on multimodal radiographs derived from grating-based X-ray imaging – A feasibility study”. In: *Physica Medica* 30.3 (May 2014), pp. 352–357. (Cited on p. 13)
DOI: 10.1016/j.ejmp.2013.11.001
URL: http://linkinghub.elsevier.com/retrieve/pii/S1120179713004298.

[251] F. G. Meinel, A. Yaroshenko, K. Hellbach, M. Bech, M. Müller, A. Velroyen, F. Bamberg, O. Eickelberg, K. Nikolaou, M. F. Reiser, F. Pfeiffer, and A. Ö. Yildirim. “Improved Diagnosis of Pulmonary Emphysema Using In Vivo Dark-Field Radiography”. In: *Investigative Radiology* 49.10 (Oct. 2014), pp. 653–658. (Cited on p. 13)
DOI: 10.1097/RLI.0000000000000067
URL: http://content.wkhealth.com/linkback/openurl?sid=WKPTLP:landingpage&an=00004424-201410000-00004.

[252] T. Michel, J. Rieger, G. Anton, F. Bayer, M. W. Beckmann, J. Durst, P. A. Fasching, W. Haas, A. Hartmann, G. Pelzer, M. Radicke, C. Rauh, A. Ritter, P. Sievers, R. Schulz-Wendtland, M. Uder, D. L. Wachter, T. Weber, E. Wenkel, and A. Zang. “On a dark-field signal generated by micrometer-sized calcifications in phase-contrast mammography”. In: *Physics in Medicine and Biology* 58.8 (Apr. 2013), pp. 2713–2732. (Cited on p. 13)
DOI: 10.1088/0031-9155/58/8/2713
URL: http://stacks.iop.org/0031-9155/58/i=8/a=2713?key=crossref.e67d1ea57577f1dc0f21fe32c030be68.

[253] P. Modregger, F. Scattarella, B. R. Pinzer, C. David, R. Bellotti, and M. Stampanoni. “Imaging the Ultrasmall-Angle X-Ray Scattering Distribution with Grating Interferometry”. In: *Physical Review Letters* 108.4 (Jan. 2012), p. 048101. (Cited on p. 13)
DOI: 10.1103/PhysRevLett.108.048101
URL: http://link.aps.org/doi/10.1103/PhysRevLett.108.048101.

[254] M. J. Mohlenkamp. “A fast transform for spherical harmonics”. In: *Journal of Fourier Analysis and Applications* 5.2-3 (Mar. 1999), pp. 159–184. (Cited on p. 53)
DOI: 10.1007/BF01261607
URL: http://link.springer.com/10.1007/BF01261607.

[255] A. Momose. “Phase-sensitive imaging and phase tomography using X-ray interferometers”. In: *Optics Express* 11.19 (2003), p. 2303. (Cited on pp. 5, 10, 11)
DOI: 10.1364/OE.11.002303
URL: http://www.opticsinfobase.org/abstract.cfm?URI=oe-11-19-2303.

[256] A. Momose, S. Kawamoto, I. Koyama, Y. Hamaishi, K. Takai, and Y. Suzuki. “Demonstration of X-Ray Talbot Interferometry”. In: *Japanese Journal of Applied Physics* 42.Part 2, No. 7B (July 2003), pp. L866–L868. (Cited on pp. 5, 10, 11)
DOI: 10.1143/JJAP.42.L866
URL: http://stacks.iop.org/1347-4065/42/L866.

[257] A. Momose and J. Fukuda. “Phase-contrast radiographs of nonstained rat cerebellar specimen”. In: *Medical Physics* 22.4 (Apr. 1995), pp. 375–379. (Cited on p. 10)
DOI: 10.1118/1.597472
URL: http://doi.wiley.com/10.1118/1.597472.

[258] C. A. C. Moraga, C. F. Westin, and J. Ruiz-Alzola. “Homomorphic Filtering of DT-MRI Fields”. In: *Medical Image Computing and Computer-Assisted Intervention - MICCAI 2003*. Berlin, Heidelberg: Springer, Nov. 2003, pp. 990–991. ISBN: 978-3-540-20464-0. (Cited on p. 101)
DOI: 10.1007/978-3-540-39903-2_137
URL: https://link.springer.com/chapter/10.1007/978-3-540-39903-2_137.

[259] G. R. Morrison and M. T. Browne. “Dark-field imaging with the scanning transmission x-ray microscope”. In: *Review of Scientific Instruments* 63.1 (1992), p. 611. (Cited on p. 10)
DOI: 10.1063/1.1143820
URL: http://scitation.aip.org/content/aip/journal/rsi/63/1/10.1063/1.1143820.

[260] J. L. Mueller and S. Siltanen. *Linear and Nonlinear Inverse Problems with Practical Applications*. Philadelphia, PA: Society for Industrial and Applied Mathematics, Oct. 2012. ISBN: 978-1-61197-233-7. (Cited on pp. 31, 36, 39, 87)
DOI: 10.1137/1.9781611972344
URL: http://epubs.siam.org/doi/book/10.1137/1.9781611972344.

[261] F. Natterer. *The Mathematics of Computerized Tomography*. Classics in Applied Mathematics. Philadelphia, PA: Society for Industrial and Applied Mathematics, Jan. 2001. ISBN: 9780898714937. (Cited on pp. 9, 25, 42)
DOI: 10.1137/1.9780898719284
URL: http://epubs.siam.org/doi/book/10.1137/1.9780898719284.

[262] F. Natterer. "Regularisierung schlecht gestellter Probleme durch Projektionsverfahren". In: *Numerische Mathematik* 28.3 (1977), pp. 329–341–341. (Cited on p. 36)
DOI: 10.1007/BF01389972
URL: http://dx.doi.org/10.1007/BF01389972.

[263] F. Natterer. "Numerical inversion of the Radon transform". In: *Numerische Mathematik* 30.1 (Mar. 1978), pp. 81–91. (Cited on pp. 27–29)
DOI: 10.1007/BF01403908
URL: http://link.springer.com/10.1007/BF01403908.

[264] F. Natterer. *The Mathematics of Computerized Tomography*. Stuttgart: B. G. Teubner, 1986. ISBN: 978-3-519-02103-2. (Cited on pp. 9, 25–27, 29, 35)
DOI: 10.1007/978-3-663-01409-6
URL: http://link.springer.com/book/10.1007%2F978-3-663-01409-6.

[265] R. Neji, N. Azzabou, N. Paragios, and G. Fleury. "A Convex Semi-definite Positive Framework for DTI Estimation and Regularization". In: *Bildverarbeitung für die Medizin 2015*. Berlin, Heidelberg: Springer, Nov. 2007, pp. 220–229. ISBN: 978-3-540-76857-9. (Cited on p. 101)
DOI: 10.1007/978-3-540-76858-6_22
URL: https://link.springer.com/chapter/10.1007/978-3-540-76858-6_22.

[266] Y. Nesterov. "A method of solving a convex programming problem with convergence rate O (1/k2)". In: *Sov. Math. Dokl.* 27.2 (1983), pp. 372–376. (Cited on pp. 43, 87).

[267] M. Nilchian and M. Unser. "Differential phase-contrast X-ray computed tomography: From model discretization to image reconstruction". In: *Biomedical Imaging (ISBI), 2012 9th IEEE International Symposium on* (2012), pp. 90–93. (Cited on pp. 45, 66, 72)
DOI: 10.1109/ISBI.2012.6235491
URL: http://ieeexplore.ieee.org/lpdocs/epic03/wrapper.htm?arnumber=6235491.

[268] M. Nilchian, C. e. d. Vonesch, P. Modregger, M. Stampanoni, and M. Unser. "Fast iterative reconstruction of differential phase contrast X-ray tomograms". In: *Optics Express* 21.5 (Mar. 2013), pp. 5511–5528. (Cited on pp. 66, 72)
DOI: 10.1364/OE.21.005511
URL: http://www.opticsinfobase.org/oe/abstract.cfm?uri=oe-21-5-5511.

[269] C. Nimsky, O. Ganslandt, P. Hastreiter, R. Wang, T. Benner, A. G. Sorensen, and R. Fahlbusch. "Preoperative and Intraoperative Diffusion Tensor Imaging-based Fiber Tracking in Glioma Surgery". In: *Neurosurgery* 56.1 (Jan. 2005), pp. 130–138. (Cited on p. 16)
DOI: 10.1227/01.NEU.0000144842.18771.30
URL: https://academic.oup.com/neurosurgery/article-lookup/doi/10.1227/01.NEU.0000144842.18771.30.

[270] J. Nocedal and S. J. Wright. *Numerical Optimization*. 2nd ed. New York, NY: Springer, 2006. ISBN: 978-0-387-30303-1. (Cited on pp. 43, 63, 82, 87)
DOI: 10.1007/978-0-387-40065-5
URL: http://www.springer.com/de/book/9780387303031.

[271] D. Paganin. *Coherent X-Ray Optics*. Oxford University Press, 2006. ISBN: 9780198567288. (Cited on pp. 5, 8)
DOI: 10.1093/acprof:oso/9780198567288.001.0001
URL: http://www.oxfordscholarship.com/view/10.1093/acprof:oso/9780198567288.001.0001/acprof-9780198567288.

[272] N. Parikh and S. Boyd. "Proximal algorithms". In: *Foundations and Trends in Optimization* 1.3 (2014), pp. 123–231. (Cited on p. 40)
DOI: 10.1561/2400000003
URL: http://www.nowpublishers.com/article/Details/OPT-003.

[273] O. Pasternak, N. Sochen, and Y. Assaf. "Variational Regularization of Multiple Diffusion Tensor Fields". In: *Visualization and Processing of Tensor Fields*. Berlin, Heidelberg: Springer, 2006, pp. 165–176. ISBN: 978-3-540-25032-6. (Cited on p. 101)
DOI: 10.1007/3-540-31272-2_9
URL: http://link.springer.com/10.1007/3-540-31272-2_9.

[274] O. Pasternak, Y. Assaf, N. Intrator, and N. Sochen. "Variational multiple-tensor fitting of fiber-ambiguous diffusion-weighted magnetic resonance imaging voxels". In: *Magnetic Resonance Imaging* 26.8 (Oct. 2008), pp. 1133–1144. (Cited on p. 16)
DOI: 10.1016/j.mri.2008.01.006
URL: http://linkinghub.elsevier.com/retrieve/pii/S0730725X08000490.

[275] K. Pearson. "On Lines and Planes of Closes Fit to Systems of Points in Space". In: *The London, Edinburgh, and Dublin Philosophical Magazine and Journal of Science* 6.2 (1901), pp. 559–572. (Cited on p. 97).

[276] X. Pennec. "Intrinsic Statistics on Riemannian Manifolds: Basic Tools for Geometric Measurements". In: *Journal of Mathematical imaging and vision* 25.1 (July 2006), pp. 127–154. (Cited on p. 16)
DOI: 10.1007/s10851-006-6228-4
URL: http://link.springer.com/10.1007/s10851-006-6228-4.

[277] X. Pennec, P. Fillard, and N. Ayache. "A Riemannian Framework for Tensor Computing". In: *International Journal of Computer Vision* 66.1 (Jan. 2006), pp. 41–66. (Cited on pp. 16, 17, 51, 57, 58, 101)
DOI: 10.1007/s11263-005-3222-z
URL: http://link.springer.com/10.1007/s11263-005-3222-z.

[278] F. Pfeiffer, T. Weitkamp, O. Bunk, and C. David. "Phase retrieval and differential phase-contrast imaging with low-brilliance X-ray sources". In: *Nature Physics* 2.4 (Mar. 2006), pp. 258–261. (Cited on pp. 5, 10, 11, 13)
DOI: 10.1038/nphys265
URL: http://www.nature.com/doifinder/10.1038/nphys265.

[279] F. Pfeiffer, M. Bech, O. Bunk, P. Kraft, E. F. Eikenberry, C. Brönnimann, C. Grünzweig, and C. David. “Hard-X-ray dark-field imaging using a grating interferometer”. In: *Nature Materials* 7.2 (Jan. 2008), pp. 134–137. (Cited on pp. 4, 5, 10–13, 102, 114)
DOI: 10.1038/nmat2096
URL: http://www.nature.com/doifinder/10.1038/nmat2096.

[280] G. Potdevin, A. Malecki, T. Biernath, M. Bech, T. H. Jensen, R. Feidenhans'l, I. Zanette, T. Weitkamp, J. Kenntner, J. Mohr, P. Roschger, M. Kerschnitzki, W. Wagermaier, K. Klaushofer, P. Fratzl, and F. Pfeiffer. “X-ray vector radiography for bone micro-architecture diagnostics”. In: *Physics in Medicine and Biology* 57.11 (June 2012), pp. 3451–3461. (Cited on pp. 14, 47)
DOI: 10.1088/0031-9155/57/11/3451
URL: http://iopscience.iop.org/0031-9155/57/11/3451/article/.

[281] A. D. Poularikas, ed. *The Transforms and Applications Handbook*. 2nd ed. CRC Press, Feb. 2000. ISBN: 978-0-8493-8595-7
URL: https://www.crcpress.com/The-Transforms-and-Applications-Handbook-Second-Edition/Poularikas/p/book/9780849385957.

[282] F. Prade, A. Yaroshenko, J. Herzen, and F. Pfeiffer. “Short-range order in mesoscale systems probed by X-ray grating interferometry”. In: *EPL (Europhysics Letters)* 112.6 (Jan. 2016), p. 68002. (Cited on pp. 15, 47–49)
DOI: 10.1209/0295-5075/112/68002
URL: http://stacks.iop.org/0295-5075/112/i=6/a=68002?key=crossref.8b1bbbac79ff18aa00568754900d0599.

[283] W. H. Press. *Numerical Recipes*. 3rd ed. The Art of Scientific Computing. Cambridge University Press, Sept. 2007. ISBN: 9780521880688. (Cited on p. 41)
URL: http://www.cambridge.org/de/academic/subjects/mathematics/numerical-recipes/numerical-recipes-art-scientific-computing-3rd-edition.

[284] E. T. Quinto. “An introduction to X-ray tomography and Radon transforms”. In: *Proceedings of Symposia in Applied Mathematics* 63 (2006), p. 1. ISSN: 0160-7634. (Cited on pp. 25, 27)
DOI: 10.1090/psapm/063
URL: http://www.ams.org/books/psapm/063/.

[285] E. T. Quinto. “Singularities of the X-ray transform and limited data tomography in $\mathbb{R}^2$ and $\mathbb{R}^3$”. In: *SIAM J. Math. Anal.* 24.5 (1993), pp. 1215–1225. (Cited on p. 27)
DOI: 10.1137/0524069
URL: http://dx.doi.org/10.1137/0524069.

[286] J. Radon. “Über die Bestimmung von Funktionen durch ihre Integralwerte längs gewisser Mannigfaltigkeiten”. In: *Akad. Wiss.* 69 (1917), pp. 262–277. (Cited on pp. 4, 9, 25, 28).

[287] J. Radon. “On the determination of functions from their integral values along certain manifolds”. In: *IEEE Transactions on Medical Imaging* 5.4 (1986), pp. 170–176. (Cited on pp. 4, 9)
DOI: 10.1109/TMI.1986.4307775
URL: http://ieeexplore.ieee.org/document/4307775/.

[288] E. A. Rakhmanov, E. B. Saff, and Y. M. Zhou. “Minimal Discrete Energy on the Sphere”. In: *Mathematical Research Letters* 1.6 (1994), pp. 647–662. (Cited on p. 54)
DOI: 10.4310/MRL.1994.v1.n6.a3
URL: http://www.intlpress.com/site/pub/pages/journals/items/mrl/content/vols/0001/0006/a003/.

[289] S. Ramani, T. Blu, and M. Unser. “Monte-Carlo SURE: A black-box optimization of regularization parameters for general denoising algorithms”. In: *IEEE Transactions on Image Processing* 17.9 (2008), pp. 1540–1554. (Cited on p. 37)
DOI: 10.1109/TIP.2008.2001404
URL: http://ieeexplore.ieee.org/document/4598837/.

[290] S. Ramani and J. A. Fessler. “Convergent iterative CT reconstruction with sparsity-based regularization”. In: *International Meeting on Fully Three-Dimensional Image Reconstruction in Radiology and Nuclear Medicine* (June 2011), pp. 302–305. (Cited on p. 45).

[291] S. Ramani, Z. Liu, J. Rosen, J. Nielsen, and J. A. Fessler. “Regularization Parameter Selection for Nonlinear Iterative Image Restoration and MRI Reconstruction Using GCV and SURE-Based Methods”. In: *IEEE Transactions on Image Processing* 21.8 (Aug. 2012), pp. 3659–3672. (Cited on p. 37)
DOI: 10.1109/TIP.2012.2195015
URL: http://ieeexplore.ieee.org/lpdocs/epic03/wrapper.htm?arnumber=6185677.

[292] S. Ramani and J. A. Fessler. “A Splitting-Based Iterative Algorithm for Accelerated Statistical X-Ray CT Reconstruction”. In: *IEEE Transactions on Medical Imaging* 31.3 (Mar. 2012), pp. 677–688. (Cited on p. 45)
DOI: 10.1109/TMI.2011.2175233
URL: http://ieeexplore.ieee.org/lpdocs/epic03/wrapper.htm?arnumber=6072266.

[293] G. N. Ramachandran and A. V. Lakshminarayanan. “Three-dimensional reconstruction from radiographs and electron micrographs: application of convolutions instead of Fourier transforms.” In: *Proceedings of the National Academy of Sciences of the United States of America* 68.9 (Sept. 1971), pp. 2236–2240. (Cited on p. 42)
DOI: 10.1073/pnas.68.9.2236
URL: http://www.pnas.org/cgi/doi/10.1073/pnas.68.9.2236.

[294] C. Raven, A. Snigirev, I. Snigireva, P. Spanne, A. Souvorov, and V. Kohn. “Phase-contrast microtomography with coherent high-energy synchrotron x rays”. In: *Applied physics letters* 69.13 (Sept. 1996), pp. 1826–1828. (Cited on p. 10)
DOI: 10.1063/1.117446
URL: http://aip.scitation.org/doi/10.1063/1.117446.

[295] M. T. Rekveldt. “Novel SANS instrument using Neutron Spin Echo”. In: *Nuclear Instruments and Methods in Physics Research Section B: Beam Interactions with Materials and Atoms* 114.3-4 (July 1996), pp. 366–370. (Cited on p. 47)
DOI: 10.1016/0168-583X(96)00213-3
URL: http://www.sciencedirect.com/science/article/pii/0168583X96002133?via%3Dihub.

[296] R. J. Renka. “Algorithm 772: STRIPACK: Delaunay triangulation and Voronoi diagram on the surface of a sphere”. In: *ACM Transactions on Mathematical Software (TOMS)* 23.3 (Sept. 1997), pp. 416–434. (Cited on pp. 54, 123)
DOI: 10.1145/275323.275329
URL: http://portal.acm.org/citation.cfm?doid=275323.275329.

[297] V. Revol, C. Kottler, R. Kaufmann, F. Cardot, P. Niedermann, I. Jerjen, T. Lüthi, U. Straumann, U. Sennhauser, and C. Urban. “Sensing small angle scattering with an X-ray grating interferometer”. In: *2010 IEEE Nuclear Science Symposium and Medical Imaging Conference (2010 NSS/MIC)*. IEEE, 2010, pp. 892–895. ISBN: 978-1-4244-9106-3. (Cited on p. 14)
DOI: 10.1109/NSSMIC.2010.5873889
URL: http://ieeexplore.ieee.org/lpdocs/epic03/wrapper.htm?arnumber=5873889.

[298] V. Revol, I. Jerjen, C. Kottler, P. Schütz, R. Kaufmann, T. Lüthi, U. Sennhauser, U. Straumann, and C. Urban. “Sub-pixel porosity revealed by x-ray scatter dark field imaging”. In: *Journal of Applied Physics* 110.4 (2011), p. 044912. (Cited on p. 14)
DOI: 10.1063/1.3624592
URL: http://scitation.aip.org/content/aip/journal/jap/110/4/10.1063/1.3624592.

[299] V. Revol, C. Kottler, R. Kaufmann, A. Neels, and A. Dommann. “Orientation-selective X-ray dark field imaging of ordered systems”. In: *Journal of Applied Physics* 112.11 (2012), p. 114903. (Cited on pp. 14, 15, 47)
DOI: 10.1063/1.4768525
URL: http://scitation.aip.org/content/aip/journal/jap/112/11/10.1063/1.4768525.

[300] V. Revol, B. Plank, R. Kaufmann, J. Kastner, C. Kottler, and A. Neels. “Laminate fibre structure characterisation of carbon fibre-reinforced polymers by X-ray scatter dark field imaging with a grating interferometer”. In: *NDT & E International* 58 (Sept. 2013), pp. 64–71. (Cited on pp. 14, 15)
DOI: 10.1016/j.ndteint.2013.04.012
URL: http://linkinghub.elsevier.com/retrieve/pii/S0963869513000686.

[301] A. Rieder. *Keine Probleme mit Inversen Problemen*. Wiesbaden: Vieweg+Teubner Verlag, 2003. ISBN: 978-3-528-03198-5. (Cited on pp. 31–34, 36)
DOI: 10.1007/978-3-322-80234-7
URL: http://link.springer.com/10.1007/978-3-322-80234-7.

[302] L. Rigon, F. Arfelli, and R. H. Menk. “Generalized diffraction enhanced imaging to retrieve absorption, refraction and scattering effects”. In: *Journal of Physics D: Applied Physics* 40.10 (May 2007), pp. 3077–3089. (Cited on p. 10)
DOI: 10.1088/0022-3727/40/10/011
URL: http://stacks.iop.org/0022-3727/40/i=10/a=011?key=crossref.b4279aa3823ee9f56022f31ec7e2f0df.

[303] L. Rigon, F. Arfelli, and R. H. Menk. “Three-image diffraction enhanced imaging algorithm to extract absorption, refraction, and ultrasmall-angle scattering”. In: *Applied physics letters* 90.11 (Mar. 2007), p. 114102. (Cited on p. 10)
DOI: 10.1063/1.2713147
URL: http://scitation.aip.org/content/aip/journal/apl/90/11/10.1063/1.2713147.

[304] W. Ring. “Structural properties of solutions to total variation regularization problems”. In: *ESAIM: Mathematical Modelling and Numerical Analysis* 34.04 (2000), pp. 799–810. (Cited on p. 39)
URL: http://journals.cambridge.org/abstract_S0764583X00001047.

[305] A. Ritter, G. Anton, and T. Weber. “Simultaneous Maximum-Likelihood Reconstruction of Absorption Coefficient, Refractive Index and Dark-Field Scattering Coefficient in X-Ray Talbot-Lau Tomography”. In: *PLOS ONE* 11.10 (Oct. 2016), e0163016. (Cited on p. 121)
DOI: 10.1371/journal.pone.0163016
URL: http://dx.plos.org/10.1371/journal.pone.0163016.

[306] R. T. Rockafellar. “Monotone Operators and the Proximal Point Algorithm”. In: *SIAM Journal on Control and Optimization* 14.5 (1976), pp. 877–898. (Cited on p. 44)
DOI: 10.1137/0314056
URL: http://epubs.siam.org/doi/10.1137/0314056.

[307] A. J. Rockmore and A. Macovski. “A Maximum Likelihood Approach to Transmission Image Reconstruction from Projections”. In: *IEEE Transactions on Nuclear Science* 24.3 (1977), pp. 1929–1935. (Cited on p. 40)
DOI: 10.1109/TNS.1977.4329128
URL: http://ieeexplore.ieee.org/document/4329128/.

[308] W. C. Röntgen. “On a New Kind of Rays”. In: *Nature* 53.1369 (Jan. 1896), pp. 274–276. (Cited on p. 3)
DOI: 10.1038/053274b0
URL: http://www.nature.com/doifinder/10.1038/053274b0.

[309] W. C. Röntgen. “Über eine neue Art von Strahlen”. In: *Sitzungsberichte der Physikalisch-Medizinischen Gesellschaft zu Würzburg*. Berlin, Heidelberg: Springer, 1896. ISBN: 978-3-642-49402-4. (Cited on pp. 3, 4).

[310] H. D. Rosas, S. Y. Lee, A. C. Bender, A. K. Zaleta, M. Vangel, P. Yu, B. Fischl, V. Pappu, C. Onorato, J.-H. Cha, D. H. Salat, and S. M. Hersch. “Altered white matter microstructure in the corpus callosum in Huntington’s disease: Implications for cortical “disconnection””. In: *NeuroImage* 49.4 (Feb. 2010), pp. 2995–3004. (Cited on p. 16)
DOI: 10.1016/j.neuroimage.2009.10.015
URL: http://linkinghub.elsevier.com/retrieve/pii/S1053811909010866.

[311] H. Rositi, V. Hubert, L. Weber, E. Ong, L. P. Berner, C. Frindel, D. Rousseau, C. Olivier, M. Langer, T. H. Cho, N. Nighoghossian, Y. Berthezène, F. Peyrin, F. Chauveau, and M. Wiart. “High throughput three-dimensional imaging of myelin fibers in the whole mouse brain”. In: *User -Dedicated Microsymposium UDM ESRF user meeting - Quantitative coherent X -ray diffraction imaging* (Feb. 2017). (Cited on p. 131)
URL: https://hal.archives-ouvertes.fr/hal-01466159.

[312] S. V. Roth, R. Döhrmann, M. Dommach, M. Kuhlmann, I. Kröger, R. Gehrke, H. Walter, C. Schroer, B. Lengeler, and P. Müller-Buschbaum. “Small-angle options of the upgraded ultrasmall-angle x-ray scattering beamline BW4 at HASYLAB”. In: *Review of Scientific Instruments* 77.8 (2006), p. 085106. (Cited on p. 10)
DOI: 10.1063/1.2336195
URL: http://scitation.aip.org/content/aip/journal/rsi/77/8/10.1063/1.2336195.

[313] L. I. Rudin, S. Osher, and E. Fatemi. “Nonlinear total variation based noise removal algorithms”. In: *Physica D: Nonlinear Phenomena* 60.1 (1992), pp. 259–268. (Cited on pp. 38, 63)
DOI: 10.1016/0167-2789(92)90242-F
URL: http://linkinghub.elsevier.com/retrieve/pii/016727899290242F.

[314] C. Runge. “Über die numerische Auflösung von Differentialgleichungen”. In: *Mathematische Annalen* 46 (1895), pp. 167–178. (Cited on p. 104).

[315] B. P. Rynne and M. A. Youngson. *Linear Functional Analysis*. Springer Undergraduate Mathematics Series. London: Springer, 2008. ISBN: 978-1-84800-004-9. (Cited on p. 23)
DOI: 10.1007/978-1-84800-005-6
URL: http://link.springer.com/10.1007/978-1-84800-005-6.

[316] B. P. Rynne and M. A. Youngson. “Preliminaries”. In: *Linear Functional Analysis*. London: Springer, 2008, pp. 1–30. ISBN: 978-1-84800-004-9
DOI: 10.1007/978-1-84800-005-6_1
URL: http://link.springer.com/10.1007/978-1-84800-005-6_1.

[317] S. Saito, Y. Mori, Y. Yoshioka, and K. Murase. “High-resolution ex vivo imaging in mouse spinal cord using micro-CT with 11.7T-MRI and myelin staining validation”. In: *Neuroscience Research* 73.4 (Aug. 2012), pp. 337–340. (Cited on p. 131)
DOI: 10.1016/j.neures.2012.05.004
URL: http://linkinghub.elsevier.com/retrieve/pii/S016801021200106X.

[318] C. G. Schroer, M. Kuhlmann, S. V. Roth, R. Gehrke, N. Stribeck, A. Almendarez-Camarillo, and B. Lengeler. “Mapping the local nanostructure inside a specimen by tomographic small-angle x-ray scattering”. In: *Applied physics letters* 88.16 (2006), p. 164102. (Cited on p. 10)
DOI: 10.1063/1.2196062
URL: http://scitation.aip.org/content/aip/journal/apl/88/16/10.1063/1.2196062.

[319] O. Scherzer, M. Grasmair, H. Grossauer, M. Haltmeier, and F. Lenzen. *Variational Methods in Imaging*. Ed. by S. S. Antman, J. E. Marsden, and L. Sirovich. Vol. 167. Applied Mathematical Sciences. New York, NY: Springer, 2009. ISBN: 978-0-387-30931-6. (Cited on pp. 37, 38)
DOI: 10.1007/978-0-387-69277-7
URL: http://link.springer.com/10.1007/978-0-387-69277-7.

[320] S. Schleede, M. Bech, K. Achterhold, G. Potdevin, M. Gifford, R. Loewen, C. Limborg, R. Ruth, and F. Pfeiffer. “Multimodal hard X-ray imaging of a mammography phantom at a compact synchrotron light source”. In: *Journal of synchrotron radiation* 19.4 (May 2012), pp. 525–529. (Cited on p. 13)
DOI: 10.1107/S0909049512017682
URL: http://scripts.iucr.org/cgi-bin/paper?S0909049512017682.

[321] S. Schleede, F. G. Meinel, M. Bech, J. Herzen, K. Achterhold, G. Potdevin, A. Malecki, S. Adam-Neumair, S. F. Thieme, F. Bamberg, K. Nikolaou, A. Bohla, A. Ö. Yildirim, R. Loewen, M. Gifford, R. Ruth, O. Eickelberg, M. Reiser, and F. Pfeiffer. “Emphysema diagnosis using X-ray dark-field imaging at a laser-driven compact synchrotron light source.” In: *Proceedings of the National Academy of Sciences of the United States of America* 109.44 (Oct. 2012), pp. 17880–17885. (Cited on p. 13)
DOI: 10.1073/pnas.1206684109
URL: http://www.pnas.org/content/109/44/17880.full.

[322] F. Schwab, S. Schleede, D. Hahn, M. Bech, J. Herzen, S. Auweter, F. Bamberg, K. Achterhold, A. Ö. Yildirim, A. Bohla, O. Eickelberg, R. Loewen, M. Gifford, R. Ruth, M. F. Reiser, K. Nikolaou, F. Pfeiffer, and F. G. Meinel. “Comparison of Contrast-to-Noise Ratios of Transmission and Dark-Field Signal in Grating-Based X-ray Imaging for Healthy Murine Lung Tissue”. In: *Zeitschrift für Medizinische Physik* 23.3 (Sept. 2013), pp. 236–242. (Cited on p. 13)
DOI: 10.1016/j.zemedi.2012.11.003
URL: http://linkinghub.elsevier.com/retrieve/pii/S0939388912001481.

[323] F. Schaff, A. Malecki, G. Potdevin, E. Eggl, P. B. Noël, T. Baum, E. G. Garcia, J. S. Bauer, and F. Pfeiffer. “Correlation of X-Ray Vector Radiography to Bone Micro-Architecture”. In: *Scientific reports* 4 (Jan. 2014). (Cited on p. 14)
DOI: 10.1038/srep03695
URL: http://www.nature.com/doifinder/10.1038/srep03695.

[324] C. Schulte zu Berge, A. Grunau, H. Mahmud, and N. Navab. *CAMPVis – A Game Engine-inspired Research Framework for Medical Imaging and Visualization*. Tech. rep. 2014. (Cited on p. 97).

[325] F. Schaff, M. Bech, P. Zaslansky, C. Jud, M. Liebi, M. Guizar-Sicairos, and F. Pfeiffer. “Six-dimensional real and reciprocal space small-angle X-ray scattering tomography”. In: 527.7578 (Nov. 2015), pp. 353–356. (Cited on p. 10)
DOI: 10.1038/nature16060
URL: http://www.nature.com/doifinder/10.1038/nature16060.

[326] K. Scherer, E. Braig, K. Willer, M. Willner, A. A. Fingerle, M. Chabior, J. Herzen, M. Eiber, B. Haller, M. Straub, H. Schneider, E. J. Rummeny, P. B. Noël, and F. Pfeiffer. “Non-invasive Differentiation of Kidney Stone Types using X-ray Dark-Field Radiography”. In: *Scientific reports* 5 (Apr. 2015), p. 9527. (Cited on p. 13)
DOI: 10.1038/srep09527
URL: http://www.nature.com/doifinder/10.1038/srep09527.

[327] C. U. Schulte zu Berge. “Real-time Processing for Advanced Ultrasound Visualization”. PhD thesis. München, 2016. (Cited on p. 97).

[328] F. Schaff, A. Bachmann, A. Zens, M. F. Zaeh, F. Pfeiffer, and J. Herzen. “Grating-based X-ray dark-field computed tomography for the characterization of friction stir welds: A feasibility study”. In: *Materials Characterization* 129 (July 2017), pp. 143–148. (Cited on p. 14)
DOI: 10.1016/j.matchar.2017.04.023
URL: http://www.sciencedirect.com/science/article/pii/S1044580317301043.

[329] F. Schaff, F. Prade, Y. Sharma, M. Bech, and F. Pfeiffer. “Non-iterative Directional Dark-field Tomography”. In: *Scientific reports* 7.1 (2017), p. 3307. (Cited on p. 15)
DOI: 10.1038/s41598-017-03307-6
URL: https://www.nature.com/articles/s41598-017-03307-6.

[330] L. Schwartz. *Théorie des distributions*. 2nd ed. Paris: Hermann, 1966. (Cited on p. 22).

[331] R. Seidel. "The upper bound theorem for polytopes: an easy proof of its asymptotic version". In: *Computational Geometry* 5.2 (Sept. 1995), pp. 115–116. (Cited on p. 124)
DOI: 10.1016/0925-7721(95)00013-Y
URL: http://linkinghub.elsevier.com/retrieve/pii/092577219500013Y.

[332] L. A. Shepp and B. F. Logan. "The Fourier reconstruction of a head section". In: *IEEE Transactions on Nuclear Science* 21.3 (1974), pp. 21–43. (Cited on p. 42)
DOI: 10.1109/TNS.1974.6499235
URL: http://ieeexplore.ieee.org/lpdocs/epic03/wrapper.htm?arnumber=6499235.

[333] J. R. Shewchuk. *An Introduction to the Conjugate Gradient Method Without the Agonizing Pain*. Tech. rep. Pittsburgh, PA, USA: Carnegie Mellon University, Mar. 1994. (Cited on pp. 43, 44, 88)
URL: %7B%7D.

[334] D. Shimao, H. Sugiyama, K. Hyodo, T. Kunisada, and M. Ando. "Evaluation of X-ray dark-field imaging in visualization of nearly clinical articular cartilage". In: *Nuclear Instruments and Methods in Physics Research Section A: Accelerators, Spectrometers, Detectors and Associated Equipment* 548.1-2 (Aug. 2005), pp. 129–134. (Cited on p. 14)
DOI: 10.1016/j.nima.2005.03.079
URL: http://linkinghub.elsevier.com/retrieve/pii/S0168900205007187.

[335] D. Shimao, H. Sugiyama, T. Kunisada, and M. Ando. "Articular cartilage depicted at optimized angular position of Laue angular analyzer by X-ray dark-field imaging". In: *Applied Radiation and Isotopes* 64.8 (Aug. 2006), pp. 868–874. (Cited on p. 14)
DOI: 10.1016/j.apradiso.2006.03.004
URL: http://linkinghub.elsevier.com/retrieve/pii/S0969804306001515.

[336] E. Y. Sidky, C. M. Kao, and X. Pan. "Accurate image reconstruction from few-views and limited-angle data in divergent-beam CT". In: *Journal of X-Ray Science and Technology* 14 (2006), pp. 119–139. (Cited on p. 39)
URL: http://content.iospress.com/articles/journal-of-x-ray-science-and-technology/xst00155.

[337] E. Y. Sidky and X. Pan. "Image reconstruction in circular cone-beam computed tomography by constrained, total-variation minimization". In: *Physics in Medicine and Biology* 53.17 (Aug. 2008), pp. 4777–4807. (Cited on p. 39)
DOI: 10.1088/0031-9155/53/17/021
URL: http://stacks.iop.org/0031-9155/53/i=17/a=021?key=crossref.3610c169110f92910d46d3a1f79aa788.

[338] S. Sidhu, G. Falzon, S. A. Hart, J. G. Fox, R. A. Lewis, and K. K. W. Siu. "Classification of breast tissue using a laboratory system for small-angle x-ray scattering (SAXS)". In: *Physics in Medicine and Biology* 56.21 (Oct. 2011), pp. 6779–6791. (Cited on p. 10)
DOI: 10.1088/0031-9155/56/21/002
URL: http://stacks.iop.org/0031-9155/56/i=21/a=002?key=crossref.f70794c13335f0bdb824f01cafc4e577.

[339] R. L. Siddon. "Fast calculation of the exact radiological path for a three-dimensional CT array". In: *Medical Physics* 12.2 (1985), pp. 252–255. (Cited on pp. 72, 98)
DOI: 10.1118/1.595715
URL: http://scitation.aip.org/content/aapm/journal/medphys/12/2/10.1118/1.595715.

[340] A. Snigirev, I. Snigireva, V. Kohn, S. Kuznetsov, and I. Schelokov. "On the possibilities of x-ray phase contrast microimaging by coherent high-energy synchrotron radiation". In: *Review of Scientific Instruments* 66.12 (Dec. 1995), pp. 5486–5492. (Cited on p. 10)
DOI: 10.1063/1.1146073
URL: http://aip.scitation.org/doi/10.1063/1.1146073.

[341] J. Song, Q. H. Liu, G. A. Johnson, and C. T. Badea. "Sparseness prior based iterative image reconstruction for retrospectively gated cardiac micro-CT". In: *Medical Physics* 34.11 (Nov. 2016), pp. 4476–4483. (Cited on p. 39)
DOI: 10.1118/1.2795830
URL: http://doi.wiley.com/10.1118/1.2795830.

[342] H. H. B. Sørensen and P. C. Hansen. "Multicore Performance of Block Algebraic Iterative Reconstruction Methods". In: *SIAM Journal on Scientific Computing* 36.5 (Sept. 2014), pp. C524–C546. (Cited on p. 120)
DOI: 10.1137/130920642
URL: http://epubs.siam.org/doi/abs/10.1137/130920642.

[343] J.-L. Starck, F. Murtagh, and J. M. Fadili. *Sparse Image and Signal Processing*. Wavelets, Curvelets, Morphological Diversity. Cambridge University Press, May 2010. ISBN: 9780521119139. (Cited on p. 40)
URL: %7B%7D.

[344] M. Stampanoni, Z. Wang, T. Thüring, C. David, E. Roessl, M. Trippel, R. A. Kubik-Huch, G. Singer, M. K. Hohl, and N. Hauser. "The first analysis and clinical evaluation of native breast tissue using differential phase-contrast mammography." In: *Investigative Radiology* 46.12 (Dec. 2011), pp. 801–806. (Cited on p. 13)
DOI: 10.1097/RLI.0b013e31822a585f
URL: http://content.wkhealth.com/linkback/openurl?sid=WKPTLP:landingpage&an=00004424-201112000-00008.

[345] G. Steidl, J. Weickert, T. Brox, P. Mrázek, and M. Welk. "On the Equivalence of Soft Wavelet Shrinkage, Total Variation Diffusion, Total Variation Regularization, and SIDEs". In: *SIAM Journal on Numerical Analysis* 42.2 (2004), pp. 686–713. (Cited on p. 39)
DOI: 10.1137/S0036142903422429
URL: http://epubs.siam.org/doi/abs/10.1137/S0036142903422429.

[346] E. O. Stejskal and J. E. Tanner. "Spin Diffusion Measurements: Spin Echoes in the Presence of a Time-Dependent Field Gradient". In: *The Journal of Chemical Physics* 42.1 (1965), pp. 288–292. (Cited on p. 16)
DOI: 10.1063/1.1695690
URL: http://scitation.aip.org/content/aip/journal/jcp/42/1/10.1063/1.1695690.

[347] S. R. Stock, F. De Carlo, and J. D. Almer. “High energy X-ray scattering tomography applied to bone”. In: *Journal of Structural Biology* 161.2 (Feb. 2008), pp. 144–150. (Cited on p. 10)
DOI: 10.1016/j.jsb.2007.10.001
URL: http://linkinghub.elsevier.com/retrieve/pii/S1047847707002535.

[348] D. Strong and T. Chan. “Edge-preserving and scale-dependent properties of total variation regularization”. In: *Inverse problems* 19.6 (2003), S165–S187. (Cited on p. 63)
DOI: 10.1088/0266-5611/19/6/059
URL: http://stacks.iop.org/0266-5611/19/i=6/a=059?key=crossref.de29564b123774dc23aaf2d408ab1582.

[349] M. Strobl. “General solution for quantitative dark-field contrast imaging with grating interferometers”. In: *Scientific reports* 4 (Nov. 2014), p. 7243. (Cited on pp. 15, 47–49)
DOI: 10.1038/srep07243
URL: http://www.nature.com/articles/srep07243.

[350] Y. Suzuki and F. Uchida. “Dark-field imaging in hard x-ray scanning microscopy”. In: *Review of Scientific Instruments* 66.2 (1995), p. 1468. (Cited on p. 10)
DOI: 10.1063/1.1145943
URL: http://scitation.aip.org/content/aip/journal/rsi/66/2/10.1063/1.1145943.

[351] D. I. Svergun and M. H. J. Koch. “Small-angle scattering studies of biological macromolecules in solution”. In: *Reports on Progress in Physics* 66.10 (Sept. 2003), pp. 1735–1782. (Cited on p. 10)
DOI: 10.1088/0034-4885/66/10/R05
URL: http://stacks.iop.org/0034-4885/66/i=10/a=R05?key=crossref.536fbea0624dc0240270c53faac55ce5.

[352] A. Tapfer, M. Bech, A. Velroyen, J. Meiser, J. Mohr, M. Walter, J. Schulz, B. Pauwels, P. Bruyndonckx, X. Liu, A. Sasov, and F. Pfeiffer. “Experimental results from a preclinical X-ray phase-contrast CT scanner.” In: *Proceedings of the National Academy of Sciences of the United States of America* 109.39 (Sept. 2012), pp. 15691–15696. (Cited on pp. 10, 13)
DOI: 10.1073/pnas.1207503109
URL: http://www.pnas.org/cgi/doi/10.1073/pnas.1207503109.

[353] M. M. Ter-Pogossian, M. E. Phelps, E. J. Hoffman, and N. A. Mullani. “A Positron-Emission Transaxial Tomograph for Nuclear Imaging (PETT)”. In: *Radiology* 114.1 (Jan. 1975), pp. 89–98. (Cited on p. 16)
DOI: 10.1148/114.1.89
URL: http://pubs.rsna.org/doi/10.1148/114.1.89.

[354] T. Thüring, R. Guggenberger, H. Alkadhi, J. Hodler, M. Vich, Z. Wang, C. David, and M. Stampanoni. “Human hand radiography using X-ray differential phase contrast combined with dark-field imaging”. In: *Skeletal Radiology* 42.6 (Apr. 2013), pp. 827–835. (Cited on p. 14)
DOI: 10.1007/s00256-013-1606-7
URL: http://link.springer.com/10.1007/s00256-013-1606-7.

[355] A. N. Tikhonov. “Solution of incorrectly formulated problems and the regularization method”. In: *Soviet Mathematics* 4 (1963), pp. 1035–1038. (Cited on p. 38).

[356] J. D. Tournier, F. Calamante, D. G. Gadian, and A. Connelly. “Direct estimation of the fiber orientation density function from diffusion-weighted MRI data using spherical deconvolution”. In: *NeuroImage* 23.3 (Nov. 2004), pp. 1176–1185
DOI: 10.1016/j.neuroimage.2004.07.037
URL: http://linkinghub.elsevier.com/retrieve/pii/S1053811904004100.

[357] J. D. Tournier, F. Calamante, and A. Connelly. “Robust determination of the fibre orientation distribution in diffusion MRI: Non-negativity constrained super-resolved spherical deconvolution”. In: *NeuroImage* 35.4 (May 2007), pp. 1459–1472. (Cited on p. 130)
DOI: 10.1016/j.neuroimage.2007.02.016
URL: http://linkinghub.elsevier.com/retrieve/pii/S1053811907001243.

[358] D. Tschumperle and R. Deriche. “Diffusion tensor regularization with constraints preservation”. In: *2001 IEEE Computer Society Conference on Computer Vision and Pattern Recognition. CVPR 2001*. IEEE Comput. Soc, Dec. 2001, pp. I–948–I–953. ISBN: 0-7695-1272-0. (Cited on p. 101)
DOI: 10.1109/CVPR.2001.990631
URL: http://ieeexplore.ieee.org/document/990631/.

[359] D. Tschumperlé and R. Deriche. “Tensor field visualization with pde’s and application to dt-mri fiber visualization”. In: *Workshop Variational Level Set Methods*. 2003. (Cited on p. 101)
URL: http://citeseerx.ist.psu.edu/viewdoc/summary?doi=10.1.1.611.6262.

[360] D. S. Tuch, T. G. Reese, M. R. Wiegell, and V. J. Wedeen. “Diffusion MRI of Complex Neural Architecture”. In: *Neuron* 40.5 (Dec. 2003), pp. 885–895. (Cited on p. 16)
DOI: 10.1016/S0896-6273(03)00758-X
URL: http://linkinghub.elsevier.com/retrieve/pii/S089662730300758X.

[361] D. S. Tuch. “Q-ball imaging”. In: *Magnetic Resonance in Medicine* 52.6 (2004), pp. 1358–1372. (Cited on pp. 16, 121, 123)
DOI: 10.1002/mrm.20279
URL: http://doi.wiley.com/10.1002/mrm.20279.

[362] M. Ulbrich and S. Ulbrich. *Nichtlineare Optimierung*. Basel: Birkhäuser, 2012. ISBN: 978-3-0346-0142-9. (Cited on pp. 43, 63)
DOI: 10.1007/978-3-0346-0654-7
URL: http://www.springer.com/de/book/9783034601429.

[363] B. Vandeghinste, B. Goossens, R. Van Holen, C. Vanhove, A. Pizurica, S. Vandenberghe, and S. Staelens. “Iterative CT Reconstruction Using Shearlet-Based Regularization”. In: *IEEE Transactions on Nuclear Science* 60.5 (Oct. 2013), pp. 3305–3317. (Cited on pp. 40, 63, 66, 72)
DOI: 10.1109/TNS.2013.2275994
URL: http://ieeexplore.ieee.org/document/6589007/.

[364] A. Velroyen, M. Bech, A. Malecki, A. Tapfer, A. Yaroshenko, M. Ingrisch, C. C. Cyran, S. D. Auweter, K. Nikolaou, M. Reiser, and F. Pfeiffer. "Microbubbles as a scattering contrast agent for grating-based x-ray dark-field imaging". In: *Physics in Medicine and Biology* 58.4 (Feb. 2013), N37–N46. (Cited on p. 14)
DOI: 10.1088/0031-9155/58/4/N37
URL: http://iopscience.iop.org.eaccess.ub.tum.de/0031-9155/58/4/N37/article/.

[365] A. Vilanova, S. Zhang, G. Kindlmann, and D. Laidlaw. "An Introduction to Visualization of Diffusion Tensor Imaging and Its Applications". In: *Visualization and Processing of Tensor Fields*. Berlin, Heidelberg: Springer, 2006, pp. 121–153. ISBN: 978-3-540-25032-6. (Cited on p. 97)
DOI: 10.1007/3-540-31272-2_7
URL: http://link.springer.com/10.1007/3-540-31272-2_7.

[366] J. Vogel. "Tomographic Reconstruction beyond Classical X-ray CT". PhD thesis. München, Sept. 2015. (Cited on pp. 5, 95).

[367] Z. Wang, B. C. Vemuri, Y. Chen, and T. H. Mareci. "A Constrained Variational Principle for Direct Estimation and Smoothing of the Diffusion Tensor Field From Complex DWI". In: *IEEE Transactions on Medical Imaging* 23.8 (Aug. 2004), pp. 930–939. (Cited on p. 101)
DOI: 10.1109/TMI.2004.831218
URL: http://ieeexplore.ieee.org/document/1318719/.

[368] Z.-T. Wang, K.-J. Kang, Z.-F. Huang, and Z.-Q. Chen. "Quantitative grating-based x-ray dark-field computed tomography". In: *Applied physics letters* 95.9 (2009), p. 094105. (Cited on p. 13)
DOI: 10.1063/1.3213557
URL: http://scitation.aip.org/content/aip/journal/apl/95/9/10.1063/1.3213557.

[369] H. Wang, A. J. Black, J. Zhu, T. W. Stigen, M. K. Al-Qaisi, T. I. Netoff, A. Abosch, and T. Akkin. "Reconstructing micrometer-scale fiber pathways in the brain: multi-contrast optical coherence tomography based tractography." In: *NeuroImage* 58.4 (Oct. 2011), pp. 984–992. (Cited on p. 131)
DOI: 10.1016/j.neuroimage.2011.07.005
URL: http://linkinghub.elsevier.com/retrieve/pii/S1053811911007658.

[370] B. E. Warren. *X-Ray Diffraction*. New York: Dover Publications, 1990. ISBN: 0486141616. (Cited on p. 5)
URL: %7B%7D.

[371] R. Watts, C. Liston, S. Niogi, and A. M. Ulu. "Fiber tracking using magnetic resonance diffusion tensor imaging and its applications to human brain development". In: *Mental Retardation and Developmental Disabilities Research Reviews* 9.3 (Nov. 2003), pp. 168–177. (Cited on p. 16)
DOI: 10.1002/mrdd.10077
URL: http://doi.wiley.com/10.1002/mrdd.10077.

[372] S. Webb. *From the Watching of Shadows*. The Origins of Radiological Tomography. New York, NY: IOP Publishing Ltd., 1990. ISBN: 9780852743058. (Cited on p. 4)
URL: %7B%7D.

[373] T. Weitkamp, A. Diaz, C. David, F. Pfeiffer, M. Stampanoni, P. Cloetens, and E. Ziegler. "X-ray phase imaging with a grating interferometer". In: *Optics Express* 13.16 (2005), pp. 6296–6304. (Cited on pp. 5, 10, 11)
DOI: 10.1364/OPEX.13.006296
URL: http://www.opticsinfobase.org/abstract.cfm?URI=oe-13-16-6296.

[374] A. Weinmann, L. Demaret, and M. Storath. "Total Variation Regularization for Manifold-Valued Data". In: *SIAM Journal on Imaging Sciences* 7.4 (Oct. 2014), pp. 2226–2257. (Cited on pp. 51, 57, 58, 101–104)
DOI: 10.1137/130951075
URL: http://epubs.siam.org/doi/abs/10.1137/130951075.

[375] A. Weinmann, L. Demaret, and M. Storath. "Mumford–Shah and Potts Regularization for Manifold-Valued Data". In: *Journal of Mathematical imaging and vision* 55.3 (2016), pp. 428–445. (Cited on pp. 51, 108)
DOI: 10.1007/s10851-015-0628-2
URL: http://link.springer.com/10.1007/s10851-015-0628-2.

[376] H. Wen, E. E. Bennett, M. M. Hegedus, and S. Rapacchi. "Fourier X-ray scattering radiography yields bone structural information." In: *Radiology* 251.3 (June 2009), pp. 910–918. (Cited on p. 14)
DOI: 10.1148/radiol.2521081903
URL: http://pubs.rsna.org/doi/abs/10.1148/radiol.2521081903.

[377] A. Williams, S. Barrus, R. K. Morley, and P. Shirley. "An efficient and robust ray-box intersection algorithm". In: *International Conference on Computer Graphics and Interactive Techniques*. New York, NY, USA: ACM Press, 2005, p. 9. (Cited on p. 72)
DOI: 10.1145/1198555.1198748
URL: http://portal.acm.org/citation.cfm?doid=1198555.1198748.

[378] J. Wolf, J. I. Sperl, F. Schaff, M. Schüttler, A. Yaroshenko, I. Zanette, J. Herzen, and F. Pfeiffer. "Lens-term- and edge-effect in X-ray grating interferometry". In: *Biomedical Optics Express* 6.12 (2015), p. 4812. (Cited on p. 13)
DOI: 10.1364/BOE.6.004812
URL: https://www.osapublishing.org/abstract.cfm?URI=boe-6-12-4812.

[379] M. Xu and L. V. Wang. "Photoacoustic imaging in biomedicine". In: *Review of Scientific Instruments* 77.4 (Apr. 2006), p. 041101. (Cited on p. 16)
DOI: 10.1063/1.2195024
URL: http://aip.scitation.org/doi/10.1063/1.2195024.

[380] Y. Yang, J. G. Brankov, and M. N. Wernick. "Content-adaptive mesh modeling for fully-3D tomographic image reconstruction". In: *Image Processing. 2002. Proceedings. 2002 International Conference on IS -*. IEEE, 2002, II–621–II–624 vol.2. ISBN: 0-7803-7622-6. (Cited on p. 72)
DOI: 10.1109/ICIP.2002.1040027
URL: http://ieeexplore.ieee.org/lpdocs/epic03/wrapper.htm?arnumber=1040027.

[381] Y. Yang and X. Tang. “The second-order differential phase contrast and its retrieval for imaging with x-ray Talbot interferometry”. In: *Medical Physics* 39.12 (Nov. 2012), pp. 7237–7253. (Cited on p. 13)
DOI: 10.1118/1.4764901
URL: http://doi.wiley.com/10.1118/1.4764901.

[382] A. Yaroshenko, F. G. Meinel, M. Bech, A. Tapfer, A. Velroyen, S. Schleede, S. Auweter, A. Bohla, A. Ö. Yildirim, K. Nikolaou, F. Bamberg, O. Eickelberg, M. F. Reiser, and F. Pfeiffer. “Pulmonary Emphysema Diagnosis with a Preclinical Small-Animal X-ray Dark-Field Scatter-Contrast Scanner”. In: *Radiology* 269.2 (Nov. 2013), pp. 427–433. (Cited on p. 13)
DOI: 10.1148/radiol.13122413
URL: http://pubs.rsna.org/doi/abs/10.1148/radiol.13122413.

[383] A. Yaroshenko, K. Hellbach, M. Bech, S. Grandl, M. F. Reiser, F. Pfeiffer, and F. G. Meinel. “Grating-based X-ray dark-field imaging: a new paradigm in radiography”. In: *Current Radiology Reports* 2.7 (May 2014), p. 57. (Cited on p. 13)
DOI: 10.1007/s40134-014-0057-9
URL: http://link.springer.com/10.1007/s40134-014-0057-9.

[384] W. Yashiro, Y. Terui, K. Kawabata, and A. Momose. “On the origin of visibility contrast in x-ray Talbot interferometry”. In: *Optics Express* 18.16 (Aug. 2010), pp. 16890–16901. (Cited on pp. 13, 14, 47)
DOI: 10.1364/OE.18.016890
URL: http://www.opticsinfobase.org/viewmedia.cfm?uri=oe-18-16-16890&seq=0&html=true.

[385] W. Yashiro, S. Harasse, K. Kawabata, H. Kuwabara, T. Yamazaki, and A. Momose. “Distribution of unresolvable anisotropic microstructures revealed in visibility-contrast images using x-ray Talbot interferometry”. In: *Physical Review B* 84.9 (Sept. 2011), p. 094106. (Cited on pp. 13, 47)
DOI: 10.1103/PhysRevB.84.094106
URL: http://link.aps.org/doi/10.1103/PhysRevB.84.094106.

[386] W. Yashiro, P. Vagovič, and A. Momose. “Effect of beam hardening on a visibility-contrast image obtained by X-ray grating interferometry”. In: *Optics Express* 23.18 (2015), p. 23462. (Cited on p. 13)
DOI: 10.1364/OE.23.023462
URL: https://www.osapublishing.org/abstract.cfm?URI=oe-23-18-23462.

[387] S.-S. Yoo, H.-J. Park, J. S. Soul, H. Mamata, H. Park, C.-F. Westin, H. Bassan, A. J. Du Plessis, R. L. Robertson Jr, S. E. Maier, S. A. Ringer, J. J. Volpe, and G. P. Zientara. “In Vivo Visualization of White Matter Fiber Tracts of Preterm- and Term-Infant Brains With Diffusion Tensor Magnetic Resonance Imaging”. In: *Investigative Radiology* 40.2 (Feb. 2005), pp. 110–115. (Cited on p. 16)
DOI: 10.1097/01.rli.0000149491.69201.cb
URL: http://content.wkhealth.com/linkback/openurl?sid=WKPTLP:landingpage&an=00004424-200502000-00009.

[388] H. Yu and G. Wang. “Compressed sensing based interior tomography”. In: *Physics in Medicine and Biology* 54.9 (Apr. 2009), pp. 2791–2805. (Cited on p. 39)
DOI: 10.1088/0031-9155/54/9/014
URL: http://stacks.iop.org/0031-9155/54/i=9/a=014?key=crossref.b486a5b14bf36e26eb140ce46b21be48.

[389] F. Zernike. “*Das Phasenkontrastverfahren bei der mikroskopischen Beobachtung*”. In: *Zeitschrift fur technische Physik* 16 (1935), pp. 454–457. (Cited on p. 4).

[390] F. Zernike. “Phase contrast, a new method for the microscopic observation of transparent objects”. In: *Physica* 9.7 (July 1942), pp. 686–698. (Cited on p. 4)
DOI: 10.1016/S0031-8914(42)80035-X
URL: http://linkinghub.elsevier.com/retrieve/pii/S003189144280035X.

[391] F. Zernike. “Phase contrast, a new method for the microscopic observation of transparent objects part II”. In: *Physica* 9.10 (Dec. 1942), pp. 974–986. (Cited on p. 4)
DOI: 10.1016/S0031-8914(42)80079-8
URL: http://linkinghub.elsevier.com/retrieve/pii/S0031891442800798.

[392] F. Zernike. “How I discovered phase contrast”. In: *Nobel Lecture* (Dec. 1953). (Cited on p. 4)
URL: https://www.nobelprize.org/nobel_prizes/physics/laureates/1953/zernike-lecture.pdf.

[393] W. Zhou, J.-F. Cai, and H. Gao. “Adaptive tight frame based medical image reconstruction: a proof-of-concept study for computed tomography”. In: *Inverse problems* 29.12 (Nov. 2013), p. 125006. (Cited on pp. 40, 66, 72)
DOI: 10.1088/0266-5611/29/12/125006
URL: http://stacks.iop.org/0266-5611/29/i=12/a=125006?key=crossref.e7a4f25fd35184970fe70a2d5dd22522.

[394] X. Zhu and P. Milanfar. “Automatic Parameter Selection for Denoising Algorithms Using a No-Reference Measure of Image Content”. In: *IEEE Transactions on Image Processing* 19.12 (Dec. 2010), pp. 3116–3132. (Cited on p. 37)
DOI: 10.1109/TIP.2010.2052820
URL: http://ieeexplore.ieee.org/lpdocs/epic03/wrapper.htm?arnumber=5484579.

Online Resources

[on1] *CUDA*. (Cited on p. 66)
URL: https://developer.nvidia.com/cuda-zone (Visited on May 27, 2017).

[on2] *Matlab*. (Cited on pp. 28, 52, 54, 75, 115, 116, 123, 126)
URL: https://www.mathworks.com/products/matlab.html (Visited on May 27, 2017).

[on3] *OpenCL*. (Cited on p. 66)
URL: https://www.khronos.org/opencl/ (Visited on May 27, 2017).

[on4] *Spherical Harmonics*. (Cited on p. 52)
URL: http://www.boost.org/doc/libs/1_64_0/libs/math/doc/html/math_toolkit/sf_poly/sph_harm.html (Visited on May 27, 2017).

[on5] S. Boyd, N. Parikh, E. Chu, B. Peleato, and J. Eckstein. *MATLAB scripts for alternating direction method of multipliers*. (Cited on p. 45)
URL: https://web.stanford.edu/~boyd/papers/admm/ (Visited on May 27, 2017).

[on6] J. Burkardt. *SPHERE_CVT*. (Cited on pp. 54, 116, 126)
URL: https://people.sc.fsu.edu/~jburkardt/m_src/sphere_cvt/sphere_cvt.html (Visited on May 27, 2017).

[on7] J. Burkardt. *SPHERE_DELAUNAY*. (Cited on pp. 54, 123, 126)
URL: https://people.sc.fsu.edu/~jburkardt/m_src/sphere_delaunay/sphere_delaunay.html (Visited on May 27, 2017).

[on8] J. Burkardt. *SPHERE_VORONOI*. (Cited on p. 54)
URL: https://people.sc.fsu.edu/~jburkardt/m_src/sphere_voronoi/sphere_voronoi.html (Visited on May 27, 2017).

[on9] K. Christensen, M. Velkey, L. M. Stoolman, L. Hessler, D. Mosley-Brower, and M. Hortsch. *Central Nervous System*. (Cited on p. 132)
URL: http://histology.medicine.umich.edu/resources/central-nervous-system (Visited on May 27, 2017).

[on10] K. Christensen, M. Velkey, L. M. Stoolman, L. Hessler, D. Mosley-Brower, and M. Hortsch. *Virtual Slide List*. (Cited on p. 132)
URL: http://histology.medicine.umich.edu/full-slide-list (Visited on May 27, 2017).

[on12] ImFusion GmbH. *ImFusion Suite*. (Cited on p. 135)
URL: https://www.imfusion.de/products/imfusion-suite (Visited on Aug. 19, 2018).

[on13] Khronos Group. *OpenGL*. (Cited on p. 66)
URL: https://www.khronos.org/opengl/ (Visited on May 27, 2017).

[on14] M. J. Mohlenkamp. *A user's guide to spherical harmonics*. (Cited on p. 53)
URL: http://www.ohio.edu/people/mohlenka../research/uguide.pdf (Visited on May 27, 2017).

[on11] NumPy Developers. *NumPy*. (Cited on p. 75)
URL: http://www.numpy.org (Visited on May 27, 2017).

[on15] A. Politis. *Spherical Harmonic Transform Library*. (Cited on pp. 52, 115, 116, 120)
URL: https://github.com/polarch/Spherical-Harmonic-Transform (Visited on May 27, 2017).

[on16] W. C. Röntgen. *Nobel Diploma*. (Cited on p. 4)
URL: http://www.nobelprize.org/nobel_prizes/physics/laureates/1901/rontgen-diploma.html (Visited on May 27, 2017).

[on17] A. Winkler. *Brainder*. (Cited on pp. 132, 133)
URL: https://brainder.org (Visited on May 27, 2017).

List of Figures

List of Code

List of Theorems

Glossary

Acronyms

μCT	Micro-CT 14, 15, 114, 126, 131, 172, 180
1D	one-dimensional 39
2D	two-dimensional 8, 9, 25–28, 39, 41, 42, 66, 104, 106, 171, 172
3D	three-dimensional 15, 25–27, 49, 51, 54, 71, 104, 106, 109, 113, 120, 171, 175
ADMM	Alternating Direction Method of Multipliers 45, 88, 91, 182
ART	Algebraic Reconstruction Technique 41, 42, 87, 179
AXDT	Anisotropic X-ray Dark-field Tomography vii, viii, x, xii, 5, 17, 21, 25, 41, 42, 44, 49–51, 75, 91, 93, 95, 98, 100, 109, 110, 112, 113, 116–121, 123, 126, 129–135, 172, 175, 177
CG	Method of Conjugate Gradients 43, 44, 85, 98, 115, 172, 179
CNS	Central Nervous System viii, 16, 17, 131, 134, 177
CPU	Central Processing Unit 66, 115, 177
CT	Computed Tomography vii, xii, 4, 5, 8–10, 14–17, 25, 27, 32, 33, 39–42, 45, 57, 72, 98, 110–113, 115, 131, 133–135, 171, 172, 177, 183
CUDA	Compute Unified Device Architecture 66, 177
D-MRI	Diffusion Magnetic Resonance Imaging 16, 17, 130, 131, 135, 178
DEI	Diffraction-Enhanced Imaging 10, 178

DTI Diffusion Tensor Imaging 16, 51, 58, 97, 101, 104, 107, 178

DWI Diffusion Weighted Image 101, 178

FBP Filtered Back-Projection 28, 29, 41, 42, 87, 177, 178

FDK Feldkamp, Davis and Kress algorithm 177

FFT Fast (discrete) Fourier Transform 41, 53, 178

FISTA Fast Iterative Soft-Thresholding Algorithm 44, 88, 179

FOV Field Of View 131, 178

GBI Grating Based Imaging 5, 10–12, 48, 131, 132, 134, 171, 179

GFA Generalized Fractional Anisotropy 121, 178

GPU Graphics Processing Unit 66, 115, 179

ISTA Iterative Soft-Thresholding Algorithm 44, 88, 179

MPI Magnetic Particle Imaging 16, 179

MRI Magnetic Resonance Imaging 16, 131, 178, 179, 185

NDT Non-Destructive Testing 4, 180

NLCG Non-Linear CG 88, 179

OpenCL Open Computing Language 66, 103, 115, 180

OpenGL Open Graphics Library 66, 180

OS Ordered Subsets 44, 179

PCA Principal Component Analysis 97, 98, 116, 180

PET Positron Emission Tomography 16, 180

PPXA Parallel ProXimal Algorithm 88, 182

RAM Random Access Memory 66, 115, 181

ROI Region Of Interest 104–107, 114, 126, 127, 129, 172, 181

SART Simultaneous Algebraic Reconstruction Technique 15, 42, 87, 96, 98, 179

SAXS Small Angle X-ray Scattering vii, 7, 8, 10, 13, 17, 47–50, 100, 120, 131, 171, 181

SESANS Spin-Echo Small-Angle Neutron Scattering 15, 47, 118, 182

SIRT Simultaneous Iterative Reconstruction Technique 42, 87, 98, 103, 179

SNR Signal-to-Noise Ratio 107, 181

SPD Symmetric Positive-Definite 43, 44, 51, 58, 182

SPECT Single-Photon Emission Computed Tomography 16, 72, 181

SQS Separable Quadratic Surrogate 43, 87, 179

STL Standard Template Library 66, 182

SVD Singular Value Decomposition 87, 181

TV Total Variation 38–40, 102, 107, 182

VR Volume Rendering 97, 114, 115, 172, 182

XTT X-ray Tensor Tomography vii–x, xii, 5, 15–17, 49, 51, 52, 91, 95–98, 100, 101, 106–113, 116–121, 123, 126, 127, 129, 130, 171, 172, 175

XVR X-ray Vector Radiography 14, 47, 182

Symbols

$C^k(\Omega)$	Banach space of k-times continuously derivable functions on X equipped with the norm $\|\cdot\|_{C^k(\Omega)} = \sum_{n=0}^{k} \sup_{x\in X} \left\|f^{(n)}(x)\right\|$. We write $C(\Omega)$ for $C^0(\Omega)$.	22, 32, 34, 38, 40, 189
$C_c^k(\Omega)$	$:= \left\{f \in C^k(\Omega) \,:\, \operatorname{supp}(f) \text{ is compact}\right\}$.	22
$L_w^p(\Omega)$	Banach space ($1 \leq p < \infty$) of p-integrable functions equipped with the norm $\|\cdot\|_{L_w^p(\Omega)}$. We use the standard short notation $L^p(\Omega) = L_1^p(\Omega)$.	23, 24, 28, 35, 37–39, 51–54, 65, 67, 112, 189
X^Y	$:= \{f : X \to Y\}$, the space of all mappings from X to Y.	22, 190
$\ell_w^p(\Omega)$	Banach space ($1 \leq p < \infty$) of sequences equipped with the norm $\|\cdot\|_{\ell_w^p(\Omega)}$. We use the standard short notation $\ell^p(\Omega) = \ell_1^p(\Omega)$.	23, 34, 35, 37–41, 53, 81, 102–104, 112, 120, 189
χ_A	Indicator function. For $X \subset A$ we define the mapping as $\chi_A : x \to \{0,1\}$ with $\chi_A = 1, \forall x \in A$ and $\chi_A = 0, \forall x \notin A$.	22, 65
$\langle x, y\rangle_X$	The inner product in a Hilbert space X of the two elements $x, y \in X$.	21–23, 28, 32, 34, 53, 54, 65, 96, 98, 112, 115
$\mathcal{F}_N f$	Fourier transform of f (N-dimentional). We omit the subscript if the dimension of f is clearly stated. The inverse transform is denoted as $\mathcal{F}_N^{-1}$.	7, 24, 27, 28, 47

$\mathcal{L}(X,Y)$	$:= \{f \in X^Y \ : \ f$ linear and bound$\}$.	22
$\mathcal{S}(\mathbb{R}^n)$	space of rapidly decreasing functions.	22, 24, 27–29
$\mathcal{P}f$	Funk-Radon transform of f.	54, 123, 124
$\mathcal{R}f$	Radon transform of f.	25–29, 41, 72, 73
$\mathcal{X}f$	X-ray transform of f.	25–27, 48, 50
$\operatorname{diag}(v)$	The diagonal matrix $D \in \mathbb{R}^{N\times N}$ with the diagonal $v \in \mathbb{R}^N$.	44, 98, 111, 113
$\operatorname{dom}(f)$	For a function $f : X \to Y$ we refer to X as domain, i.e. $\operatorname{dom}(f) := X$.	22, 35, 41, 190
$\operatorname{ran}(f)$	For a function $f : X \to Y$ we refer to Y as range, i.e. $\operatorname{ran}(f) := Y$.	22, 35–37, 41, 190
I_s	Riesz potential of order s.	28, 29, 41, 42
σ^n	Standard Lebesque measure on the sphere $\mathbb{S}^n$ and the short notation $s := \sigma^1$,$\sigma := \sigma^2$, i.e $\int_{\mathbb{S}^2} \sigma(u) = 4\pi$.	28, 29, 53, 54, 110–113
$\{e_k\}_{k=0}^{K-1}$	Standard basis for the Euclidean vector-space $\mathbb{R}^K$.	9, 21
Pos_3	The space of symmetric rank-2 tensors (positive symmetric matrices) which is a subset of $\mathbb{R}^{3\times3}$. Sometimes this space is also denoted as Sym_3^+.	16, 22, 51, 52, 55, 57, 58, 96, 99, 101–104, 107
Sym_3	The space of symmetric matrices which is a subset of $\mathbb{R}^{3\times3}$.	22, 190
$f * g$	Convolution of f and g.	7, 23, 24, 47

> *Indeed*

— Teal'c
Stargate SG-1